Establishing a GC-MS/MS method to quantify redox markers in NDUFS4 knockout mice

MT Jooste

orcid.org 0000-0003-2841-2405

Dissertation accepted in partial fulfilment of the requirements for the degree *Master of Science in Biochemistry* at the North-West University

Supervisor: Prof JZ Lindeque

Co-supervisor: Prof BC Vorster

Graduation May 2024

It is not the strongest of the species that survives and not the most intelligent that survives. It is the one that is the most adaptable to change – Charles Darwin

We are all of us walking communities of bacteria. The world shimmers, a pointillist landscape made of tiny living beings – Lynn Marguilis

Nothing in life is to be feared, it is only to be understood. Now is the time to understand more, so that we may fear less – Marie Curie

Preface and Acknowledgements

Taking on this study was certainly one of the most joyous and channelling endeavours I had to endure throughout my entire academic career at the North-West University. At times experiments kept me up until late at night while some moved on through to early morning hours. At times success seemed like an object in the distant future just out of reach and touch however, to achieve success I realised it required refining of experiments and a whole lot of repeating. As such, this study has certainly taught me that even through hard and dark times, never ever give up!

I would like to thank my supervisor, **Prof Zander Lindeque** for his guidance throughout this study. Your logical inputs on experiments and instrumentation were always greatly appreciated. Thank you for all the advice you gave me in regard to experimental troubleshooting and identifying the origin of experimental failure. You were always ready to listen to my experimental problems I was facing, and you always gave credit where it was due. You thoroughly knew your way around analytical equipment and as for your tips and tricks, they were such a great help, and I can honestly say that I adopted those tricks as SOP's. Your knowledge of metabolism and biochemistry as a whole made it an exciting trip to your office if I did not understand something, because I knew that you would guide me into the right direction and therefore, I would always walk out of your office a wiser man. Casual office chats on science or unrelated topic in your office were the best and I thank you for this and all the laughter we shared. Thank you for everything you taught me throughout my Honours and Masters, it was a great honour and privilege to have you as my supervisor!

I would like to thank my co-supervisor, **Prof Chris Vorster** and CHM for making the GC-QQQ available to conduct this study. Thank you for your valuable inputs on calibrator preparation and being there to assess the progress I made throughout these two years. Thank you for steering me in the right direction for experiments that seemed too tough to complete. Thank you to the staff of CHM for always greeting me with a smile and the small talk in between corridors.

A warm thanks to the **Mito-Family** and all the students sitting in **Mito II** for the support you provided me, even if it was just a smile and small talk over some coffee.

Thank you to the **North-west University Preclinical Drug Development Platform (PCDDP)** staff, for the housing and care provided to the mice used in this study. Thank you to all the mice that gave their lives in the pursuit of science and understanding complex diseases.

I would also like to thank my parents, **Kobie and Schantell Jooste** for all of the support and financial aid you provided me throughout my whole academic career. Thank you, dad, for always helping me with technical support on word documents and pointing out writing errors. Thank you, mom, for always being there when I need someone to talk to, and thank you for always listening to me. Without the continuous support of my parents this study would not have been possible and therefore I would always be forever grateful to them.

Lastly, I would like to thank the Boys "Mr. P and Mr. C". The time I had with you guys is something I would never forget for the rest of my life. The late-night talks between you guys was the highlight of some of my days and I would always be grateful to you two.

Abstract

Through normal metabolic reactions, electron carriers such as nicotinamide adenine dinucleotide reduced and flavin adenine dinucleotide reduced (NADH and $FADH_2$) are formed through various metabolic pathways which drive the mitochondrial electron transport chain in the mitochondrial matrix towards adenosine triphosphate (ATP) synthesis. NADH and $FADH_2$ donates electrons to complex I and II of the electron transport chain (ETC) respectively, regenerating oxidized NAD^+ and FAD^+ levels which would ultimately be reduced again. Leigh syndrome (LS) is a phenotype characterized by mutations of the NADH:ubiquinone oxidoreductase subunit S4 (NDUFS4) gene, causing complex I deficiency and with that, disturbance of the NAD^+/NADH redox pair. Targeting reduced and oxidized constituents (redox metabolites) could reveal whether a patient has a redox (NAD^+/NADH) imbalance and if possible treatment options could restore the balance. As such, diagnosing patients with redox imbalance requires accurate and reproducible quantification of redox metabolites. Due to the reactive nature of NAD(P)H and NAD(P), reliable quantification of these species remains difficult, which prompts researchers to rather quantification redox metabolites such as pyruvate and lactate to investigate redox state. Also, to confirm hypothesis generating studies such as untargeted metabolomics investigating redox status, a method that is able to quantify metabolites linked to redox metabolism more accurately is required to confirm the hypothesis of previous untargeted studies. As such, a gas chromatography-tandem mass spectrometry (GC-MS/MS) method was developed to accurately quantify 24 redox metabolites, aiding treatment studies focusing on restoring redox balance. The newly developed method was applied to NDUFS4 KO and WT mouse liver, brain, and heart tissue to reveal changes in redox metabolites as a result of NAD/NADH redox imbalance. Multiple perturbations in redox markers were revealed throughout the liver brain and heart tissue, with some of the perturbations only occurring in certain tissue types. The heart exhibited the most perturbations in redox metabolites and redox ratios, followed by the liver and then the brain. As a whole, it seemed that the liver released accumulated redox metabolites into the circulation, while the heart and brain import the accumulated intermediates of metabolism to restore redox balance to ensure that energy homeostasis is maintained.

Key terms: NADH, NAD^+, Complex I, Reduced, Oxidized, Redox metabolites, Redox imbalance, NDUFS4, Quantify, GC-MS/MS.

TABLE OF CONTENTS

List of abbreviations:

µL: Microliter

2HG: 2-hydroxyglutarate

2KG: 2-ketoglutarate

2-k-3-mbut: 2-keto-3-methylbutyrate

2-k-3-mval: 2-keto-3-methylvalerate

2-k-4-mval: 2-keto-4-methylvalerate

2-OH-3-mval: 2-hydroxy-3-methylvalerate

2-OH-4mval: 2-hydroxy-3-methylvalerate

3HBA: 3-hydroxybutyric acid

3PBA: 3-phenylbutyric acid

ACA: Acetoacetate

ATP: Adenosine triphosphate

BCAA: Branch chain amino acid

BCKA: Branch chain ketoacid

BCKADH: Branch chain ketoacid dehydrogenase

BSTFA: B, O-bis(trimethylsilyl)trifluoroacetamide

C19: Nonadecanoic acid

°C: Degrees Celsius

CE: Collision energy

CI: Chemical ionization

CI: Complex I

CII: Complex II

CID: Collision induced dissociation

CO_2: Carbon dioxide

CoA: Coenzyme A

CV: Coefficient of Variance

DNA: Deoxyribonucleic acid

dMRM: Dynamic multiple reaction monitoring

EI: Electron Impact Ionization

ESI: Electrospray Ionization

FAME: Fatty acid methyl ester

FAD: Oxidized Flavin adenine dinucleotide

FADH: Reduced Flavin adenine dinucleotide

FDR: False discovery rate

GC: Gas Chromatography

GDH: Glutamate dehydrogenase

GLUT: Glucose transporter

GSH: Reduced Glutathione

GSSG: Oxidized Glutathione

HPLC: High-pressure Liquid Chromatography

HT: Heterozygous

ID: Identification

IDH2: Isocitrate dehydrogenase 2

IEM: Inborn errors of metabolism

kDa: Kilodalton

KO: Knock-out

LC: Liquid Chromatography

LOD: Limit of Detection

LOQ: Limit of Quantification

LS: Leigh Syndrome

MDH1: Malate dehydrogenase 1

MDH2: Malate dehydrogenase 2

MELAS: Mitochondrial encephalomyopathy lactic acidosis and stroke-like episodes

mg: Milligram

mm: millimetre

MOX: Methoxyamine

MRM: Multiple Reaction Monitoring

ms: Milliseconds

MS/MS: Tandem mass spectrometry

MS: Mass Spectrometry

MSTFA: N-methyl-N-trimethylsilyltrifluoroacetamide

MS2: Mass spectrometer 2

MTBSTFA: N-tert-butyldimethylsilyl-N-methyltrifluoroacetamide

mtDNA: Mitochondrial Deoxyribonucleic acid

NAD: Oxidized nicotinamide adenine dinucleotide

NADH: Reduced nicotinamide adenine dinucleotide

NADP: Oxidized nicotinamide adenine dinucleotide phosphate

NADPH: Reduced nicotinamide adenine dinucleotide phosphate

NBS: Newborn screening

nDNA: Nuclear Deoxyribonucleic acid

NDUFS4: NADH:ubiquinone oxidoreductase iron-sulphur protein 4

$Ndufs4^{+}/^{+}$: Wildtype

$Nudfs4^{-}/^{-}$: Knockout

ng: Nanogram

NMR: Nuclear Magnetic Resonance

NNT: Nicotinamide nucleotide transhydrogenase

PCR: Polymerase chain reaction

PDH: Pyruvate dehydrogenase

ppm: parts per million

PPP: Pentose Phosphate Pathway

Q2: Collision cell 2

QC: Quality Control

QQQ: Triple Quadrupole

Quali: Qualifier

Quant: Quantifier

CV: Coefficient of variance

RC: Respiratory chain

RNS: Reactive Nitrogen Species

ROS: Reactive Oxygen Species

SIM: Single Ion Monitoring

TBDMCS: tert-butyldimethylchlorosilane

tBDMS: tert-butyldimethylsiliyl

TCA: Tricarboxylic acid cycle

TMCS: Trimethylchlorosilane

TMS: Trimethylsilyl

TOF: Time-of-Flight

WT: Wild-type

LIST OF FIGURES

CHAPTER 1 - INTRODUCTION

1 Introduction to redox metabolism

An organism's metabolism refers to the various reactions that small molecular products (metabolites) undergo to produce adenosine triphosphate (ATP) as an energy source which ultimately contributes to the normal functioning of the organism (Spinelli & Haigis, 2018). Central to metabolism is the respiratory chain (RC), consisting of protein complexes imbedded in the innermembrane of mitochondria. The RC is responsible for the vast majority of ATP generated within the cell (Detmer & Chan, 2007). Complex I (NADH:ubiquinone oxidoreductase) (CI) of the RC consists of several subunits with the NDUFS4 subunit playing an essential role in the stabilization and architecture of CI (Leong *et al*, 2012). Mutations in encoding regions for CI subunits cause the severe mitochondrial disease known as Leigh syndrome (LS), which manifests in the early neonatal period as failure to thrive, seizures, encephalopathy and blindness (Irwin *et al.*, 2013). Impaired CI activity causes the accumulation of reduced constituents (e.g. reduced nicotinamide dinucleotide [NADH]) and associated 'redox' metabolites, which can be quantified to aid diagnostic procedures and to monitor treatments.

Redox metabolites are intermediates involved in oxidation and reduction reactions in various pathways. Many redox reactions are catalyzed by dehydrogenases which use NAD^+ as coenzyme. When CI is impaired and NADH accumulates, these reactions slow or reverse which leads to perturbed ratios of the substrates and products (i.e. redox metabolites) of the respective dehydrogenases. A comparison of these redox ratios could thus reveal whether a patient (or model animal) has a redox ($NADH:NAD^+$) imbalance, and also whether specific treatments restore this balance. Needless to say, accurate/reproducible quantification is mandatory when redox metabolites are screened in the clinical setting (Castelli *et al.*, 2021).

Most of the redox metabolites are classified as organic acids which are compounds with a carboxylic acid functional group. Organic acids are native to almost all metabolic pathways from intermediary metabolism including the TCA cycle, carbohydrate metabolism, fatty acid oxidation and protein metabolism (Hoffmann & Feyh, 2003). They are easily derivatized and analysed with gas chromatography (GC) even though various other specialized analytical platforms like liquid chromatography (LC), nuclear magnetic resonance (NMR) and mass spectrometry (MS) can also be used. This study aimed to develop and employ a gas chromatography-tandem mass spectrometry (GC-MS/MS) analytical method to achieve reproducible quantification of key redox metabolites when studying NDUFS4 knockout mice tissue samples.

GC-based metabolomics require derivatization, of which the synthesis of trimethylsilyl (TMS)-derivatives are the most popular (Zarate *et al*, 2017). Unfortunately, TMS-derivatives are not

always ideal for targeted analysis as the commonly acquired $[M-15]^+$ ions are usually low in abundance and result in low sensitivity when used for detection and quantification (Vielhauer *et al.*, 2011). To overcome the low sensitivity of the $[M-15]^+$ ions, N-tert-butyldimethylsilyl-N-methyltrifluoroacetamide (MTBSFTA) derivatization is a promising alternative which yields tert-butyldimethylsilyl (tBDMS) derivatives with an abundant $[M-57]^+$ ion. This study exploited this characteristic of MTBSTFA derivatization with the development of a multiple reaction monitoring (MRM) detection method able to specifically detect target redox metabolites with proper sensitivity.

CHAPTER 2 – LITERATURE STUDY

2 The mitochondria and redox metabolism explored through metabolomics

2.1 Mitochondria and complex I deficiency

The mitochondrion is a double membrane organelle common to eukaryotic cells which consists of protein complexes embedded in the inner membrane. These protein complexes (also known as the RC) function as proton pumps, generating a proton motor force that drives ATP synthase (Complex V) to synthesize ATP (Detmer & Chan, 2007). Dietary fats, carbohydrates and proteins are metabolized through various metabolic pathways and finally shuttled to the tricarboxylic acid (TCA) cycle where they are fully oxidized to yield the reducing constituents NADH and $FADH_2$ (Walsh *et al.*, 2018). These reducing constituents donate electrons to Complex I (CI) and Complex II (CII) of the RC to pump protons into the intermembrane space, which ultimately causes the proton gradient to produce ATP via the action of the F_1F_0-subunit of ATP synthase (Watt *et al.*, 2010). Finally, large numbers of ATP synthesized by the mitochondria acts as a universal energy source for the cell, fuelling the energetic needs required for biological processes.

The mitochondria are not only a hub for catabolic reactions and ATP synthesis, but also play an integral role in certain anabolic reactions. These anabolic reactions include the biosynthesis of fatty acids, cholesterol, certain amino acids, nucleotides and heme (Ahn & Metallo, 2015). Metabolic by-products are also formed in the mitochondria as a result of normal metabolic processes. These metabolic by-products include reactive oxygen species (ROS), which when synthesised at high levels causes oxidative damage to DNA, proteins and lipids (i.e. oxidative stress) and at low concentrations act as important signalling molecules for various cellular functions (Schieber & Chandel, 2014). Additionally, mitochondria are also responsible for Ca^{2+} signalling and uptake, which plays an integral part in metabolic reactions and various cellular signalling pathways (Szabadkai & Duchen, 2008). More so, the activity of certain enzymes from the TCA cycle is affected by mitochondrial Ca^{2+} levels and thus affects the rate at which reducing constituents are synthesised in the TCA cycle (Glancy & Balaban, 2012). Altogether, the normal functioning of mitochondria within a biological system is of major importance in cellular processes, metabolism, signalling and scavenging pathways, therefore mitochondrial dysfunction can affect a wide range of cellular activities and in the end cellular death.

The RC complexes are transcribed from both mitochondrial DNA (mtDNA) and nuclear DNA (nDNA), with a total of 92 genes encoding for the complex subunits of the RC. The nuclear genome encodes for 79 subunits with the mitochondrial genome encoding the remaining 13 subunits (Chinnery & Hudson, 2013). Each mitochondrion contains multiple copies of mtDNA with mutations affecting either all mtDNA (homoplasmy) present, or only a select few copies (heteroplasmy) (Saneto & Sedensky, 2013). mtDNA inheritance is strictly maternal which is different from nDNA inheritance (DiMauro & Davidzon, 2005). Also, mtDNA lacks histones and are mostly made up of exons. The highly oxidative environment of the mitochondria caused by ROS production results in mtDNA acquiring mutations at a much faster rate than nDNA (DeBalsi *et al.*, 2017). Mitochondrial repair machinery has recently been discovered by scientists however, it is thought to be less effective than nDNA repair machinery because of the high mtDNA copy numbers present in either homoplasmic or heteroplasmic forms (Stewart & Chinnery, 2015).

Complex I (NADH:ubiquinone oxidoreductase) is one of the largest protein complexes imbedded in the inner mitochondrial membrane and is at the core of cellular metabolism. NADH produced in pathways such as the TCA cycle and β-oxidation is oxidized to NAD^+ by CI (Benard *et al.*, 2007). CI is assembled through 53 subunits with 46 of them being encoded by nDNA and 7 encoded by mtDNA. The nuclear NDUFS4 gene transcribes for a subunit of CI important in the assembly of the complex. Mutations in the coding sequence of the NDUFS4 gene causes instability when CI is assembled which in turn results in significant lower CI activity (Leong *et al.*, 2012). NDUFS4 gene mutations account for up to 11 % of respiratory complex I deficiencies (Ortigoza-Escobar *et al.*, 2016) with LS being the most commonly characterized phenotype in patients (Leshinsky-Silver *et al.*, 2009). The symptoms include ataxia, mental and growth disability with frequent episodes of dystonia (Breuer *et al.*, 2013). Furthermore, LS patients also suffer from renal failure, cardiomyopathy and diabetes mellitus and thus LS patients usually present with clinical features which are quite diverse (Lake *et al.*, 2015). Currently there are no effective treatments for LS, and clinicians usually aim to treat the symptoms of patients, with the emphasis on vitamin supplementation and a ketogenic diet (Lim & McFarland, 2019). Due to the rapid decline in health observed in patients with LS, it is imperative that screening procedures for patients is done at an early stage to ensure that vitamin supplementation can be done to alleviate symptoms. More importantly, the search for effective treatment is supported by our understanding of the biochemical basis of the disease and each patient's response.

A common finding when screening patients with LS, is an elevated lactate/pyruvate ratio manifesting as lactic acidemia in the urine and blood. However, in some instances patients exhibit normal lactate/pyruvate ratios in which a lactate measurement should be done after ingesting glucose as nutritional source (Baertling *et al.*, 2014). Therefore, urinary and blood lactate/pyruvate ratio measurements are not always sufficient to screen for patients with LS, nor to monitor

treatment. Other metabolites that can be targeted for measurements are amino acids and organic acids, due to these metabolites being profoundly affected in patients with LS (Schubert Baldo & Vilarinho, 2020). LS can also be caused by mutations in encoding regions for the RC originating from mtDNA, which usually present the same clinical manifestations of LS originating from nDNA mutations (Gerards *et al*., 2015). Nonetheless, patients with suspected LS can also undergo genetic diagnosis, in which mtDNA is isolated from biochemically affected tissue such as muscle biopsy and subsequently analysed through the full sequencing of the patients mtDNA (Baertling *et al.*, 2014). However, in this case of mtDNA genetic sequencing, identifying the genetic defect is challenging because patients with suspected mitochondrial disorders display varying clinical features and due to the fact that the mitochondrial disorder could originate from mutations in the nuclear genome or mitochondrial genome (Koopman *et al.*, 2012).

To circumvent the challenges associated with genetic screening procedures for mitochondrial disease, targeted metabolomics through the use of tandem mass spectrometry (MS/MS) can be used. Since the launch of the newborn screening program (NBS) in the 1960's, the usage of platforms such as LC-MS/MS and GC-MS has been regarded as gold standards in the clinical setting to screen for accumulating metabolites caused by specific metabolic disorders (Vogel *et al.*, 2015). In the case of screening procedures for inborn errors of metabolism (IEM), a targeted approach utilizing GC-MS and LC-MS/MS are preferred due to their increased precision, accuracy and specificity over the conventional flow injection analysis (FIA) MS/MS (FIA-MS/MS) methods (Filee *et al.*, 2013).

Knock-out (KO) of the NDUFS4 gene in mouse models has been widely used by researchers to study CI deficiencies due to homozygous NDUFS4 KO mice displaying similar LS like symptoms as observed in humans (Kruse *et al.*, 2008). Moreso, large similarities exist between whole-body NDUFS4 KO mice and LS patients, which occur at a metabolic level with perturbation in the redox balance due to the accumulation of pyruvate and lactate in LS patients and the NDUFS4 mouse model (Van de Wal *et al*., 2022). Multiple studies confirm that impaired CI activity causes accumulation of NADH within the mitochondria and since most of the dehydrogenase enzymes in the TCA cycle utilizes NAD^+ which is already in minute concentrations, feedback inhibition occurs and ends up ultimately haltering the TCA cycle (Scheffler I.E. 2015).

2.2 NAD^+/NADH ratio and redox metabolism

Homeostasis of NAD^+/NADH and $NADP^+$/NADPH ratios are extremely important in the normal functioning of the cell, due to these coenzymes participating in multiple redox reactions and cellular activities (Ying, 2008). Generally speaking, NAD^+/NADH are involved in many catabolic

reactions while $NADP^+$/NADPH drive reduction in anabolic pathways. These coenzymes also play an integral role in the defence against oxidative stress (Agledal *et al.*, 2010) and with the dysregulation of $NADP^+$/NADPH ratios due to mitochondrial disease, the cellular environment is susceptible to adverse ROS damage. Complex I of the respiratory chain is one of the major consumers of NADH and since the balance of cellular energy within a cell is dependable on the redox state of available NAD^+, homeostasis of the $NAD(P)^+$/NAD(P)H ratio and normal functioning of the mitochondrial respiratory chain is of great importance in healthy functioning cells (Bilan & Belousov, 2016). Many dehydrogenase enzymes in various metabolic pathways use NAD^+ as coenzyme when oxidizing the substrate, which consequently leads to the reduction of NAD^+ to NADH. A well-known metabolic pathway consisting of multiple dehydrogenase enzymes located within the mitochondria, is the TCA cycle which reduces NAD^+ to NADH at multiple steps in the pathway and thus providing the RC (specifically complex I) with adequate amounts of reducing constituents (Yang & Sauve, 2016).

Since the inner mitochondrial membrane is impermeable to reduced cytosolic NAD(P) (Cantó *et al.*, 2015), electrons are shuttled to the mitochondrial matrix (and eventually CI) via metabolite shuttles, of which the best described are the malate-aspartate shuttle and the glycerol-3-phosphate shuttle. With the malate-aspartate shuttle, cytosolic oxaloacetate is reduced to malate which can enter the mitochondrion in exchange for aspartate (which replenishes the cytosolic oxaloacetate pool). In the matrix, malate dehydrogenase oxidizes malate to oxaloacetate, producing NADH in the process. The oxaloacetate is converted to aspartate through transamination and gets exported via the same shuttle (Houtkooper *et al.*, 2010). The net reaction of this shuttle is thus the import of electrons to the mitochondrial matrix.

The glycerol-3-phosphate shuttle requires the enzyme glycerol-3-phosphate dehydrogenase, which in the cytosol, catalyses the formation of glycerol-3-phosphate with the oxidation of NADH to NAD^+. Inside the mitochondria, the same enzyme catalyses the reverse reaction in which glycerol-3-phosphate is converted to dihydroxyacetone phosphate with the reduction of FAD to $FADH_2$, whereas $FADH_2$ donates electrons to CII of the RC (McKenna *et al.*, 2006).

The $NADP^+$/NADPH, and reduced / oxidized glutathione (GSH/GSSG) ratios play an equally important role in redox balance and normal cellular metabolism. NADPH is used as a coenzyme in reducing GSSG to GSH, with GSH being utilized for the removal of H_2O_2 and thus acting as an essential antioxidant (Handy & Loscalzo, 2017). Reduction of GSSG to GSH can also be indirectly affected by glucose-6-phosphate dehydrogenase (G6PD), due to this enzyme catalysing the rate-limiting step in the pentose-phosphate-pathway (PPP) which contributes to most of the cellular NADPH produced within the cell (Yang & Sauve, 2016). A source of mitochondrial NADPH is produced through isocitrate dehydrogenase 2 (IDH2), which in the presence of oxygen and the coenzyme $NADP^+$, catalyses the decarboxylation of isocitrate to α-ketoglutarate (Rydström,

2006). Therefore, IDH2 also participates in maintaining cellular NADPH levels and thus the homeostasis of redox balance within the cell. Nicotinamide nucleotide transhydrogenase (NNT) is also an important mitochondrial enzyme in regard to the overall maintenance of the NAD^+/NADH and $NADP^+$/NADPH ratios. NNT can catalyse the forward and reverse reaction of NADH + $NADP^+$ -> NAD^+ + NADPH and thus providing the cell with the essential pools of reducing constituents to maintain redox balance (Ho *et al.*, 2017).

As the NAD^+/NADH redox couple, $NADP^+$ and NADPH are both essential coenzymes for cellular metabolism. In the case of NADPH, the biosynthesis of certain amino acids, fatty acids and the functioning of ribonucleotide reductase involved in nucleotide synthesis, all require NADPH as a reducing constituent for these anabolic processes. As previously discussed, $NADP^+$ is utilized as coenzyme in the PPP and reduced to NADPH providing reducing components for anabolic reactions. More so, it is also used for the synthesis of phospholipids, triacylglycerols and cholesterol (Agledal *et al.*, 2010). All in all, a summary of the metabolic pathways utilizing NAD^+ or NADH is represented in Figure 2.1.

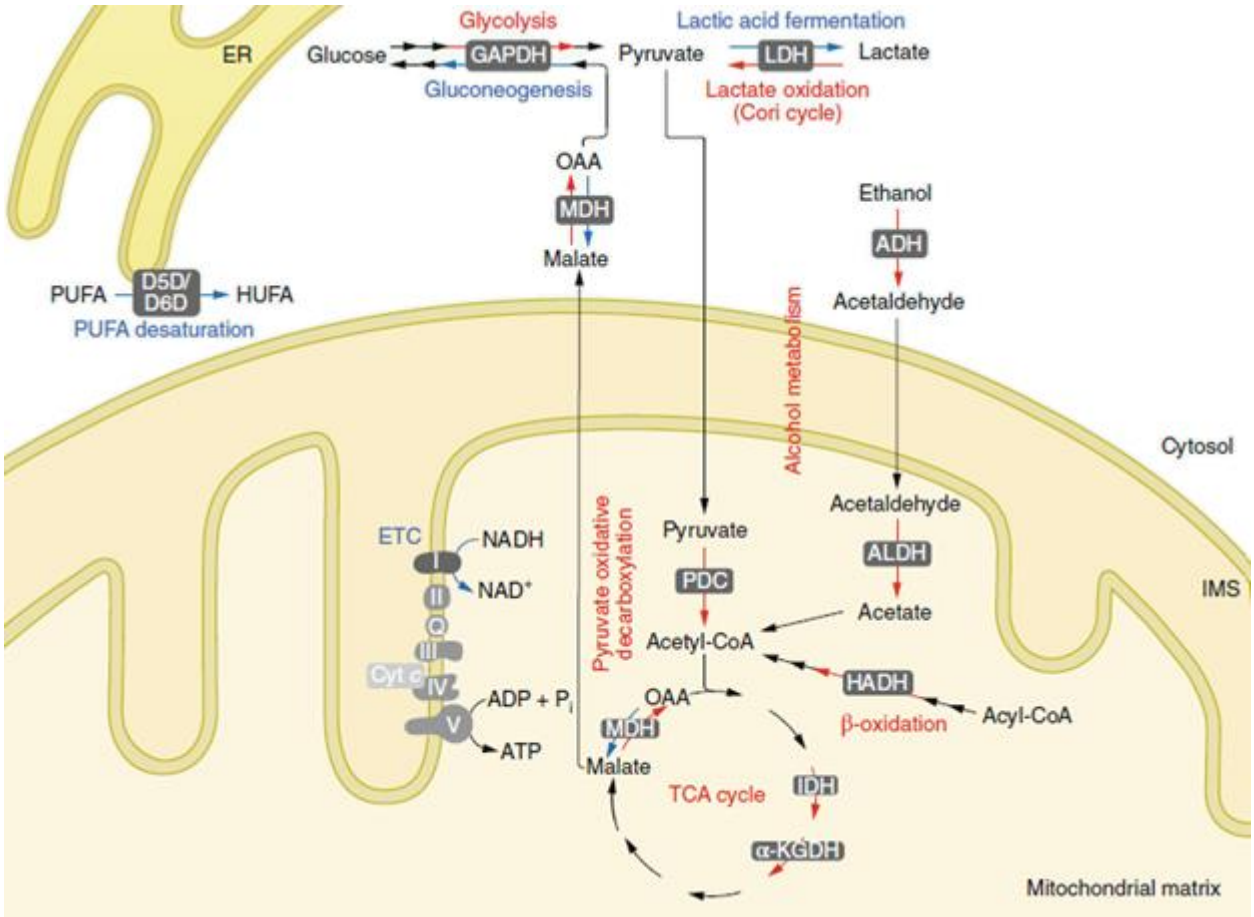

Figure 2.1: Metabolic pathways representing the anaplerosis and the fate of TCA intermediates (Katsyuba *et al.*, 2020)

2.3 Measuring redox metabolism

Measuring $NAD(P)^+$/NAD(P)H levels in cells as well the concentration of these coenzymes compartmentally would provide researchers with key information about the overall redox and metabolic status of the cell. Unfortunately, accurate measurements of these coenzymes are no easy feat, due to the majority of these coenzymes being bound to dehydrogenase enzymes *in vivo* and due to the concentration and reactivity of the redox couple being highly variable across different compartments in the cell (Vina *et al.*, 2016). Some studies measure NAD^+/NADH levels *in vivo* through procedures such as: enzymatic cycling assays, capillary electrophoresis, high performance liquid chromatography (HPLC), and spectrophotometric techniques. These studies typically employ standard procedures such as centrifugation, filtering and heat exposure in their workflow which can result in metabolite degradation and interaction of target compounds with filter material, affecting the yield and this recorded concentration of cellular NAD^+/NADH (Matuszczyk *et al.*, 2015). Due to all these factors, it makes the accurate analysis of NAD^+/NADH ratios to assess the redox status of an organism quite cumbersome. Recently, scientists have developed genetically encoded NADH fluorescence sensors which can be introduced into cells targeting specific subcellular compartments for the accurate analysis of NADH levels in various organelles. Unfortunately, these sensors cannot be used in mice models and patients. Moreover, they are only able to measure NADH fluorescent signals, and thus only partial information about the redox couple NAD^+/NADH in different compartments of the cell is uncovered (Zhao & Yang, 2016).

Given the intricate role $NAD(P)^+$/NAD(P)H plays in metabolism, and the sensitivity of dehydrogenases for redox imbalance, the ratio between substrates and products of these enzymes (i.e., redox metabolites) can reveal a cell/organism's redox status (Xiao *et al*., 2018). It is for this reason that the lactate/pyruvate ratio is often used for the diagnosis and monitoring of LS (Section 2.1). Unfortunately, this redox ratio is a rather a reflection of cytosolic redox state (Corkey & Deeney, 2020). As such, a solution for the analysis of mitochondrial redox status could be through measuring acetoacetate (ACA) and 3-hydroxybutyric acid (3HBA) levels. These two ketone bodies are restrictively produced within the mitochondria through the mitochondrial enzyme 3-hydroxybutyric acid dehydrogenase which requires the coenzymes NAD^+ and NADH to function (Vina *et al.*, 2016). Ideally, assessment of all organic acids linked to redox metabolism can thus reveal much about a cell/organism's redox status.

2.4 Organic acids disturbed by NDUFS4 gene deletion

Organic acids are mono-, di- or tricarboxylic acids with secondary ketone or hydroxyl groups, or both functional groups linked with a certain number of carbons (Becker *et al*., 2015). Organic acids are derived from different metabolic pathways such as: TCA cycle, carbohydrate

metabolism, fatty acid oxidation and protein metabolism (Tsoukalas *et al*., 2017). Analysis of (urinary) organic acids provides a comprehensive reflection of the status of many metabolic pathways in a biological system and is often used in the clinical setup to acquire the health and nutritional status of a patient (Jones & Bennett, 2010). More often than not, the accumulation of organic acids is tremendously pathological (Goldberg *et al.*, 2006) therefore, the accurate identification and quantification of these organic acids are imperative for the detection and/ or prevention of metabolic disease. Inherited metabolic disorders like propionic acidemia, methylmalonic acidemia and tyrosinemia (just to name a few) are diagnosed with the elevated concentration of key organic acids in the biofluids of patients. When propionyl-CoA carboxylase is defective, it causes the accumulation of propionic acid and propionic acid derivatives, hence the name: propionic acidemia. Likewise, methylmalonic acidemia is characterised by the defective methylmalonyl-CoA mutase and diagnosed by elevated methylmalonic acid (and methylcitrate) (Baumgartner *et al*., 2014).

NDUFS4 deficient mice also display alterations in organic acid concentrations, specifically TCA cycle intermediates, along with increased plasma lactate and decreased pyruvate (Grange *et al*., 2021). Markedly increased levels of citrate, aconitate and isocitrate are often detected due to impaired activity of NAD^+ dependent isocitrate dehydrogenase (Yoon *et al.*, 2022). Investigation of heart tissue from NDUFS4 deficient mice also revealed increased levels of the following ketoacids: α-ketoisocaproic acid, β-hydroxy-β-methylbutyric acid, α-keto-β-methylvaleric acid, α-ketoisovaleric acid which is due to impaired activity of ketoacid dehydrogenase enzymes from branch-chain amino acid metabolism, requiring NAD^+ as a cofactor to function (Yoon *et al.*, 2022).

NDUFS4 KO mice brain tissue analysis revealed increase levels of palmitic acid, stearic acid and oleic acid with decreased levels of 9,10-dihydroxystearic acid accounting for the increased flux through the enzyme stearoyl-CoA desaturase to generate NAD^+ since the NAD^+/NADH ratio is decreased in these NDUFS4-deficient mice (Terburgh *et al.*, 2021). Lastly, other significantly affected metabolites include: α-hydroxyglutaric acid, N-acetylglutamic acid, γ-aminobutyric acid, erythronic acid, pipecolic acid and α-aminoadipic acid with pipecolic acid and α-aminoadipic acid alterations caused by impaired lysine catabolism, since lysine catabolism depends on the bioavailability of NAD^+ (Terburgh *et al.*, 2021).

Ketogenesis refers to the synthesis of ketone bodies such as acetone, acetoacetate and 3HBA from fatty acid derived acetyl-CoA which occurs during glucose deprived conditions (McPherson & McEneny, 2012) The conversion of acetoacetate, derived from acetyl-CoA, to 3-hydroxybutyric acid yields NAD^+ (Elamin *et al.*, 2017), and since its known that NDUFS4 KO mice suffer from decreased NAD^+/NADH ratio, potential elevated 3HBA might be seen during analysis as a means of compensation for the loss of homeostasis between NAD^+ and NADH. Clearly, the redox imbalance in NDUFS4 KO mice play a key role on the altered organic acid profiles seen, which

warrant proper characterisation of redox metabolites. More importantly, since all of the abovementioned metabolites are connected to redox metabolism through the redox couple NAD^+/NADH, accurate measurements of these compounds could in turn reveal the redox state of the organism without the problems of measuring NAD^+/NADH.

2.5 GC-MS vs. GC-MS/MS metabolomics

Metabolomics studies are usually attempts at identifying and quantifying small molecule metabolites produced by a biological system through catabolism and anabolism (Newgard C.B. 2017). Various analytical equipment can be used to study the metabolism of a biological system, but the most commonly used techniques are GC, LC, liquid chromatography-mass spectrometry (LC-MS), gas chromatography-mass spectrometry (GC-MS) and NMR (Sandlers, Y. 2017). NMR is capable of identifying and quantifying a wide range of metabolites as well as elucidating structural information (Agin *et al.*, 2016). A pitfall of NMR is its relatively poor sensitivity, which renders NMR unable to identify metabolites with a low concentration within a biological sample (Kohler *et al.*, 2016). In contrast, MS coupled with a hyphenated technique such as GC or LC, allows for the quick analysis of a range of metabolites, even if the metabolites of interest are of low abundance within a biological sample (Marshall & Powers, 2017).

LC-MS has the ability to detect a range of intact metabolites and with installation of traditional reverse phase columns, these systems are able to separate metabolites based on their polarity, ranging from non-polar to slightly polar analytes (Gowda & Djukovic, 2014). The separation of polar compounds suffers from drawbacks such as: large consumption of mobile phase during runs (higher running costs) and polar compounds being insoluble in large quantities of organic solvent, whereas even in the case of utilizing a reverse phase column, polar compounds are less retained (Ruta *et al.*, 2010).

GC-MS has overall better chromatographic resolution than LC due to the typical column length being significantly longer. With compounds in the gaseous phase and the common use of electron impact (EI) ionization, this technique does not suffer from ion suppression (Gowda & Djukovic, 2014). More so, GC-MS is capable of broad-based metabolite analyses with arguably better sensitivity and selectivity. With the commonly used 70 eV EI ionization, metabolite identification is facilitated through the matching of mass spectra from reference compound libraries, especially in untargeted analyses (Wang *et al.*, 2015). In most clinical setups, organic acid analysis is preferably done on a GC-MS system due to the increased chromatographic resolution and increasing availability of commercial and/or public spectral libraries (Christou *et al.*, 2014).

To accurately identify organic acids in a biological sample through initial GC separation and then identification through MS, various scanning methods can be performed. In the case of GC-MS

based metabolomics, a targeted or untargeted approach can be taken by either using the MS in static or scanning mode, respectively. In most cases, untargeted metabolomics studies utilizing GC-MS operate in the full scan mode whereas in targeted studies operate the MS in selected ion monitoring (SIM) mode (Wu *et al.*, 2020). Both modes can successfully identify metabolites and provide researchers with qualitative/quantitative information, however, the full scan method often suffers from poor sensitivity due to short dwell times at each m/z, which prompts researchers to use the SIM method for superior sensitivity.

In GC-MS/MS analysis, a few scanning and static methods can be utilized depending on the type of analyses that needs to be done. The different modes include: precursor ion scan, product ion scan, neutral loss ion scan and multiple reaction monitoring (MRM). In targeted metabolomics studies and routine analytical laboratories, MRM analysis of target compounds is extensively used as it provides excellent metabolite quantification and easier data processing than scanning/untargeted methods (Xu *et al.*, 2019). In comparison to the standard SIM mode of GC-MS, operating a GC-MS/MS in MRM mode provides for far better specificity and increased sensitivity (Kvitvang *et al.*, 2011; Dettmer-Wilde & Engewald, 2014). Furthermore, to obtain even better sensitivity and throughput when analysing metabolites on a GC-MS/MS system, the MRM mode can be run in dynamic MRM mode (Zhou & Yin, 2016), which identifies each compound based on their retention time with previously stored ion transitions and retention times as opposed to standard MRM's utilizing time segmentation (Caprioli *et al.*, 2018).

For all the advantages of the GC-MS/MS, one major shortcoming limits its use in routine, targeted analyses (especially when compared to LC-MS/MS). With LC-MS/MS MRM analysis, the molecular ion is typically selected as precursor ion, which is fragmented in the collision induced dissociation (CID) cell and a specific product ion detected to allow specific detection of a target compound. With the use of EI as ion source in the GC-MS/MS system, the target compound is already fragmented and molecular ion virtually absent (or in very low concentration) (Mirnaghi & Caudy, 2014). Softer ionization sources such as chemical ionization (CI) can circumvent this problem albeit not without adding other problems like sensitivity issues. Our research group previously used CI with methane but could not maintain the same sensitivity level over short periods due to the source getting dirty fairly quickly.

For the analysis of compounds on a GC or LC system, the molecules must be ionized and in a gaseous state before these ions can reach the mass spectrometer, which is achieved through either soft or hard-ionization (Agin *et al.*, 2016). EI (hard), a hard type of ionization, and electrospray ionization (ESI) which is a soft type of ionization are most commonly used in metabolomics studies (Gowda & Djukovic, 2014). When using a GC-MS, EI is usually preferred as ionization type due to the spectra obtained from EI fragmentation exhibiting great reproducibility and widely available spectral libraries to compare analyte fragment spectra with.

On the contrary, ESI is mostly suitably for LC-MS/MS systems since ESI leads to the formation of gaseous ions needed to be detected by the MS and is most effective in the analysis of larger molecules such as proteins and smaller peptides (Griffiths & Wang, 2009).

2.6 Derivatization of organic acids

GC-MS analyses of organic acids require a derivatization step for the conversion of these polar compounds to specific derivatives which are more volatile and stable for GC-MS analyses (Zarate *et al.*, 2017). Derivatization with alkylation and silylation agents are mostly used in GC-MS metabolomics studies and provides researchers with coverage of a wide range of metabolites (Zarate *et al.*, 2017). MSTFA is often used as silylation agent in GC-MS metabolomics, producing TMS-derivatives which give characteristic $[M-15]^+$ fragment ions with EI. However, these fragmented ions are usually very low in concentration and thus have a low sensitivity when using it as a quantification ion in SIM or scanning methods (Ohie *et al*, 2000). As mentioned, utilizing EI as ionization type, causes extensive fragmentation of the compound which results in a relatively low intensity for the molecular ion (Fancy & Rumpel, 2008), which can be problematic for setting up selective MRM detection of target compounds.

A possible solution to this problem could be to use MTBSTFA as derivatization agent, yielding tBDMS-derivatives which gives an abundant $[M-57]^+$ ion (as per Figure 2.2) with EI ionization that is stable to hydrolysis (Jarukas *et al.*, 2020). Multiple studies have also shown that these tBDMS-derivatives form relatively easily and correspond to higher sensitivity and repeatable results (Gunnar *et al*., 2005). More importantly, this derivatization allows for the selection of more specific, high mass precursor ions when doing MS/MS analysis. In addition to tBDMS, methoxyamine hydrochloride (MOX) can be used prior to silylation, which improves the analytical signal through decreasing the number of derivatization products formed from the same compound (Beale *et al.*, 2018).

Get a new image for malic acid below

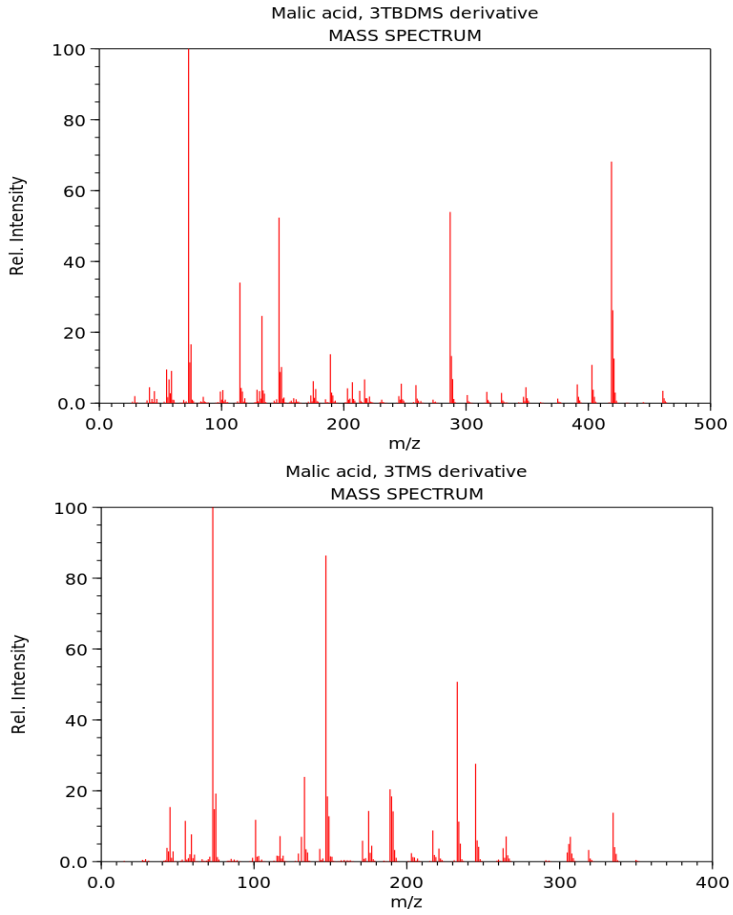

Figure 2.2: Mass spectrums representing the abundant fragment ions of malate derivatized with MTBSTFA and BSTFA respectively (Acree *et al*., 2024)

2.7 Characterisation of methods in metabolomics studies

Untargeted metabolomics is a hypothesis generating approach which makes use of the relative quantification of as many metabolites as possible. Due to inherent limitations of this approach, it is important to confirm findings and test formulated hypotheses with targeted analysis. Hence, targeted metabolomics is the downstream validation (and application) of detected concentration differences and metabolite identities of untargeted analysis. Our research group has characterized NDUFS4 KO mice tissue with untargeted metabolomics and highlighted the impact of redox imbalance on organ-specific metabolism (Terburgh *et al*., 2019, Terburgh *et al*., 2021). Perturbations in the following redox metabolites were observed by these mentioned studies, hydroxy C16 & C18 fatty acids, 2-hydroxyglutarate as well as certain TCA intermediates from other studies (Coetzer J., 2020, Horak W., 2020). However, these findings still need to be confirmed with targeted analysis.

Targeted metabolomics studies require suitable analytical methods and techniques to ensure the optimal (accurate / reproducible) quantification of target compounds. Many targeted methods still

rely on relative quantification with the help of internal standards like stable isotopes. The aim of these methods is to confirm metabolite concentration differences between experimental groups (through slightly better quantitation) and to confirm metabolite IDs. They typically rely more on repeatability or intermediate precision than accuracy/reproducibility and make use of quality control samples to assure reliable results. In other cases, reproducibility (interlaboratory reliability) is important (such as in the clinical setup), in which an analytical method needs to produce the same results over a large time interval and/or across different laboratories (Tiwari & Tiwari, 2010). Such methods typically incorporate matrix-matched external calibrators in addition to using internal standards to control analytical bias (or to improve accuracy). Regardless of the exact approach, targeted methods are usually well characterized in terms of specificity/ selectivity, linearity, accuracy (or rather accepted bias), precision and limit of detection (LOD) and limit of quantification (LOQ) (Tiwari & Tiwari, 2010).

Selectivity refers to the analytical method's ability to quantify and distinguish a specific analyte from other metabolites within a biological sample (Koek *et al.*, 2011). Linearity aims to measure the relationship between the analyte concentration in the biological sample and the signal obtained from the detector (Koek *et al.*, 2011). Accuracy entails the familiarity between mean test results obtained from the developed method and the actual concentration of the analyte (Koek *et al.*, 2011). Accuracy can also rather be defined as a component of error which in turn relates to bias such as the divergence of expected results from experiments to the accepted reference values (Tiwari & Tiwari, 2010). While absolute quantification is possible with new technologies, the focus is more on conforming to a predetermined bias (reference range) in practice.

Precision revolves around the measurement of a specific analyte when the developed method is applied repeatedly to a homogenous volume of the biological matrix in several aliquots (Koek *et al.*, 2011). LOQ can be described as the lowest quantifiable amount of a given analyte, with acceptable precision and accuracy (Koek *et al.*, 2011). Furthermore, in our study, limit of detection (LOD) will also be assessed, which entails the lowest detectable concentration of a specific analyte in a biological sample (Shrivastava & Gupta, 2011).

CHAPTER 3 EXPERIMENTAL DESIGN

3 Aim, objectives and experimental design

3.1 Problem statement

Mitochondrial disorders are quite rare (1 in 5000) and result in moderate (e.g. Type 2 diabetes) to severe clinical presentations (e.g. LS, which is characterized by neurological defects) (Bakare *et al*., 2021). Mitochondrial disorders are complex and remain poorly understood due to the inherent characteristics of the organelle. Complex I deficiency is the most common defect in the mitochondrial respiratory chain, which not only results in impaired energy production, but also a redox imbalance that has negative implications on metabolism as a whole (Swalwell *et al*., 2011). Previous metabolomics-based studies (by our group) (Terburgh *et* al., 2019, Horaw W., 2020, Terburgh *et* al., 2021) on the whole-body NDUFS4 KO mouse, a complex I deficiency model, also found metabolic perturbations associated with redox imbalance (Van der Walt *et al*., 2021). It is then no surprise that several studies by leaders in the field (like Prof Jan Smeitink and other researchers) (De Haas *et al*., 2017), are targeting this redox imbalance when developing therapeutic strategies.

Ideally, NAD(P)H and NAD(P) levels should be monitored when testing treatment options but due to the reactive nature of these coenzymes, it is difficult to quantify them reliably (especially in tissue samples) (Vina *et al*., 2016). Instead, metabolite ratios are commonly used in the clinical setup, like the lactate:pyruvate ratio, which gives an indication of the redox state *in vivo*. With the hypothesis-generating, relative quantification approach of untargeted metabolomics, confirmation of our previous findings with targeted methods are necessary. Hence, a need exists for a method that is able to quantify metabolites involved in redox metabolism more accurately, to confirm previous findings (hypotheses); and to aid treatment studies at our institution that are focused on restoring redox balance.

3.2 Aim and Objectives

The aim of this study was to develop a GC-MS/MS method to accurately quantify metabolites involved in redox metabolism in NDUFS4 knockout mice liver, brain and heart tissue.

Successful development and evaluation of the method were achieved with the completion of the following objectives:

- Optimisation of MRM transitions and associated conditions for selected organic acids derivatized with MTBSTFA containing 1% TBDMCS.
- Optimisation of chromatographic separation of selected organic acids
- Setting up external calibrators of the selected compounds in appropriate matrices.
- Assessment and characterisation of method performance using external calibrators
- Analysis and quantification of selected organic acids on NDUFS4 knockout mice tissues using the established method.

3.3 Experimental design

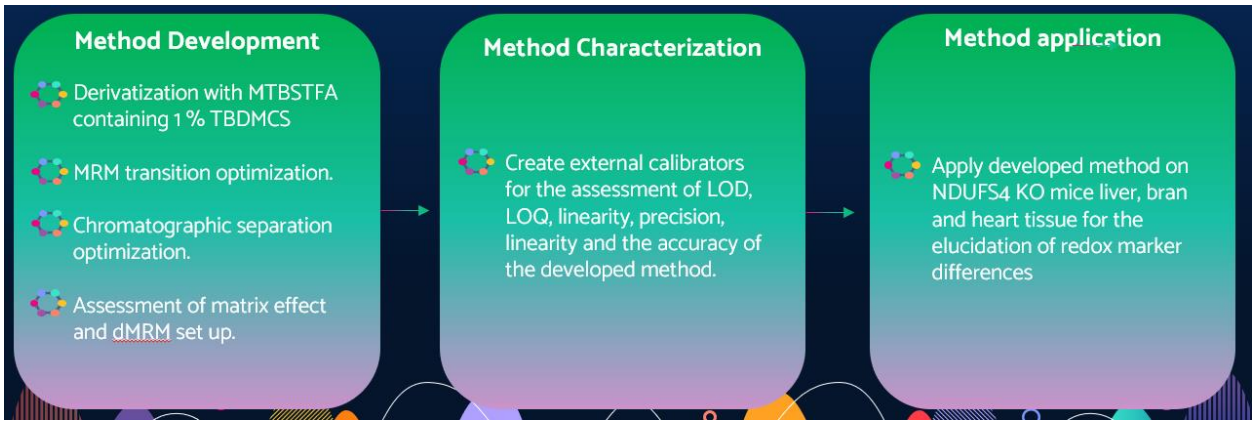

Figure 3.1: Experimental design

Figure 3.1 represents a summary of the experimental design, outlying the different objectives at the method development, characterisation and application section.

CHAPTER 4 – MATERIALS AND METHODS

4 Materials, methods and method optimisation

4.1 Chemical standards and reagents

HPLC grade Methanol (67-56-1), Chloroform (67-66-3) and Water (7732-18-5) were purchased from Sigma-Aldrich (Merck Group) and MedChemExpress supplied through Biotechnology Hub Africa. Internal standards, 3-phenylbutyric acid (116807-5G) and nonadecanoic acid (C19) (N5252-1G) were also purchased from Sigma-Aldrich (Merck Group), whilst all analytical standards and derivatization agent are listed in Table 4.1 below. Genotyping and PCR reagents are provided by the Quick-DNA Miniprep Plus Kit (D4068T) purchased from Inqaba Biotech.

Table 4.1: Analytical standards and their representative CAT numbers

Compound	CAT number
Sodium 2-keto-3-methylbutyrate	198994-5G
DL-2-keto-3-methylvalerate sodium salt	K7125-5G
L-2-hydroxy-3-methylbutyrate	379093-1G
DL-2-hydroxyglutarate	94577-100MG
L-Lactate	L1750-10G
L-Aspartic acid	A9256-100G
DL-Malate	94916-100MG
Oxaloacetate	O4126-1G
Pyruvate	107360-25G
2-ketoadipic acid	HY-113227-10MG
2-hydroxyadipic acid	HY-113101-25MG
2-ketoglutarate	K1128-5G
DL-3-hydroxybutyrate	H6501-5G
Lithium Acetoacetate	A8509-25G
Trans-aconitate	122750-25G
Sodium citrate tribasic dihydrate	251275-5G
DL-Isocitrate	HY-W009362-50MG
2-keto-4-methylvalerate	68255-1G
2-hydroxy-3-methylvalerate	80529-50MG
2-hydroxyisocaproic acid	219819-1G
DL-3-hydroxydecanoate	H3648-5MG
3-hydroxyisovalerate	HY-113409-500MG
DL-3-hydroxypalmitate	H4398-10MG
3-hydroxypropionate, 30% solution in water	792659-1G
Methylmalonate	M54058-5G
Succinylacetone	20011-10MG
Trisodium 2-Methylcitrate, racemixture of diastereomers	59464-10MG
n-tert-Butyldimethylsilyl-N-methyltrifluoroacetamide (1% tert-butyldimethylchlorosilane)	M-108-5X1ML
Pyridine	1946012501

The derivatization agent MTBSTFA containing 1% TBDMCS was used as silylation agent for the silylation of organic acids.

4.2 Instrument specifications

To carry out separation and detection of the set redox metabolites, an Agilent's 7890B GC-system coupled to an Agilent 7010B triple quadrupole mass spectrometer was used. The hyphenated system included an Agilent 7693 autosampler utilizing a 10 µL Hamilton syringe and needle wash vials containing an acetone: isopropanol (1:1) mixture. Column parameters used for the optimisation of each organic acid MRM were as follows: Restek Rxi-1ms column (CAT: 13323) (100 % dimethyl polysiloxane), 30 meters, 0.32 millimeter internal diameter and 0.25 µm film thickness. The injection volume was 1 µL in split mode (10:1), with the inlet temperature kept constant at 250 °C. Helium was used as carrier gas at a constant pressure of 1 mL/min with a post run of 1.2 mL/min (not optimised). Nitrogen was used as collision gas in the collision cell (Q2) at 1.5 mL/min.

Explanation of the method specifications and method parameters are explained in Section 4.6.4.

4.3 Standard preparation

In preparation for MRM optimisation, a 2 mL and 1 mL stock and working solution was prepared respectively for each standard, with the initial dissolving of the standard in methanol or chloroform followed by dilution with HPLC grade water or methanol (depending on the polarity of the standard). Standards were prepared to reach a 2000 ppm stock and 200 ppm working solution which was further used throughout the method development phase. From the working solution (200 ppm) of each organic acid standard, different volumes (µL) were added to Eppendorf tubes and dried under a gentle nitrogen stream. The dried residue was resuspended into the respective matrices to create calibrators ranging from 0 to 1000 ng metabolite / mg tissue. A more detailed explanation of external calibrator preparation is outlined in Section 4.5.1. The internal standards, 3-phenylbutyric acid and nonadecanoic acid (C19), were dissolved in methanol and diluted with HPLC grade water to obtain a final concentration of 200 ppm.

4.4 Method development

4.4.1 Optimisation of MRM transitions

Of each metabolite standard a 100 µL of each working solution (Section 4.3) was dried under a gentle stream of nitrogen and resuspended into 50 µL of pyridine. Samples were derivatized by transferring 20 µL of MTBSTFA (containing 1 % TBDMCS) to each sample with a Hamilton

syringe and left at room temperature for 10 minutes (Adiels *et al*., 2010. Patel *et al*., 2017). These standards were injected and optimised separately on the GC-MS/MS system. The same injection volume and system conditions were used as mentioned in Section 4.6.3 except for the temperature gradient and varying modes such as scan and product ion scan modes for the identification of precursor and product ions. The GC temperature gradient was set to 70°C - 300°C for 8.7 minutes for the manual optimisation of MRM's for each standard (Table 4.2). This gradient allowed for relatively quick elution of all compounds while separating target peak(s) from solvent, derivatization reactants and derivatization variants (target compound not fully derivatized). The MRM optimisation results are presented and explained in greater detail in Section 5.1.

Table 4.2: Modified oven temperature gradient for optimisation of chromatographic separation of standards

Ramp	Rate (°C/min)	Temperature (°C)	Hold time (min)	Run time (min)
	0	70	1	1
1	30	150	0	3.667
2	60	300	1	7.167

To optimize the MRM's, an initial MS2 scan was conducted throughout the chromatographic run in Table 4.2, with no CID fragmentation. This allowed for the identification of $[M-57]^+$ ions representing the chosen organic acids. This initial MS2 scan was performed through scanning a mass range of 100-800 m/z with a scan time of 50 milliseconds to identify abundant precursor ions. As a rule of thumb, the highest mass (for optimal specificity) with the highest intensity (for optimal sensitivity) was selected if the molecular ion $[M+H]^+$ or $[M-57]^+$ ion was absent. All organic acids were identified through the presence of the $[M-57]^+$ and had their retention times recorded which would aid the following scanning methods. One or more abundant precursor ions were selected to perform a product ion scan with subsequent CID fragmentation at varying collision energy (CE) (5 - 10 eV). Again, the fragment(s) with the highest mass and highest intensity was selected to ensure sensitive and specific detection. A quantitative and qualitative precursor - and product ion pair of each organic compound was set up in an MRM method. The most intense precursor and product ion pair was chosen as quantitative ion while a less intense, but still specific precursor and product ion pair was chosen as qualitative transition. The quantitative transition pair provides sensitive detection of the target compound while the qualitative transition provides optimal specificity to confirm detection and quantification of the correct compound in a complex biological matrix. During the MRM scans for each organic acid, the dwell time was left at 20 ms to ensure accurate analysis of each fragment ion.

4.4.2 Optimisation of chromatographic separation

Similar to the previous section, 100 µL of each metabolite standard (working solution) was dried under nitrogen and derivatized (Section 4.3). These standards were injected separately to optimize chromatographic separation. Optimised chromatographic conditions were verified with the injection of a mixture of these standards (with final concentration of 100 ppm). The same injection volume and system conditions were used as mentioned in Section 4.6.4, using the optimised MRM methods to detect the target compounds. The standard working solution (Section 4.3) was analysed on the GC-MS/MS system with the oven temperature modified at certain time intervals throughout the chromatographic run to ensure sufficient separation of all metabolites. The rate by which the oven temperature increased during the run was increased at appropriate points for optimal resolution. The rate at which the oven temperature increased is described in Table 4.2.

4.4.3 Metabolite interference in biological matrix

The biological matrix could influence chromatographic separation and selective detection of the target compounds. Hence, it was necessary to verify optimised separation and detection conditions with the analysis of biological samples (non-spiked and spiked samples). Although MRM transitions are specific, they are not unique to a compound. In other words, it is likely that the optimised MRM transitions could also detect other compounds in the complex biological sample. It is thus necessary to confirm this and whether it will interfere with quantification (when a non-targeted compound elutes close to the target compound). In such cases, the chromatography was adapted to gain specificity of detection.

Liver, brain and heart tissue was spiked with 100 µL of each standard working solution and prepared with a modified stepwise Bligh and Dyer extraction method (Section 4.6.3). Approximately 50 mg of brain, liver and heart tissue (from WT mice previously stored from Nel, D. 2020 study) was homogenised in the presence of water (1.5 µL water per mg tissue), through 5 mm and 7 mm steel beads in a vibration mill (Redge) for 3 minutes at 30 Hz, respectively, while brain tissue was homogenised for 3 minutes at 20 Hz. The homogenate was transferred to 5 mL Eppendorf centrifuge tubes and the steel beads were removed from each sample. 6 µL methanol per mg tissue was added to each sample respectively, followed by centrifugation for 5 minutes at 3000 g and 4 °C. After centrifugation, 8 µL chloroform, 4 µL water and 1 µL internal standard (3-phenylbutyric acid and nonadecanoic acid) per mg tissue was added to each sample respectively, followed by vortexing each sample for 30 seconds. Lastly, each sample was subjected to another round of centrifugation for 5 minutes at 2000 g and 4 °C.

From the top phase 200 µL, and 100 µL of the bottom phase of each sample were transferred to separate Agilent GC-vials which were then dried under a Nitrogen stream. The dried extract of each sample was resuspended with 50 µL pyridine and vortexed for 30 seconds. After resuspension, each sample was derivatized with MTBSTFA containing 1 % TBDMCS and was left to react with the sample for 10 minutes at room temperature. Lastly, the derivatized solution of each sample was transferred to separate Agilent GC-inserts followed by analyses on an Agilent GC-MS/MS system as per Section 4.6.4. After the Rt of each redox metabolite was confirmed within each biological matrix, the same procedure was carried out without spiking the biological matrix to confirm the presence of each redox metabolite and as such, the specificity of each metabolite MRM can be assessed within a complex biological matrix. The Rt of each redox metabolite within the respective matrices differed slightly from their Rt in solvent and is discussed in more detail in Section 5.1.

Chromatographic conditions were further optimised to circumvent the co-elution of interfering (non-specific detected) compounds with target metabolites (Section 5.1.1)

The non-specific peaks detected closely to the desired organic acids had their retention time recorded, to ensure the dismissal of these interfering compounds with the use of dynamic MRMs (next section).

4.4.4 Dynamic MRM's

As described in Section 4.4.3, non-specific detection of compounds in the complex biological sample was noted. A transition "start-stop" window was created for each compound with the retention time of the interfering peaks in mind. This window specifies the time (minutes) before (Left retention time) and after (Right retention time) a target compound at which the transitions for that compound should be active. Not only does it allow the exclusion of interfering peaks but also improved dwell times as compared to conventional MRM. The Left and Right Rt for each transition were set up in such a manner that the total window for each peak stretched at least 1 minute (Left Rt delta: 0.5 minutes & Right Rt delta: 0.5 minutes in most cases) and did not contain peak areas recorded from other closely eluting compounds. This was done due to the fact that the initial development of MRM's for each compound was conducted in solvent and not within the target matrix itself. As such, employing dynamic MRM's (dMRM) with specific time windows for each transition increases the dwell time for each transition which enhances the sensitivity and reproducibility of each targeted redox marker.

With the use of dMRM, each transition had varying average dwell times, ranging from 52.6 ms to 249.1 ms. The Tables 4.3 – 4.6 represent the parameters for each dMRM transition divided into 4 different methods. Choosing a qualifier and quantifier transition for each of the targeted redox

markers ensure that verification of a peak of interest can be made whilst ruling out a possible false positive result. As such, if a significant statistical change is observed in one of the targeted redox markers between the KO and WT group, one can verify this significant change with another chosen transition unique to that redox marker. Setting up a quantifier and qualifier transition for each target compound in one dMRM method, results in a significant lowering of dwell time (ms) per transition and henceforth decreased data points per peak, which would result in less reliable quantification. As such, all transitions were divided into 4 different dMRM methods (with the same oven temperature gradient) to ensure a minimum dwell time of 40 ms per transition and at least 20 data points per peak, offering reliable quantification of each redox marker within the respective matrices. As such, for the establishment of each redox marker Rt within the biological matrices and for the application of the method, each extracted sample is analysed with all dMRM methods, starting with dMRM method 1, and continuing on to dMRM method 4.

Table 4.3: dMRM conditions for Method 1

Compound Name	Mono,di, tri or tetra-tBDMS	Qualifier / Quantifier	Precursor Ion	Product Ion	RT (min)	Left RT delta	Right RT delta	Dwell time (ms)	CE
2-keto-3-methylbutyrate	Mono-tBDMS	Qualifier	174.2	159	4.71	0.4	0.5	137.9547	6
2-keto-3-methylbutyrate	Mono-tBDMS	Quantifier	129.1	75	4.72	0.5	0.5	193.5614	5
2-keto-3-methylvalerate	Mono-tBDMS	Qualifier	143.2	75.1	5.65	0.4	0.3	165.7242	6
2-keto-3-methylvalerate	Mono-tBDMS	Quantifier	188.2	159	5.65	0.5	0.3	147.2042	5
Lactate	Di-tBDMS	Qualifier	233.3	147.2	7.78	0.5	0.5	124.1107	5
Lactate	Di-tBDMS	Quantifier	261.2	147.2	7.79	0.5	0.5	119.4976	6
Pyruvate	Di-tBDMS	Qualifier	259.2	147.1	8.42	0.5	0.2	96.37151	7
Pyruvate	Di-tBDMS	Quantifier	259.2	189.2	8.42	0.5	0.2	175.1254	6
2-OH-3-methylbutyrate	Di-tBDMS	Quantifier	261.3	147.1	9.51	0.5	0.5	124.0412	6
2-OH-3-methylbutyrate	Di-tBDMS	Qualifier	289.3	147.1	9.52	0.5	0.5	119.381	7
3PBA	Mono-tBDMS	Qualifier	105.3	77	10.38	0.5	0.5	96.19664	20
3PBA	Mono-tBDMS	Quantifier	221.3	105.1	10.38	0.5	0.5	96.19664	5
PyruvateDimer	Di-tBDMS	Qualifier	329.2	147.1	12.45	0.4	0.6	249.1134	8
PyruvateDimer	Di-tBDMS	Quantifier	197.1	169.1	12.46	0.3	0.7	249.1134	7
Malate	Tri-tBDMS	Quantifier	287	73.1	13.96	0.5	0.2	128.2241	10
Malate	Tri-tBDMS	Qualifier	419.4	73.1	13.97	0.4	0.5	80.56683	5
Oxaloacetate	Tri-tBDMS	Qualifier	417.4	73.1	14.08	0.4	0.6	98.42227	16
Oxaloacetate	Tri-tBDMS	Quantifier	417.4	147	14.08	0.4	0.5	57.44719	16
L-Aspartate	Tri-tBDMS	Qualifier	418.3	390.2	14.16	0.4	0.5	64.83496	7
L-Aspartate	Tri-tBDMS	Quantifier	390.3	73	14.16	0.5	0.5	70.60712	13
2-OH-gluterate	Tri-tBDMS	Qualifier	433.4	147.1	14.43	0.3	0.1	47.33824	16
2-OH-gluterate	Tri-tBDMS	Quantifier	433.4	73	14.43	0.3	0.1	47.33824	16
C19	Mono-tBDMS	Qualifier	355.5	75.1	15.79	0.5	0.5	165.8901	12
C19	Mono-tBDMS	Quantifier	355.5	131.2	15.79	0.5	0.5	165.8901	12

Table 4.4: dMRM conditions for Method 2

Compound Name	Mono,di, tri or tetra-tBDMS	Qualifier / Quantifier	Precursor Ion	Product Ion	RT (min)	Left RT delta	Right RT delta	Dwell time (ms)	CE
3-OH-butyrate	Di-tBDMS	Qualifier	275.2	147.1	9.35	0.4	0.5	165.7287	6
3-OH-butyrate	Di-tBDMS	Quantifier	233.2	147.1	9.35	0.4	0.5	165.7287	7
Acetoacetate	Di-tBDMS	Qualifier	273.2	147.2	10.34	0.3	0.7	193.553	15
Acetoacetate	Di-tBDMS	Quantifier	199.2	73.1	10.55	0.7	0.4	172.6968	11
3PBA	Mono-tBDMS	Qualifier	105.3	77	10.37	0.5	0.5	96.23668	20
3PBA	Mono-tBDMS	Quantifier	221.3	105.1	10.37	0.5	0.5	96.23668	5
2KG	Di-tBDMS	Quantifier	215.3	73.1	12.59	0.5	0.5	249.1361	10
2KG	Di-tBDMS	Qualifier	317.2	157	12.6	0.5	0.4	165.6388	7
2KG	Tri-tBDMS	Quantifier	375.3	147.1	14.53	0.5	0.1	83.36657	15
2KG	Tri-tBDMS	Qualifier	431.3	147.2	14.54	0.5	0.15	78.11944	17
2-OH-adipic acid	Tri-tBDMS	Qualifier	245.2	147.1	14.88	0.3	0.5	54.24089	7
2-OH-adipic acid	Tri-tBDMS	Quantifier	447.4	245.2	14.88	0.5	0.5	63.62008	7
2-ketoadipic acid	Tri-tBDMS	Quantifier	445.4	375.4	14.96	0.5	0.2	54.25306	13
2-ketoadipic acid	Tri-tBDMS	Qualifier	375.3	147.1	14.96	0.35	0.2	47.30619	6
Aconitic acid	Tri-tBDMS	Qualifier	461.4	73.1	15	0.5	0.5	55.76522	17
Aconitic acid	Tri-tBDMS	Quantifier	327.2	147.1	15	0.5	0.5	55.76522	12
C19	Mono-tBDMS	Qualifier	355.5	75.1	15.79	0.5	0.5	57.35187	12
C19	Mono-tBDMS	Quantifier	355.5	131.2	15.79	0.5	0.5	57.35187	12
Citrate	Tetra-tBDMS	Qualifier	459.4	73.1	15.9	0.5	0.5	58.01313	13
Citrate	Tetra-tBDMS	Quantifier	591.5	431.4	15.9	0.5	0.5	58.01313	12
Isocitrate	Tetra-tBDMS	Qualifier	591.6	459.3	15.97	0.5	0.5	85.74452	14
Isocitrate	Tetra-tBDMS	Quantifier	403.4	147	15.97	0.5	0.5	85.74452	8

Table 4.5: dMRM conditions for Method 3

Compound Name	Mono,di, tri or tetra-tBDMS	Qualifier / Quantifier	Precursor Ion	Product Ion	RT (min)	Left RT delta	Right RT delta	Dwell time (ms)	CE
3PBA	Mono-tBDMS	Qualifier	105.3	77	10.37	0.5	0.5	103.1676	20
3PBA	Mono-tBDMS	Quantifier	221.3	105.1	10.37	0.5	0.5	103.1676	5
2-keto-3-methylbutyrate	Di-tBDMS	Quantifier	287.2	147	11.09	0.5	0.5	68.54606	11
2-keto-3-methylbutyrate	Di-tBDMS	Qualifier	287.2	189.1	11.1	0.4	0.6	62.22388	11
3-OH-isovaleric acid	Di-tBDMS	Qualifier	289.3	189.2	11.22	0.5	0.3	58.17289	6
3-OH-isovaleric acid	Di-tBDMS	Quantifier	289.3	147.1	11.22	0.5	0.3	58.17289	7
2-OH-3-methylvalerate	Di-tBDMS	Qualifier	275.3	147.2	11.5	0.5	0.5	59.70715	7
2-OH-3-mval/2-OH-4-mval	Di-tBDMS	Quantifier	303.3	147.1	11.5	0.5	0.5	59.70715	10
2-k-3-mval/2-k-4-mval	Di-tBDMS	Qualifier	301.3	147.2	11.7	0.5	0.4	81.94658	10
2-k-3-mval/2-k-4-mval	Di-tBDMS	Quantifier	301.3	189.2	11.7	0.5	0.4	81.94658	10
3-OH-decanoic acid	Di-tBDMS	Qualifier	359.3	147	13.84	0.5	0.5	137.9607	9
3-OH-decanoic acid	Di-tBDMS	Quantifier	313.4	147	13.84	0.5	0.5	137.9607	7
C19	Mono-tBDMS	Qualifier	355.5	75.1	15.79	0.5	0.5	89.57777	12
C19	Mono-tBDMS	Quantifier	355.5	131.2	15.79	0.5	0.5	89.57777	12
3-OH-palmitic acid	Di-tBDMS	Quantifier	443.5	147.1	16.08	0.6	0.4	89.53883	11
3-OH-palmitic acid	Di-tBDMS	Qualifier	327.4	73	16.16	0.5	0.5	121.3181	15

Table 4.6: dMRM conditions for Method 4

Compound Name	Mono,di, tri or tetra-tBDMS	Qualifier / Quantifier	Precursor Ion	Product Ion	RT (min)	Left RT delta	Right RT delta	Dwell time (ms)	CE
3-OH-propionate	Di-tBDMS	Quantifier	261.2	147	9.09	0.45	0.5	165.9091	9
3-OH-propionate	Di-tBDMS	Qualifier	261.2	189.2	9.09	0.5	0.5	277.0586	6
Methylmalonate	Di-tBDMS	Qualifier	289.3	73.3	10.31	0.5	0.5	124.1042	8
Methylmalonate	Di-tBDMS	Quantifier	289.3	147.2	10.31	0.5	0.5	124.1042	6
3PBA	Mono-tBDMS	Quantifier	221.3	105.1	10.38	0.5	0.5	123.9801	5
3PBA	Mono-tBDMS	Qualifier	105.3	77	10.38	0.5	0.5	193.5312	20
Succinylacetone	Di-tBDMS	Qualifer	329	169.1	13.81	0.5	0.5	165.5518	13
Succinylacetone	Di-tBDMS	Quantifier	169.1	75.1	13.81	0.8	0.5	249.0926	20
C19	Mono-tBDMS	Qualifier	355.5	75.1	15.8	0.5	0.5	124.0672	12
C19	Mono-tBDMS	Quantifier	355.5	131.2	15.8	0.5	0.5	124.0672	12
2-methylcitrate	Tetra-tBDMS	Qualifier	447.4	73	16.22	0.5	0.5	123.8439	20
2-methylcitrate	Tetra-tBDMS	Quantifier	605.6	447.4	16.22	0.5	0.5	123.8439	10

4.5 Method Characterisation

4.5.1 External calibration preparation

Frozen liver, brain and heart samples from knockout (KO) and wild type (WT) mice were obtained from a previous study (Nel, 2022), in which tissue samples from each organ was homogenised in the presence of saline (100 mg tissue: 100 mL saline) with the different tissue types being homogenised separately through the use of a Potter Elvehjem homogeniser. The saline used as solution for homogenisation was made through adding 9 grams of sodium chloride to 1 Liter MiliQ water. After homogenisation, the entire homogenate was transferred to a dialysis tube with a 3.5 kilodalton (kDa) cut off. The dialysis tube was suspended in saline and left on a magnetic stirrer. The homogenate was dialyzed in 1 L saline for 24 hours to strip the sample of metabolites. After the initial 24 hours, the old saline was replaced with freshly made saline. The homogenate was left suspended in the saline for another 24 hours and incubated at 60 °C for 6 hours to ensure denaturation of any biological enzymes still present, consequently stopping enzymatic activity. The homogenate (stripped matrix) was frozen at – 80°C until use.

The stripped matrix was spiked with target organic acids to characterize the method and to use for quantification during method implementation. The calibration was set up to enable quantification of organic acids within the concentration range of: 1000, 750, 500, 250, 100 and 0 ng/mg (ng metabolite per mg tissue). Firstly, 200 ppm working solution of each organic acid (26 organic acids in total in respective solvents mentioned in Section 4.3) were transferred to their respective calibration Eppendorf tubes as per:

- 1000 ng/mg calibrator required 75 µL of each organic acid working solution.
- 750 ng/mg calibrator required 56.25 µL of each organic acid working solution.
- 500 ng/mg calibrator required 37.5 µL of each organic acid working solution.
- 250 ng/mg calibrator required 18.75 µL of each organic acid working solution.
- 100 ng/mg calibrator required 7.5 µL of each organic acid working solution.
- The blank sample required no organic acids.

Each calibrator was then dried through a SpeedVac until roughly 100 µL remained in each tube. 1520 µL stripped liver, brain or heart tissue homogenate was resuspended in each calibrator tube and vortexed for 30 seconds. The volume contained within each calibrator tube was then split into 3 samples (triplicate) per concentration level, which left each sample having theoretically 50 mg of tissue per sample. These calibrators were stored at -80°C until use. Each sample was then subjected to a modified Bligh and Dyer two-phase extraction method before derivatization (Section 4.4.1) and analysis (Section 5.3).

4.5.2 Characterisation of the developed method

The external calibrators prepared and analysed in triplicate (Section 4.5.1) were used to characterise the performance of the developed method (in other words, establishing limits and variance). Typical performance measurements: precision, accuracy, LOD, LOQ and linearity and R^2 were determined through the analysis of the external calibrators according to the prescribed ISO17025 guidelines (Beskan *et al*., 2020). Coefficient of variance (CV) values at each concentration level were used for measuring the precision of the method with a 25 % cut off, while accuracy of the method was determined by comparing measured experimental values to the true values of each calibration level and thus the deviation of an experimental result to that of the true value (Rudaz & Feinberg, 2018). LOD was calculated as the sum of the average of the normalized baseline peak in the blank samples (non-spiked) and three times the standard deviation of the baseline (expressed as concentrations). Lastly, the LOQ was calculated in the same manner as LOD with the only exception being, ten times the standard deviation was added to the average normalized baseline in the blank samples (Konieczka P., 2007).

4.6 Method application

4.6.1 Animal housing and breeding program

Ethical approval was acquired from the North-West University Animal Care, Health and Safety Research Ethics Committee (NWU-00784-22-A5) for a category 0 study. For the execution of the study, the complex I knock out and wild type mice [Ndufs4 -/-] and [Ndufs4 +/+] respectively) were used to assess the redox status and the effect of a complex I deficiency.

The mice were housed at the preclinical drug development platform (PCDDP), at the Vivarium located at the North-West University. Six WT and six KO mice were obtained as a result of the breeding program maintained by the PCDDP. Due to KO mice never reaching sexual maturity, heterozygous mice (HT) (Ndufs4 -/+) was used in breeding cages. In comparison to WT mice, KO mice are smaller in size with also smaller organs. As per their KO, they represent similar biochemical markers to that of patients with LS, making them an excellent model organism to study biochemical changes related to CI deficiencies. To ensure normality across the dietary intake between two model organisms, a standard laboratory rodent diet (Rodent Breeder, #12RM1845) produced by Lab Chef, Nutrition Hub Pty Ltd, Western Cape, South-Africa) was given to the KO, WT and HT mice. Selected mice were euthanized by cervical dislocation, and the chosen tissue was harvested by trained staff from the PCDDP. All tissue samples were immediately snap frozen with liquid nitrogen inside respective Eppedorf tubes and stored at -80 °C until further use.

To elaborate further on the different tissue types, the liver, brain and heart were selected as target organs for biochemical analysis. As described later in the Section 5.5., the liver is an organ which acts as a metabolic hub for anabolic and catabolic processes, importing and exporting a wide range of metabolites. Also, the brain and heart are both vital organs which require large amounts of energy as per their high energetic needs for functional normality. As such, these three target organs were selected as tissue types to assess redox metabolites in NDUFS4 KO and WT mice.

4.6.2 Genotyping of NDUFS4 KO and WT mice

To carry out the application of the developed method on NDUFS4 KO and WT mice, genotypes of each mouse used for the application had to be confirmed. Confirmation of genotypes was carried out through DNA isolation from mouse liver, polymerase chain reaction (PCR) amplification and lastly, agarose gel electrophoresis.

DNA isolation: a small (2 mm) piece of mouse liver for each sample was removed from the dissected liver through a sterilized scalpel and thawed on ice. 95 µL nuclease free water, 95 µL DNA Solid Tissue buffer blue and 10 µL proteinase K was added to each liver sample and then incubated at 55 °C for 2.5 hours. After the incubation time was complete, each sample was vortexed for 10 seconds. 25 µL of DNA elution buffer per sample, was pipetted into a sterilized microcentrifuge tube (total of 600 µL DNA elution buffer for repeated addition) and incubated at 65 °C on a heating block.

400 µL Genomic Binding Buffer was added to each sample with subsequent vortex of each sample for 10 seconds. Thereafter, each sample was subjected to centrifugation at 12 000 x G for 1 minute for the removal of insoluble particles. After centrifugation, each sample supernatant was transferred to a Zymo-Spin IIC-XL Column with an added collection tube below each Spin Column. All samples were subjected to centrifugation at 12 000 x G for 1 minute, whereas the flowthrough in the collection tube was discarded after centrifugation. Each Zymo Spin column was then transferred to a new sterilized collection tube whilst adding 400 µL DNA Pre-Wash Buffer to each spin column.

Each sample was centrifuged with a new collection tube at 12 000 x G for 1 minute, thereafter the eluent of each sample was discarded. 700 µL g-DNA wash buffer was added to each spin column and centrifuged at 12 000 x G for 1 minute. The flow through of each collection tube was discarded and another 200 µL g-DNA wash buffer was added to each spin column. After the last addition of g-DNA wash buffer each spin column was subjected to another round of centrifugation at 12 000 x G for 1 minute. Hereafter, all samples had their collection tubes discarded whilst transferring the spin column to a sterilised 1.5 µL microcentrifuge tube. 25 µL of the pre-warmed DNA elution buffer was added to each spin column matrix and left to incubate at room temperature for 5

minutes. After room temperature incubation, each spin column was centrifuged at 16 000 x G for 1 minute to ensure the elution of the DNA from each liver sample through the spin column matrix. Lastly, 25 µL of pre-warmed DNA-elution buffer was added to each spin column and left to incubate at room temperature for 5 minutes and after incubation, each spin column was subjected to the last centrifugation step of 16 000 x G for 1 minute.

The eluted DNA (50 µL) was now contained within each 1.5 µL microcentrifuge tube and was used to determine each sample's DNA concentration and purity for further PCR amplification.

For determining the concentration and DNA purity of the isolated DNA, a NanoDrop (Thermo Fisher Scientific) was used. The NanoDrop was cleaned with MiliQ water and blank, 1 µL (DNA elution buffer), was added on the lower sampling arm to take a blank measurement. The NanoDrop system was then cleaned with MiliQ water following the addition of the first sample of isolated DNA. The DNA concentration (ng / µL) and purity (260 nm / 280 nm absorbance ratio) was noted for each sample whilst cleaning the NanoDrop system with MiliQ water after each sample measurement.

For PCR amplification, each sample DNA was diluted with nuclease free water to obtain a concentration of 25 ng / µL DNA per sample. A master mix was prepared in a 1.5 µL sterilized microcentrifuge tube containing as per the following table.

Table 4.7: PCR reaction calculations based on the number of samples (n)

Reagent	C1	Units	C2	Units	V1 (µL)	Master Mix (µL)
2 X Phire Tissue Direct PCR	2	X	1	X	5	5 X n
NDUFS4 1060 Forward Primer (Iqaba Biotech)	10	µM	0.5	µM	0.5	0.5 X n
NDUFS4 Reverse Primer (Inqaba Biotech)	10	µM	0.5	µM	0.5	0.5 X n
Nuclease free water	/	µM	/	µM	3	3 X n
Sample DNA	25	ng / µL	25	ng / µL	1	/
Total volume (µL)						10

After the master mix was prepared as per Table 4.7, the contents were vortexed for 10 seconds and 9 µL of the master mix was pipetted into separate sterilized PCR tubes. Afterwards, 1 µL of sample DNA was added to each sterilized PCR tube containing the master mix. Each PCR tube was then placed into a T100 Thermal cycler (Bio-Rad) preloaded with the PCR protocol listed in Table 4.8.

Table 4.8: Phire protocol used for the amplification of DNA samples isolated from KO and WT mouse tail-snips and liver.

Step	Temperature (°C)	Time (minutes) and Repetitions
1	98	05:00
2	98	00:05
3	57.3	00:05
4	72	00:20
5	/	X34 (Step 2 - 4)
6	72	01:00
7	4	∞

After PCR amplification of each DNA sample, the amplified DNA was separated according to band size via agarose gel electrophoresis. A 15 X 10 cm gel was used to separate the bands of the amplified DNA samples while the gel was prepared by dissolving 0.75 g agarose in 75 mL pre-prepared bionic buffer whilst heating in a microwave at low heat. After the agarose has been dissolved and cooled down to room temperature, 2 µL ethidium bromide was added to the dissolved agarose.

The 15 X 10 cm gel was then poured whilst avoiding the formation of bubbles, and a 20 well comb was added to the gel to form the wells for each DNA sample. After the gel was set after 30 minutes, the comb was removed.

The premade 100 – 1500 bp DNA ladder (3 µL) was diluted with 7 µL nuclease free water whereas each sample was diluted with 23.3 µL nuclease free water. Each sample, with the ladder and preamplified control DNA, was mixed via repeated aspirations with a pipette, and loaded into each well (10 µL). The agarose gel was then run at 40 V for 10 minutes and thereafter, 75 V for an hour on Electrophoresis equipment (Thermo Fisher Scientific) to ensure sufficient DNA band separation.

The gel was imaged on a ChemiDoc MP (Bio-Rad) system and visualised within Image Lab (v 5.2.1) with expected bands for the NDUFS4 gene at 1229 bp (WT), 1229 and 429 bp (HT) and a single 429 bp band for KO mice as shown in Figure 4.2.

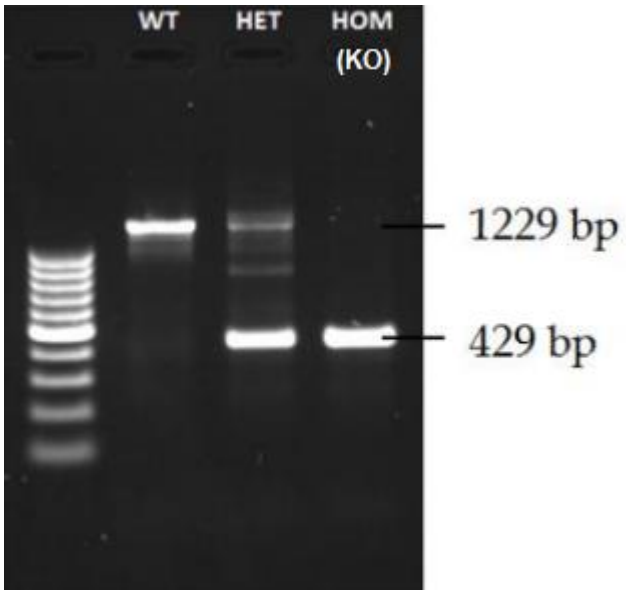

Figure 4.1: Proposed result for gel electrophoresis and separation of wildtype, heterozygous and knock-out NDUFS4 mice

4.6.3 Standard metabolite extraction procedure

A modified two-phase Bligh and Dyer extraction procedure utilizing the solvents water, methanol and chloroform (Bligh & Dyer, 1959; Gullberg *et al*., 2004), was used to extract metabolites from brain, liver and heart KO and WT tissue, respectively. The addition of each solvent was as follows: 6 µL methanol, 1.5 µL water and 8 µL chloroform for each mg tissue used, with the addition of methanol before homogenisation and the addition of water and chloroform after homogenisation (two-step addition of solvents). 50 µL of each internal standard namely: C19 (200 ppm) and 3-phenylbutyric acid (200 ppm) was added to each sample during the addition of water and chloroform. After vibration mill homogenisation, all samples were centrifuged at 3000 x G for 5 minutes at 4 °C. 200 µL of the top and 100 µL of the bottom organic phase was transferred to a GC-vial and dried under a vacuum via SpeedVac. After the homogenate dried, 50 µL of pyridine was added to each GC-vial to resuspend the dried homogenate. Thereafter, each sample was subjected to derivatization as outlined in Section 4.4.1. After derivatization, each sample was carried over to a GC-vial insert and analysed on a GC-MS/MS with instrument and analysis specifications listed in Section 4.6.4.

4.6.4 Method specifications for analyses of biological samples

Each sample was injected and analysed on 4 different dMRM methods at 3 cycles per second, with the first three methods containing the targeted redox markers, while the last method contained biomarkers for specific IEM diseases. The 3 redox methods ranged from 19 – 24 MRMs per method with a minimum and maximum dwell time of 40 and 332 ms respectively. The last method contained a total of 12 MRMs with a minimum and maximum dwell time of 80 and 332 ms respectively. The retention time window specifications for each dMRM method are listed in Section 4.4.4.

As per previous adjustments to the method temperature gradient the final oven program listed in Table 4.9 was used throughout the characterisation and application of the method.

Table 4.9: Final oven temperature gradient indicating rate of temperature increase at each time interval for the final separation of all target compounds.

Ramp	Rate (°C/min)	Temperature (°C)	Hold time (min)	Run time (min)
Initial	0	70	1	1
1	12	135	1.5	7.91
2	2	145	1.5	10.25
3	23	300	0	16.98
4	0	300	1	17.98

CHAPTER 5 RESULTS AND DISCUSSION

5 Method development results

5.1 Optimisation of MRM transitions

An MRM method was developed for the specific detection of target metabolites. MRM transitions for each organic acid standard were optimised on the GC-MS/MS utilizing EI as ionization source as described in Section 4.4. Firstly, a MS2 scan (Figure 5.1) was acquired for each of the derivatized standards to identify the number of peaks (derivatives) produced as well as to confirm masses with published or theoretical data. The mass spectrum of each compound was analysed to identify the most abundant ions with highest mass (more often than not the $[M-57]^+$ ion). For the sake of simplicity, the process of MRM optimisation will be showcased with lactate only.

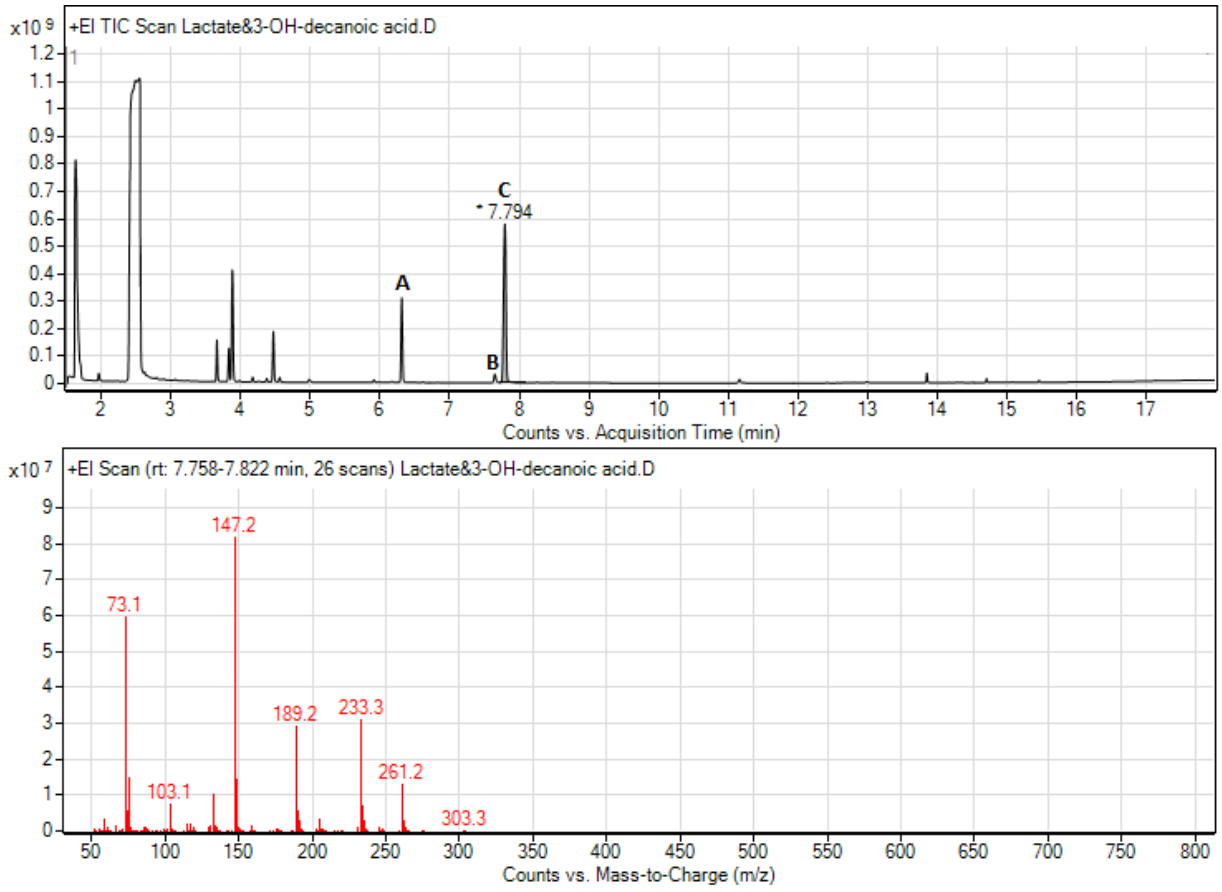

Figure 5.1: Chromatogram and mass spectrum of lactate (di-tBDMS) analysed through a MS2 scan. (For chromatogram: Intensity over run time in minutes, for MS: Intensity over m/z ratio)

Figure 5.1 shows the chromatogram of lactate derivatized with MTBSTFA. Three peaks were detected with the first abundant peak that of the derivatization reagent (peak A). Peak B was a contaminant while peak C (Rt: 7.794 min) was our target compound lactate. The mass spectrum of di-tBDMS lactate (peak C) is also presented in Figure 5.1. Lactate provided a characteristic $[M-57]^+$ ion of 261.2 m/z while the molecular ion (318.1 m/z) was absent. A more abundant 233.2 m/z ion was found and selected with the $[M-57]^+$ ion as precursors for the product ion scan step.

Next, a product ion scan was performed with fragmentation of the precursor ions in the collision cell with varying collision energies, which yielded the chromatogram presented in Figure 5.2 with peak B representing lactate. The Rt for lactate (4.997 min) in this run differed from the previous run due to constant adaptation of the oven temperature gradient between different standards.

A product ion scan was performed with both lactate precursor ions (261.2 and 233.2 m/z) to identify suitable product ions (Figure 5.2). Four fragmentation spectra are shown in Figure 5.2, two for each of the precursor ions fragmented at 5 and 10 CE voltage. As seen in Figure 5.2, a CE voltage of 10 caused complete fragmentation of the precursor ion (blue diamond). As a rule of thumb, the less precursor ion detected the better, as it means that more of it was converted to fragment ions. Following this initial product ion scan, various product ion scans were conducted at different CE voltages. Each transition produced an abundant 147.2 ion with this fragment having the highest intensity at a CE of 6 and 5 for the respective precursors. The selected precursor and product ion pairs (i.e. MRM transitions) with optimal CE volts were added to an MRM method and confirmed with a final analysis of the standard.

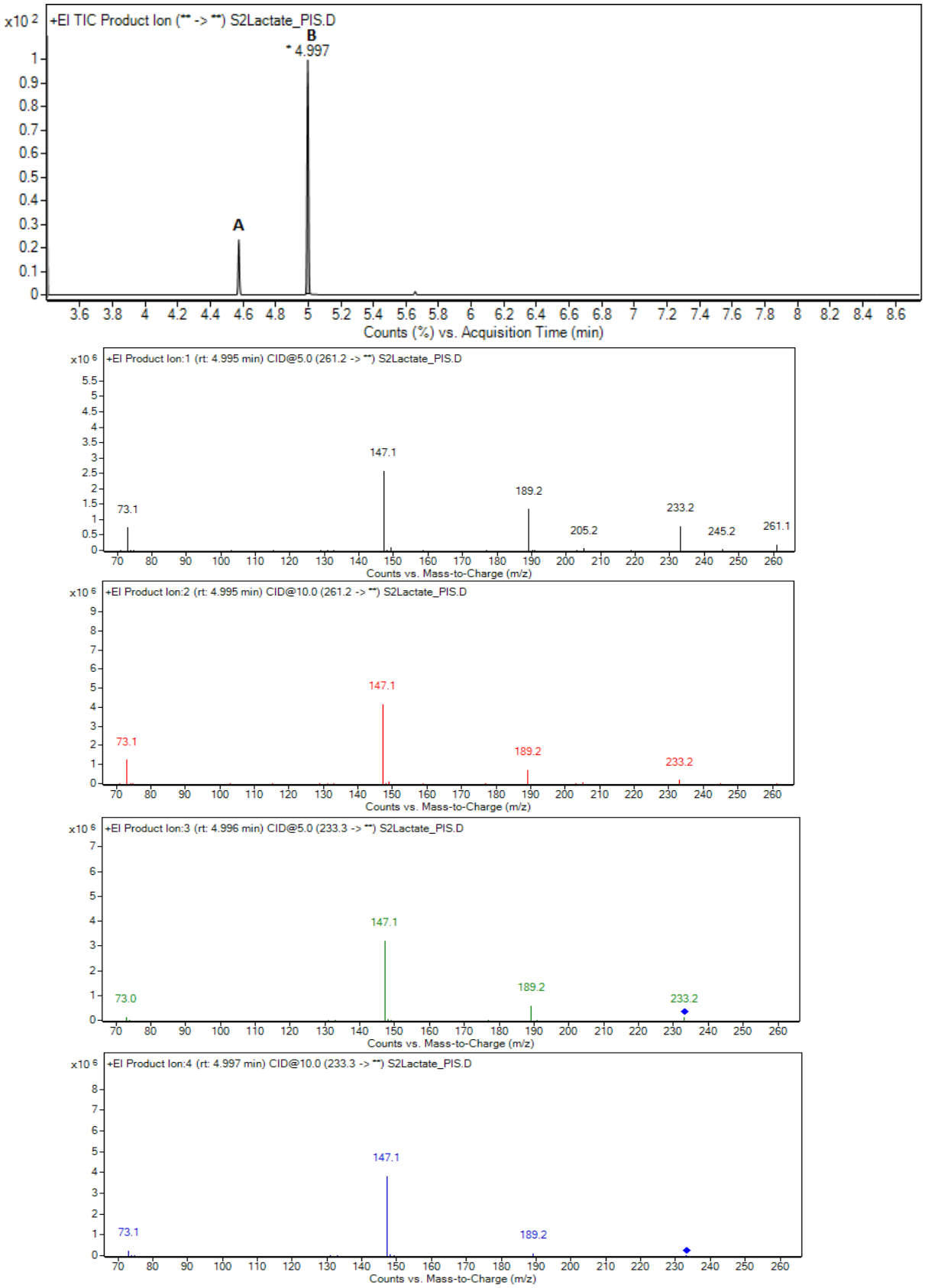

Figure 5.2: Chromatogram and mass spectrums of lactate (di-tBDMS) product ion scan at different CE (For chromatogram: Intensity over time in minutes, for MS: Intensity over m/z ratio)

Each standard had one precursor/product ion pair selected as qualifier, for accurate identification of that specific compound. Another precursor/product ion pair was selected per standard as quantifier, for the sensitive detection and quantification of that specific compound. With the optimal CE known for each compound precursor/product ion pair, MRM scans were performed.

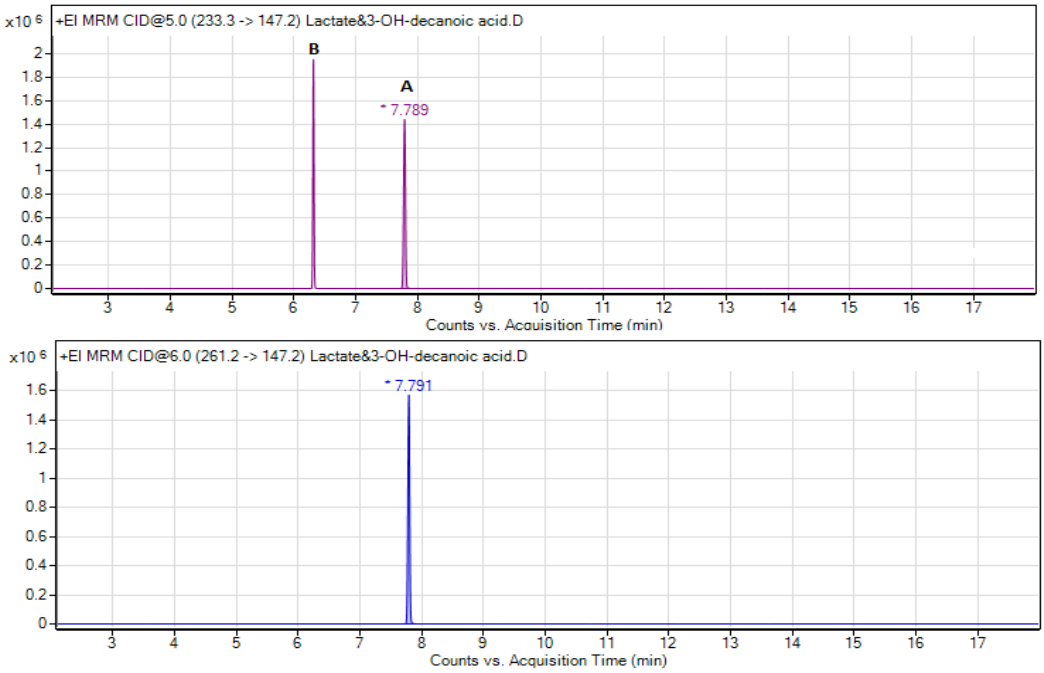

Figure 5.3: Chromatogram showing the detection of lactate (di-tBDMS) with optimised MRM transitions (Intensity over run times in minutes)

Figure 5.3 shows the specific detection of lactate (Peak A) with the optimised MRM transitions (261.2 → 147.2 m/z @ 6eV and 233.3 → 147 m/z @ 5 eV). Peak B on the top chromatogram represents a derivatization reactant which has the same transition as lactate's 233.3 → 147 m/z MRM transition. The use of MRM detection has a noticeable drop in baseline which aids sensitivity. With the MRM transitions for lactate (di-tBDMS) optimised, the possible matrix effect can be determined when analysing lactate within a biological matrix for the assessment of non-specific detection (interfering compounds) and possible retention time shifts.

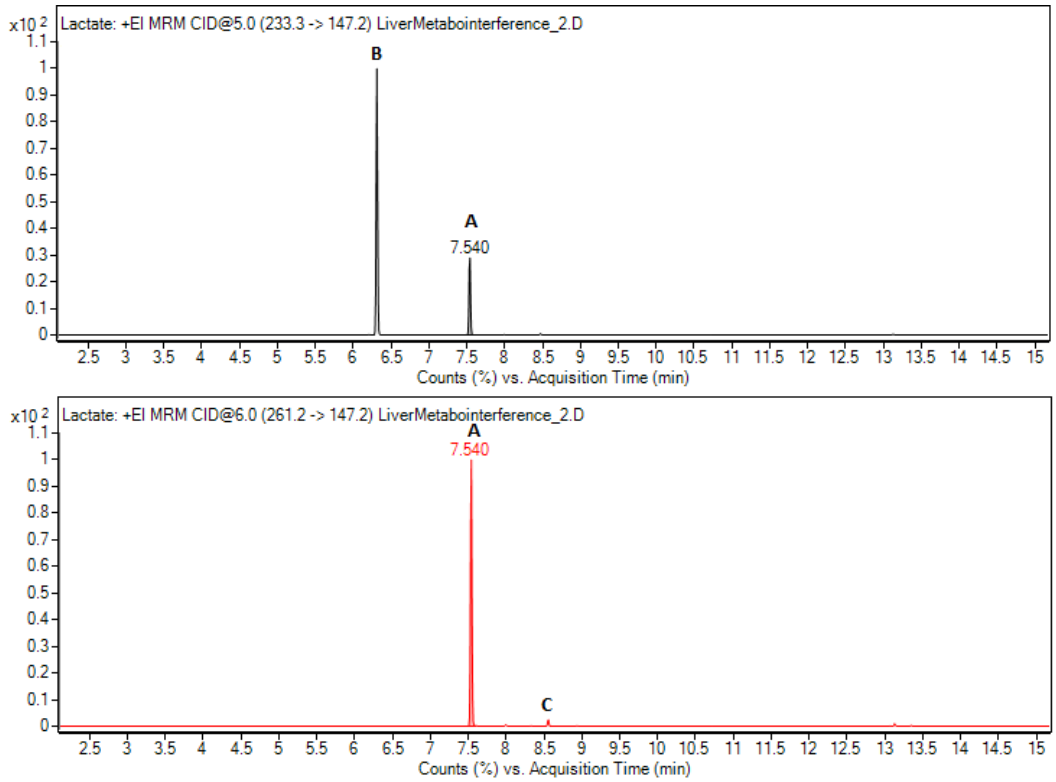

Figure 5.4: Chromatogram of di-tBDMS Lactate MRM transitions within liver tissue spiked with the analytical standard (Intensity over run time in minutes)

As seen in Figure 5.4, the optimised MRM transitions for lactate was identified as peak A on both chromatograms. Rt differs not as per the matrix effect but rather adaptation of the oven gradient throughout the MRM development of each organic acid standard. After adaptations the final oven temperature gradient was determined (Section 5.2) and all redox markers underwent MS scans again to record the final Rt that will be used to set up dMRM transitions (Section 5.2). Nonetheless, as per Figure 5.4, the transitions for lactate identified unspecifically two compounds (peak B & C) that eluted relatively distant from peak A within the liver matrix. These unknowns eluted more than 1 minute before and after lactate. Even though the retention time of lactate with our initial temperature gradient shifted slightly with the addition of a biological matrix (solvent Rt: 7.89 min & Liver matrix Rt: 7.78 min), these detected peaks would not interfere with the detection and quantification of lactate, especially when using dMRM. This process of identifying matrix interfering peaks was conducted for all the targeted redox markers across the three tissue types.

5.2 Optimisation of chromatographic separation and dMRM windows

The oven gradient was adapted to avoid co-elution of target compounds and the elution of interfering peaks close to the target compounds within the biological matrices. Figure 5.5 shows the final temperature gradient used after optimisation. This gradient was used when analysing the target compounds in mouse samples. With the finalization of the temperature gradient, new retention times were recorded for all the standards to create a dMRM method with appropriate

transition windows. This dMRM method was tested in tissue and the detection of lactate is showcased in Figure 5.6.

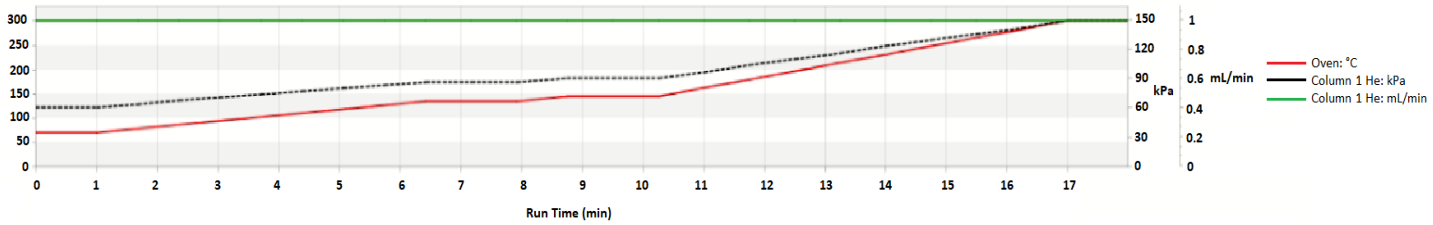

Figure 5.5: Final oven temperature gradient used for separation of all target compounds (Temperature in °C over run time in minutes)

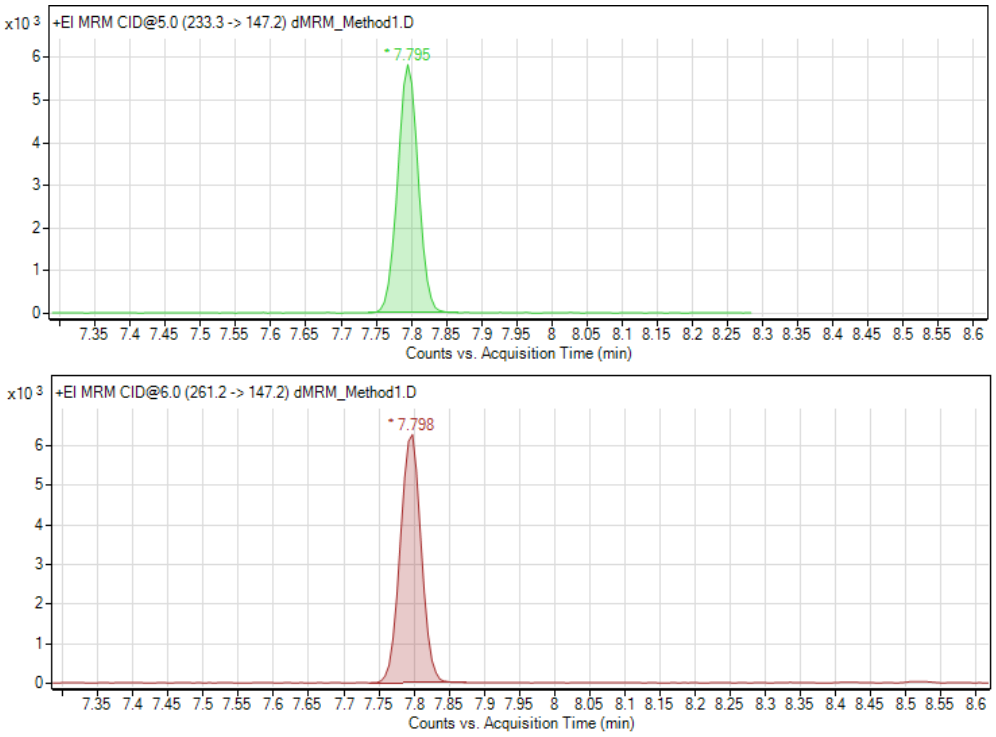

Figure 5.6: Specific detection of di-tBDMS lactate within a biological matrix with optimised dMRM conditions (Intensity over run time in minutes)

As seen in Figure 5.6, the dMRM quantifier and qualifier transitions of lactate detected the peak at Rt: 7.795 within the set window (7.3 - 8 min). No other interfering peaks were detected with this window which aids downstream data processing. Similar results were acquired for the other standards (results not shown).

5.3 Method characteristics: calibration curves, LOD's, LOQ's and other parameters

Stripped matrix samples spiked with standards of the target compounds in the range of 0 - 1000 ng metabolite / mg tissue was prepared and analysed in triplicate. Calibration curves for each

standard were plotted and used to determine precision, accuracy, LOD, LOQ, linearity and R^2. dMRM data was processed through Agilent MassHunter Quantitative software and peak areas of detected compounds exported to excel. To account for sample specific variation, all peak areas were normalised with the internal standard, 3-phenylbutyric acid. The normalised peak area was multiplied with the concentration of the internal standard (200 ng/mg) to acquire relative concentration of each compound. Each calibration curve was therefore constructed by using the relative concentration (normalised peak area) plotted against the expected (true) concentration. This was done for each tissue type separately. A complete summary of the redox marker validation parameters is presented in Appendix A.

5.3.1 Mouse Liver Calibration curves

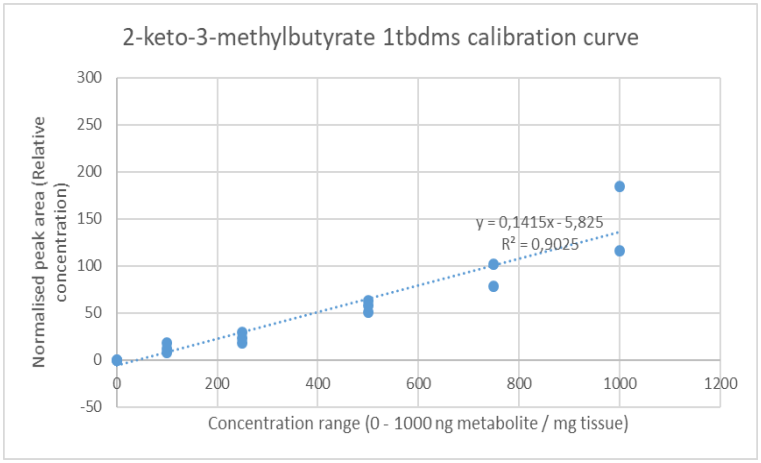

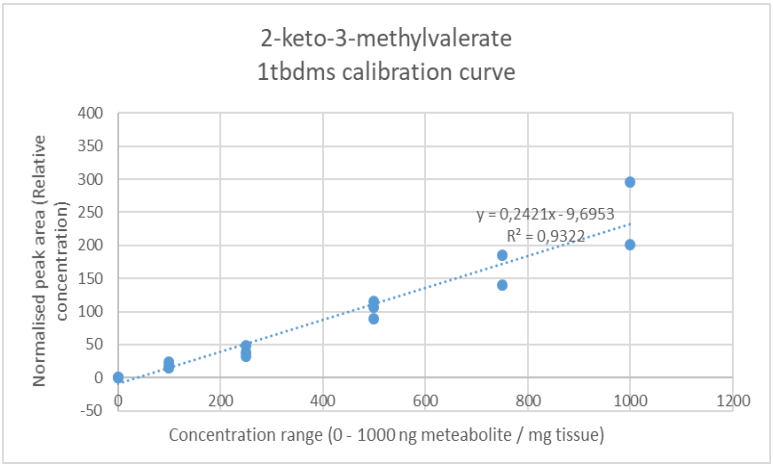

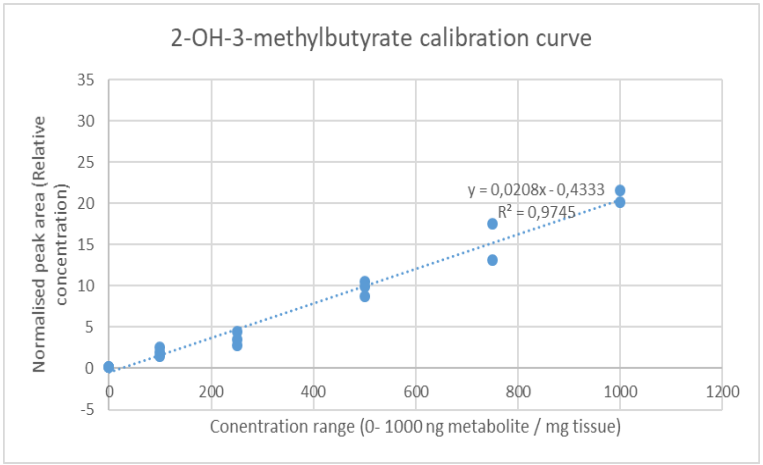

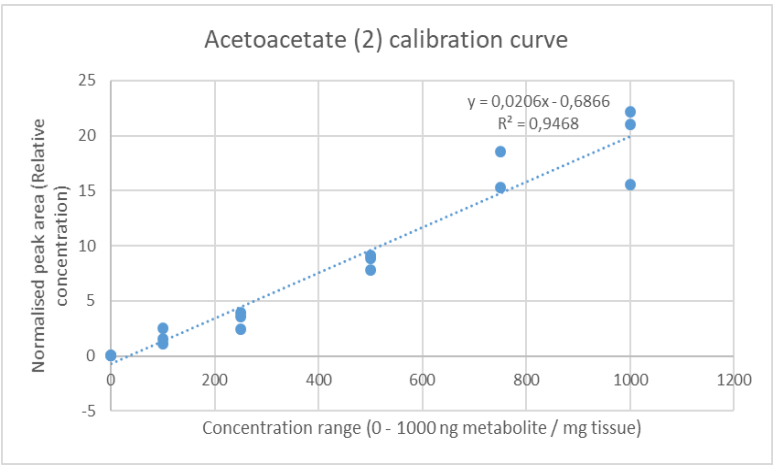

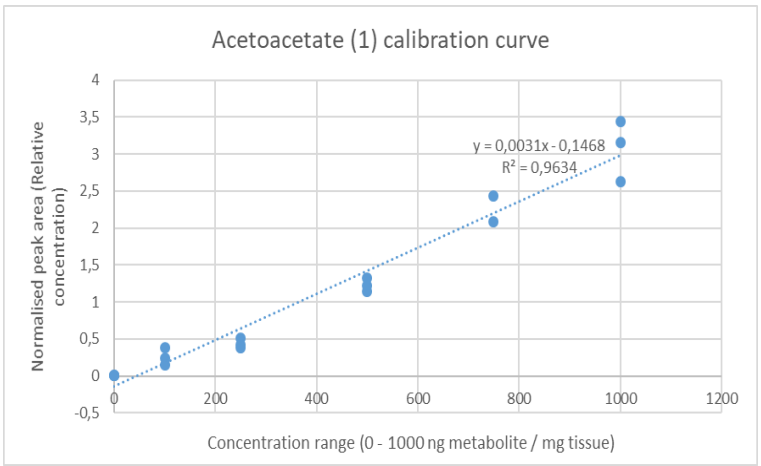

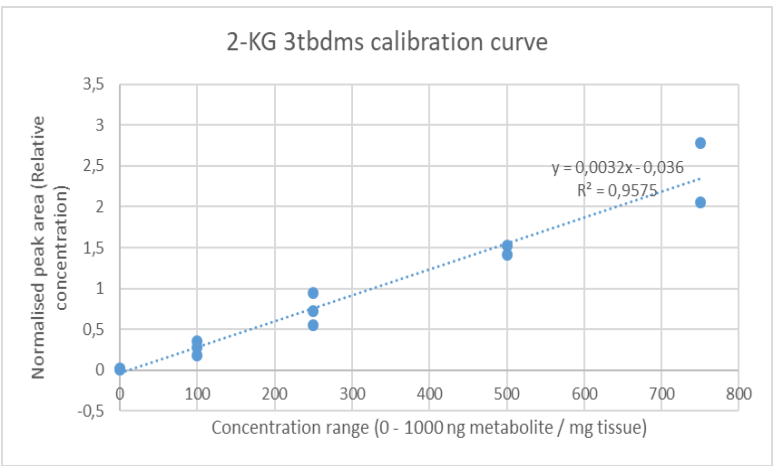

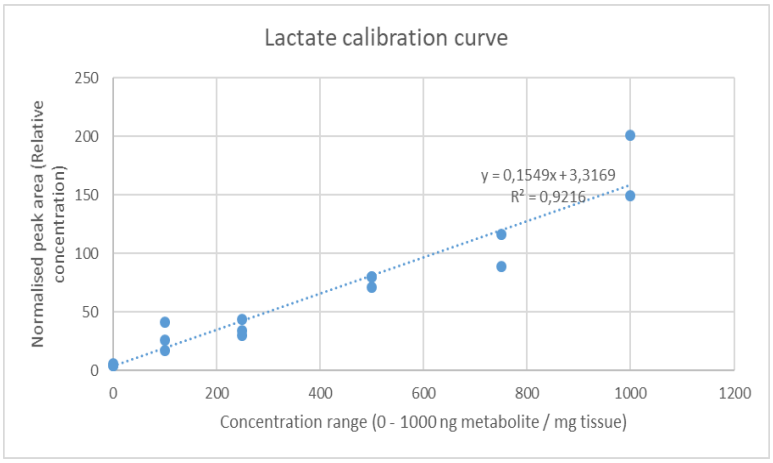
Lactate calibration curve
Normalised peak area (Relative concentration)
y = 0,1549x + 3,3169
R² = 0,9216
Concentration range (0 - 1000 ng metabolite / mg tissue)

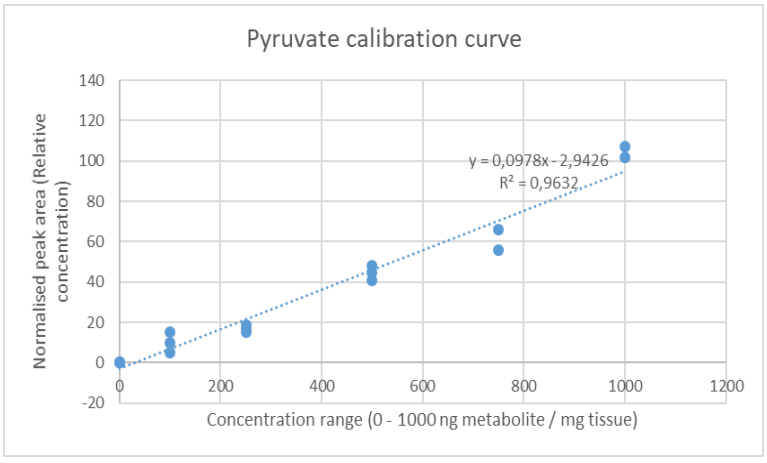
Pyruvate calibration curve
Normalised peak area (Relative concentration)
y = 0,0978x - 2,9426
R² = 0,9632
Concentration range (0 - 1000 ng metabolite / mg tissue)

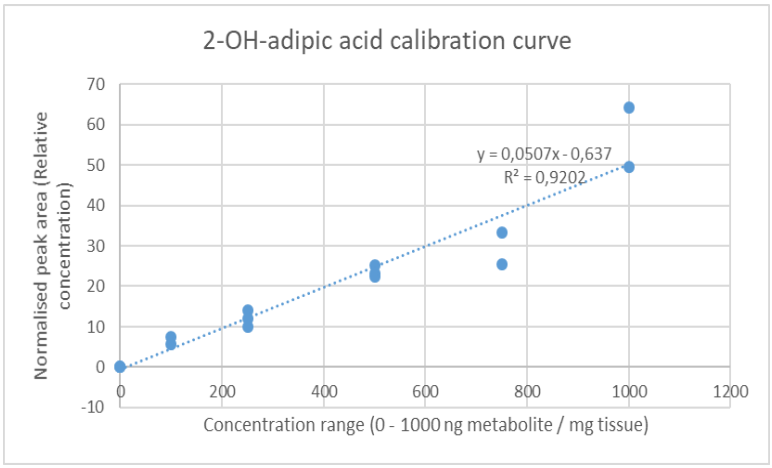
2-OH-adipic acid calibration curve
Normalised peak area (Relative concentration)
y = 0,0507x - 0,637
R² = 0,9202
Concentration range (0 - 1000 ng metabolite / mg tissue)

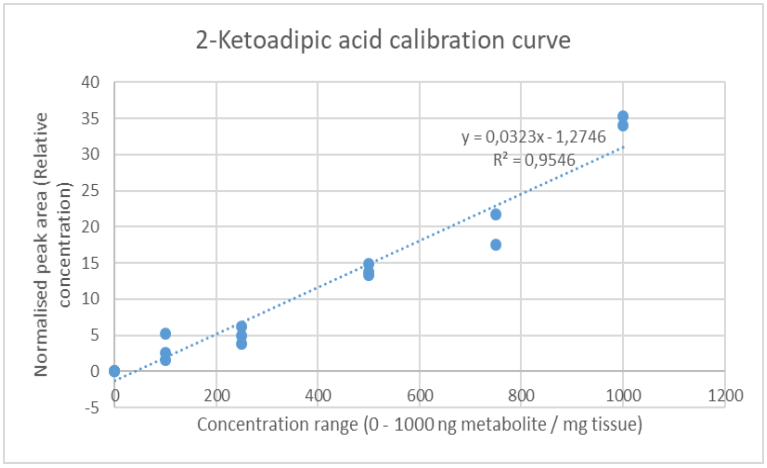
2-Ketoadipic acid calibration curve
Normalised peak area (Relative concentration)
y = 0,0323x - 1,2746
R² = 0,9546
Concentration range (0 - 1000 ng metabolite / mg tissue)

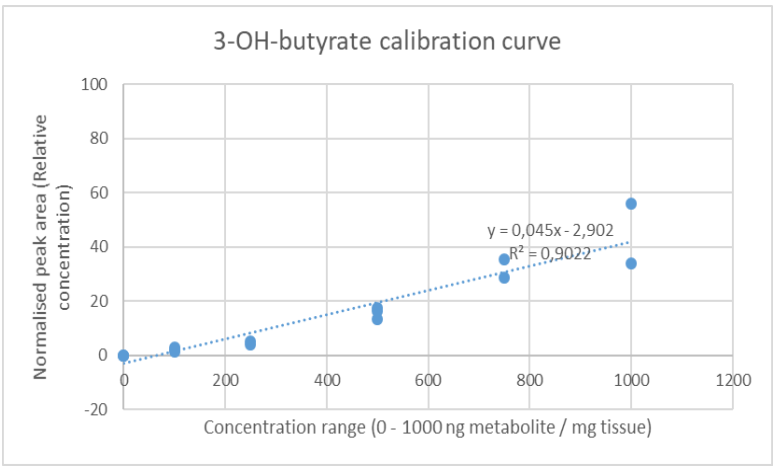
3-OH-butyrate calibration curve
Normalised peak area (Relative concentration)
y = 0,045x - 2,902
R² = 0,9022
Concentration range (0 - 1000 ng metabolite / mg tissue)

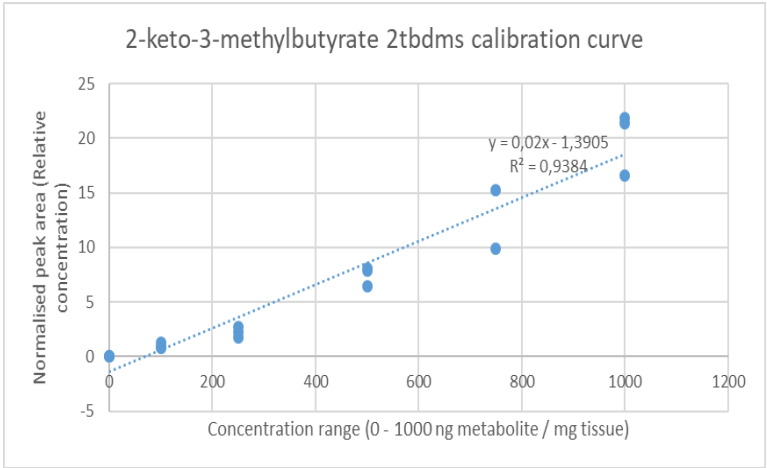
2-keto-3-methylbutyrate 2tbdms calibration curve
Normalised peak area (Relative concentration)
y = 0,02x - 1,3905
R² = 0,9384
Concentration range (0 - 1000 ng metabolite / mg tissue)

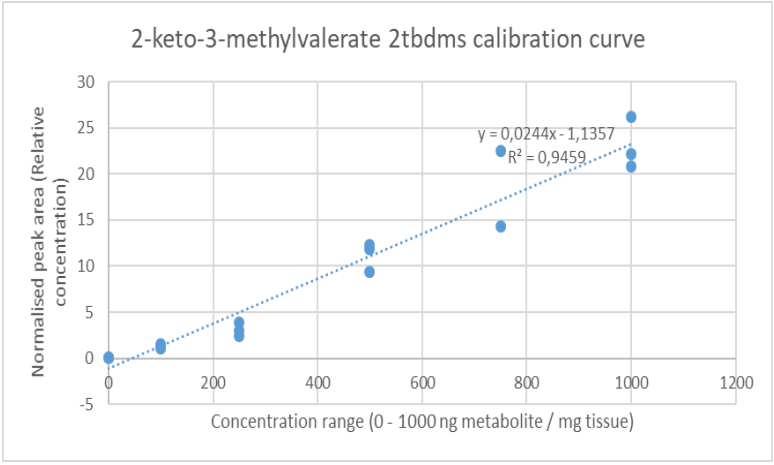
2-keto-3-methylvalerate 2tbdms calibration curve
Normalised peak area (Relative concentration)
y = 0,0244x - 1,1357
R² = 0,9459
Concentration range (0 - 1000 ng metabolite / mg tissue)

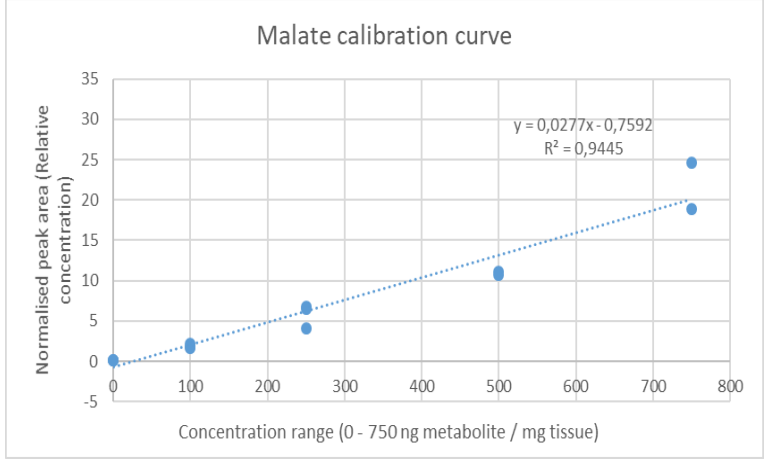
Malate calibration curve
Normalised peak area (Relative concentration)
y = 0,0277x - 0,7592
R² = 0,9445
Concentration range (0 - 750 ng metabolite / mg tissue)

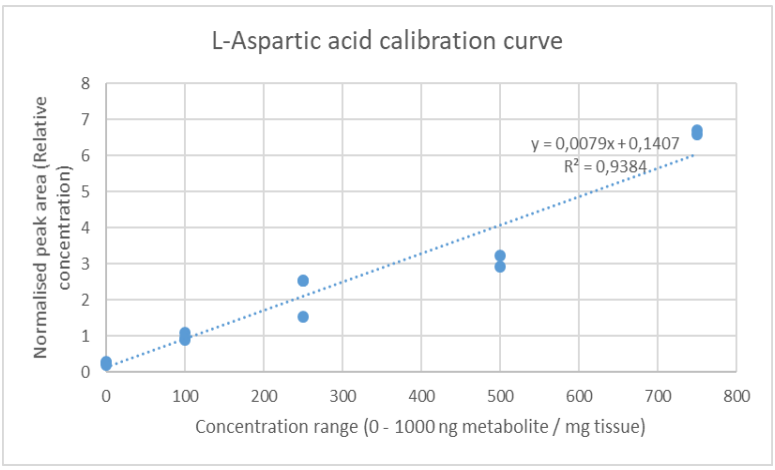
L-Aspartic acid calibration curve
Normalised peak area (Relative concentration)
y = 0,0079x + 0,1407
R² = 0,9384
Concentration range (0 - 1000 ng metabolite / mg tissue)

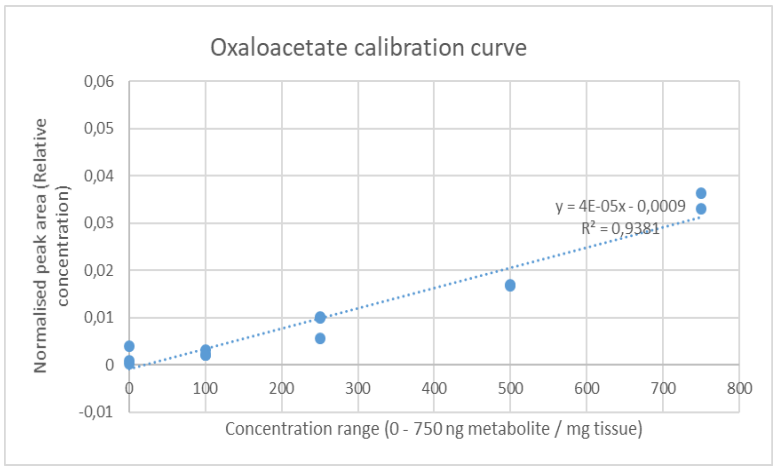
Oxaloacetate calibration curve
Normalised peak area (Relative concentration)
y = 4E-05x - 0,0009
R² = 0,9381
Concentration range (0 - 750 ng metabolite / mg tissue)

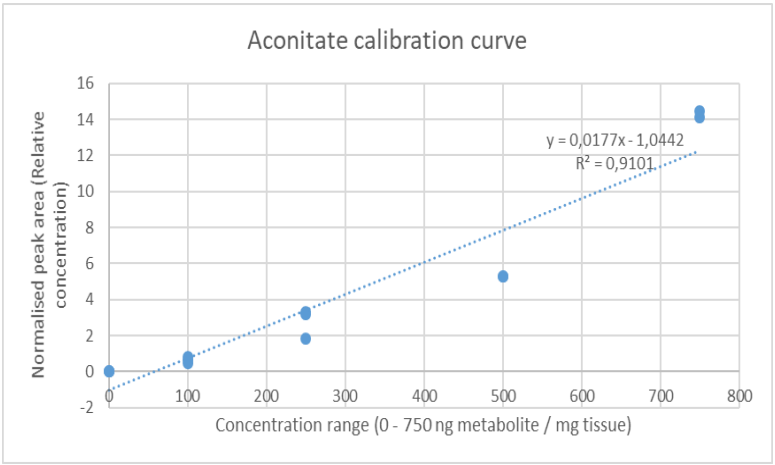
Aconitate calibration curve
Normalised peak area (Relative concentration)
y = 0,0177x - 1,0442
R² = 0,9101
Concentration range (0 - 750 ng metabolite / mg tissue)

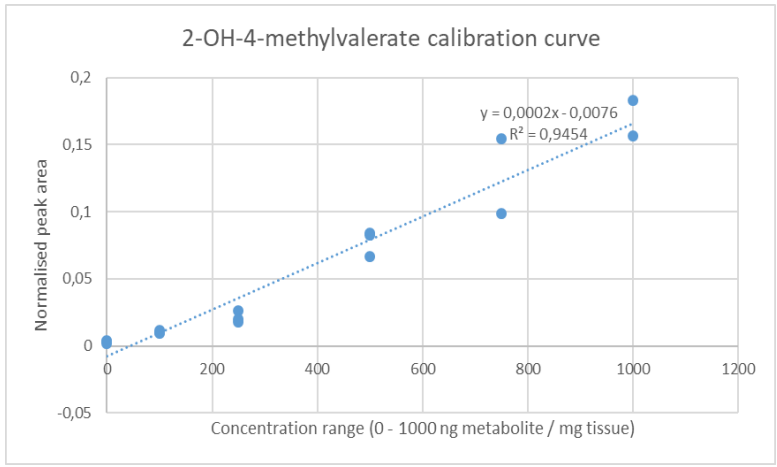
2-OH-4-methylvalerate calibration curve
Normalised peak area
y = 0,0002x - 0,0076
R² = 0,9454
Concentration range (0 - 1000 ng metabolite / mg tissue)

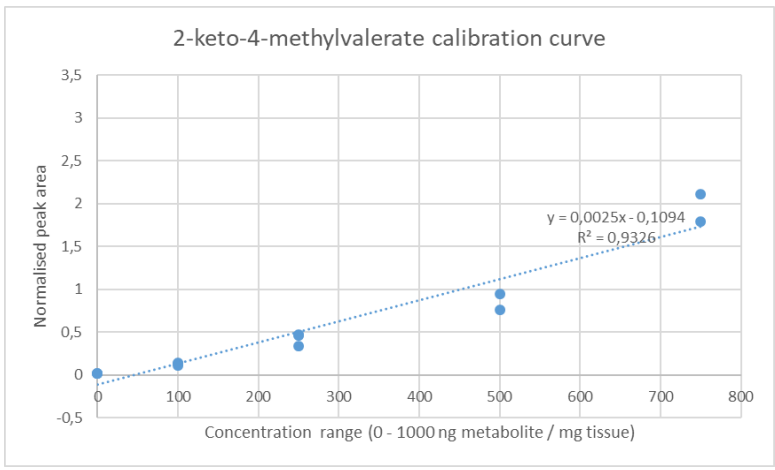
2-keto-4-methylvalerate calibration curve
Normalised peak area
y = 0,0025x - 0,1094
R² = 0,9326
Concentration range (0 - 1000 ng metabolite / mg tissue)

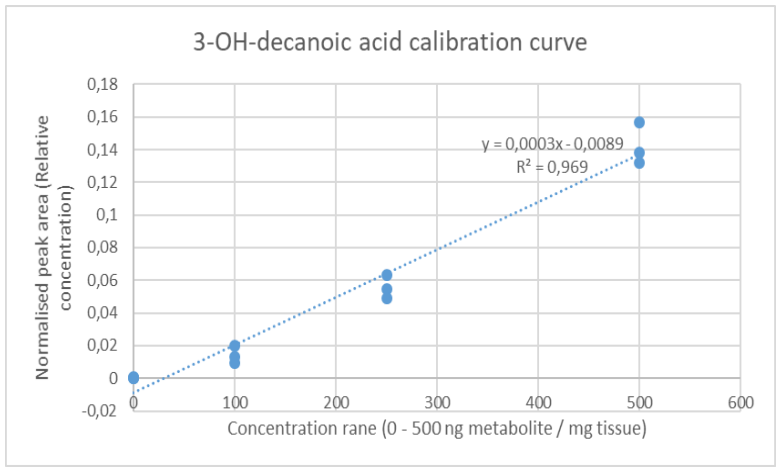
3-OH-decanoic acid calibration curve
Normalised peak area (Relative concentration)
y = 0,0003x - 0,0089
R² = 0,969
Concentration rane (0 - 500 ng metabolite / mg tissue)

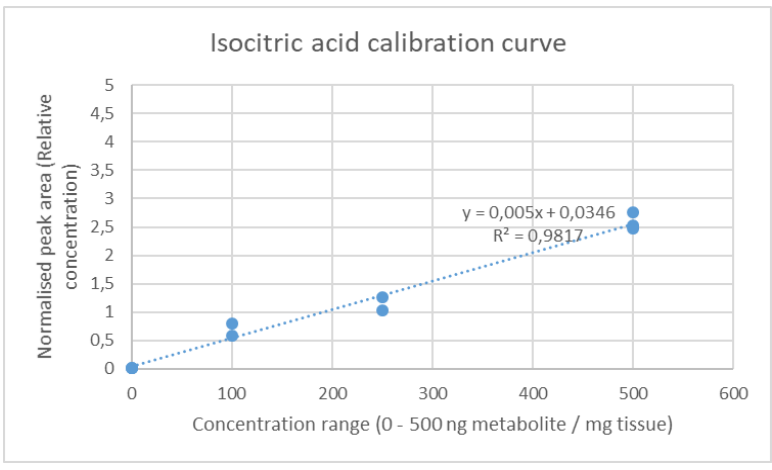
Isocitric acid calibration curve
Normalised peak area (Relative concentration)
y = 0,005x + 0,0346
R² = 0,9817
Concentration range (0 - 500 ng metabolite / mg tissue)

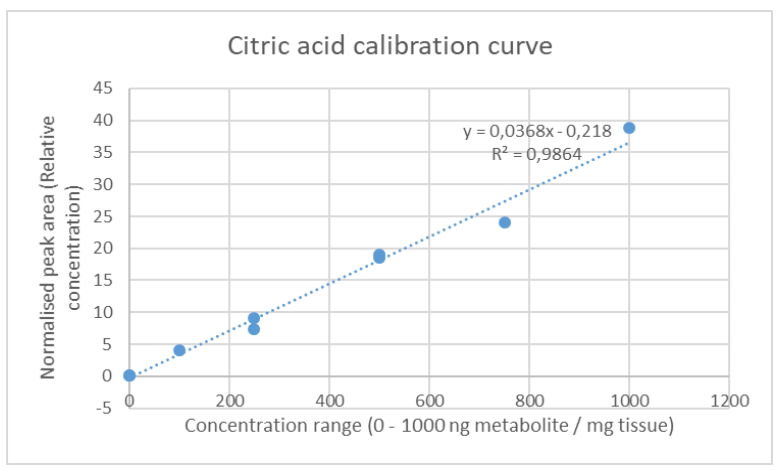
Citric acid calibration curve
Normalised peak area (Relative concentration)
y = 0,0368x - 0,218
R² = 0,9864
Concentration range (0 - 1000 ng metabolite / mg tissue)

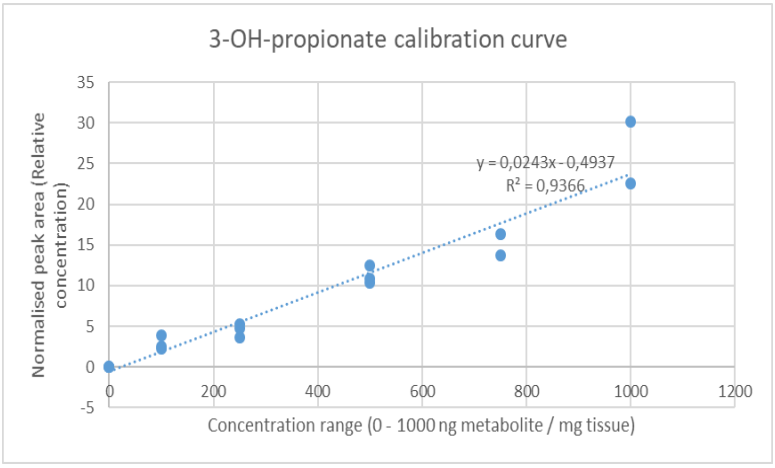

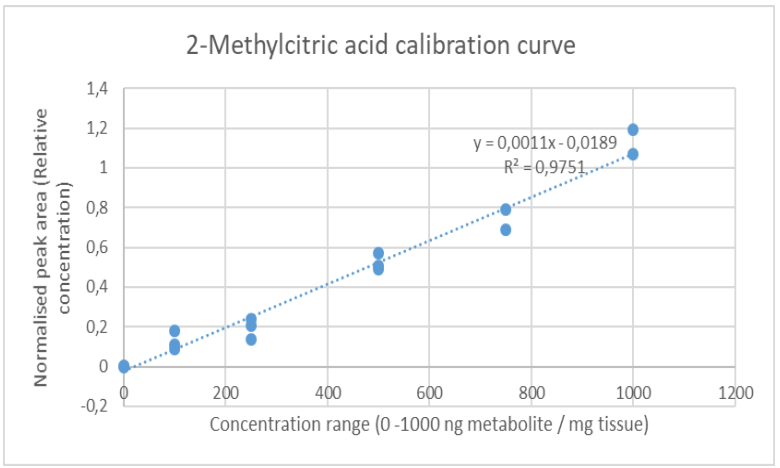

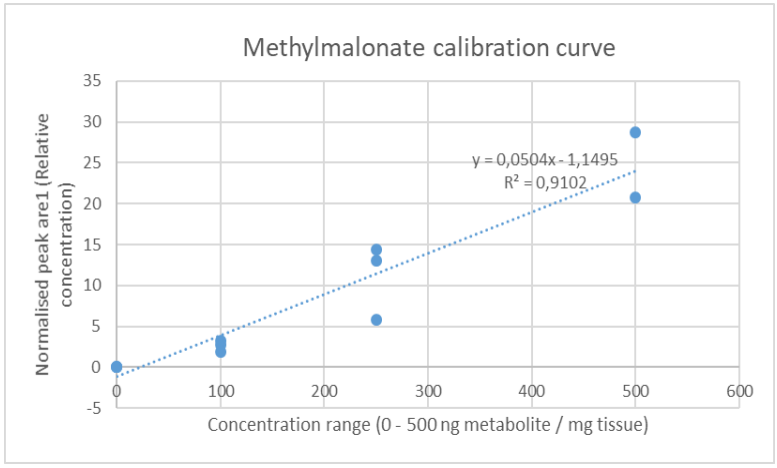

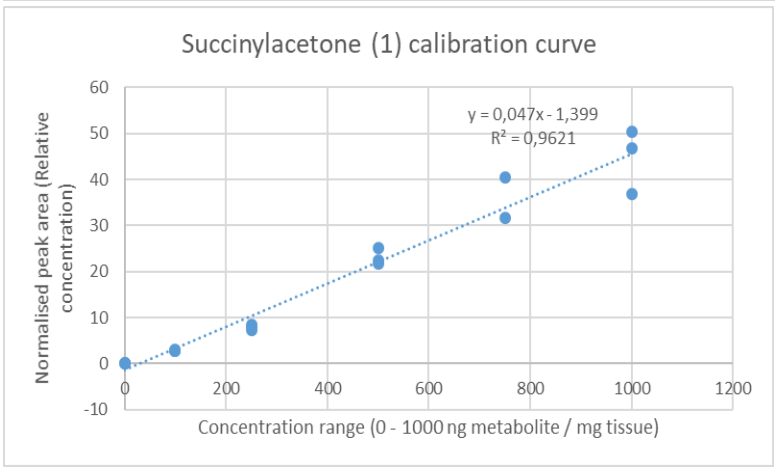

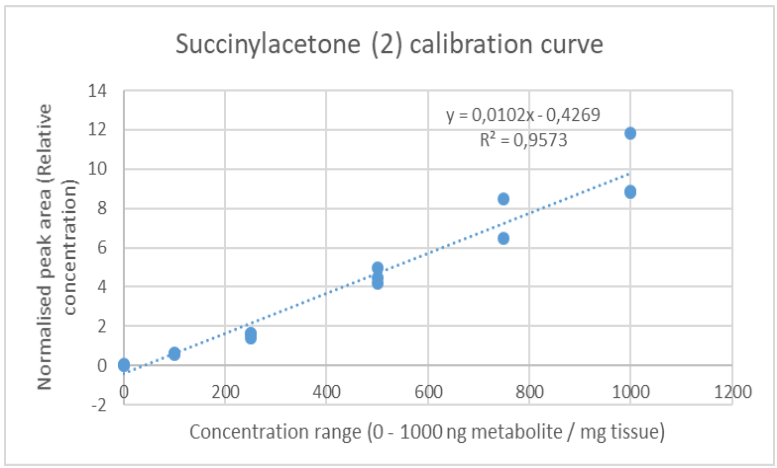

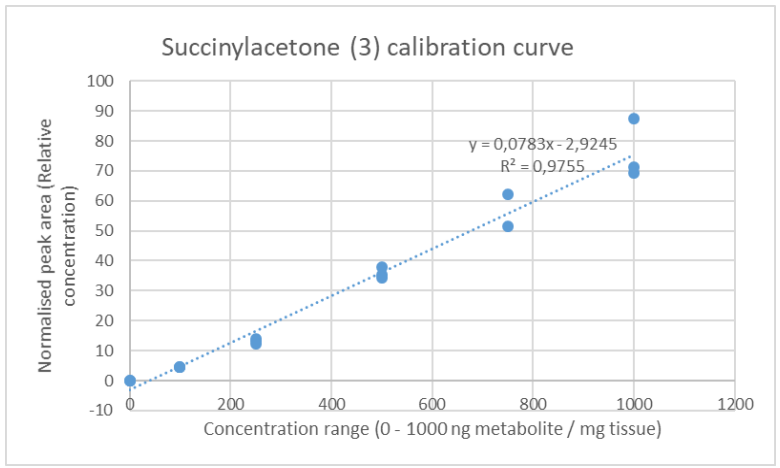

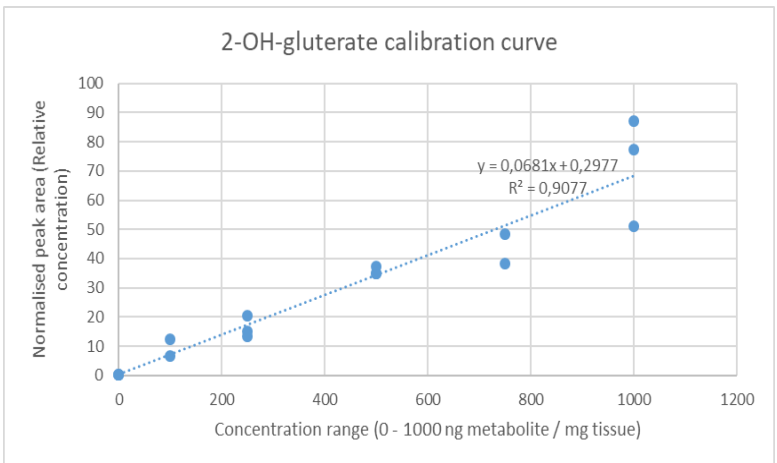

Figures 5.7: Liver calibration curves of the 26 targeted compounds

As per Figures 5.7, each compound gave a linear response with R^2 ranging from 0.9022 to 0.9864. The calibration curves for compounds with R^2 above 0.9 indicate a linear relationship between instrument response and compound concentration and could therefore be quantified in the tested range (Koek *et al.*, 2011).

In addition, most calibration curves were constructed with the entire concentration range (0 - 1000 ng/mg), except for L-aspartate, malate, oxaloacetate, 2-ketoglutarate (3 tBDMS), aconitic acid, and 2-keto-4-methylvaleric acid which did not include the 1000 ng/mg tissue triplicates. 3-Hydroxydecanoic acid and methylmalonate was the only two compounds which did not include the 1000 and 750 ng/mg tissue triplicates as they exhibited a lot of variation at these levels. At certain calibration curves the 750 calibration level exhibited the most variation which could be linked to a pipetting error during the transfer of each organic acid working solution or through variation in the drying efficiency for this particular calibration level. Hence, their optimal linear range are the lower concentration points of the calibration curve. Moreso, the plotted triplicate samples of the highest calibration range exhibited linearity at the lower calibration range. This was most probably due to these compounds reaching the end of the first linear calibration range, marking the changepoint into the second linear portion of the calibration curve.

Broadly, most of the compounds had a relatively low or negative y intercept as per their regression lines, which are indicative of effective metabolite stripping (Section 4.5.1). Compounds such as L-aspartate (qualifier and quantifier), oxaloacetate (qualifier), isocitrate (quantifier) and 2-OH-adipic acid (qualifier) had relatively higher y-intercepts than the other compounds which could be due to ineffective stripping of these compounds from the liver matrix.

Table 5.10: Method performance characteristics of liver calibrators

Compound	LOD (ng/mg)	LOQ (ng/mg)	Accuracy (%)	R^2	Linear range (ng/mg)
Lactate	22.834	58.848	98.42	0.9216	0 - 1000
2-OH-gluterate	2.826	11.304	101.31	0.9077	0 – 1000
Pyruvate	35.659	38.223	95.99	0.9627	0 – 1000
2-keto-3-methylbutyrate 1tBDMS	44.803	46.831	104.44	0.9025	0 – 1000
2-keto-3-methylvalerate 1tBDMS	41.538	43.069	103.70	0.9322	0 – 1000
2-OH-3-methylbutyrate	33.979	41.629	99.80	0.9745	0 – 1000
Acetoacetate (2)	31.587	31.798	93.325	0.9444	0 – 1000
Acetoacetate (1)	48.690	50.577	94.12	0.9634	0 – 1000
2-ketoglutarate 3tBDMS	17.403	23.425	93.69	0.9575	0 – 750
2-OH-adipic acid	14.000	15.293	100.54	0.9202	0 – 1000
2-ketoadipic acid	40.221	41.214	99.72	0.9546	0 – 1000
3-OH-butyrate	74.269	75.065	89.78	0.9022	0 – 1000
2-keto-3-methylbutyrate 2tBDMS	73.090	77.285	92.16	0.9384	0 – 1000
2-keto-3-methylvalerate 2tBDMS	52.394	57.827	85.63	0.9459	0 – 1000

2-keto-3-methylvalerate 2tBDMS	8.393	14.586	89.45	0.9442	0 – 1000
Malate	35.098	41.027	105.74	0.9445	0 – 750
L-Aspartate	28.371	54.233	122.51	0.936	0 – 750
Oxaloacetate	97.604	159.515	92.69	0.9103	0 – 750
Aconitate	59.284	59.705	97.84	0.9101	0 – 750
Citrate	9.423	11.171	95.40	0.986	0 – 1000
Isocitrate	0.788	2.143	107.94	0.981	0 – 500
2-keto-4-methylvalerate 2tBDMS	49.557	50.551	90.85	0.9326	0 – 750
2-OH-4-methylvalerate	69.252	110.275	90.56	0.9454	0 - 1000
3-OH-decanoic acid	33.938	42.297	97.89	0.969	0 – 500
3-OH-propionate	23.138	24.616	106.70	0.9366	0 – 1000
2-Methylcitric acid	19.401	22.740	95.95	0.9751	0 – 1000
Methylmalonate	23.295	23.757	113.72	0.9102	0 - 500
Succinylacetone (1)	30.504	31.476	101.29	0.9621	0 – 1000
Succinylacetone (2)	46.060	48.941	90.46	0.9573	0 – 1000
Succinylacetone (3)	37.478	39.010	103.25	0.9718	0 – 1000

Table 5.10 shows the LOD, LOQ, R^2, accuracy and linear range of each organic acid optimised in mouse liver tissue. The LOD of these selected organic acids ranged from 0.788 ng/mg - 213.559 ng/mg, whereas the LOQ's ranged from 5.561 ng/mg - 560.103 ng/mg. The highest LOD and LOQ calculated from each organic acid calibration curve was just above 100 ng/mg (first spiked sample) which indicates that the method could sufficiently detect organic acids at low concentrations while being able to be distinguished from analytical noise.

To calculate the accuracy of each target compound, an additional 500 ng/mg sample was analysed and the regression line used to calculate the concentration of the respective compound in this sample as if unknown. For example, the accuracy of lactate was 98.42 % and was calculated in the following way: Lactate regression line formula was y = 0.1549x + 3.3169. With the randomly selected 500 ng/mg concentration range normalised peak area being 79.645 and thus y = 79.645. 7. The calculation of x generated a predicted absolute concentration (ng metabolite / mg tissue) of 492.148. Therefore, the predicted absolute concentration 492.148 can be divided by the actual concentration 500 and expressed in %, yielding an accuracy of 98.42 %. Thus, there is a relatively large agreement between the nominal concentration (actual concentration) and the experimental concentration which indicates that the optimised method (for that particular compound) is indeed accurate and that experimental absolute concentrations can be determined accurately from the generated calibration curve regression line formula.

The accuracy across all compounds ranged from 85.63 % - 122.51 %, whereas the accuracy for both l-aspartate's transitions were above the arbitrary 15 % accuracy cut off. All other transitions for the selected organic acids resembled good accuracy (not 15 % above or below 100 %) and is therefore a good indication of the selectivity and specificity when analysing the selected organic acids with the used MRM transitions, within a mouse liver matrix.

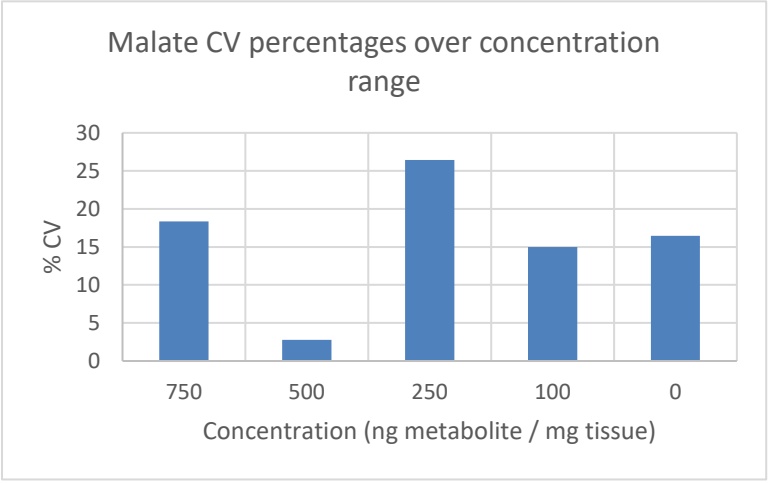

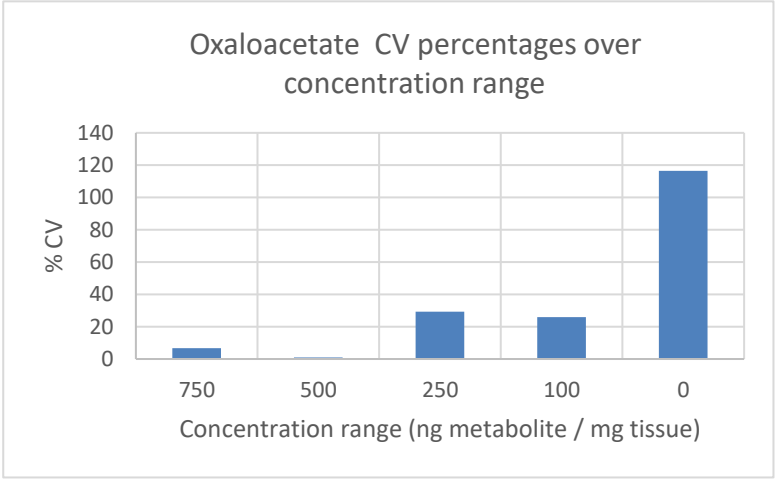

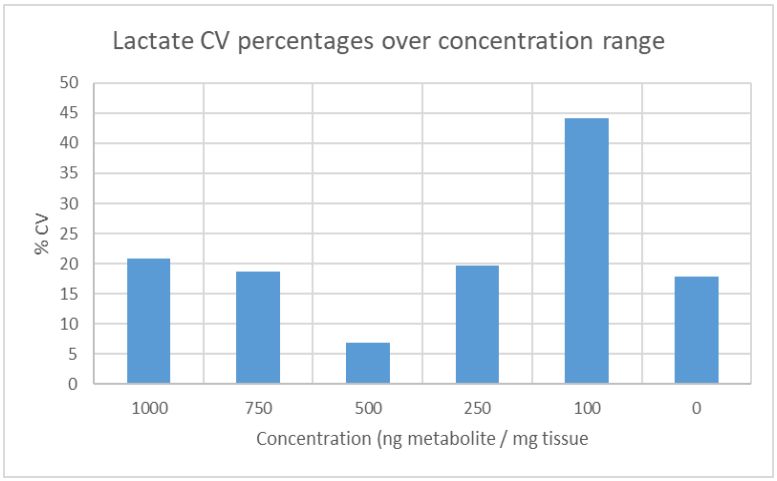
Lactate CV percentages over concentration range
% CV
50
45
40
35
30
25
20
15
10
5
0
1000
750
500
250
100
0
Concentration (ng metabolite / mg tissue

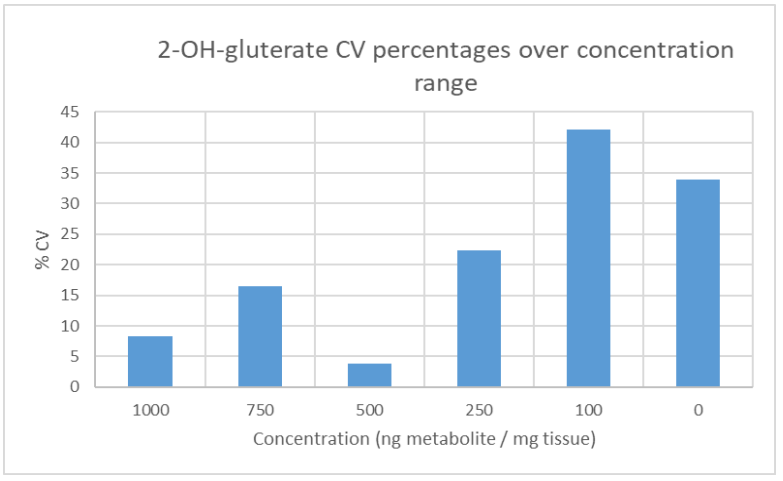
2-OH-gluterate CV percentages over concentration range
% CV
45
40
35
30
25
20
15
10
5
0
1000
750
500
250
100
0
Concentration (ng metabolite / mg tissue)

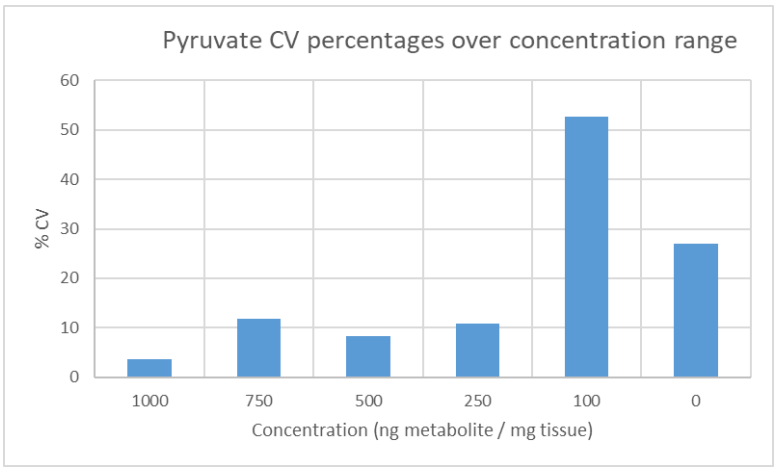
Pyruvate CV percentages over concentration range
% CV
60
50
40
30
20
10
0
1000
750
500
250
100
0
Concentration (ng metabolite / mg tissue)

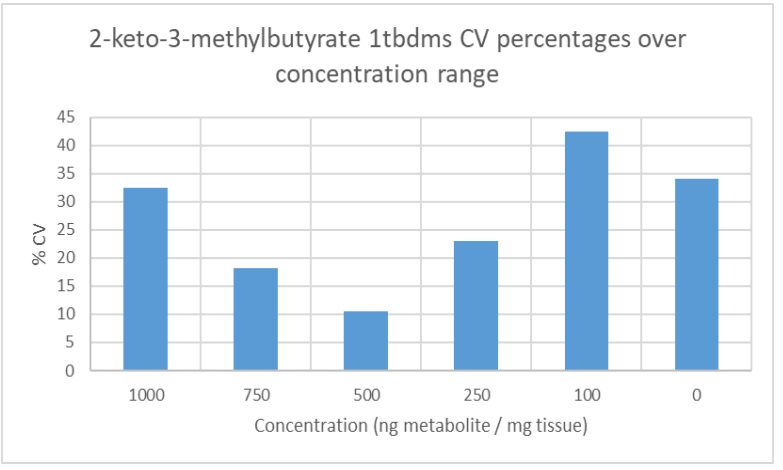
2-keto-3-methylbutyrate 1tbdms CV percentages over concentration range
% CV
45
40
35
30
25
20
15
10
5
0
1000
750
500
250
100
0
Concentration (ng metabolite / mg tissue)

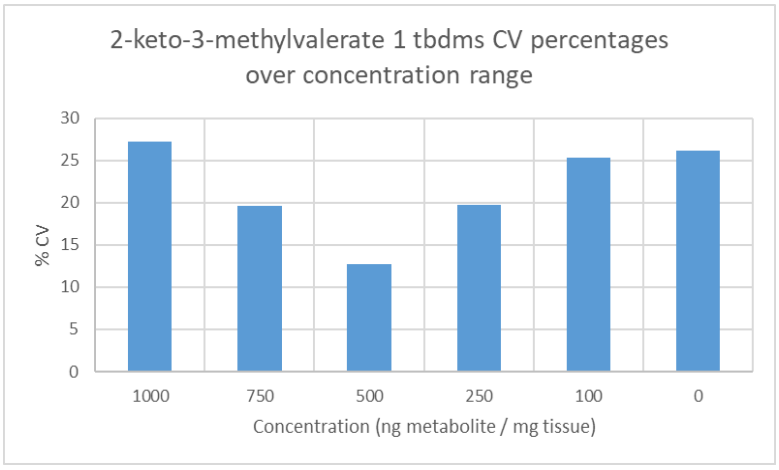
2-keto-3-methylvalerate 1 tbdms CV percentages over concentration range
% CV
30
25
20
15
10
5
0
1000
750
500
250
100
0
Concentration (ng metabolite / mg tissue)

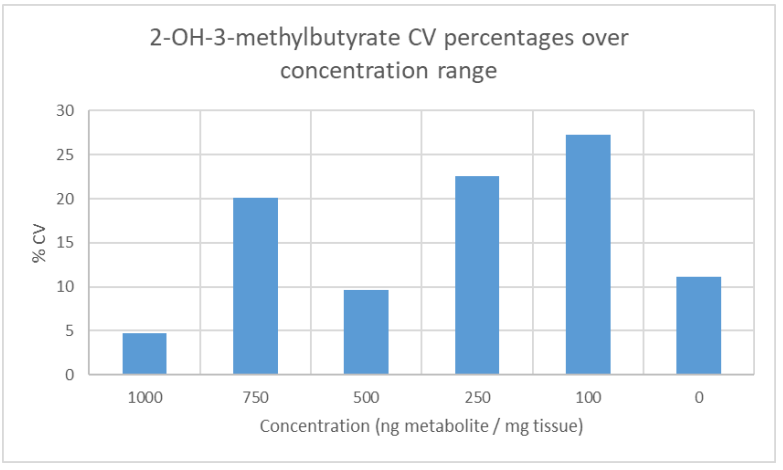
2-OH-3-methylbutyrate CV percentages over concentration range
% CV
30
25
20
15
10
5
0
1000
750
500
250
100
0
Concentration (ng metabolite / mg tissue)

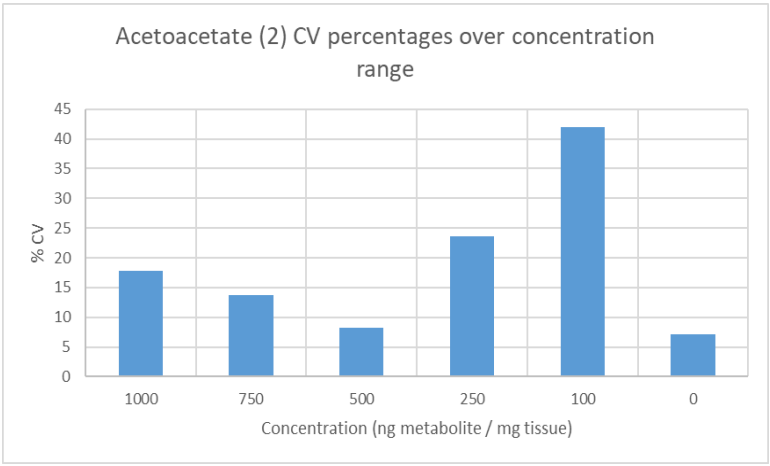
Acetoacetate (2) CV percentages over concentration range
% CV
45
40
35
30
25
20
15
10
5
0
1000
750
500
250
100
0
Concentration (ng metabolite / mg tissue)

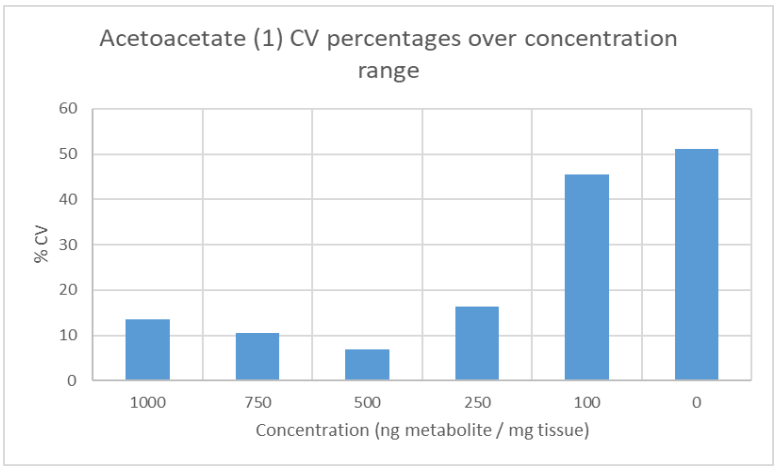
Acetoacetate (1) CV percentages over concentration range
% CV
60
50
40
30
20
10
0
1000
750
500
250
100
0
Concentration (ng metabolite / mg tissue)

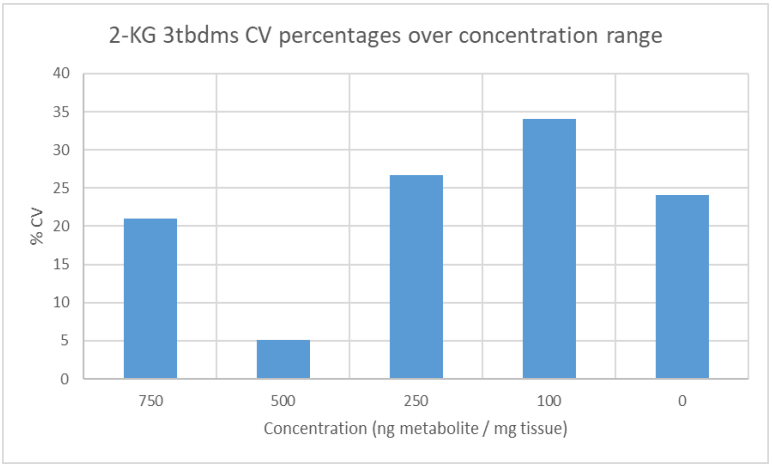
2-KG 3tbdms CV percentages over concentration range
% CV
40
35
30
25
20
15
10
5
0
750
500
250
100
0
Concentration (ng metabolite / mg tissue)

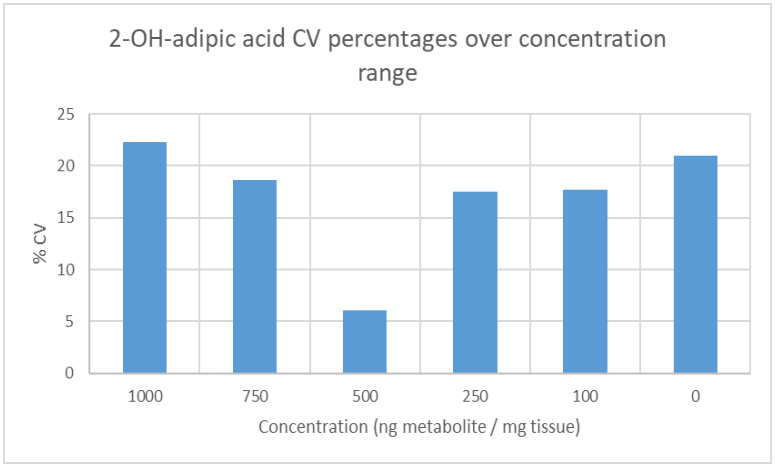
2-OH-adipic acid CV percentages over concentration range
% CV
25
20
15
10
5
0
1000
750
500
250
100
0
Concentration (ng metabolite / mg tissue)

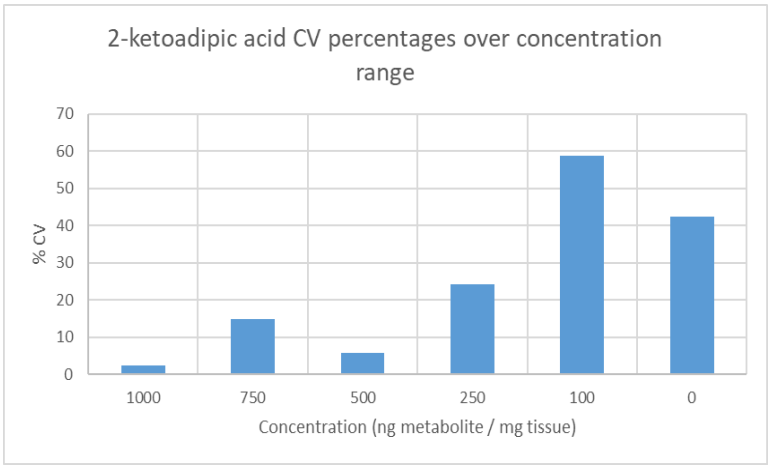
2-ketoadipic acid CV percentages over concentration range
% CV
70
60
50
40
30
20
10
0
1000
750
500
250
100
0
Concentration (ng metabolite / mg tissue)

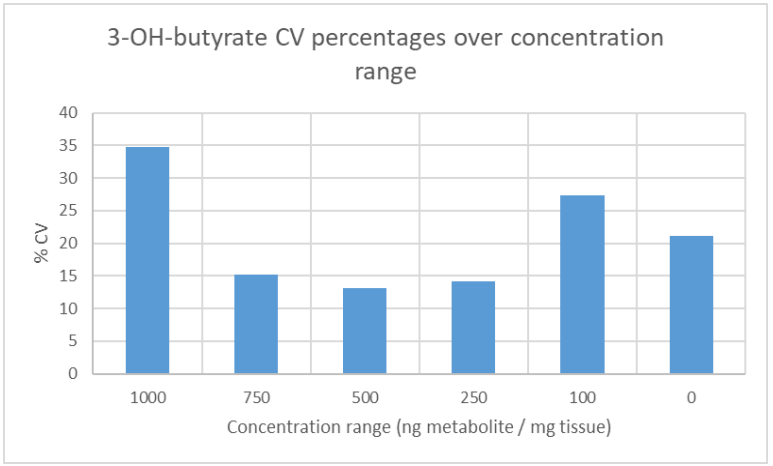
3-OH-butyrate CV percentages over concentration range
% CV
40
35
30
25
20
15
10
5
0
1000
750
500
250
100
0
Concentration range (ng metabolite / mg tissue)

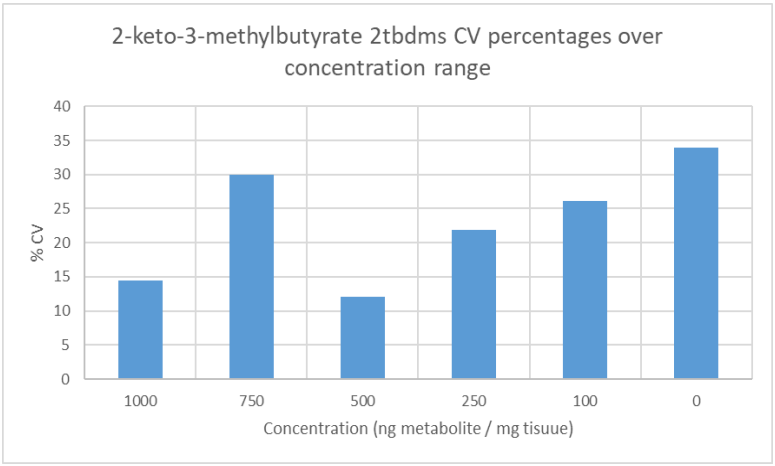
2-keto-3-methylbutyrate 2tbdms CV percentages over concentration range
% CV
40
35
30
25
20
15
10
5
0
1000
750
500
250
100
0
Concentration (ng metabolite / mg tisuue)

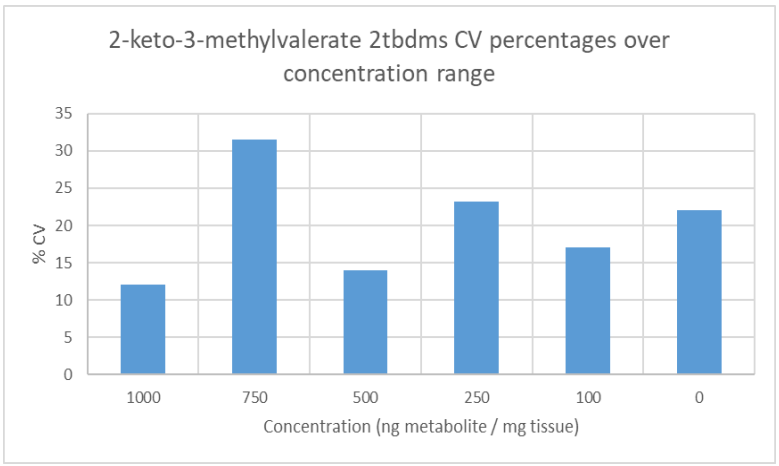
2-keto-3-methylvalerate 2tbdms CV percentages over concentration range
% CV
35
30
25
20
15
10
5
0
1000
750
500
250
100
0
Concentration (ng metabolite / mg tissue)

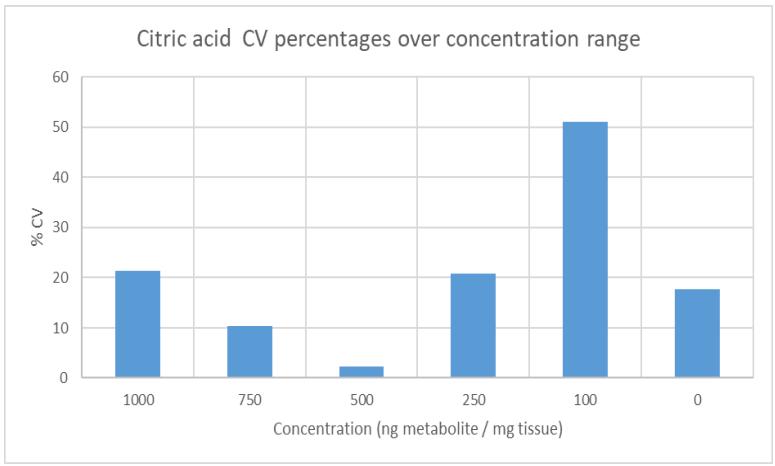
Citric acid CV percentages over concentration range
% CV
60
50
40
30
20
10
0
1000
750
500
250
100
0
Concentration (ng metabolite / mg tissue)

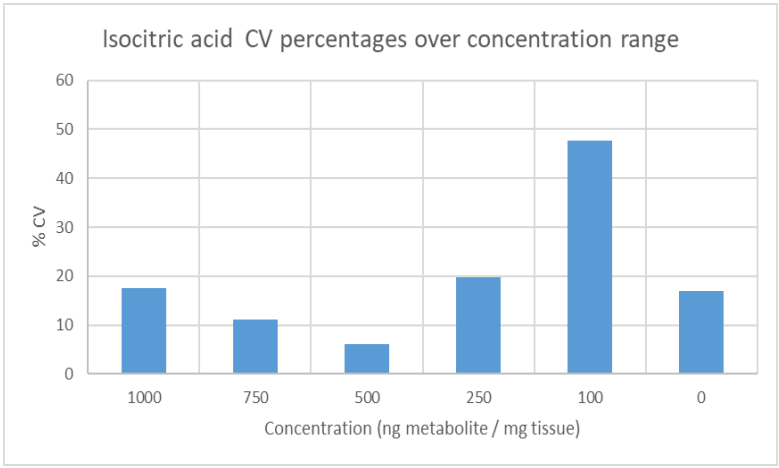
Isocitric acid CV percentages over concentration range
% CV
60
50
40
30
20
10
0
1000
750
500
250
100
0
Concentration (ng metabolite / mg tissue)

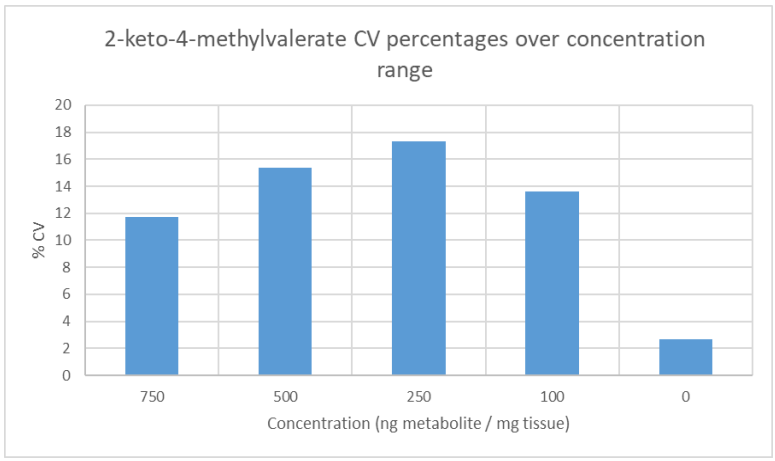
2-keto-4-methylvalerate CV percentages over concentration range
% CV
20
18
16
14
12
10
8
6
4
2
0
750
500
250
100
0
Concentration (ng metabolite / mg tissue)

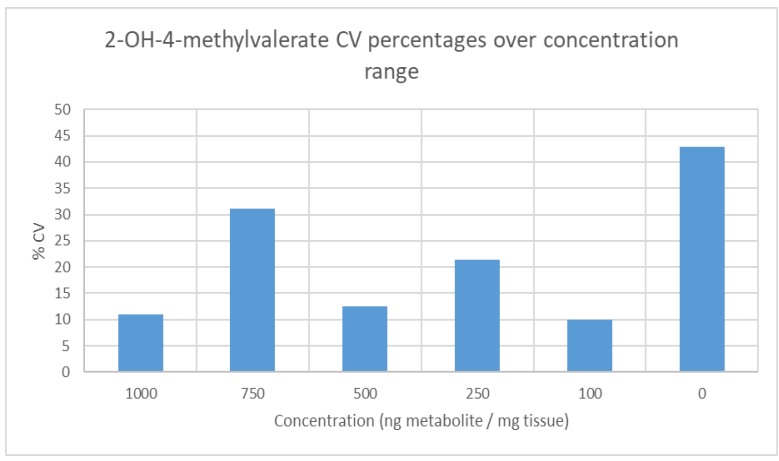
2-OH-4-methylvalerate CV percentages over concentration range
% CV
50
45
40
35
30
25
20
15
10
5
0
1000
750
500
250
100
0
Concentration (ng metabolite / mg tissue)

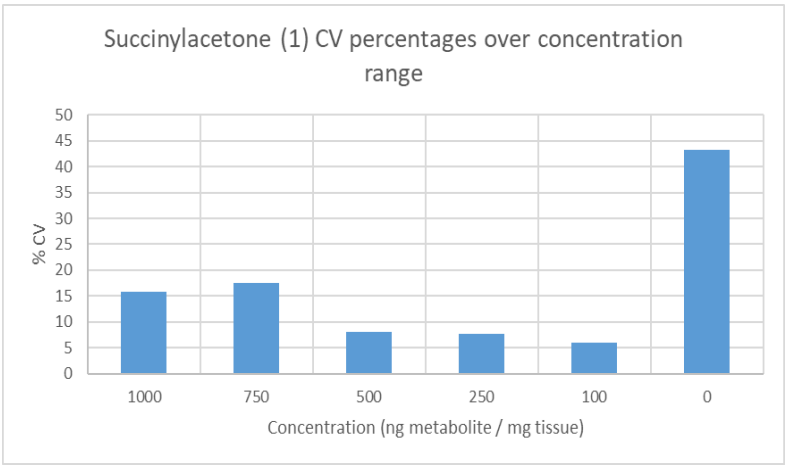
Succinylacetone (1) CV percentages over concentration range
% CV
50
45
40
35
30
25
20
15
10
5
0
1000
750
500
250
100
0
Concentration (ng metabolite / mg tissue)

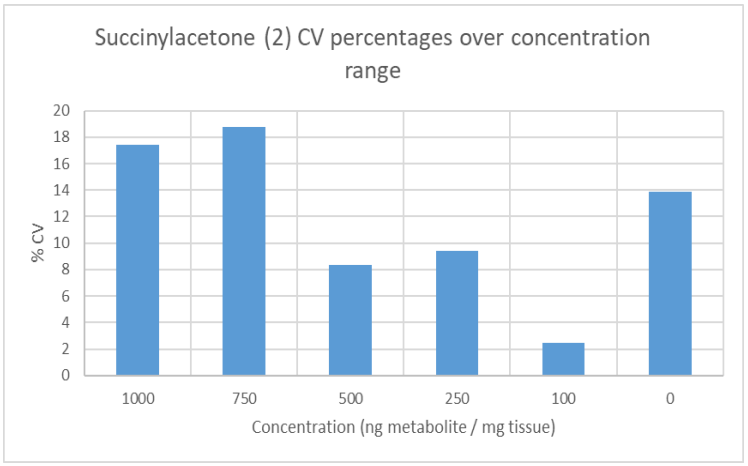
Succinylacetone (2) CV percentages over concentration range
% CV
20
18
16
14
12
10
8
6
4
2
0
1000
750
500
250
100
0
Concentration (ng metabolite / mg tissue)

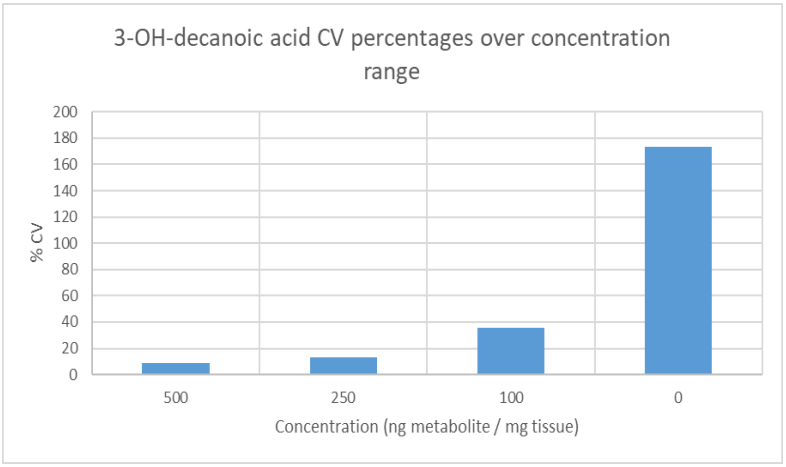
3-OH-decanoic acid CV percentages over concentration range
% CV
200
180
160
140
120
100
80
60
40
20
0
500
250
100
0
Concentration (ng metabolite / mg tissue)

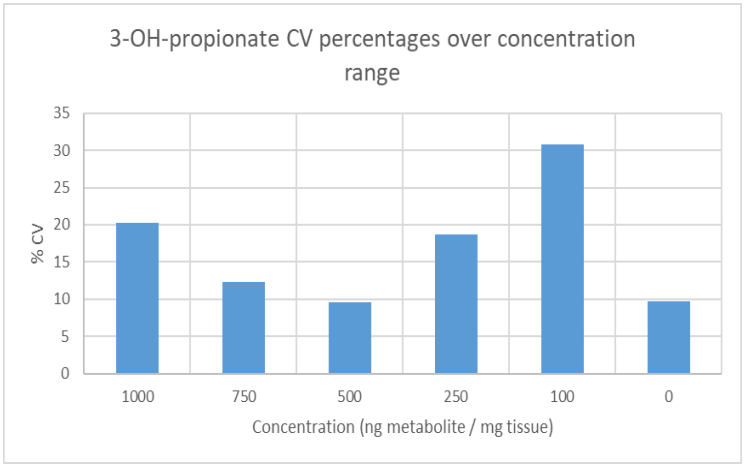
3-OH-propionate CV percentages over concentration range
% CV
35
30
25
20
15
10
5
0
1000
750
500
250
100
0
Concentration (ng metabolite / mg tissue)

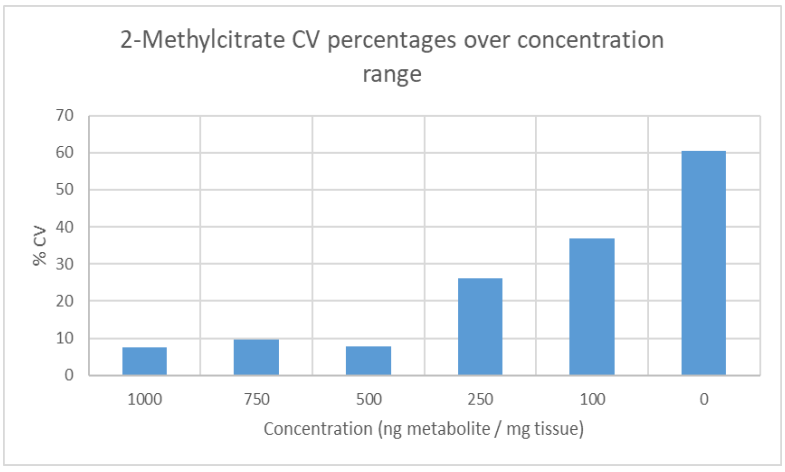
2-Methylcitrate CV percentages over concentration range
% CV
70
60
50
40
30
20
10
0
1000
750
500
250
100
0
Concentration (ng metabolite / mg tissue)

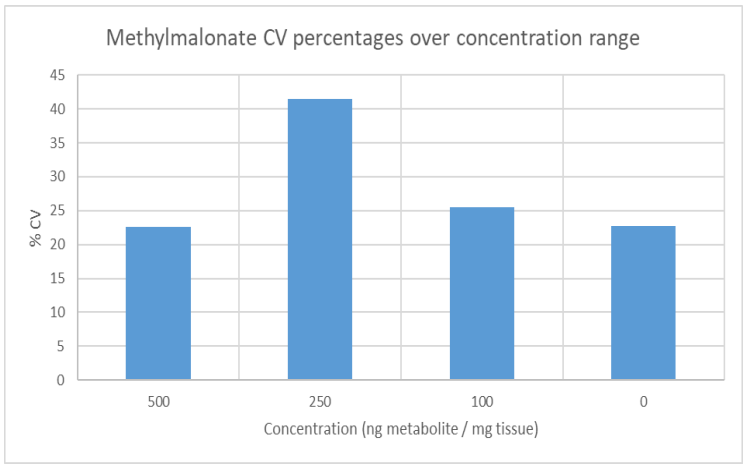
Methylmalonate CV percentages over concentration range
% CV
45
40
35
30
25
20
15
10
5
0
500
250
100
0
Concentration (ng metabolite / mg tissue)

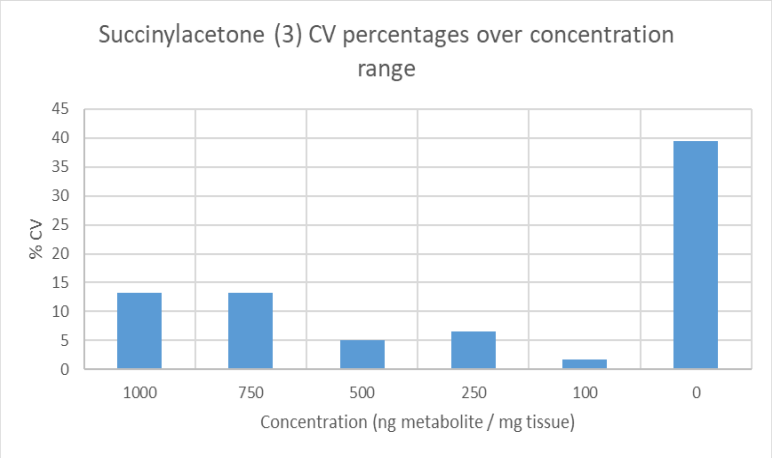

Figures 5.8: Bar graphs representing the CV percentages over the calibration concentration of selected organic acids

Figures 5.8 represents various bar graphs indicating the CV expressed in percentages, over the concentration range used for compound calibration (0 - 1000 ng metabolite / mg tissue).

Table 5.11: Summarized variance over the liver calibration range. The total number of compounds with CV above and below 25 % at each calibration point in mouse liver are indicated.

Concentration range (ng/mg)	Total with % CV's < 25	Total with % CV's > 25
1000	18	3
750	26	3
500	31	0
250	24	7
100	13	18
Blank	15	14

The following compounds: L-aspartate, malate, oxaloacetate, 2-ketoglutarate (3 tBDMS), aconitic acid, 2-keto-4-methylvaleric acid, 3-OH-decanoic acid and methylmalonate had CV graphs constructed without the 1000 ng/mg range, whereas the 750 ng/mg tissue range was also left out during the construction of 3-OH-decanoic acid and methylmalonate CV graphs. As previously discussed, the 1000 and in some cases, the 750 calibration points were not within the linear concentration range for these compounds, and thus were left out for the calculation of CV percentages.

Throughout triplicate analysis of each compound at different concentrations in mouse liver, the order of increasing variation expressed as percentage were as follows: 500 < 750 < 1000 < 250 < Blank < 100. According to Table 5.11, the 0 - 250 concentration range exhibited the highest

number of variations between each triplicate sample as well as the highest number of incidences in which the % CV was above 25%. Expectedly, the variance increases the closer one gets to the LOD and LOQ of the compound. Another possible explanation of the variance observed at the low concentration samples could have been due to pipetting error, as this calibration point required the pipetting of small volume standards. On the contrary, the 500 - 1000 concentration range exhibited the least amount of variation, except in the cases of the mentioned compounds above. The 500 ng/mg concentration replicates, exhibited the least amount of variation and had no instances of a CV % above 25%. The reason why it is important to note the variance at each level during method characterisation is to establish a confidence interval or bias when calculating the concentrations in biological samples. MS is relatively expensive and more time consuming than many other analytical techniques (like spectrophotometry). It is therefore not common practice to run all samples in triplicate as with other techniques. The recorded variance values assure the analyst that the determined concentration is within a reasonable number of error (if accuracy is also confirmed).

5.3.2 Mouse Brain Calibration curves

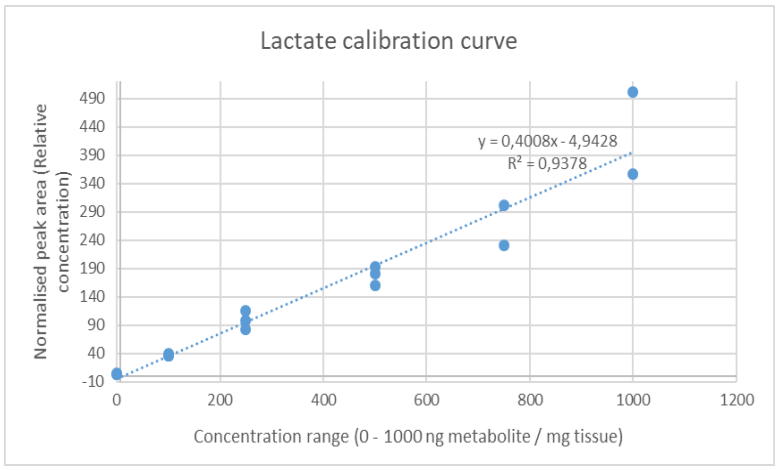

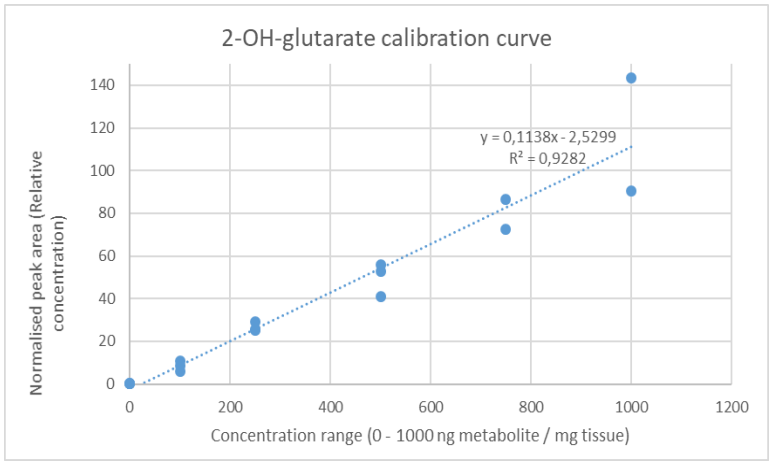

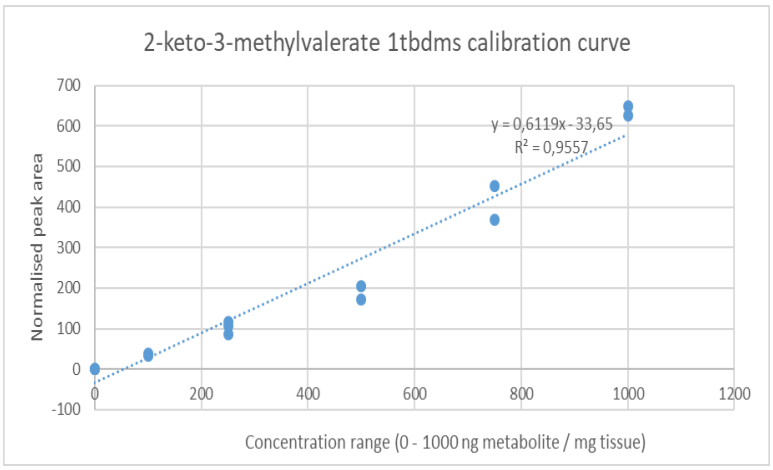

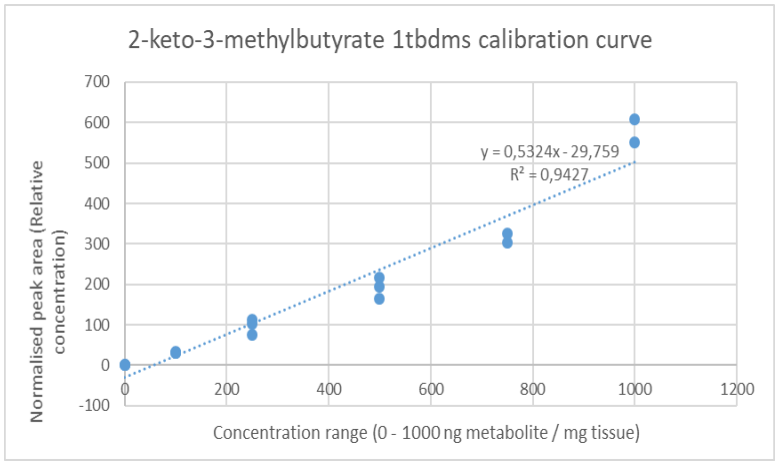

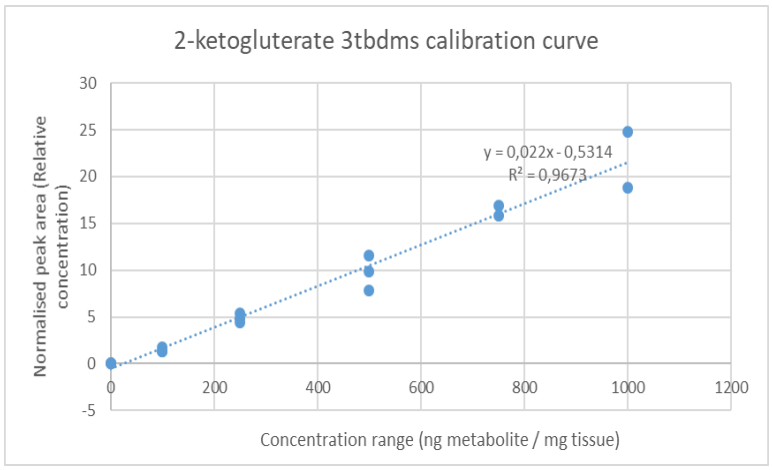

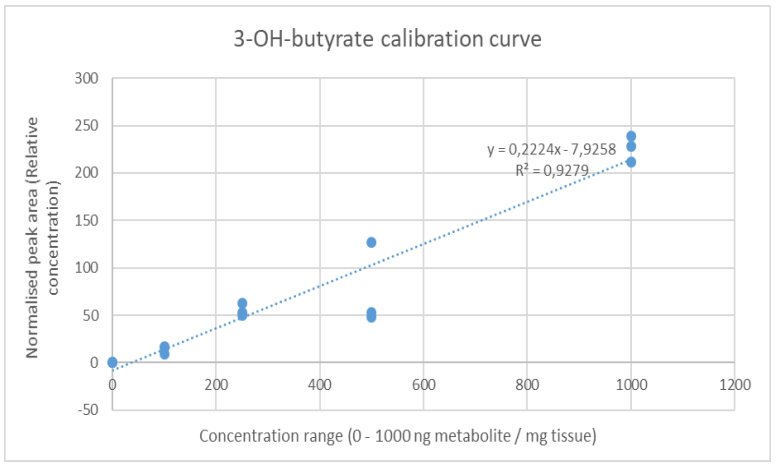

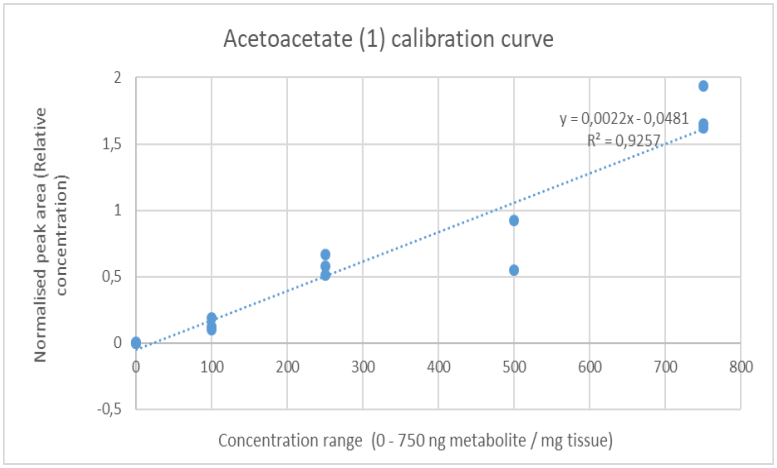
Acetoacetate (1) calibration curve
y = 0,0022x - 0,0481
R² = 0,9257
Normalised peak area (Relative concentration)
Concentration range (0 - 750 ng metabolite / mg tissue)

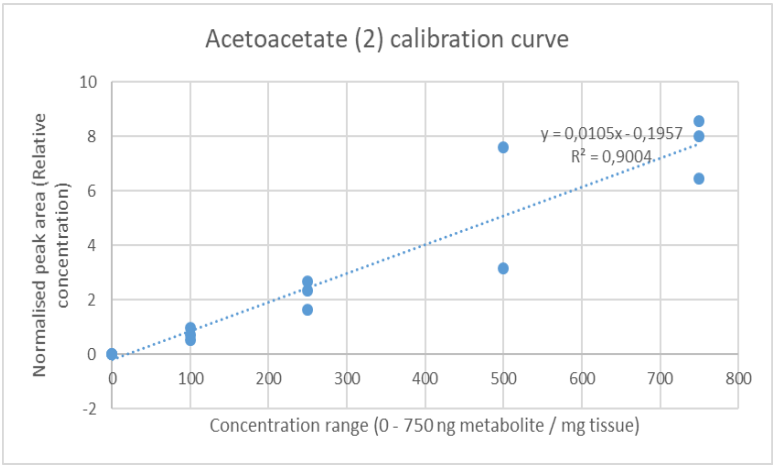
Acetoacetate (2) calibration curve
y = 0,0105x - 0,1957
R² = 0,9004
Normalised peak area (Relative concentration)
Concentration range (0 - 750 ng metabolite / mg tissue)

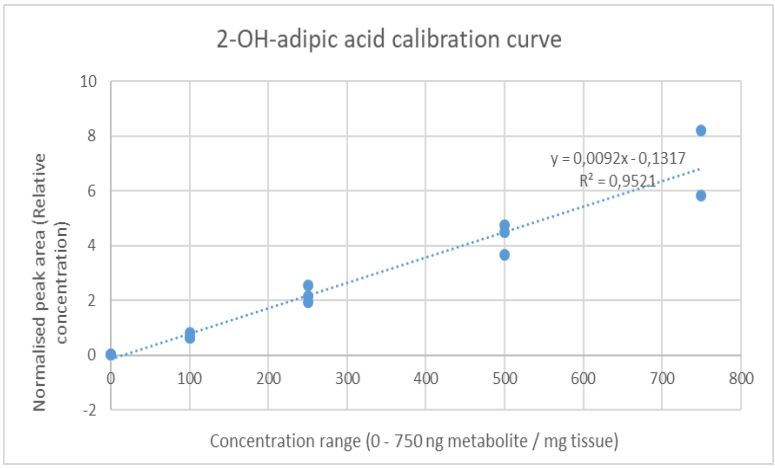
2-OH-adipic acid calibration curve
y = 0,0092x - 0,1317
R² = 0,9521
Normalised peak area (Relative concentration)
Concentration range (0 - 750 ng metabolite / mg tissue)

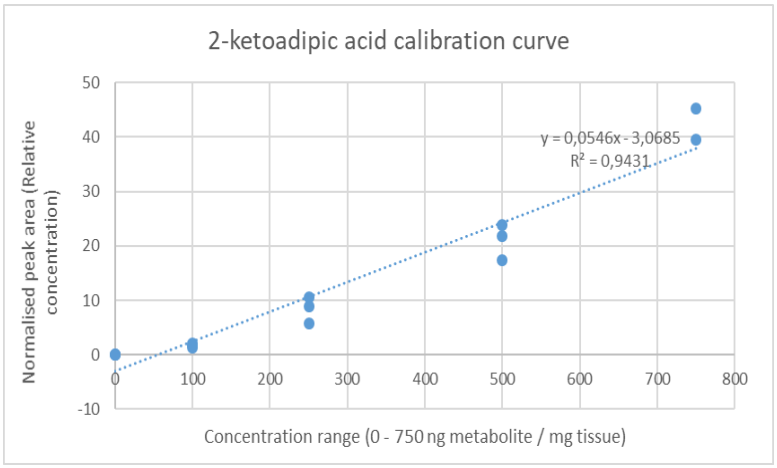
2-ketoadipic acid calibration curve
y = 0,0546x - 3,0685
R² = 0,9431
Normalised peak area (Relative concentration)
Concentration range (0 - 750 ng metabolite / mg tissue)

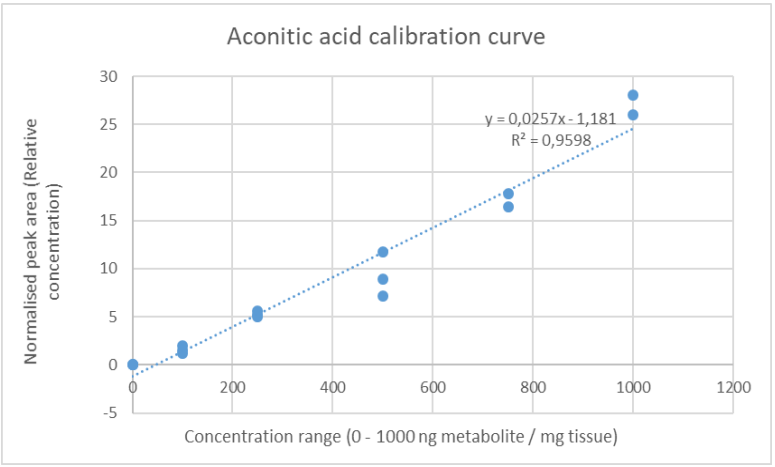
Aconitic acid calibration curve
y = 0,0257x - 1,181
R² = 0,9598
Normalised peak area (Relative concentration)
Concentration range (0 - 1000 ng metabolite / mg tissue)

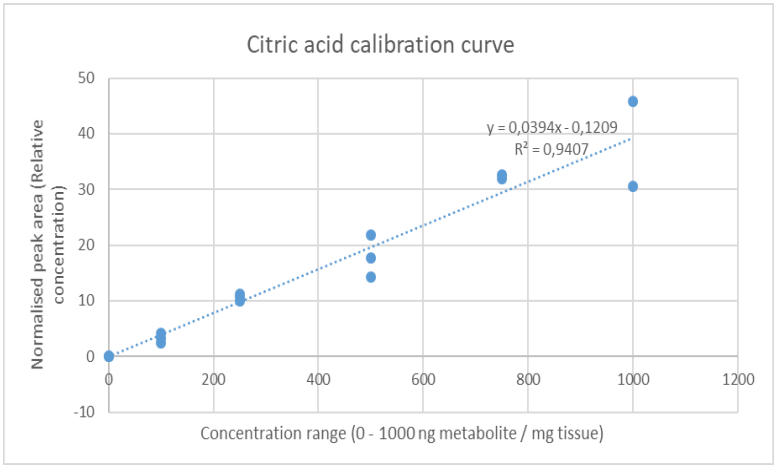
Citric acid calibration curve
y = 0,0394x - 0,1209
R² = 0,9407
Normalised peak area (Relative concentration)
Concentration range (0 - 1000 ng metabolite / mg tissue)

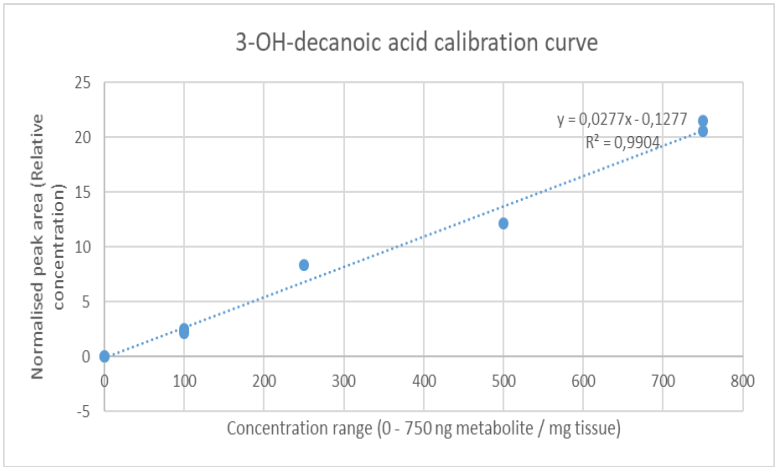
3-OH-decanoic acid calibration curve
y = 0,0277x - 0,1277
R² = 0,9904
Normalised peak area (Relative concentration)
Concentration range (0 - 750 ng metabolite / mg tissue)

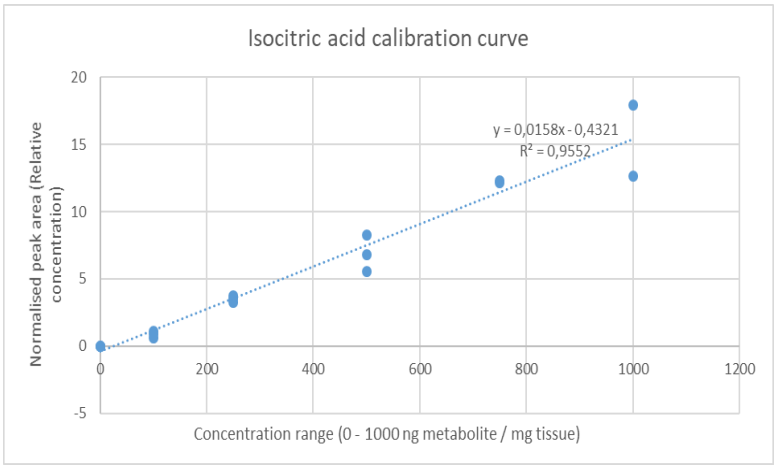
Isocitric acid calibration curve
y = 0,0158x - 0,4321
R² = 0,9552
Normalised peak area (Relative concentration)
Concentration range (0 - 1000 ng metabolite / mg tissue)

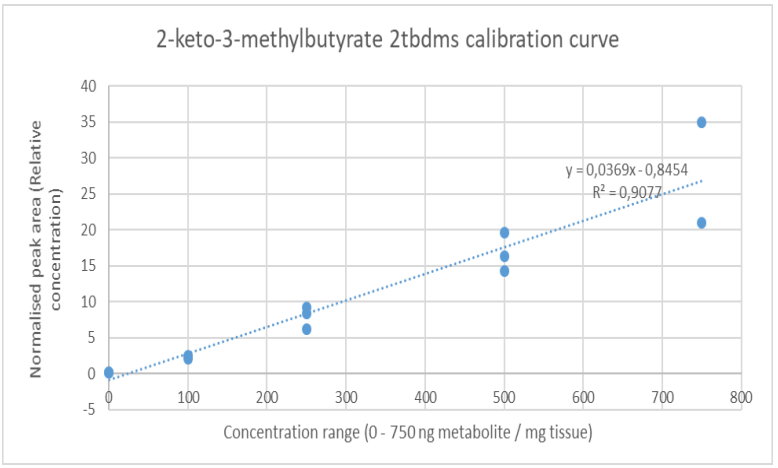
2-keto-3-methylbutyrate 2tbdms calibration curve
y = 0,0369x - 0,8454
R² = 0,9077
Normalised peak area (Relative concentration)
Concentration range (0 - 750 ng metabolite / mg tissue)

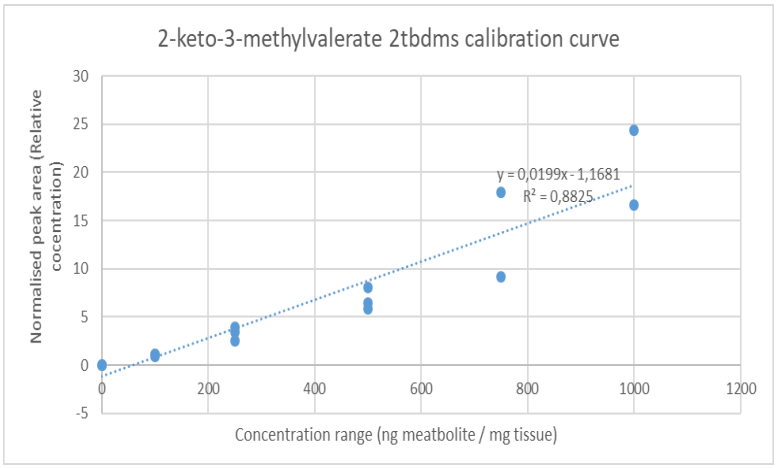
2-keto-3-methylvalerate 2tbdms calibration curve
y = 0,0199x - 1,1681
R² = 0,8825
Normalised peak area (Relative cocentration)
Concentration range (ng meatbolite / mg tissue)

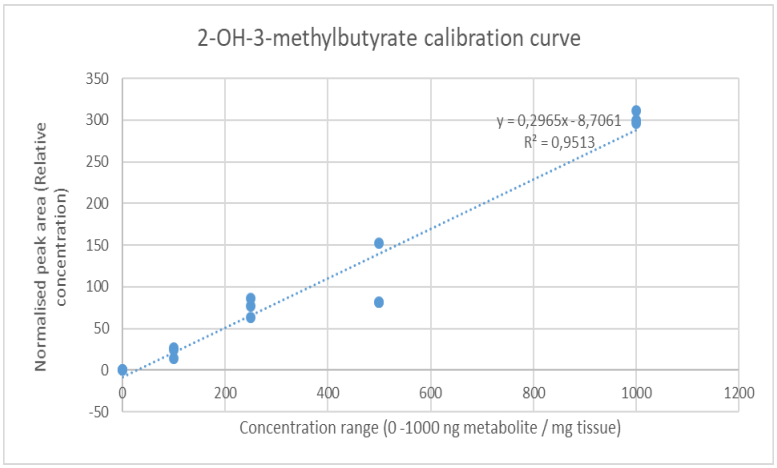
2-OH-3-methylbutyrate calibration curve
y = 0,2965x - 8,7061
R² = 0,9513
Normalised peak area (Relative concentration)
Concentration range (0 -1000 ng metabolite / mg tissue)

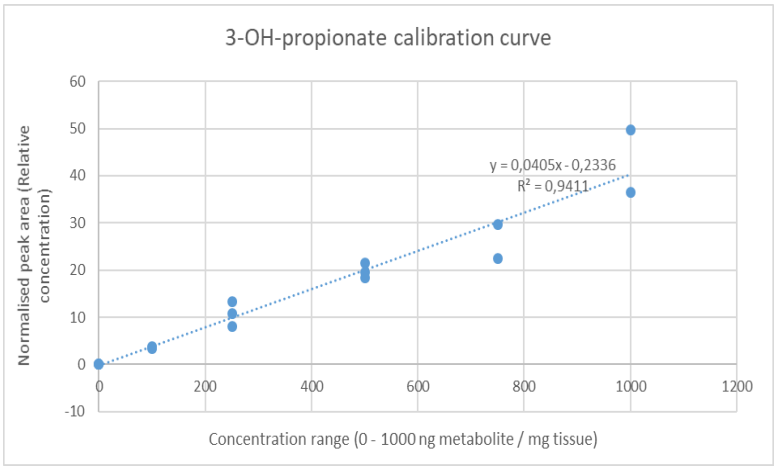
3-OH-propionate calibration curve
y = 0,0405x - 0,2336
R² = 0,9411
Normalised peak area (Relative concentration)
Concentration range (0 - 1000 ng metabolite / mg tissue)

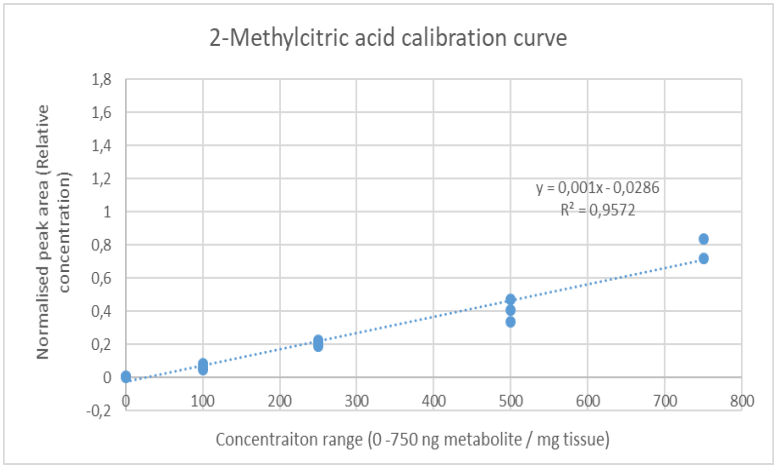
2-Methylcitric acid calibration curve
y = 0,001x - 0,0286
R² = 0,9572
Normalised peak area (Relative concentration)
Concentraiton range (0 -750 ng metabolite / mg tissue)

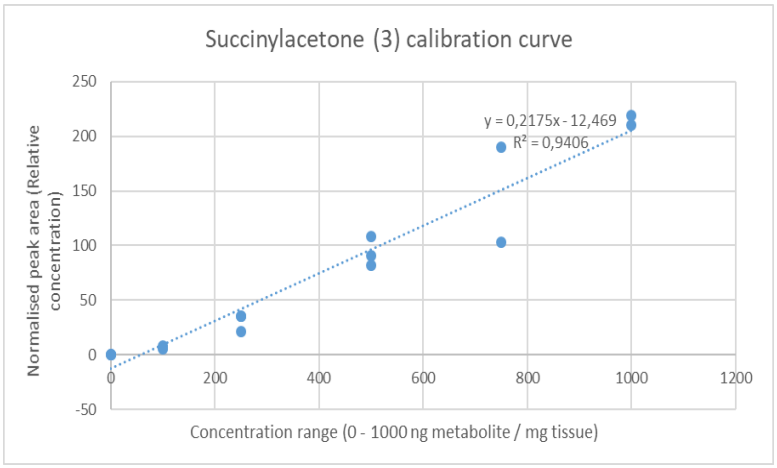
Succinylacetone (3) calibration curve
y = 0,2175x - 12,469
R² = 0,9406
Normalised peak area (Relative concentration)
Concentration range (0 - 1000 ng metabolite / mg tissue)

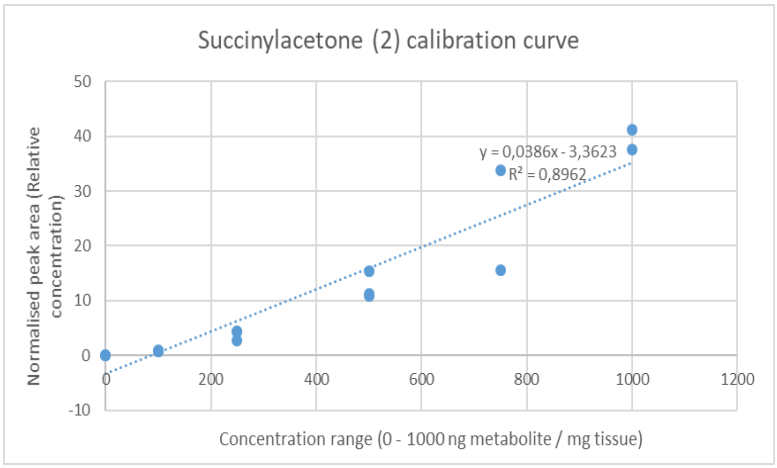
Succinylacetone (2) calibration curve
y = 0,0386x - 3,3623
R² = 0,8962
Normalised peak area (Relative concentration)
Concentration range (0 - 1000 ng metabolite / mg tissue)

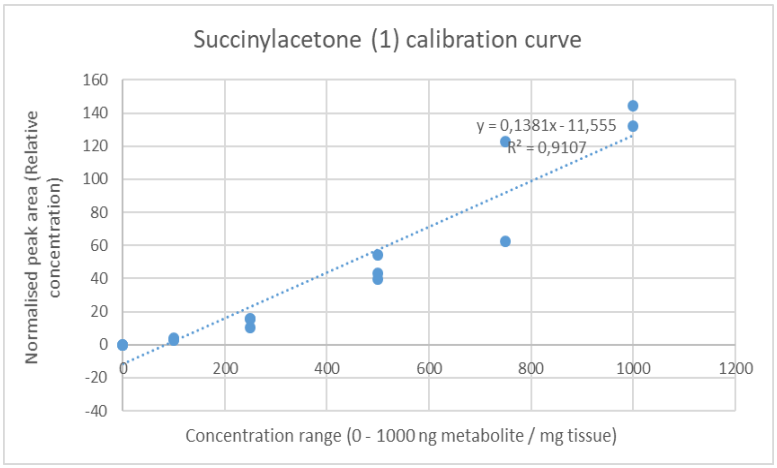
Succinylacetone (1) calibration curve
y = 0,1381x - 11,555
R² = 0,9107
Normalised peak area (Relative concentration)
Concentration range (0 - 1000 ng metabolite / mg tissue)

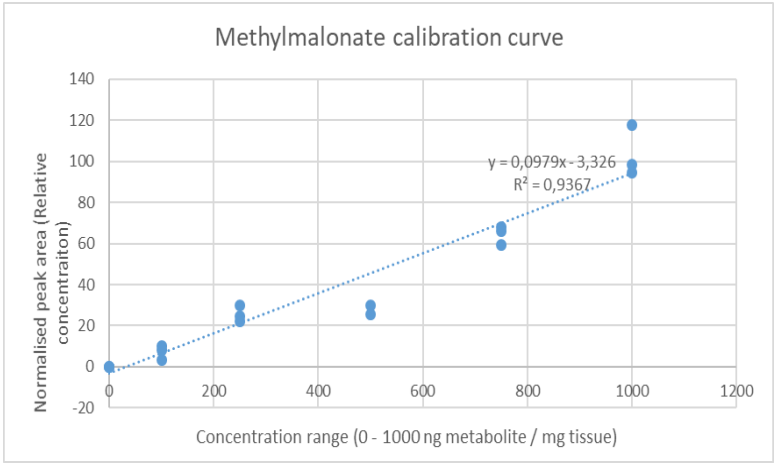
Methylmalonate calibration curve
y = 0,0979x - 3,326
R² = 0,9367
Normalised peak area (Relative concentraiton)
Concentration range (0 - 1000 ng metabolite / mg tissue)

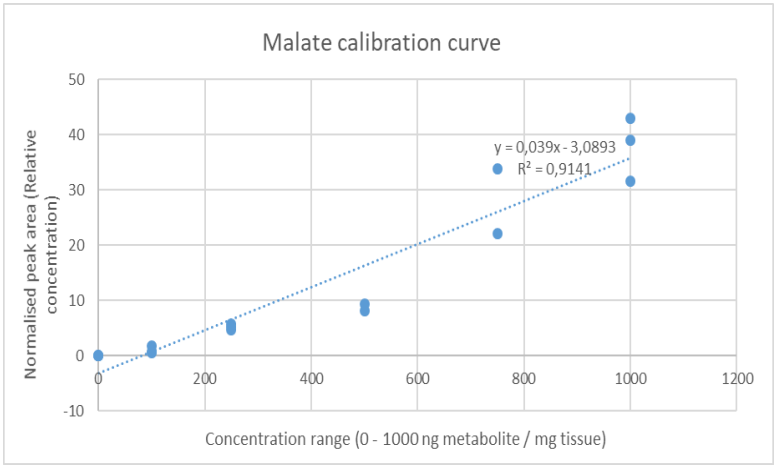
Malate calibration curve
y = 0,039x - 3,0893
R² = 0,9141
Normalised peak area (Relative concentration)
Concentration range (0 - 1000 ng metabolite / mg tissue)

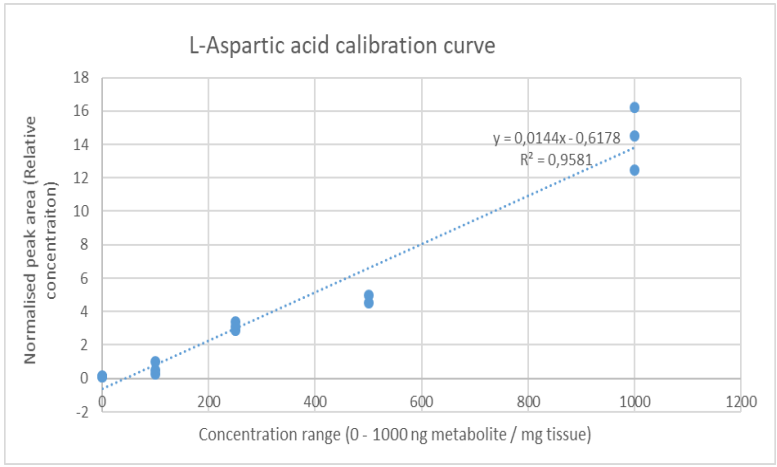
L-Aspartic acid calibration curve
y = 0,0144x - 0,6178
R² = 0,9581
Normalised peak area (Relative concentraiton)
Concentration range (0 - 1000 ng metabolite / mg tissue)

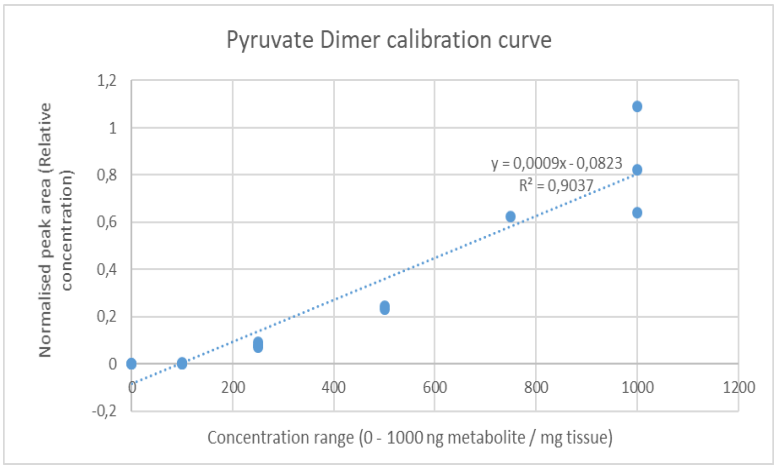

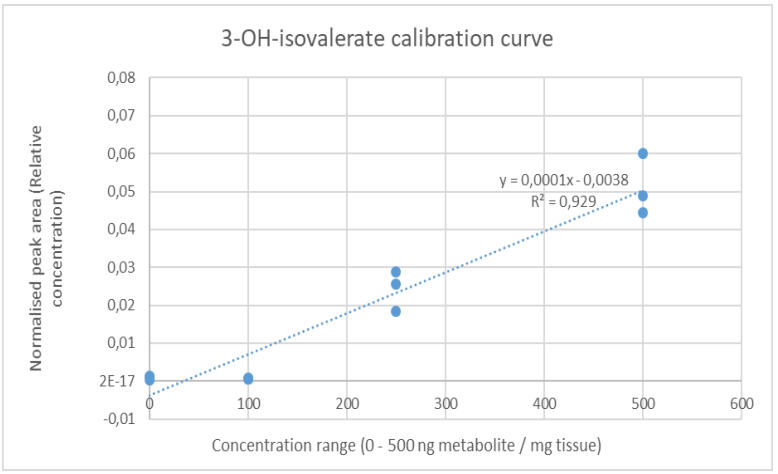

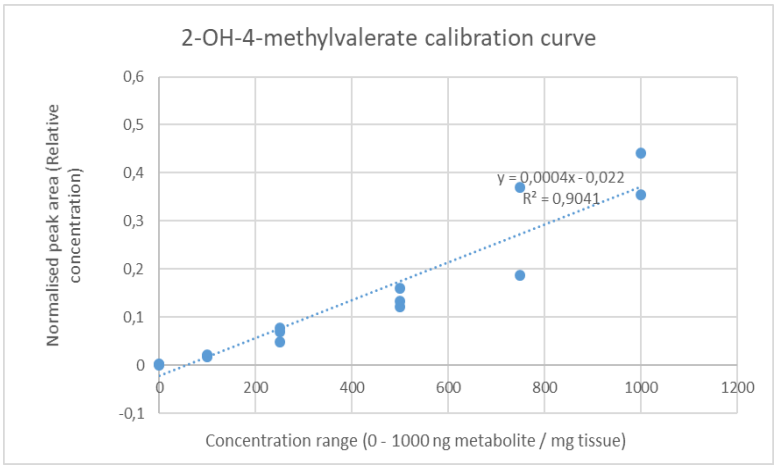

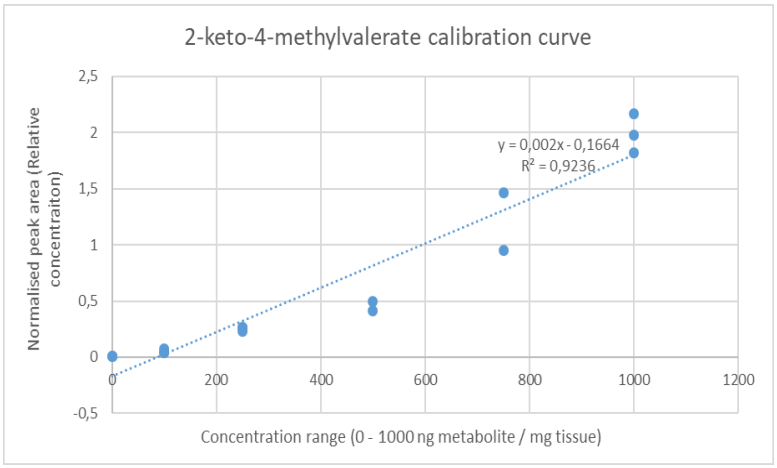

Figures 5.9: Brain calibration curves for the targeted 26 compounds

As previously explained, each calibration curve was expressed as normalised peak area (relative concentration) over the concentration range with the regression line formula and R squared value present in each curve. Taken together, all calibration curves listed in Figures 5.9, had good linearity ranging from 0.8825 – 0.9673, whilst the calibration curves for 2-keto-3-methylbutyrate 2 tBDMS and succinylacetone (2) had R^2 values below 0.9. Consequently, compounds that had an $R^2 > 0.9$ could therefore be quantified within the mouse brain due to the partially linear to linear relationship between the instrument response and compound concentration. In contrast, the transitions of the compounds mentioned above with $R^2 < 0.9$ could only be used for semi-quantification purposes.

All compounds had calibration curves constructed with the entire concentration range which represents each compound's linear range, except the following: acetoacetate (1 & 2), 2-OH-adipic acid, 2-ketoadipic acid, 2-keto-3-methylbutyrate di-tBDMS, 2-methylcitric acid and 3-OH-

isovalerate. These compounds did not include the 1000 ng/mg triplicate samples due to high variation. The calibration curves for these compounds also entail that the upper limit of the calibration curve was not within the linear concentration range for these compounds. The calibration curves for 3-OH-butyrate and L-aspartate were constructed with the exclusion of the 750 triplicate samples, due to this concentration point exhibiting high variation throughout these two compounds. Lastly, the calibration curve for 3-OH-isovalerate qualifier, excluded the triplicate samples of the 1000 ng/mg and 750 ng/mg calibration level. This was done due to these two concentration ranges exhibiting high variation across triplicate samples for 3-OH-isovalerate. Another possible explanation could be that the 1000 and 750 ng/mg was not within the optimal linear range for 3-OH-isovalerate.

Taken together, all compounds had a negative or close to zero y intercept according to each regression line, which indicates effective stripping of the metabolite from the mouse brain matrix.

Table 5.12: Brain organic acid LOD, LOQ, Linearity and Accuracy

Compound	LOD (ng/mg)	LOQ (ng/mg)	Accuracy (%)	R^2	Linear range (ng/mg)
Lactate	19.143	27.979	100.53	0.9485	0 – 1000
2-OH-gluterate	23.586	25.042	97.14	0.9282	0 – 1000
2-keto-3-methylvalerate 1tBDMS	92.499	93.245	101.15	0.9363	0 – 1000
2-keto-3methylbutyrate 1tBDMS	58.922	64.449	91.49	0.9427	0 – 1000
2-Ketoglutarate 3tBDMS	24.709	24.800	93.93	0.9673	0 – 1000
3-OH-butyrate	36.078	36.155	104.45	0.9279	0 – 1000
Acetoacetate (1)	11.849	13.581	104.22	0.912	0 – 750
Acetoacete (2)	20.891	22.716	95.78	0.9004	0 – 750
2-OH-adipic acid	7.205	8.068	107.65	0.9513	0 – 750
2-ketoadipic acid	57.393	58.220	98.09	0.9431	0 – 750
Aconitate	46.572	47.168	100.56	0.9598	0 – 1000
Citrate	6.376	10.286	89.82	0.9407	0 – 1000
Isocitrate	14.238	14.310	92.55	0.9466	0 – 1000
2-keto-3-methylbutyrate 2tBDMS	27.360	28.166	112.75	0.9077	0 – 750
2-OH-3-methylbutyrate	29.557	29.653	109.01	0.9513	0 – 1000

2-keto-3-methylvalerate 2tBDMS	61.617	63.163	92.51	0.8825	0 – 1000
3-OH-decanoic acid	5.194	6.095	113.99	0.9904	0 – 750
3-OH-propionate	7.472	7.721	97.92	0.9411	0 – 1000
2-Methylcitric acid	42.724	66.388	88.53	0.9572	0 – 750
Succinylacetone (3)	54.565	54.873	96.27	0.9346	0 – 1000
Succinylacetone (2)	87.599	87.833	97.17	0.8962	0 – 1000
Succinylacetone (1)	83.803	83.953	94.65	0.9107	0 – 1000
Methylmalonate	34.290	34.673	114.96	0.9367	0 - 1000
Malate	81.380	83.431	90.37	0.9141	0 – 1000
L-Aspartate	45.842	58.631	108.88	0.9521	0 – 1000
Pyruvate Dimer (1)	91.200	92.281	71.97	0.9053	0 – 1000
Pyruvate Dimer (2)	94.457	96.825	75.57	0.9037	0 – 1000
3-OH-isovalerate	60.816	94.994	97.43	0.929	0 - 500
2-keto-4-methylvalerate	88.722	94.050	85.32	0.9236	0 – 1000
2-OH-4-methylvalerate	67.571	86.605	91.00	0.9041	0 – 1000

Table 5.12 represents the LOD, LOQ, R^2, accuracy and linear range for each organic acid MRM transition optimised within mouse brain tissue. To determine the linear range for each marker, visual inspection of each calibration curve was conducted. As per table 12, the LOD's for the selected organic acids ranged from 6.376 ng/mg - 94.407 ng/mg, whereas the LOQ's ranged from 7.721 ng/mg - 96.825 ng/mg. The calculated LOD for the selected organic acids were below the lowest concentration point of the calibration curve and therefore indicates that these organic acids can be detected sufficiently whilst being able to distinguish from analytical noise. Furthermore, as per the LOQ's, each transition could be used to quantify these selected organic acids, even if the metabolites are relatively in low concentration within the mouse brain.

The accuracy of each organic acid MRM transition was calculated in the same manner as per mouse liver calibration, with the accuracy of each transition in the mouse brain matrix ranging from 71.97 % - 114.96 %. Pyruvate dimer's qualifier and quantifier were the only two transitions that were below the 15 % accuracy cut off, while all other transitions were within the 85 % - 115 % accuracy range. The % accuracy for all the transitions, except pyruvate dimer's, indicates a relatively large agreement between nominal and experimental concentration and therefore, experimental absolute concentration can be generated accurately from each calibration curve regression line formula. Also, this % accuracy for almost all transitions indicates good sensitivity and selectivity for each transition when identifying and quantifying the selected organic acids in mouse brain tissue.

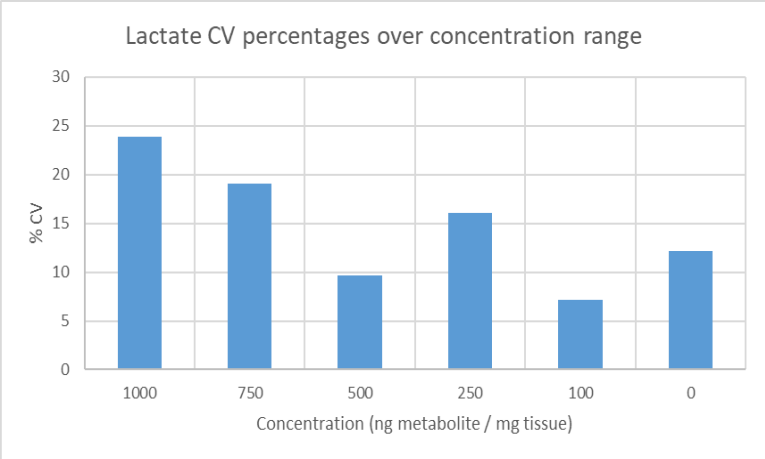
Lactate CV percentages over concentration range
% CV
30
25
20
15
10
5
0
1000
750
500
250
100
0
Concentration (ng metabolite / mg tissue)

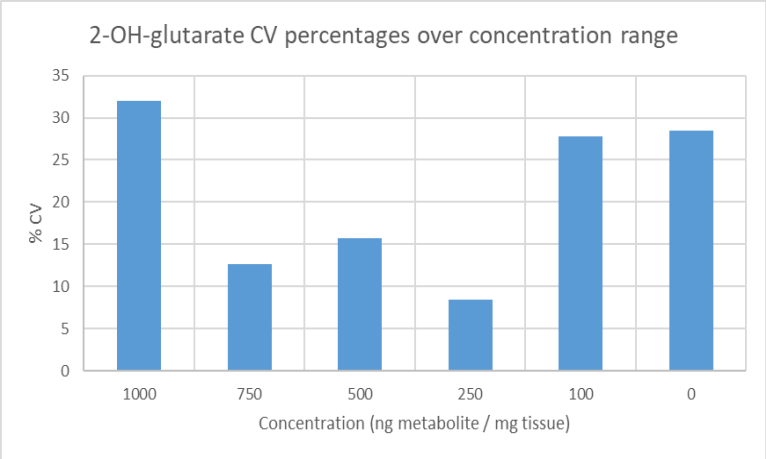
2-OH-glutarate CV percentages over concentration range
% CV
35
30
25
20
15
10
5
0
1000
750
500
250
100
0
Concentration (ng metabolite / mg tissue)

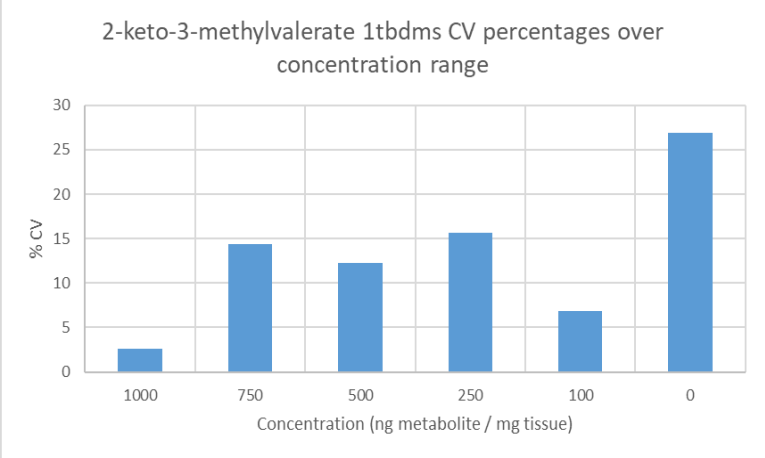
2-keto-3-methylvalerate 1tbdms CV percentages over concentration range
% CV
30
25
20
15
10
5
0
1000
750
500
250
100
0
Concentration (ng metabolite / mg tissue)

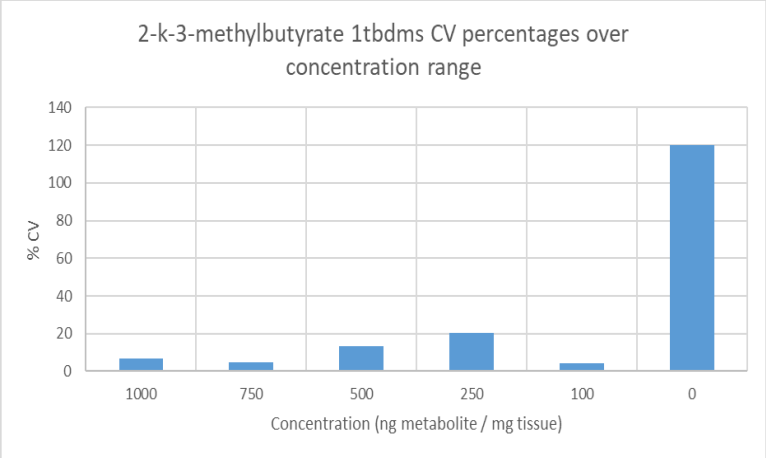
2-k-3-methylbutyrate 1tbdms CV percentages over concentration range
% CV
140
120
100
80
60
40
20
0
1000
750
500
250
100
0
Concentration (ng metabolite / mg tissue)

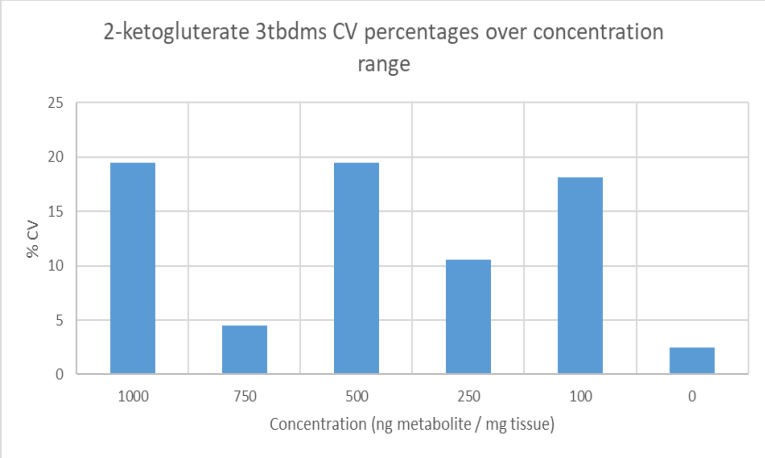
2-ketogluterate 3tbdms CV percentages over concentration range
% CV
25
20
15
10
5
0
1000
750
500
250
100
0
Concentration (ng metabolite / mg tissue)

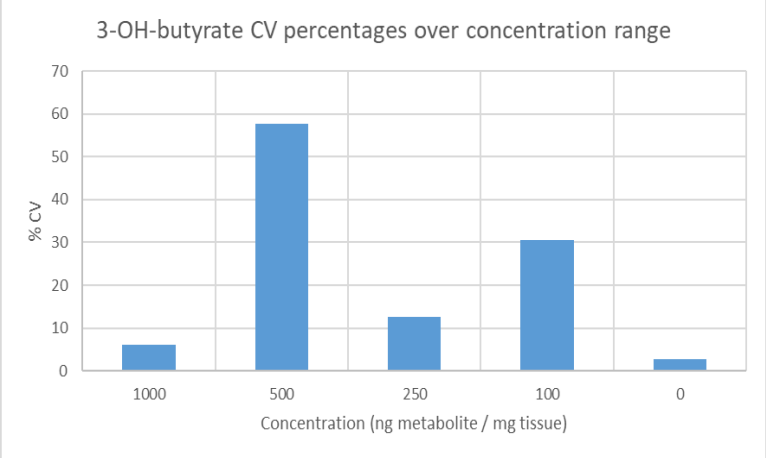
3-OH-butyrate CV percentages over concentration range
% CV
70
60
50
40
30
20
10
0
1000
500
250
100
0
Concentration (ng metabolite / mg tissue)

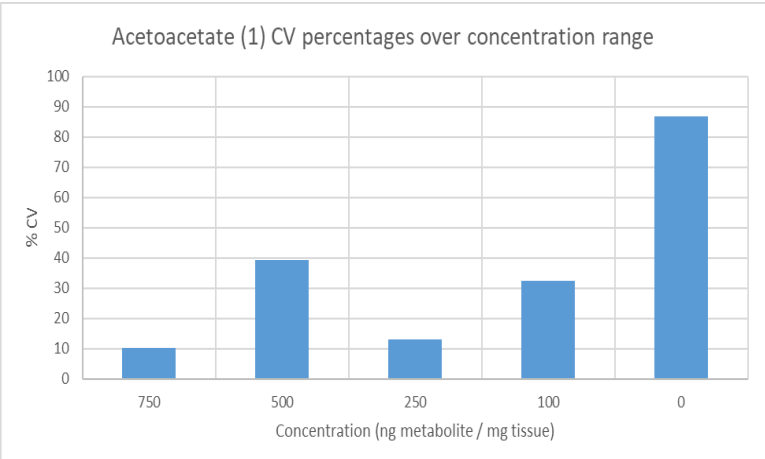
Acetoacetate (1) CV percentages over concentration range
% CV
100
90
80
70
60
50
40
30
20
10
0
750
500
250
100
0
Concentration (ng metabolite / mg tissue)

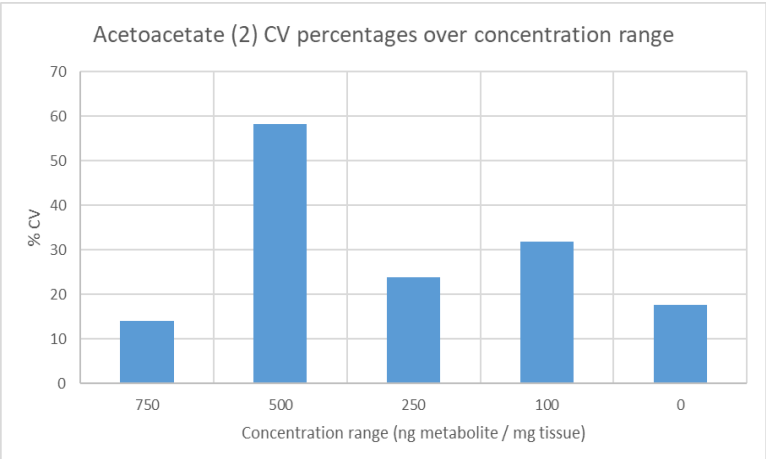
Acetoacetate (2) CV percentages over concentration range
% CV
70
60
50
40
30
20
10
0
750
500
250
100
0
Concentration range (ng metabolite / mg tissue)

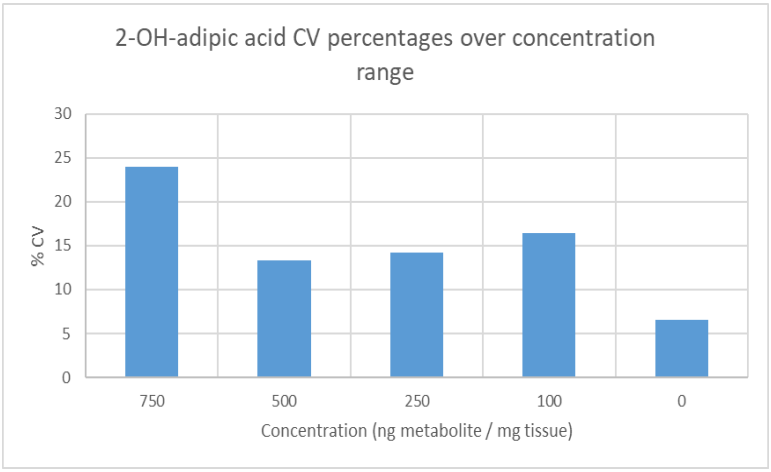
2-OH-adipic acid CV percentages over concentration range
% CV
30
25
20
15
10
5
0
750
500
250
100
0
Concentration (ng metabolite / mg tissue)

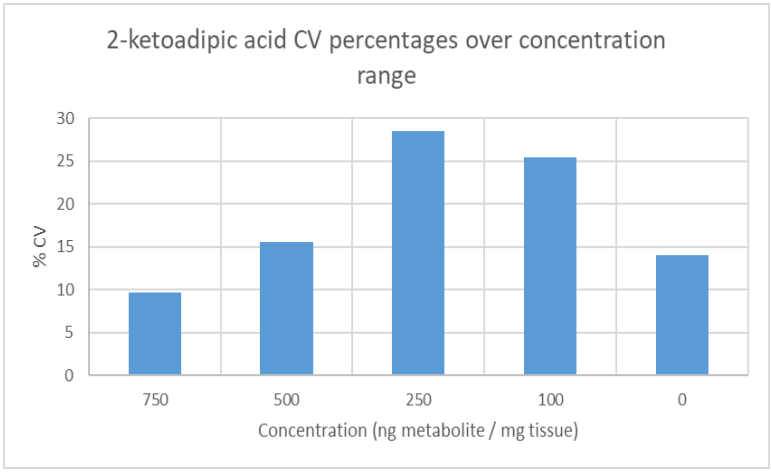
2-ketoadipic acid CV percentages over concentration range
% CV
30
25
20
15
10
5
0
750
500
250
100
0
Concentration (ng metabolite / mg tissue)

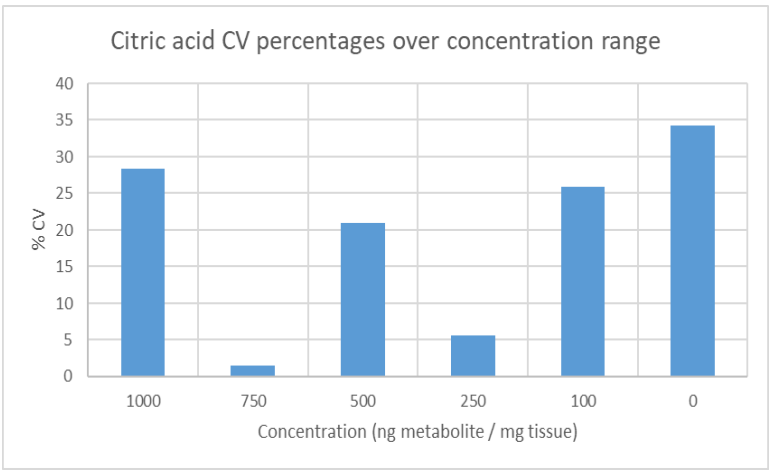
Citric acid CV percentages over concentration range
% CV
40
35
30
25
20
15
10
5
0
1000
750
500
250
100
0
Concentration (ng metabolite / mg tissue)

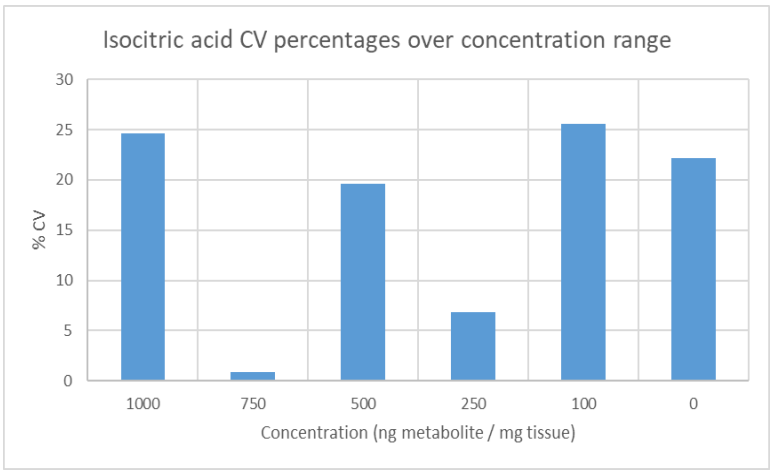
Isocitric acid CV percentages over concentration range
% CV
30
25
20
15
10
5
0
1000
750
500
250
100
0
Concentration (ng metabolite / mg tissue)

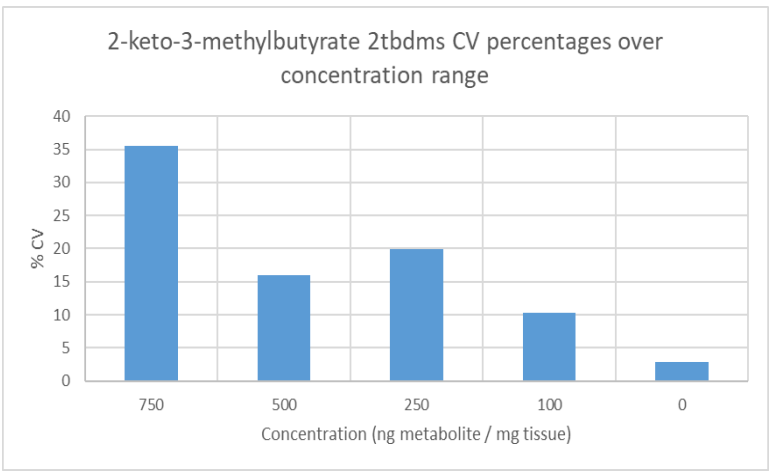
2-keto-3-methylbutyrate 2tbdms CV percentages over concentration range
% CV
40
35
30
25
20
15
10
5
0
750
500
250
100
0
Concentration (ng metabolite / mg tissue)

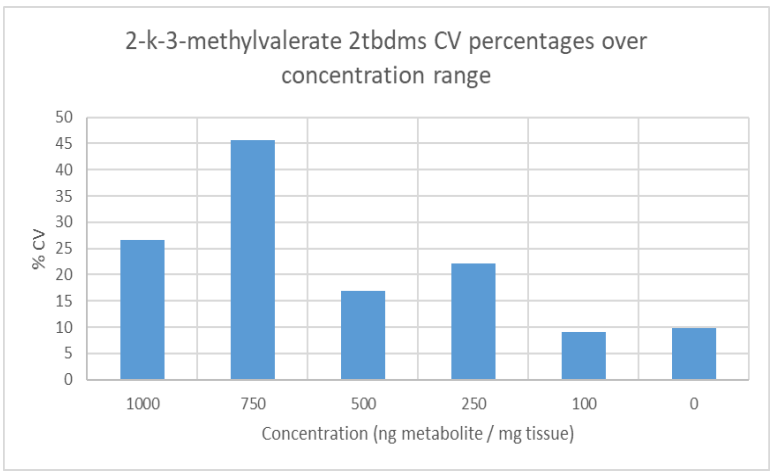
2-k-3-methylvalerate 2tbdms CV percentages over concentration range
% CV
50
45
40
35
30
25
20
15
10
5
0
1000
750
500
250
100
0
Concentration (ng metabolite / mg tissue)

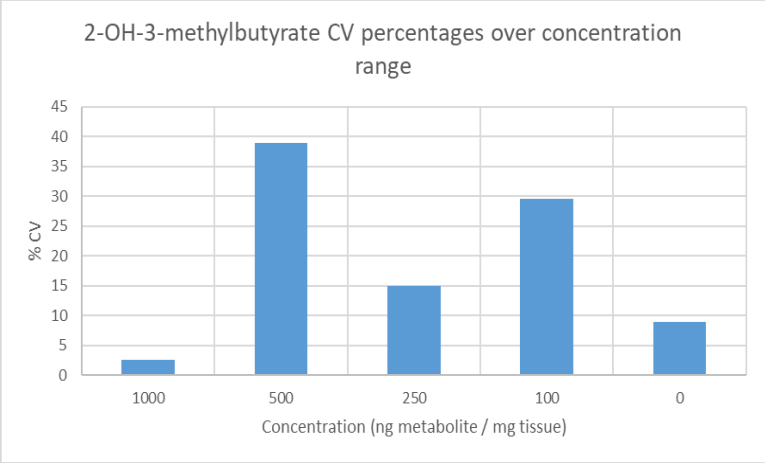
2-OH-3-methylbutyrate CV percentages over concentration range
% CV
45
40
35
30
25
20
15
10
5
0
1000
500
250
100
0
Concentration (ng metabolite / mg tissue)

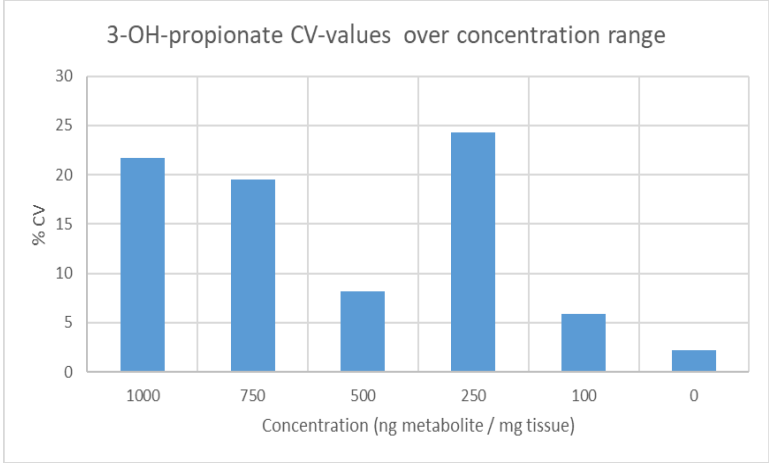
3-OH-propionate CV-values over concentration range
% CV
30
25
20
15
10
5
0
1000
750
500
250
100
0
Concentration (ng metabolite / mg tissue)

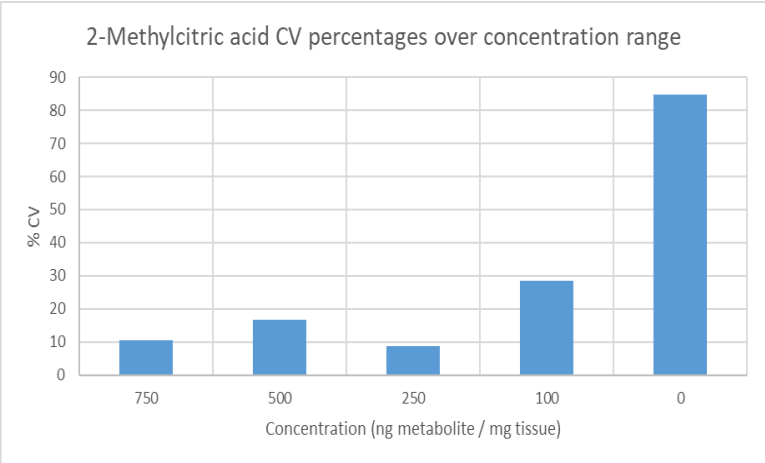
2-Methylcitric acid CV percentages over concentration range
% CV
90
80
70
60
50
40
30
20
10
0
750
500
250
100
0
Concentration (ng metabolite / mg tissue)

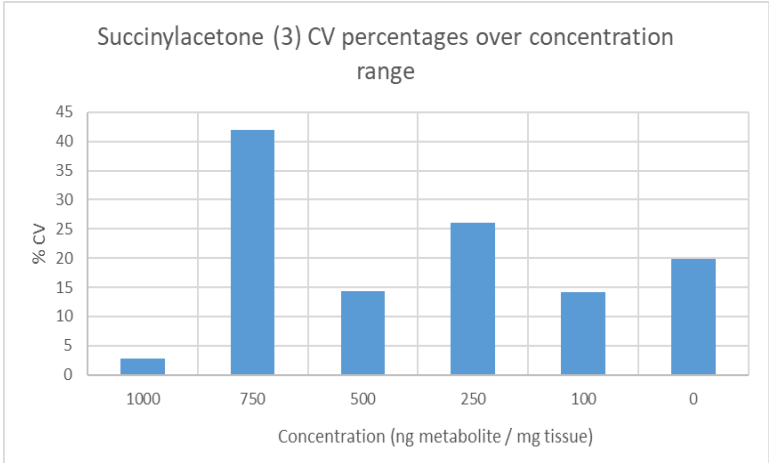
Succinylacetone (3) CV percentages over concentration range
% CV
45
40
35
30
25
20
15
10
5
0
1000
750
500
250
100
0
Concentration (ng metabolite / mg tissue)

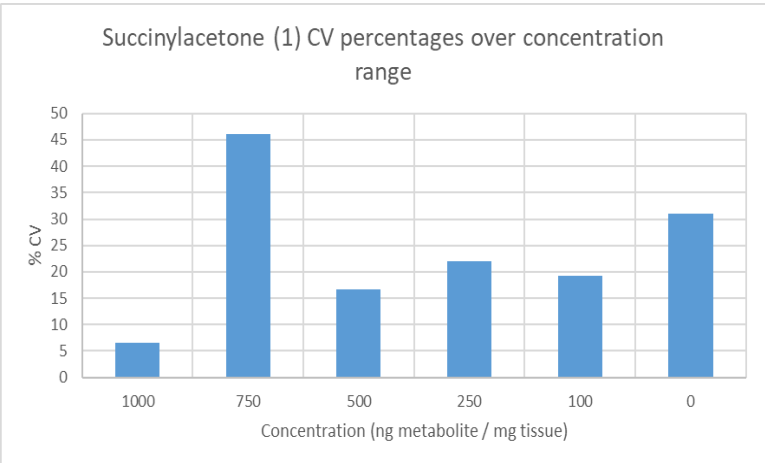
Succinylacetone (1) CV percentages over concentration range
% CV
50
45
40
35
30
25
20
15
10
5
0
1000
750
500
250
100
0
Concentration (ng metabolite / mg tissue)

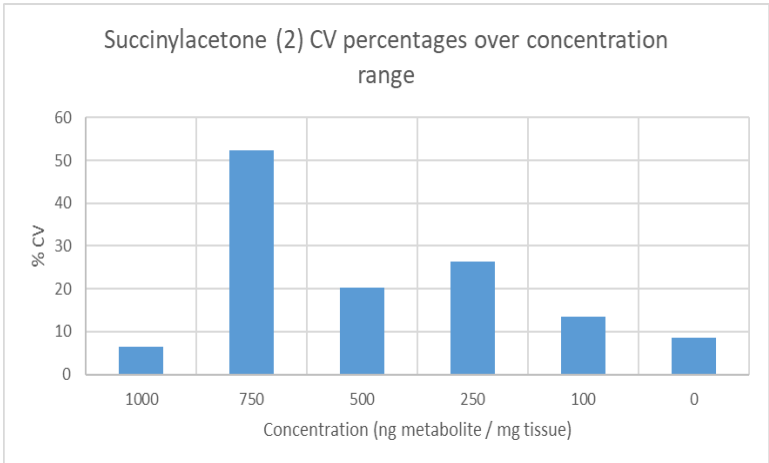
Succinylacetone (2) CV percentages over concentration range
% CV
60
50
40
30
20
10
0
1000
750
500
250
100
0
Concentration (ng metabolite / mg tissue)

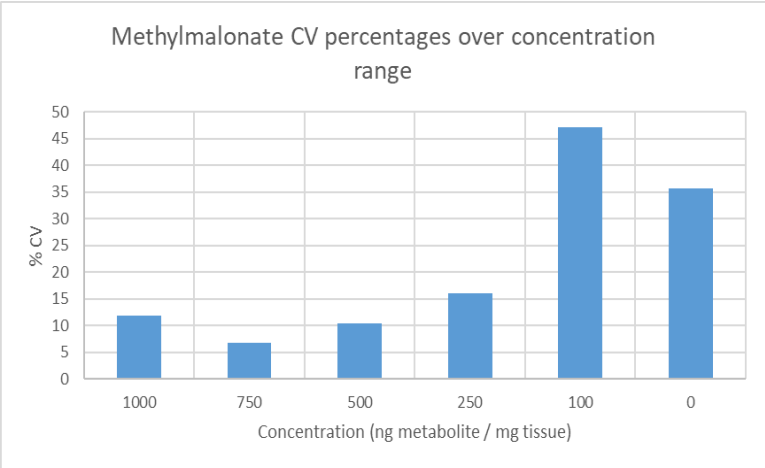
Methylmalonate CV percentages over concentration range
% CV
0
5
10
15
20
25
30
35
40
45
50
1000
750
500
250
100
0
Concentration (ng metabolite / mg tissue)

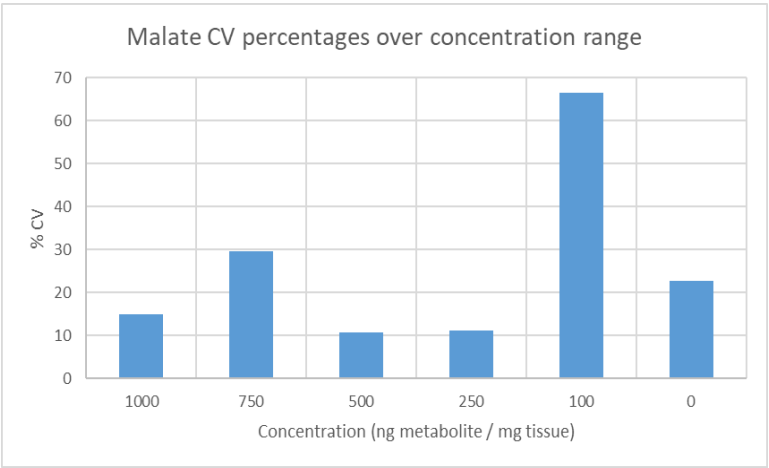
Malate CV percentages over concentration range
% CV
0
10
20
30
40
50
60
70
1000
750
500
250
100
0
Concentration (ng metabolite / mg tissue)

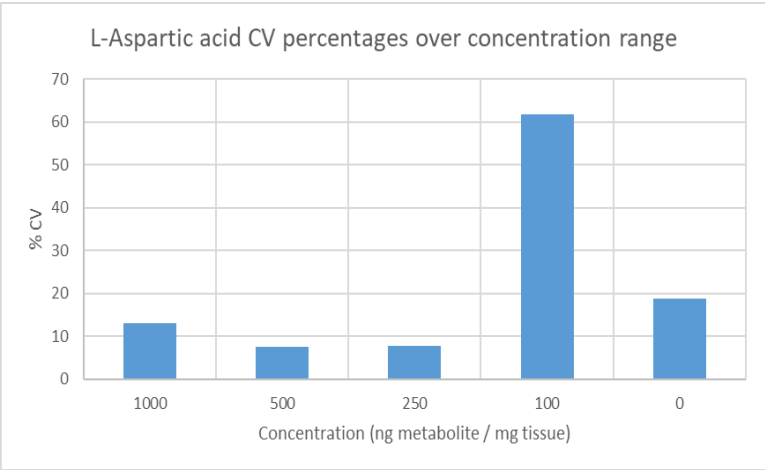
L-Aspartic acid CV percentages over concentration range
% CV
0
10
20
30
40
50
60
70
1000
500
250
100
0
Concentration (ng metabolite / mg tissue)

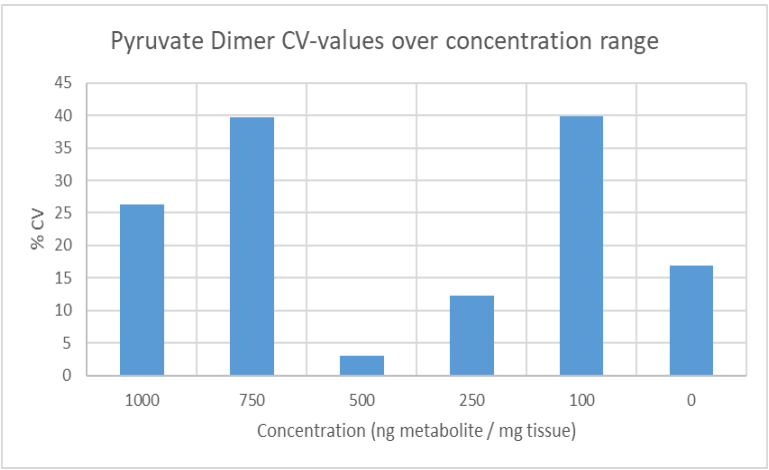
Pyruvate Dimer CV-values over concentration range
% CV
0
5
10
15
20
25
30
35
40
45
1000
750
500
250
100
0
Concentration (ng metabolite / mg tissue)

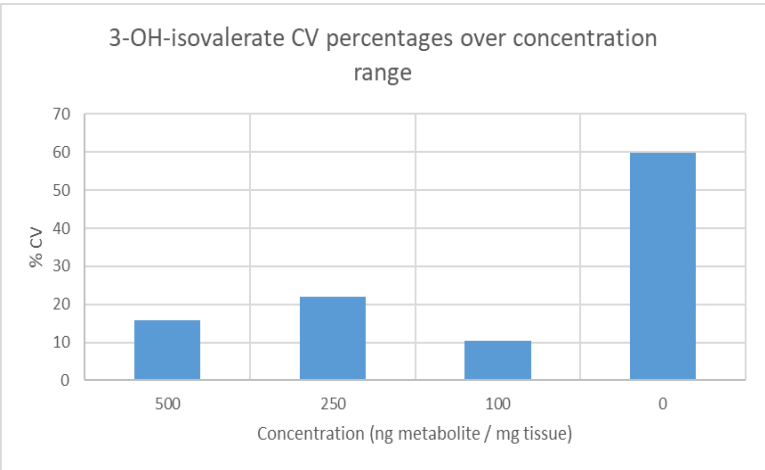
3-OH-isovalerate CV percentages over concentration range
% CV
0
10
20
30
40
50
60
70
500
250
100
0
Concentration (ng metabolite / mg tissue)

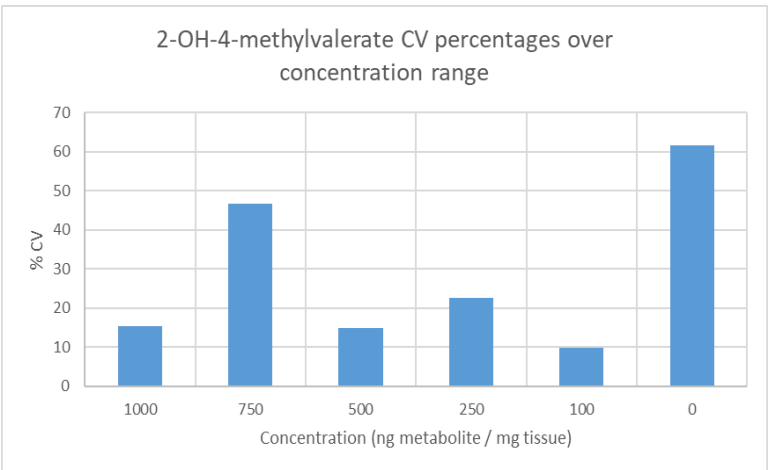
2-OH-4-methylvalerate CV percentages over concentration range
% CV
0
10
20
30
40
50
60
70
1000
750
500
250
100
0
Concentration (ng metabolite / mg tissue)

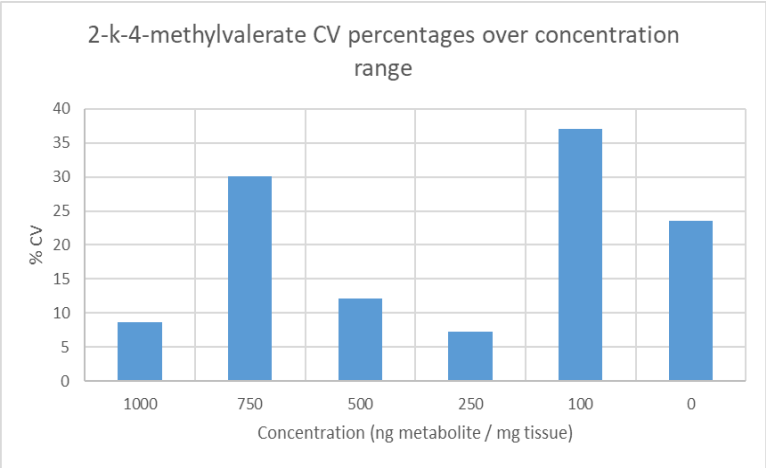

Figure 5.10: Bar graphs representing the CV percentages over the calibration concentration range of selected organic acids

Table 5.13: Summarized variance over the brain calibration range. The total number of compounds with CV above and below 25 % CV cut off at each calibration point in mouse brain are indicated.

Concentration range (ng/mg)	Total with % CV's < 25	Total with % CV's > 25
1000	16	5
750	13	9
500	23	4
250	25	2
100	13	14
Blank	16	11

As described in the construction of the mouse brain calibration curves, the CV bar graphs listed in Figures 5.10, of the following compounds: acetoacetate (1 & 2), 2-OH-adipic acid, 2-ketoadipic acid, 2-keto-3-methylbutyrate 2tBDMS, 2-methylcitric acid and 3-OH-isovalerate, were constructed without including either the 1000, 750, both or in few causes just without the 750 calibration point.

With triplicate analysis of each compound at different concentrations in the mouse brain, the order of increasing variation expressed in % CV were as follows: 250 < 500 < Blank < 1000 < 750 < 100. As stipulated in Table 5.13, the 0 and 100 concentration range exhibited the most variation, whereas the 250 and 500 concentration range had the least variation. Again, larger variation is expected close to the LOD and LOQ, with pipetting of small volumes playing a role. The blank triplicate samples exhibited the second most variation, which could have been due to ineffective stripping of the mouse brain matrix; however, the variance observed in the mouse brain matrix was less than that observed in mouse liver. This indicates that the mouse brain matrix was

stripped from metabolites more effectively than the mouse liver matrix. Considering that the 250 ng/mg and 500 ng/mg calibration range had the least variation between triplicate samples, it can be stated that the organic acid transitions within these two calibration points can generate experimental results reliably and with consistency.

Lastly, when the % accuracy was calculated for each MRM transition in the mouse brain, the 250-concentration range was used and was interchanged with the 500 concentration range in certain cases.

5.3.3 Mouse Heart Calibration curves

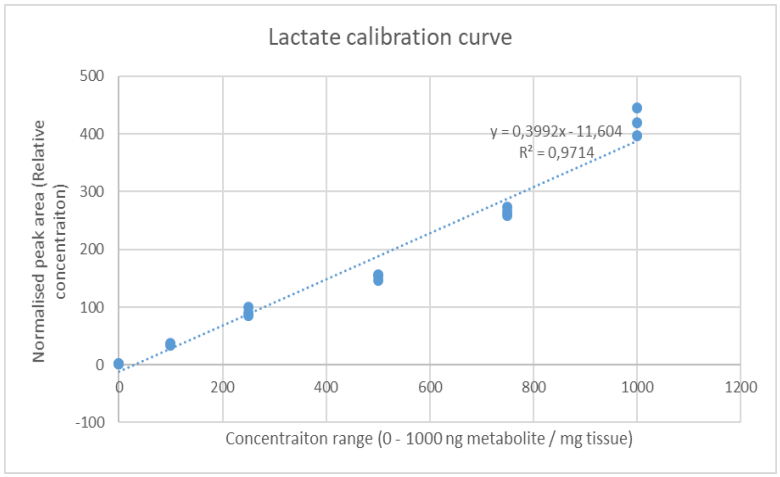

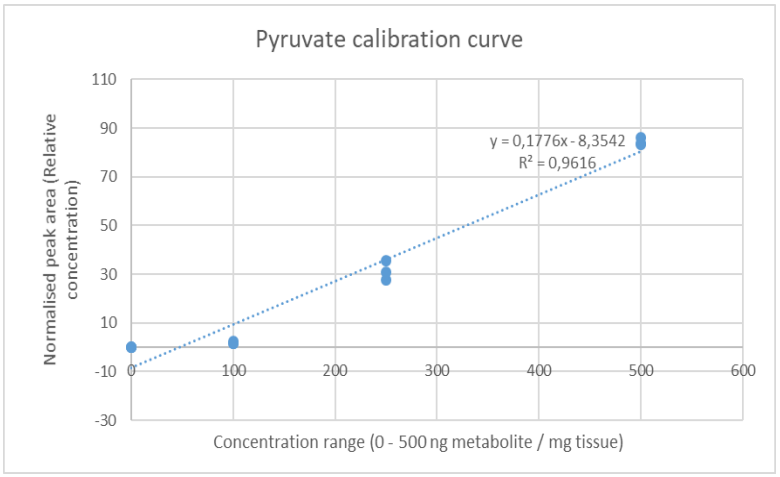

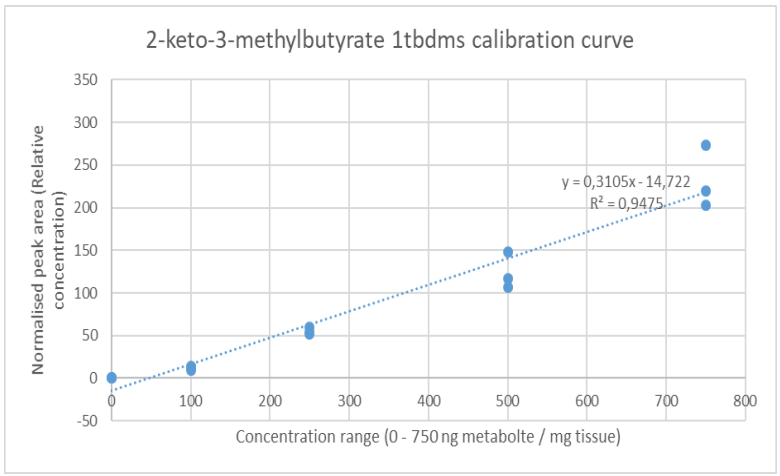

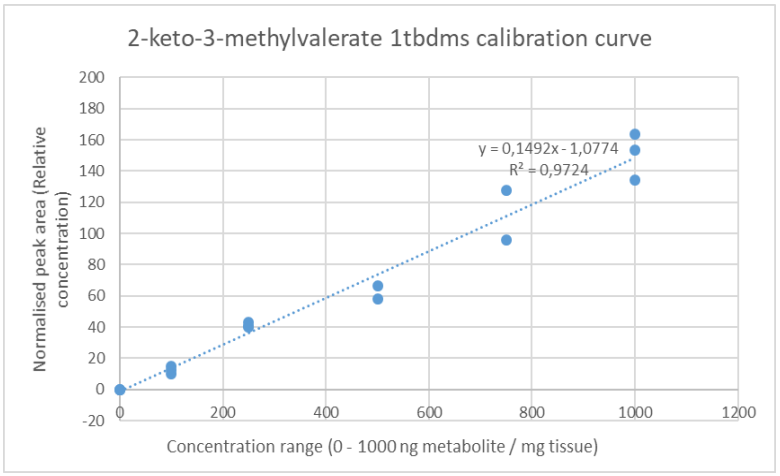

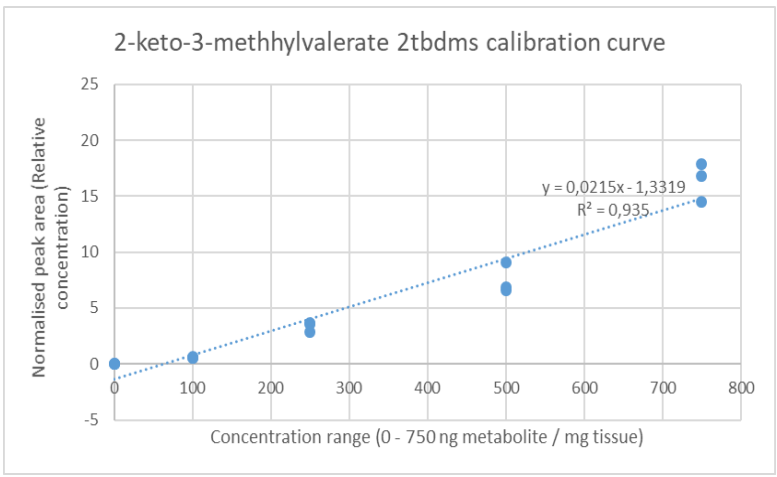

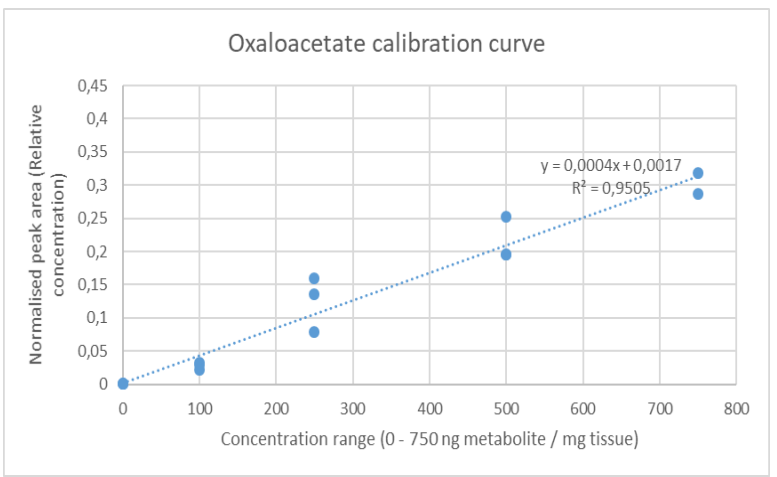

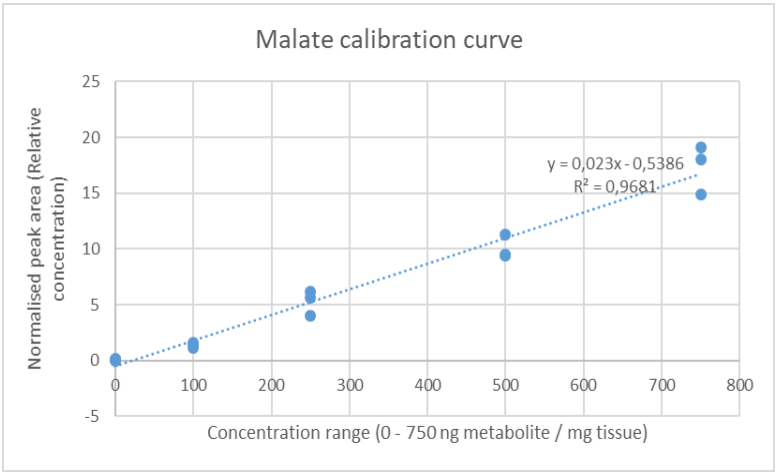
Malate calibration curve
Normalised peak area (Relative concentration)
y = 0,023x - 0,5386
R² = 0,9681
Concentration range (0 - 750 ng metabolite / mg tissue)

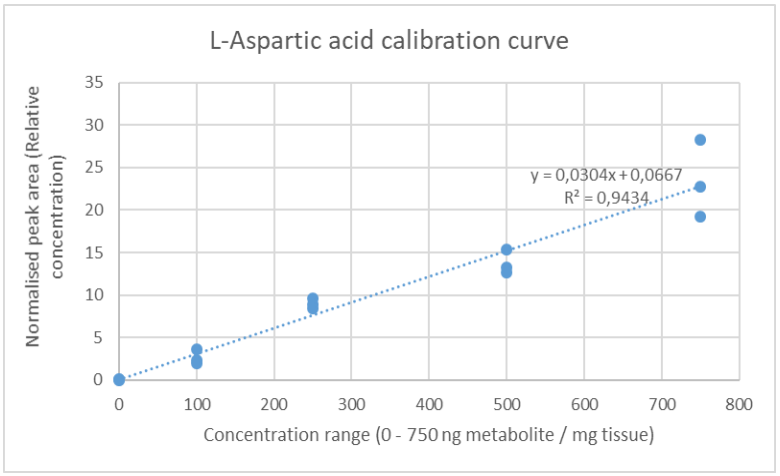
L-Aspartic acid calibration curve
Normalised peak area (Relative concentration)
y = 0,0304x + 0,0667
R² = 0,9434
Concentration range (0 - 750 ng metabolite / mg tissue)

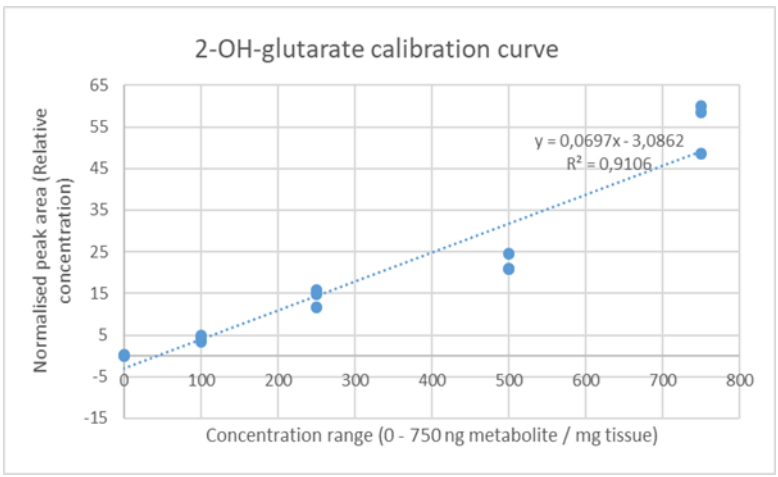
2-OH-glutarate calibration curve
Normalised peak area (Relative concentration)
y = 0,0697x - 3,0862
R² = 0,9106
Concentration range (0 - 750 ng metabolite / mg tissue)

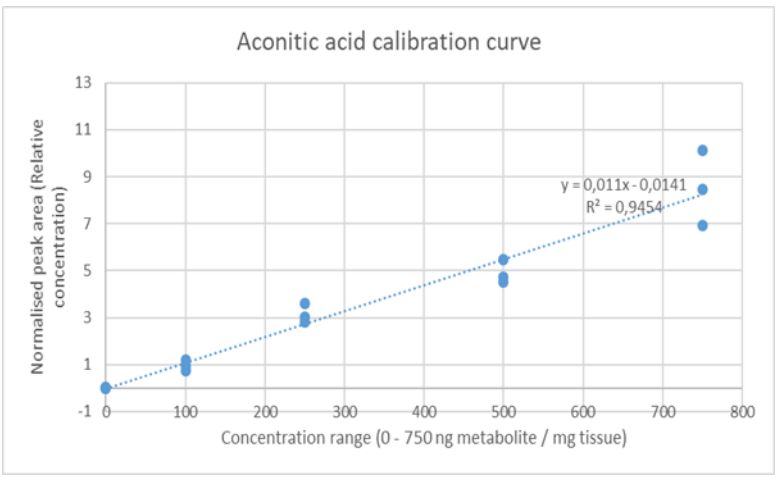
Aconitic acid calibration curve
Normalised peak area (Relative concentration)
y = 0,011x - 0,0141
R² = 0,9454
Concentration range (0 - 750 ng metabolite / mg tissue)

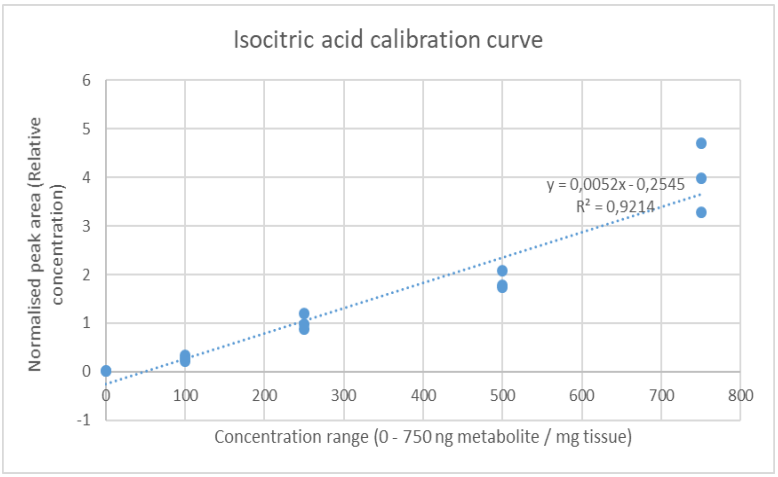
Isocitric acid calibration curve
Normalised peak area (Relative concentration)
y = 0,0052x - 0,2545
R² = 0,9214
Concentration range (0 - 750 ng metabolite / mg tissue)

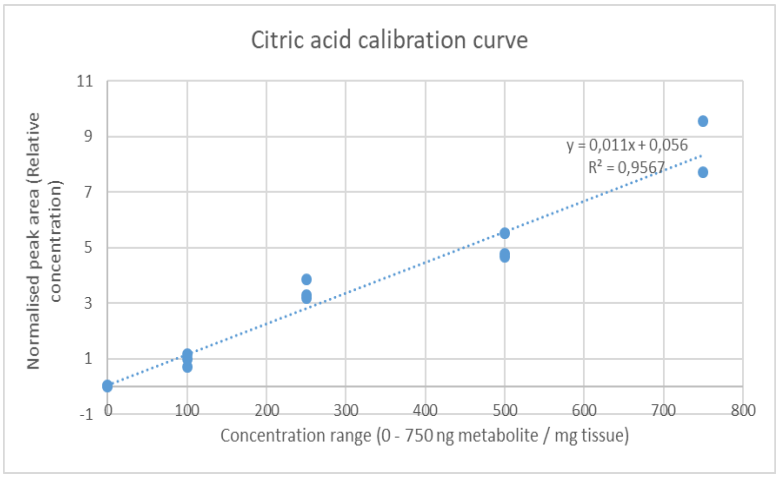
Citric acid calibration curve
Normalised peak area (Relative concentration)
y = 0,011x + 0,056
R² = 0,9567
Concentration range (0 - 750 ng metabolite / mg tissue)

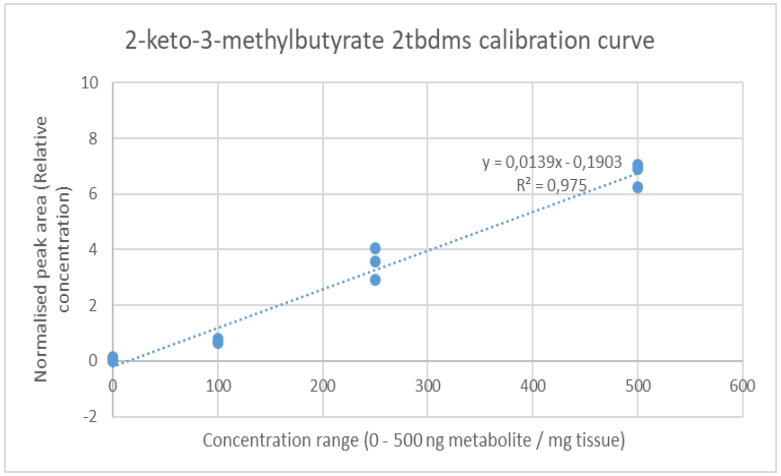
2-keto-3-methylbutyrate 2tbdms calibration curve
y = 0,0139x - 0,1903
R² = 0,975
Normalised peak area (Relative concentration)
Concentration range (0 - 500 ng metabolite / mg tissue)

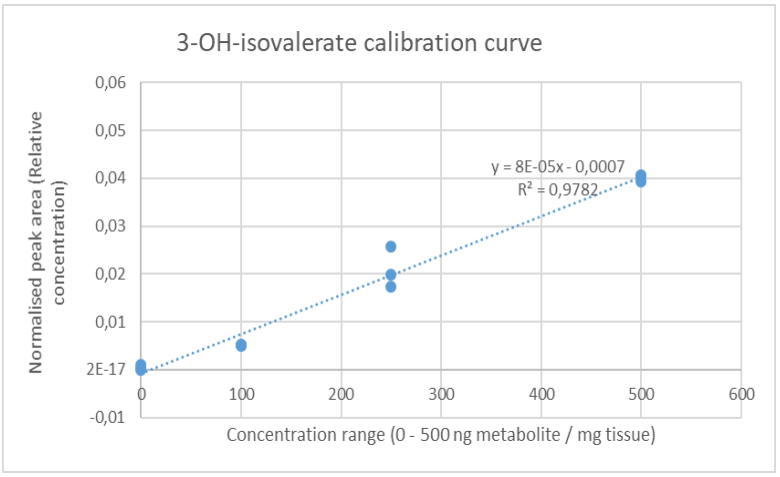
3-OH-isovalerate calibration curve
y = 8E-05x - 0,0007
R² = 0,9782
Normalised peak area (Relative concentration)
Concentration range (0 - 500 ng metabolite / mg tissue)

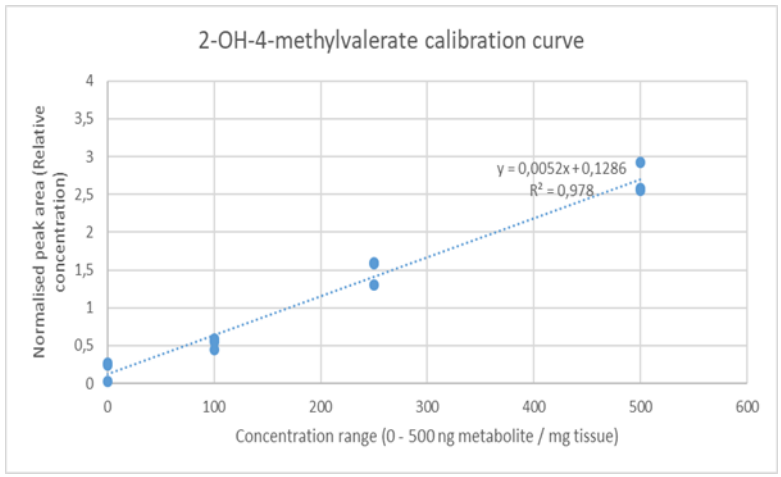
2-OH-4-methylvalerate calibration curve
y = 0,0052x + 0,1286
R² = 0,978
Normalised peak area (Relative concentration)
Concentration range (0 - 500 ng metabolite / mg tissue)

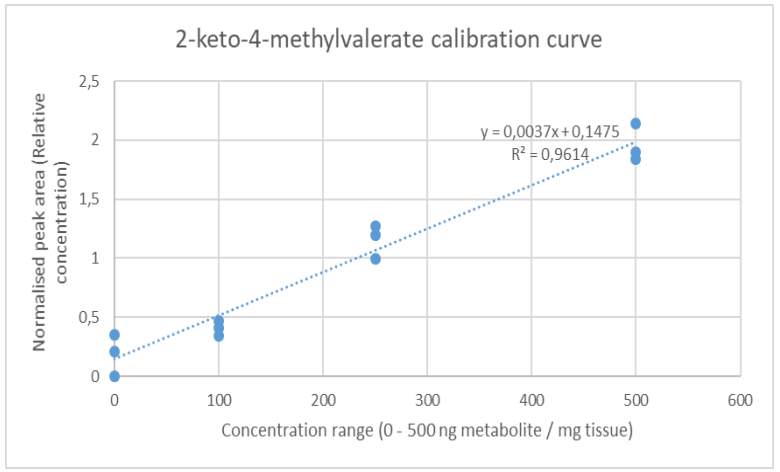
2-keto-4-methylvalerate calibration curve
y = 0,0037x + 0,1475
R² = 0,9614
Normalised peak area (Relative concentration)
Concentration range (0 - 500 ng metabolite / mg tissue)

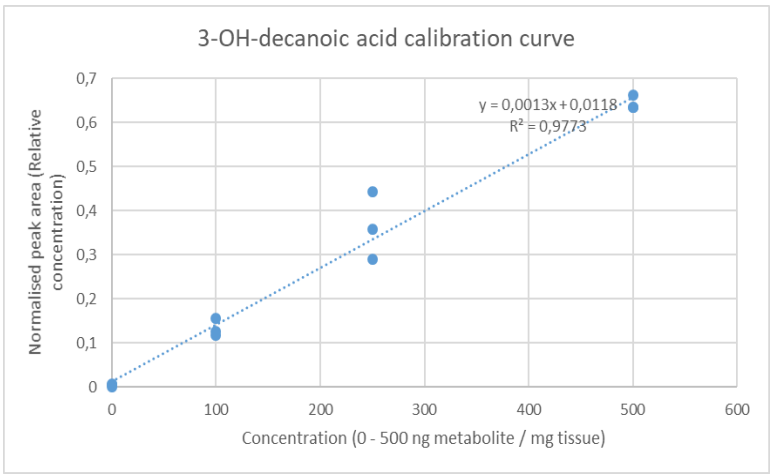
3-OH-decanoic acid calibration curve
y = 0,0013x + 0,0118
R² = 0,9773
Normalised peak area (Relative concentration)
Concentration (0 - 500 ng metabolite / mg tissue)

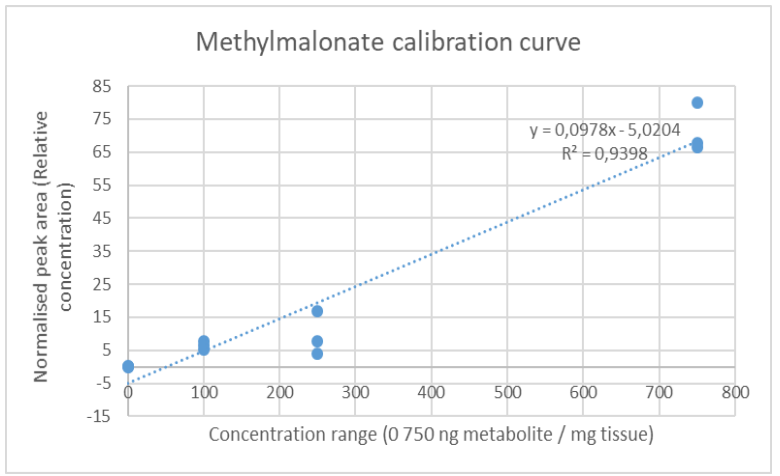
Methylmalonate calibration curve
y = 0,0978x - 5,0204
R² = 0,9398
Normalised peak area (Relative concentration)
Concentration range (0 750 ng metabolite / mg tissue)

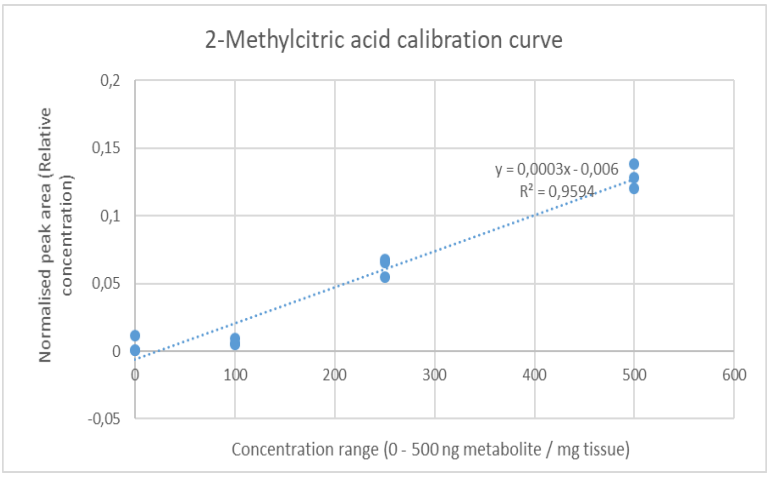
2-Methylcitric acid calibration curve
y = 0,0003x - 0,006
R² = 0,9594
Normalised peak area (Relative concentration)
Concentration range (0 - 500 ng metabolite / mg tissue)

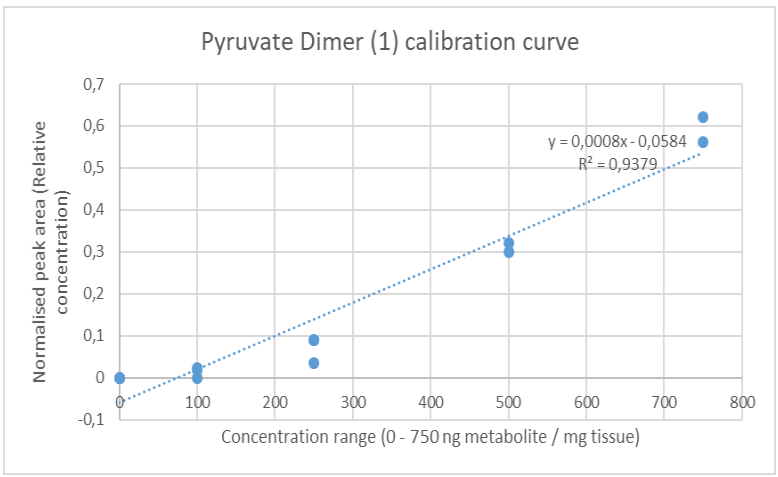
Pyruvate Dimer (1) calibration curve
y = 0,0008x - 0,0584
R² = 0,9379
Normalised peak area (Relative concentration)
Concentration range (0 - 750 ng metabolite / mg tissue)

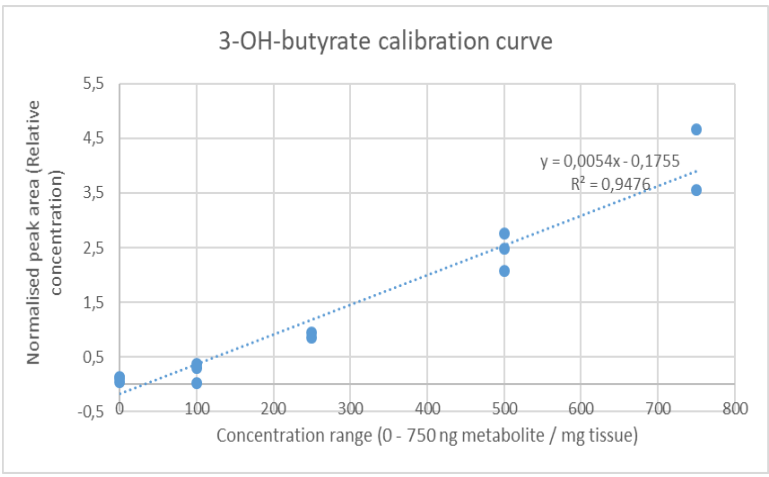
3-OH-butyrate calibration curve
y = 0,0054x - 0,1755
R² = 0,9476
Normalised peak area (Relative concentration)
Concentration range (0 - 750 ng metabolite / mg tissue)

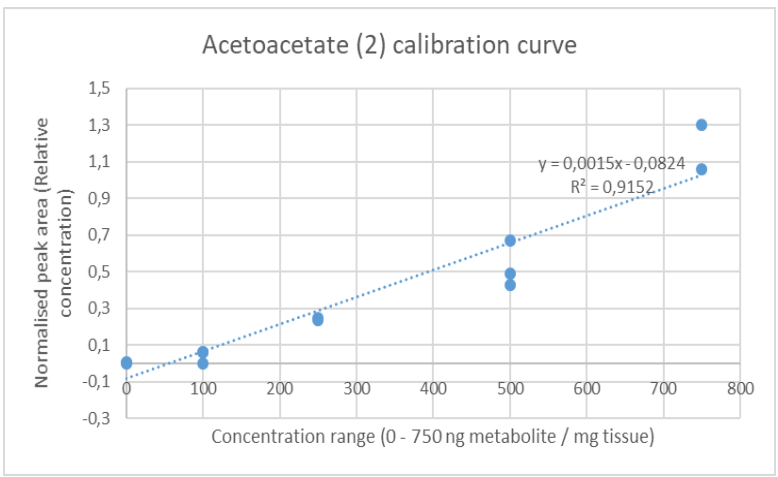
Acetoacetate (2) calibration curve
y = 0,0015x - 0,0824
R² = 0,9152
Normalised peak area (Relative concentration)
Concentration range (0 - 750 ng metabolite / mg tissue)

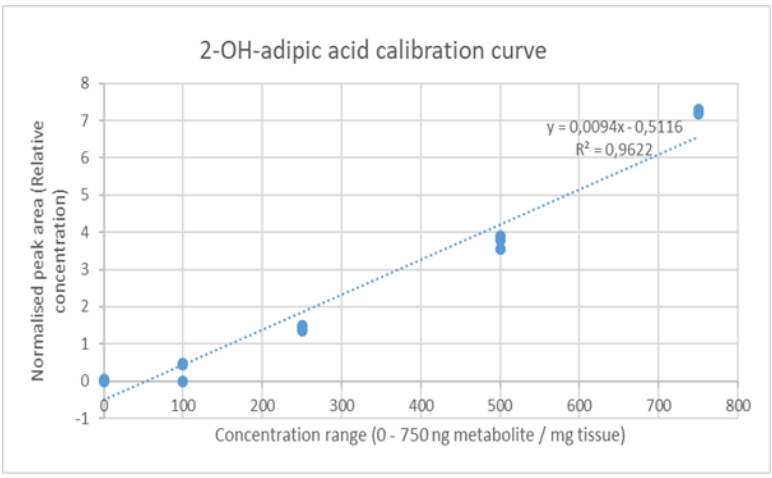
2-OH-adipic acid calibration curve
y = 0,0094x - 0,5116
R² = 0,9622
Normalised peak area (Relative concentration)
Concentration range (0 - 750 ng metabolite / mg tissue)

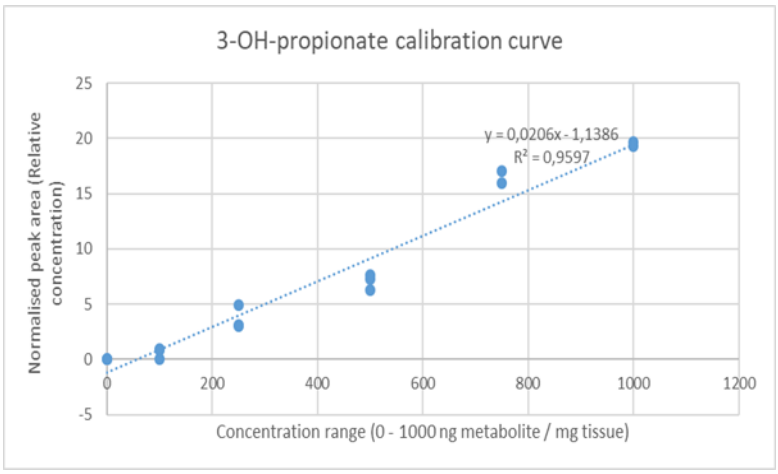
3-OH-propionate calibration curve
y = 0,0206x - 1,1386
R² = 0,9597
Normalised peak area (Relative concentration)
Concentration range (0 - 1000 ng metabolite / mg tissue)

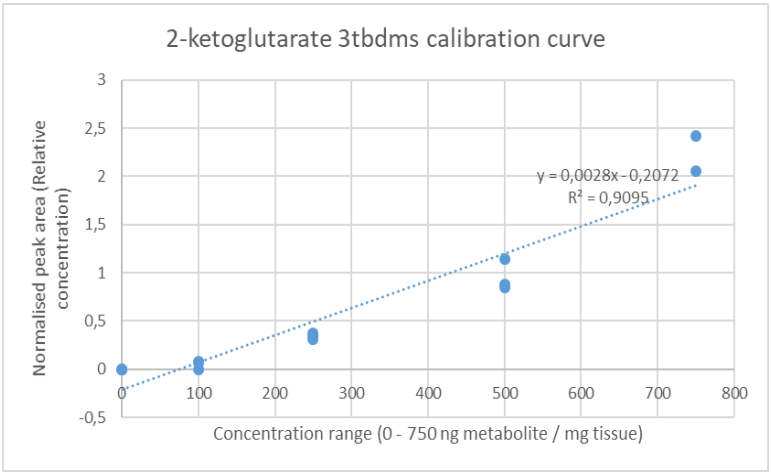

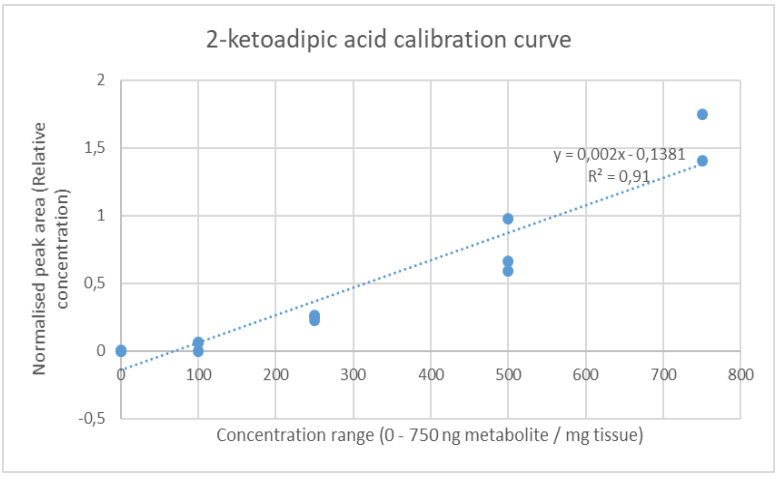

Figures 5.11: Heart calibration curves for the targeted 26 compounds

Each calibration curve was constructed and expressed as normalised peak area (relative concentration) over the concentration range whereas the regression line formula and R squared value are given with each curve. Taking Figures 5.11 together, all calibration curves resembled good linearity ranging from 0.9095 - 0.9782. As such, all the calibration curves resembled a good linear relationship between instrument response and compound concentration. Additionally, the compounds with an $R^2 > 0.9$ can be used for quantification of the compound in the mouse heart matrix.

Table 5.14: Mouse heart LOD's, LOQ's, accuracy and linearity

Compound	LOD (ng/mg)	LOQ (ng/mg)	Accuracy (%)	R^2	Linear range (ng/mg)
Lactate	36.681	39.459	112.31	0.9714	0 – 1000
Pyruvate	47.819	50.242	104.55	0.9616	0 – 500
2-keto-3-methylbutyrate 1tBDMS	47.414	47.415	87.15	0.9475	0 – 750
2-keto-3-methylvalerate 1tBDMS	7.779	8.045	111.67	0.9724	0 – 1000
2-keto-3-methylvalerate 2tBDMS	62.487	63.019	89.69	0.935	0 – 750
Oxaloacetate	2.449	13.626	96.6	0.9505	0 – 750
Malate	32.044	47.767	102.9	0.9681	0 – 750
L-Aspartate	5.748	19.733	101.10	0.9434	0 – 750
2-OH-gluterate	49.582	58.614	102.54	0.9106	0 – 750
Aconitate	4.065	8.894	99.36	0.9454	0 – 750
Citrate	1.011	11.704	99.17	0.9567	0 – 750
Isocitrate	50.954	52.669	88.05	0.9214	0 – 750
2-keto-3methylbutyrate 2tBDMS	34.344	69.131	90.14	0.975	0 – 500
3-OH-decanoic acid	1.505	19.027	95.93	0.9773	0 – 500

2-OH-4-methylvalerate	87.922	270.115	113.23	0.978	0 – 500
3-OH-isovalerate	35.608	83.028	103.15	0.9782	0 – 500
2-keto-4-methylval 2tBDMS	152.966	484.765	92.38	0.9614	0 – 500
Methylmalonate	55.488	62.784	87.79	0.9398	0 – 750
2-Methylcitric acid	94.229	234.024	95.67	0.9594	0 – 500
Pyruvate Dimer (1)	74.234	76.432	89.60	0.9379	0 – 750
3-OH-butyrate	78.727	143.919	98.81	0.9476	0 – 750
Acetoacetate (2)	61.459	71.965	100.29	0.9152	0 – 750
2-ketoglutarate 3tBDMS	75.107	76.978	93.48	0.9095	0 – 750
2-OH-adipic acid	63.512	79.267	92.75	0.9622	0 – 750
2-ketoadipic acid	72.859	79.574	111.56	0.91	0 – 750
3-OH-propionate	60.052	67.296	84.32	0.9597	0 – 1000

Table 5.14 represents the LOD, LOQ, accuracy, R^2 and linear range for each organic acid optimised within the mouse heart matrix. As seen in Table 8, the LODs for the selected organic acids ranged from 1.011 ng /mg - 152.966 ng /mg, with the LOQs ranging from 8.045 ng/mg - 484.765 ng/mg. The LOD range of all transitions were within the lower concentration range of the calibration curve (0 - 250 ng/ mg), signifying that each organic acid can be detected at low concentrations whilst being distinguished from analytical noise. On the other hand, the LOQs of all the transitions, except 5, were within the lowest calibration range (0 - 100 ng/mg), denoting that organic acids low in concentration can be quantified.

The accuracy of the optimised conditions was calculated in the same manner as during the mouse liver and brain calibration. Accuracy of the organic acids in the mouse heart matrix ranged from 84.32 % - 113.23 %. 3-OH-propionate's transition was the only transition over the 15 % accuracy cut off, whilst all other transitions were within the 85 % - 115 % accuracy range. Henceforth, all the selected organic acid transitions mentioned in Table 8, except one, resembles a large agreement between expected concentration and experimental concentration. This implies that these transitions can be used to determine absolute concentrations accurately from each calibration curve's regression line formula, within the mouse heart matrix.

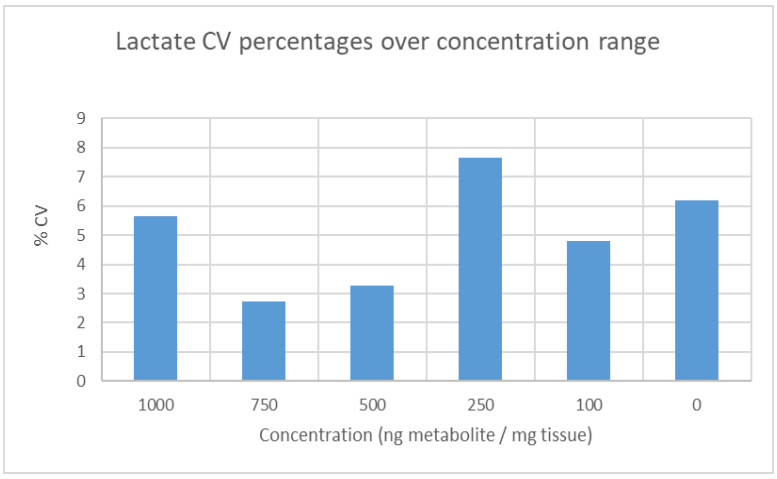

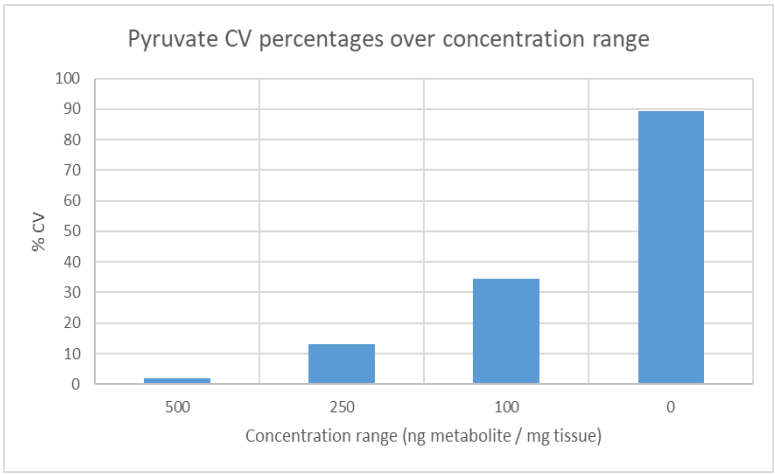

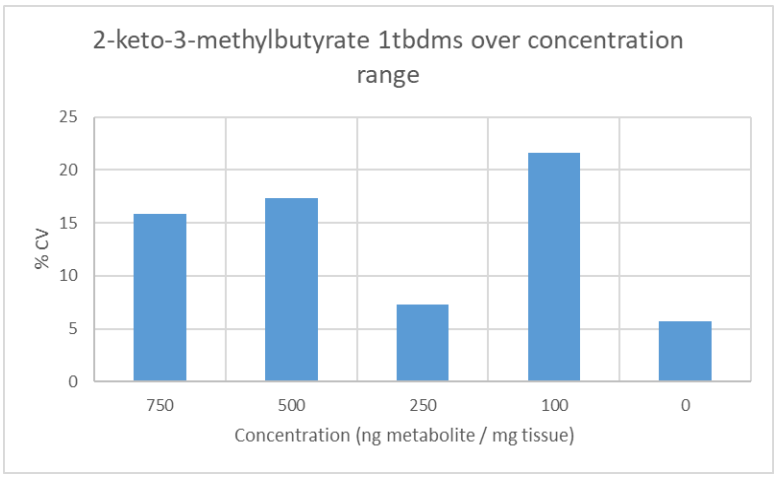
2-keto-3-methylbutyrate 1tbdms over concentration range
% CV
25
20
15
10
5
0
750
500
250
100
0
Concentration (ng metabolite / mg tissue)

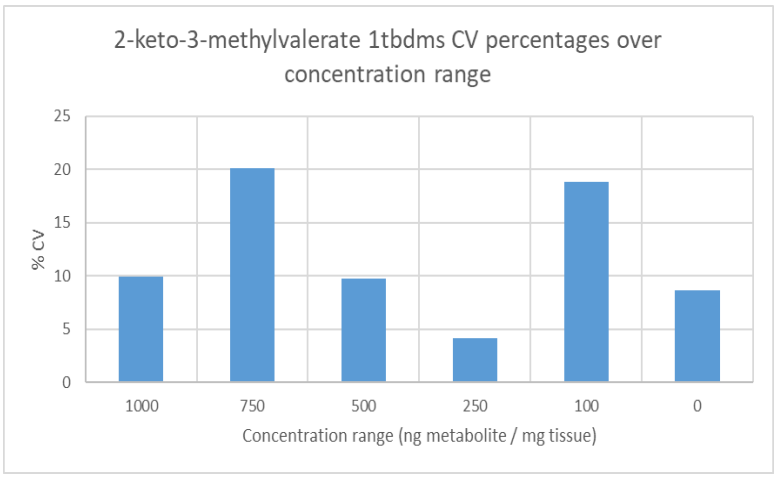
2-keto-3-methylvalerate 1tbdms CV percentages over concentration range
% CV
25
20
15
10
5
0
1000
750
500
250
100
0
Concentration range (ng metabolite / mg tissue)

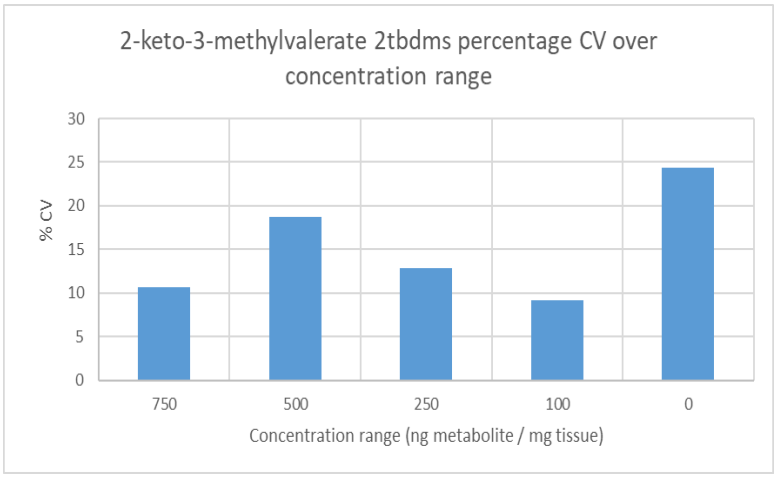
2-keto-3-methylvalerate 2tbdms percentage CV over concentration range
% CV
30
25
20
15
10
5
0
750
500
250
100
0
Concentration range (ng metabolite / mg tissue)

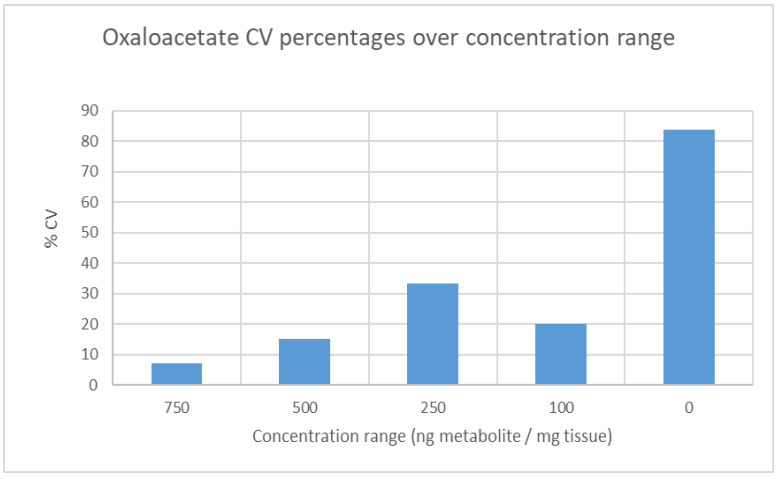
Oxaloacetate CV percentages over concentration range
% CV
90
80
70
60
50
40
30
20
10
0
750
500
250
100
0
Concentration range (ng metabolite / mg tissue)

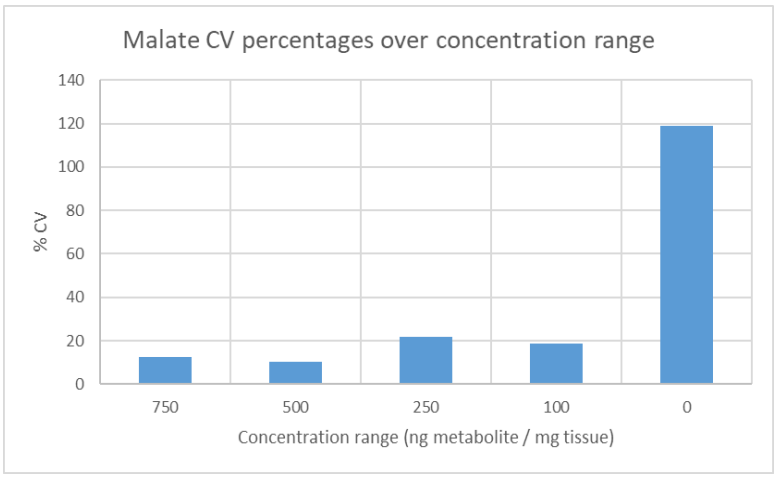
Malate CV percentages over concentration range
% CV
140
120
100
80
60
40
20
0
750
500
250
100
0
Concentration range (ng metabolite / mg tissue)

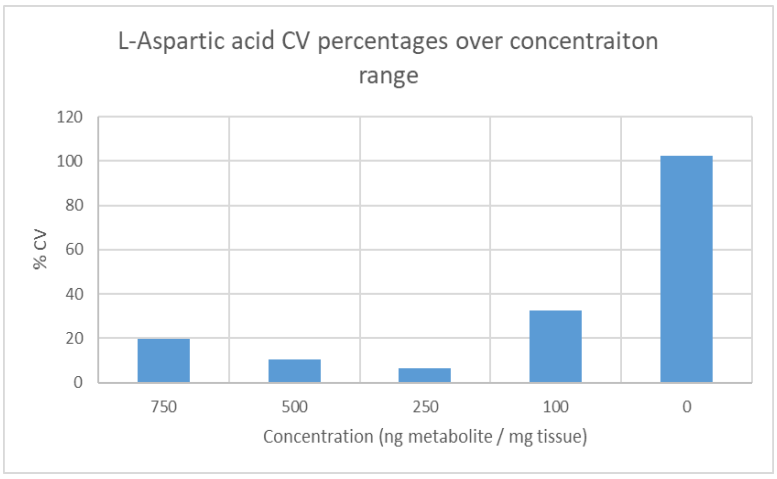
L-Aspartic acid CV percentages over concentraiton range
% CV
120
100
80
60
40
20
0
750
500
250
100
0
Concentration (ng metabolite / mg tissue)

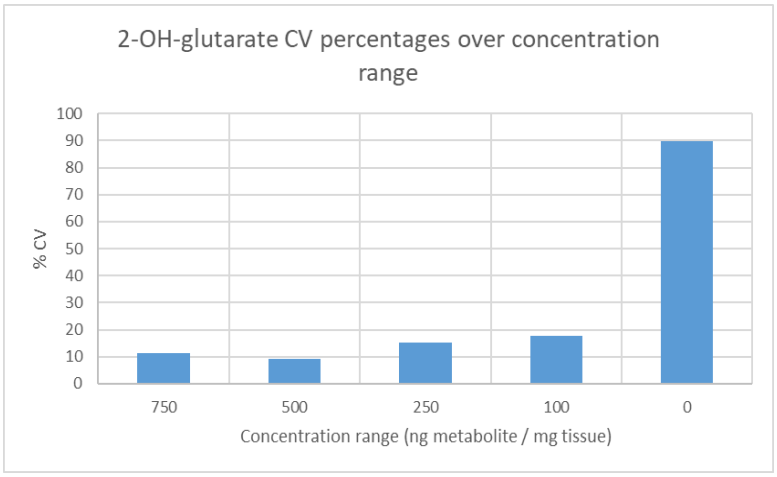
2-OH-glutarate CV percentages over concentration range
% CV
100
90
80
70
60
50
40
30
20
10
0
750
500
250
100
0
Concentration range (ng metabolite / mg tissue)

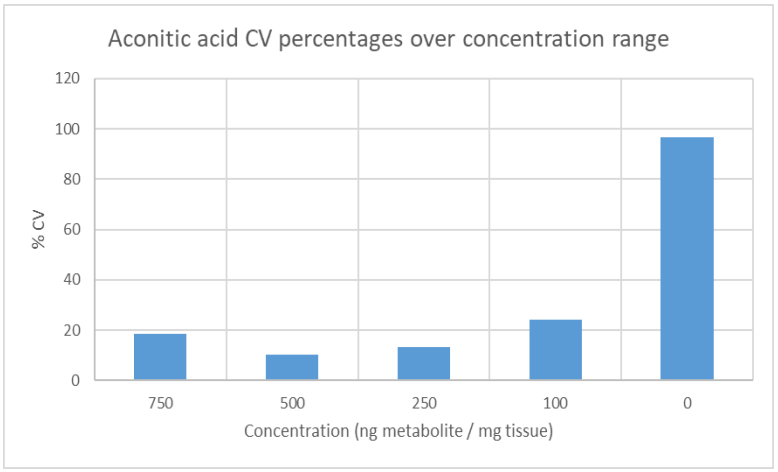
Aconitic acid CV percentages over concentration range
% CV
120
100
80
60
40
20
0
750
500
250
100
0
Concentration (ng metabolite / mg tissue)

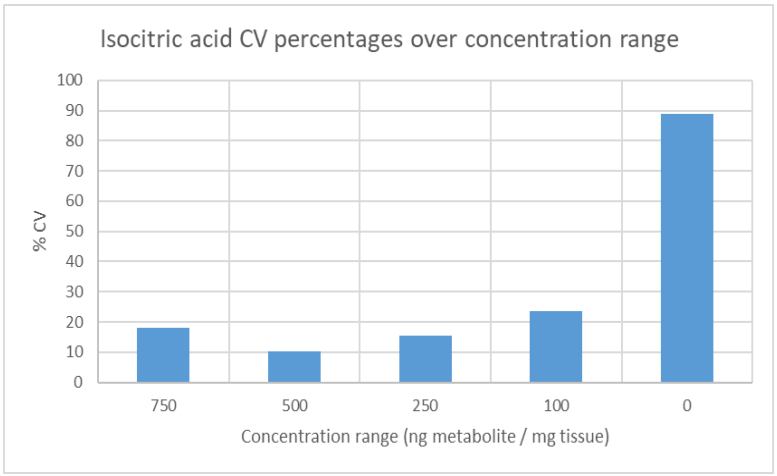
Isocitric acid CV percentages over concentration range
% CV
100
90
80
70
60
50
40
30
20
10
0
750
500
250
100
0
Concentration range (ng metabolite / mg tissue)

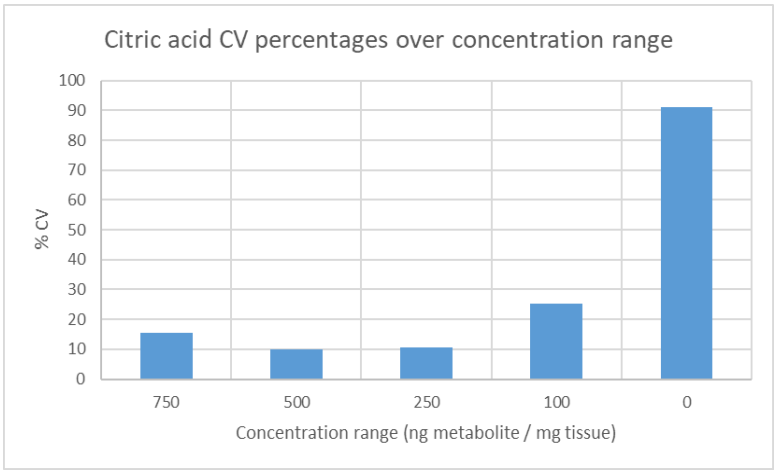
Citric acid CV percentages over concentration range
% CV
100
90
80
70
60
50
40
30
20
10
0
750
500
250
100
0
Concentration range (ng metabolite / mg tissue)

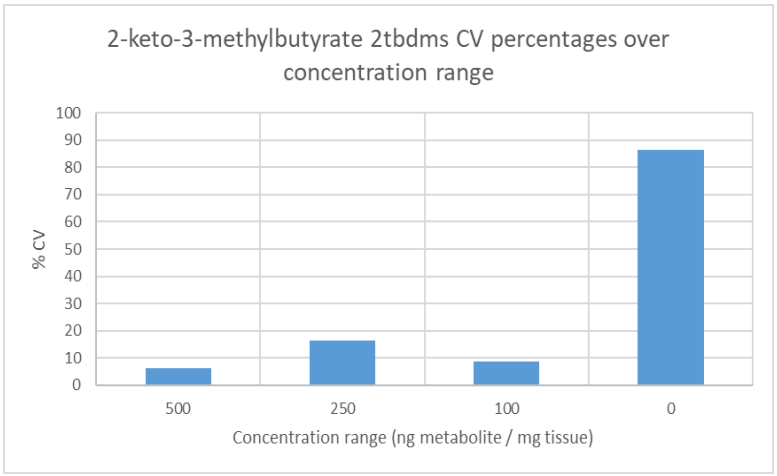
2-keto-3-methylbutyrate 2tbdms CV percentages over concentration range
% CV
100
90
80
70
60
50
40
30
20
10
0
500
250
100
0
Concentration range (ng metabolite / mg tissue)

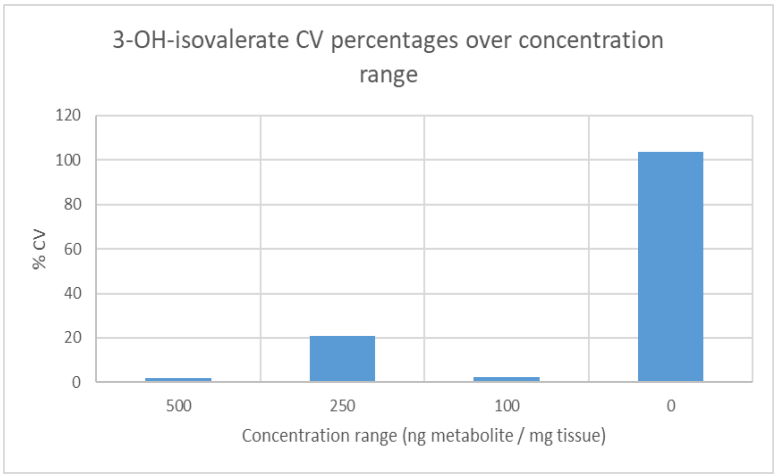
3-OH-isovalerate CV percentages over concentration range
% CV
120
100
80
60
40
20
0
500
250
100
0
Concentration range (ng metabolite / mg tissue)

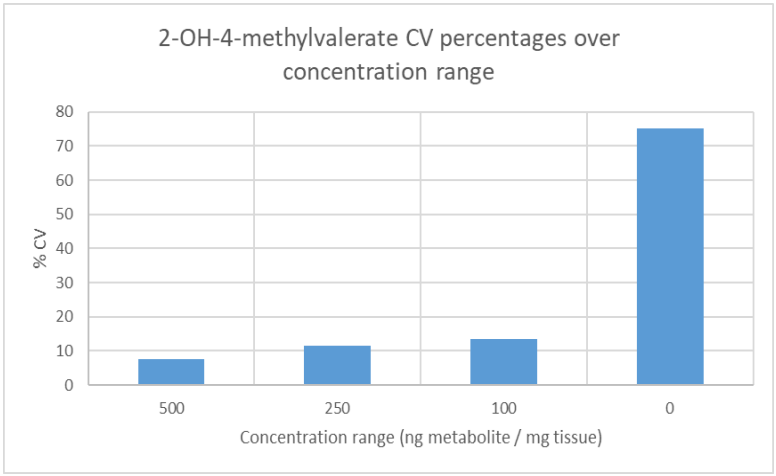
2-OH-4-methylvalerate CV percentages over concentration range
% CV
0
10
20
30
40
50
60
70
80
500
250
100
0
Concentration range (ng metabolite / mg tissue)

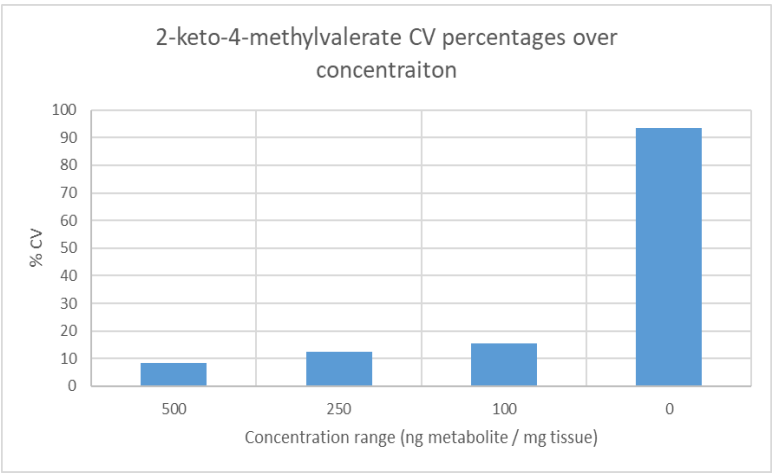
2-keto-4-methylvalerate CV percentages over concentraiton
% CV
0
10
20
30
40
50
60
70
80
90
100
500
250
100
0
Concentration range (ng metabolite / mg tissue)

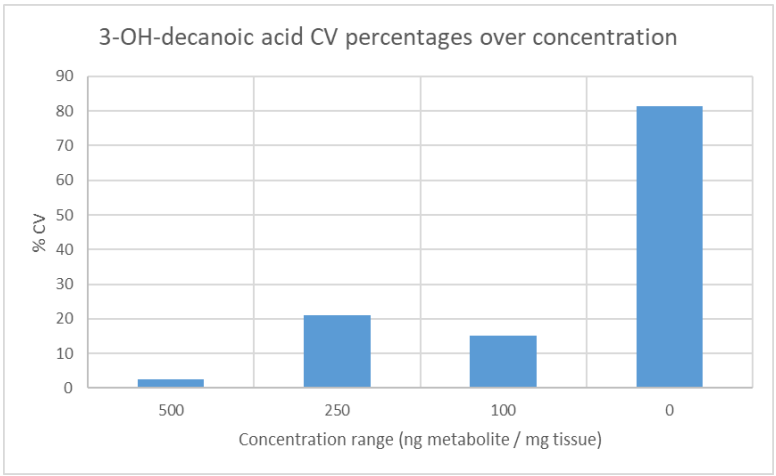
3-OH-decanoic acid CV percentages over concentration
% CV
0
10
20
30
40
50
60
70
80
90
500
250
100
0
Concentration range (ng metabolite / mg tissue)

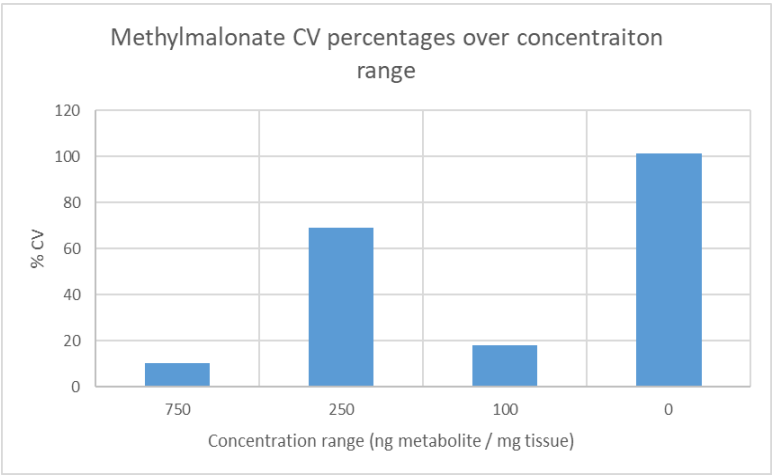
Methylmalonate CV percentages over concentraiton range
% CV
0
20
40
60
80
100
120
750
250
100
0
Concentration range (ng metabolite / mg tissue)

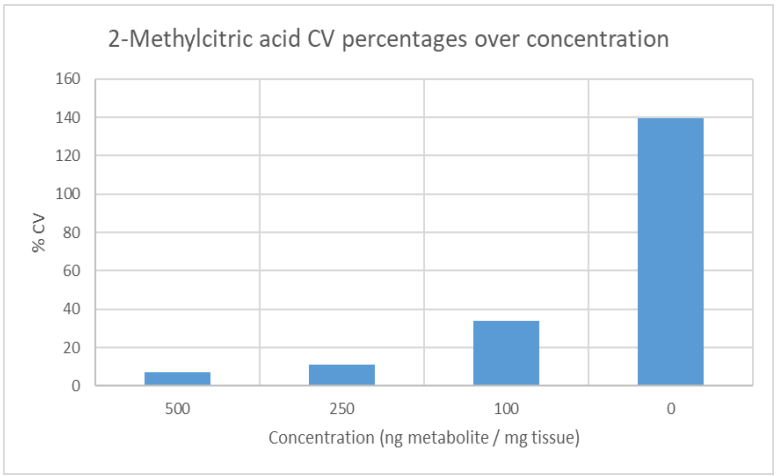
2-Methylcitric acid CV percentages over concentration
% CV
0
20
40
60
80
100
120
140
160
500
250
100
0
Concentration (ng metabolite / mg tissue)

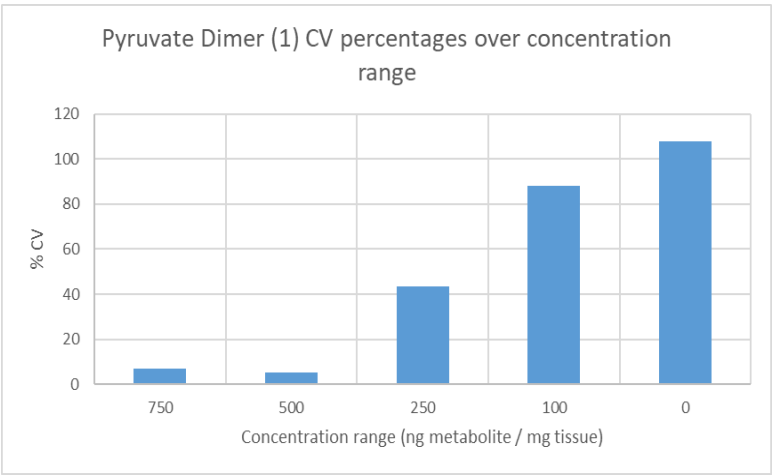
Pyruvate Dimer (1) CV percentages over concentration range
% CV
0
20
40
60
80
100
120
750
500
250
100
0
Concentration range (ng metabolite / mg tissue)

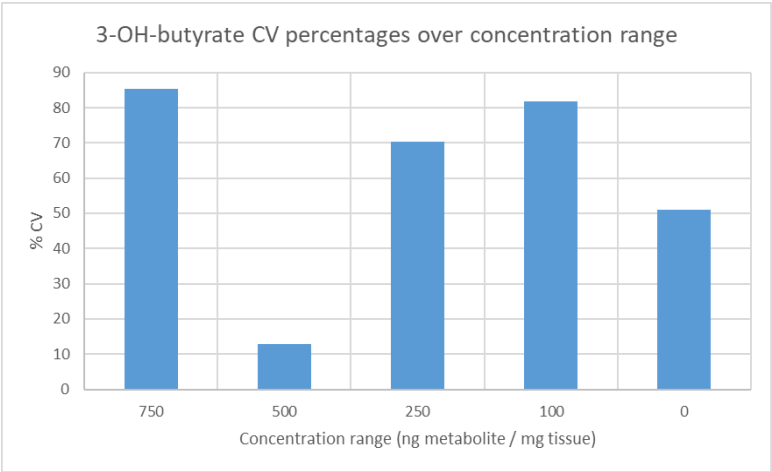

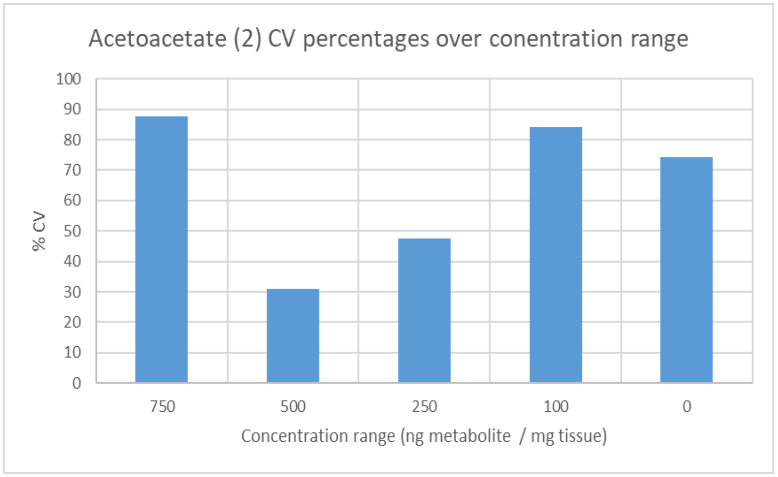

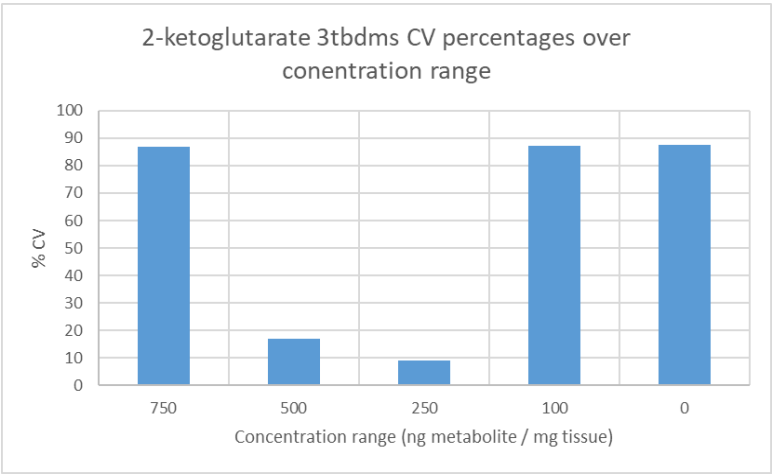

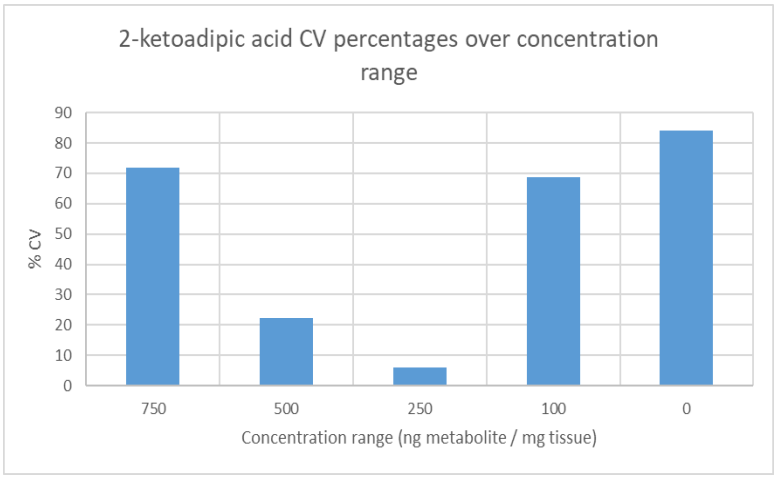

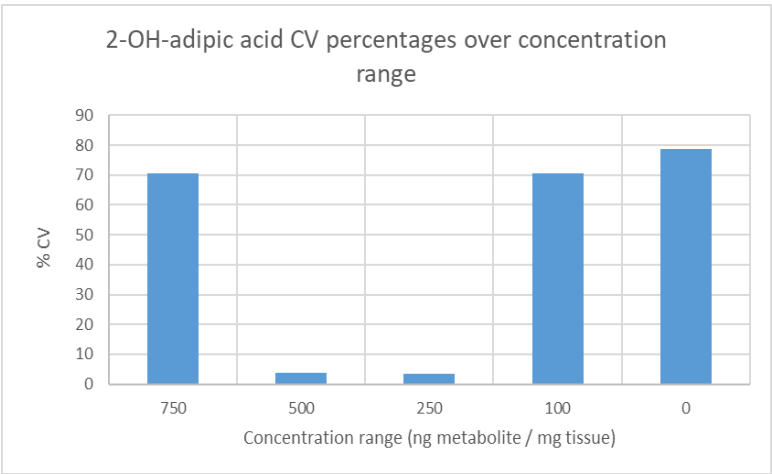

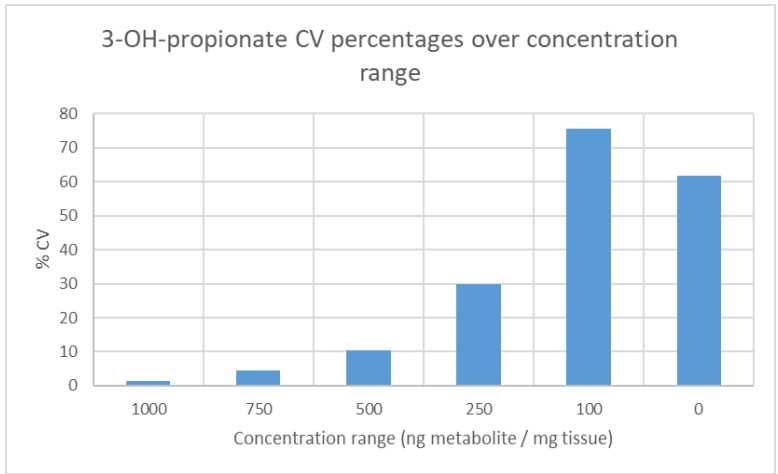

Figures 5.12: Bar graphs representing the CV percentages over calibration concentration range of selected organic acids

Table 5.15: Summarized variance over the brain calibration range. The total number of compounds with CV above and below 25 % CV cut off at each calibration point in mouse heart are indicated.

Concentration (ng/mg)	Total with CV % < 25	Total with CV % > 25
1000	3	0
750	14	5
500	24	1
250	20	5
100	15	10
Blank	3	22

As outlaid in Table 5.15, most compounds exhibited large variation between triplicate samples of the 1000 and 750 concentration range with only two transitions (methylmalonate) not including the 500 calibration level, as such most of these compounds had their CV-graphs (Figures 5.12) constructed without the two highest calibration ranges. As per Table 5.15, the 1000 calibration range will not be included in the presentation of increasing variance per concentration group, due to this calibration point only containing 5 MRM transitions. Triplicate analysis of the selected organic acids at different concentrations within the mouse heart matrix, revealed an increase in variation as follows: 500 < 250 < 750 < 100 < Blank. On this account, the blank and 100 ng/mg calibration points exhibited the most variation expressed in % CV across triplicate samples, which could be due to ineffective stripping of metabolites from the heart matrix. In comparison to the calibration point with the most variation in the liver and brain tissue (100), the high variation exhibited in the blank calibration point of the heart could be due to the protein rich matrix in the heart. Since the heart is mostly made of muscle for contractility purposes, dialysis stripping could be ineffective in reducing the matrix response when the blank calibration point was analysed in triplicate. Consequently, if less matrix components were stripped, the instrument response for the set compounds in the blank sample could be much higher than a theoretical concentration of 0, and therefore contributes to the high variation observed in the blank sample. Overall, the least % variation was observed in the 500 ng/mg calibration point with minimal to some variation observed in the 250 ng/mg and 750 ng/mg range. By these means, reliable as well as consistent experimental results can be generated within this calibration range. Lastly, the 500 ng/mg calibration point was chosen to calculate the accuracy of each MRM transition.

5.4 Method application: investigating redox ratios in Ndufs4 KO mice

5.4.1 Confirmation of KO and WT mice genotype

The genotypes of Ndufs4 KO (n = 6) and WT (n = 6) mice were determined and confirmed with PCR and gel electrophoresis. The results are shown in Figure 5.18 A & B.

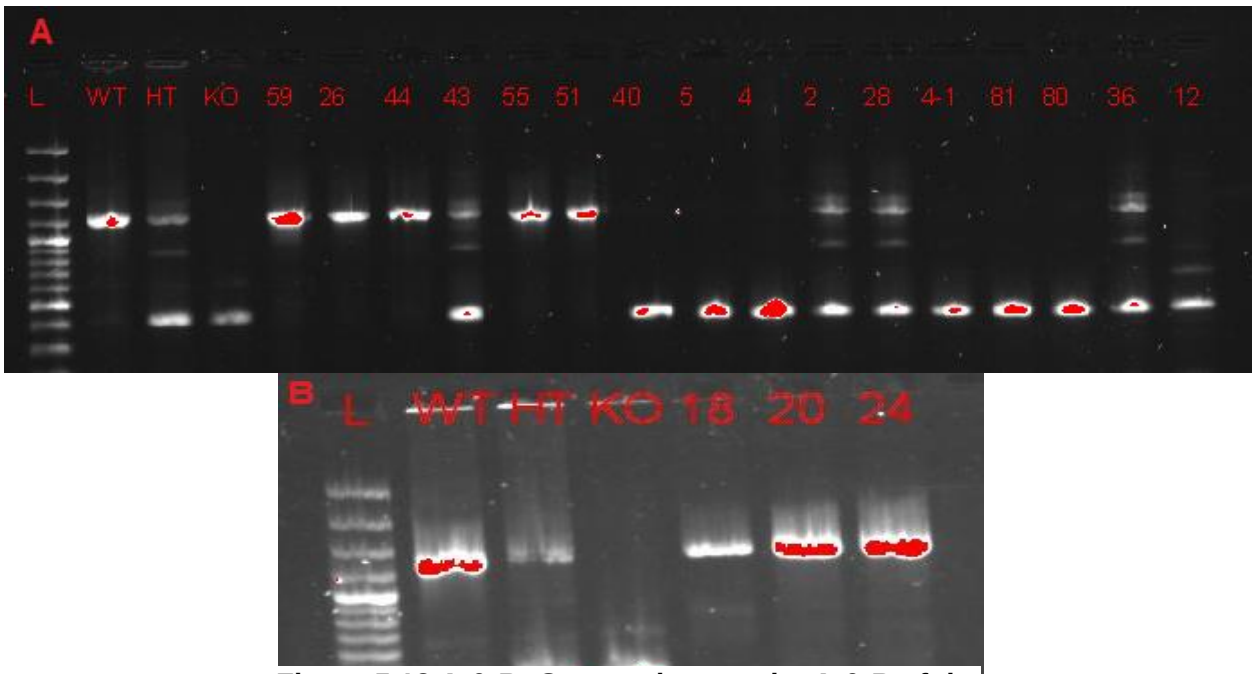

Figure 5.13 A & B: Genotyping results A & B of the mice acquired with sample numbers used for the application: 59, 26, 44, 55, 51, 40, 5, 4, 4_1, 81, 80 and 18

As seen in Figure 5.13A and 5.13B, the first four lanes contain DNA ladder and control samples of each potential genotype (KO, HT and WT). The rest of the lanes contain mice samples specified by each mouse's number. The WT samples used for the application of the study are represented by the following sample numbers: 59, 26, 44, 55, 51 and 18. While the KO samples were present in the following wells: 40, 5, 4, 4_1, 81, and 80. WT samples were visually identified by the major top band at 1229 bp, while the KO samples were visually identified by the major lower band at 429 bp, whereas each KO and WT sample visualised the same bands as the control DNA for KO and WT mice. The amount of tissue used from each mouse (liver, heart and brain) is noted in Appendix A.

To assess the redox state differences between NDUFS4 KO and WT mice, 5 calibration ranges were analysed adjacent with each KO and WT sample in the following sequence:

Table 5.16: Sample order analysed with method 1 throughout method 4

Vial number	Sample
1	FAMES
2	QC / 250 calibrator
3	KO40
4	WT26
5	500 calibrator
6	KO5
7	WT59
8	KO4
9	100 calibrator
10	WT51
11	KO4_1
2	QC / 250 calibrator
13	WT18
14	WT55
15	Blank calibrator
16	KO80
17	WT44
18	KO81
19	1000 calibrator
2	QC / 250 calibrator

As outlined by Table 5.16, each tissue type was run on the same sequence as above with method 1 loaded to be analysed first in each sample, continuing to method 2, 3, and 4. After 77 injections, another fatty acid methyl ester (FAME) sample was run in MS scan mode to check and confirm that the system was still working efficiently after the injection of all samples. The first and last injected FAME sample was comparable in terms of chromatographic separation and peak intensity and retention time. The sample was analysed with the same chromatographic conditions used for the biological samples in order to have a retention index for confirming metabolite identities when peaks drift slightly. Because of this, the peaks eluting at the end of the chromatogram are not as resolved as the other peaks eluting earlier in the chromatogram.

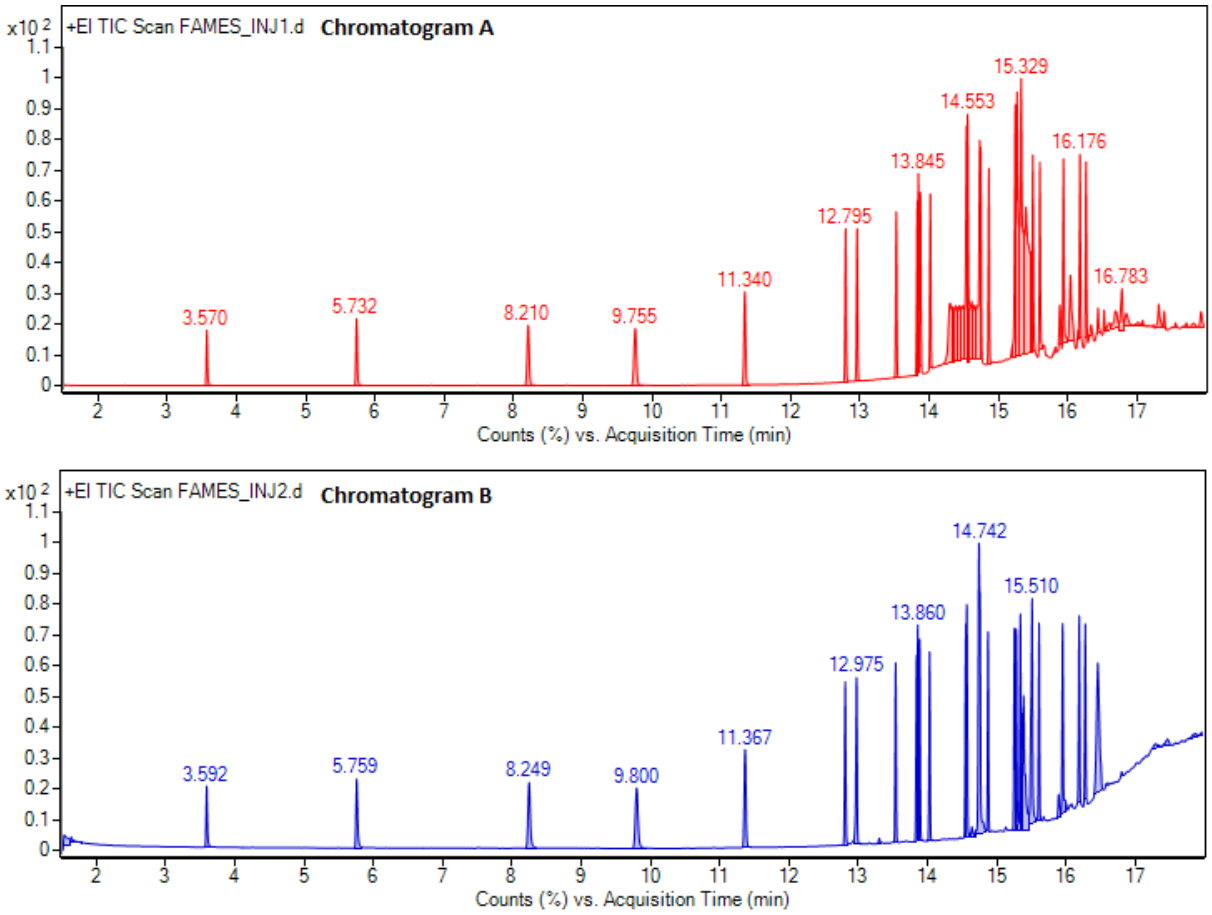

Figure 5.14: Chromatogram A and B indicating the FAME injection before and after each sample injection

Figure 5.14 represents the same FAME sample injected before and after sample analyses, and were used for the calculation of precision and accuracy of each dMRM transition, within each dMRM method.

5.4.2 Data Acquisition and statistical analysis

Three repeats of the same QC sample (250 calibrator) were injected before, in between and after sample analyses, and were used for the calculation of precision and accuracy of each dMRM transition, within each dMRM method.

All samples were processed via Agilent MassHunter Quantitative software. The data was exported to Microsoft Excel whereas calibration curves for each analyte was constructed to quantify each metabolite, in the same manner as described in Section 5.3. Ratios of redox pairs were also determined followed by statistical analyses. Significant differences between sample groups in the calculated concentration of target metabolites and ratios were identified with univariate statistical tests (t-test, FDR corrected p-values and effect size), performed in Microsoft Excel and MetaboAnalyst 5 (Pang *et al*., 2021). Differences were considered significant when p-

values < 0.05 indicating statistical significance (two-tailed distribution) and effect size (≥ 0.8 indicating a strong practical significance between the groups) (Venter, L. 2017). Effect size allows researchers to evaluate differences between the mean of two groups and whether a practical significance exists (Goulet-Pelletier & Cousineau, 2018), and was expressed as practical significant differences in the KO group. Also, false discovery rate (FDR) corrected p-value was calculated to identify significant features while incurring a low proportion of false positives (Venter, L. 2017). MetaboAnalyst 5 was also used for the construction of boxplots to visually represent metabolite differences between the groups.

5.5 Method application on NDUFS4 KO and WT mice liver, heart, and brain tissue

5.5.1 Liver Redox Metabolism

Table 5.17A: Statistical results of liver redox metabolites

Compound	p-value	FDR corrected p-value	Effect size	EF degree	HMDB Code
Citrate	0,0151	0,3490	1,3370	↓	HMDB0000094
Lactate	0,0604	0,4198	1,0121	↓	HMDB0000190
2-OH-glutarate	0,0830	0,4198	0,9414	↓	HMDB0000694
Malate	0,1075	0,4198	0,8824	↑	HMDB0000744
2-keto-3-methylvalerate	0,1078	0,4198	0,6856	NA	HMDB0000491
2-OH-4-methylvalerate	0,1095	0,4198	0,9033	↑	HMDB0000665
Pyruvate	0,1408	0,4227	0,7570	NA	HMDB0000243
L-Aspartate	0,1563	0,4227	0,7094	NA	HMDB0000191
3-OH-butyrate	0,1654	0,422	0,8603	↑	HMDB0000357
3-OH-isovalerate	0,3116	0,7167	0,5417	NA	HMDB0000754
Acetoacetate	0,3608	0,7297	0,3930	NA	HMDB0000060

2-OH-3-methylbutyrate	0,4331	0,7297	0,3382	NA	HMDB0000354
Pyruvate Dimer	0,4428	0,7297	0,3644	NA	HMDB0000243
3-OH-palmitate	0,4442	0,7297	0,3853	NA	HMDB0010734
2-ketoadipic acid	0,4996	0,7334	0,3484	NA	HMDB0000225
2-keto-4-methylvalerate	0,5108	0,7334	0,3059	NA	HMDB0000695
2-OH-adipic acid	0,5420	0,7334	0,2869	NA	HMDB0000321
3-OH-decanoate	0,7059	0,8783	0,2098	NA	HMDB0002203
Isocitrate	0,7256	0,8783	0,1736	NA	HMDB0000193
2-keto-3-methylbutyrate	0,8632	0,9886	0,0954	NA	HMDB0000019
2-ketoglutarate	0,9553	0,9886	0,0316	NA	HMDB0000208
Aconitate	0,9783	0,9886	0,0151	NA	HMDB0000072
Oxaloacetate	0,9886	0,9886	0,0073	NA	HMDB0000223

Table 5.17B: Statistical results of liver redox ratios

Redox Ratio	p-value	FDR corrected p-value	Effect size	EF degree	HMDB Code
2-OH-glutaerate / 2-ketoglutarate	0,0091	0,0667	1,8311	↓	NA
Citrate / Aconitate	0,0121	0,0667	1,4065	↓	NA
Lactate / Pyruvate	0,0541	0,1986	1,0419	↓	NA
Malate / Oxaloacetate	0,0986	0,2595	0,9116	↓	NA
Malate / L-Aspartate	0,1179	0,2595	0,9025	↑	NA
3-OH-butyrate / Acetoacetate	0,3494	0,6406	0,4058	NA	NA
2-OH-adipic acid / 2-ketoadipic acid	0,5713	0,8870	0,2699	NA	NA
Citrate / Isocitrate	0,6462	0,8870	0,2279	NA	NA
Isocitrate / 2-ketogluterate	0,7257	0,8870	0,1731	NA	NA
2-OH-4-mvalerate/ 2-keto-4-methylvalerate	0,8272	0,9099	0,0982	NA	NA
2-OH-3-methylbutyrate / 2-keto-3-methylbutyrate	0,9364	0,9364	0,0435	NA	NA

Tables 5.17A and 5.17B represents the statistical results for liver redox metabolites and ratios, respectively giving an overall estimation on the significantly affected redox metabolites and their ratios. The p-value indicates statistical significance between the KO and WT mice at 3 redox ratios and a metabolite coupled to redox metabolism. These mentioned differential metabolites were found to be decreased in KO mice as per each ratio and metabolite effect size. In addition, 2 redox ratios and 2 redox metabolites were also found to be decreased in the KO group as per effect sizes. The metabolites and their ratios mentioned above all belong to the TCA cycle or are anaplerotic entry points into the TCA cycle, possibly suggesting slower metabolic reactions within the TCA ycle.

Only 3 redox metabolites and 1 redox ratio pair was increased in the KO group when compared to the WT group. These metabolites all are representatives of the TCA cycle, BCAA catabolism and ketogenesis pathways.

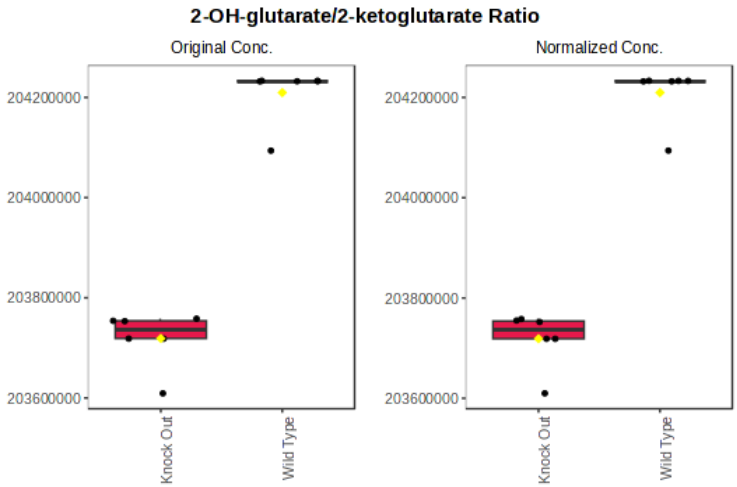

Figure 5.15: Box plots of 2-OH-glutarate / 2-ketoglutarate measurements in KO and WT mice liver

As per Table 5.17A and Figure 5.15, the effect size of 2-OH-glutarate indicates decreased levels within the KO group compared to the WT group, without being statistically significant. As previously described, 2HG can be produced via the mitochondrial enzyme malate dehydrogenase and can also be converted back to 2-ketoglutarate via 2-OH-glutarate dehydrogenase utilizing FAD+ as coenzyme. As previously described at the 2-OH-glutarate / 2-ketoglutarate ratio, this redox ratio might not be as profoundly affected as others. Also, as theorized, minute 2-ketoglutarate might be available for the synthesis of 2HG to regenerate NAD+ and therefore could be the reason as to why 2HG was less pronounced in the KO group.

Referring to Table 5.17B, the redox ratio 2-hydroxyglutarate: 2-ketoglutarate was identified to be markedly decreased in the KO group according to its effect size and p-value. 2-ketoglutarate is a

well-studied TCA intermediate and entry point to the TCA cycle for glutamate. Glutamate can be converted to 2-ketoglutarate via the mitochondrial enzyme glutamate dehydrogenase with the subsequent reduction of NAD+ to NADH, fuelling the TCA cycle with 2-ketoglutarate in the case of high dietary glutamate intake or glutamate biosynthesis during glucose deprivation (Smith *et al*., 2019). Moreover, 2-ketoglutarate and glutamate take part in transamination reactions when amino acids are catabolized, with liver transaminases preferring 2-ketoglutarate as substrate. 2-ketoglutarate can also be synthesized from isocitrate inside the mitochondrial matrix, via isocitrate dehydrogenase, reducing NAD+ to NADH in the process (Akram M., 2014). 2-Ketoglutarate can by catalyzed to 2HG by the mitochondrial enzyme malate dehydrogenase 1 (MDH1), subsequently oxidizing NADH back to NAD+, whereas a subtype of malate dehydrogenase 1 can catalyze the same reaction in the cytosol, which also generates NAD+ (Intlekofer *et al*., 2015). With impaired complex I activity, it was expected that the conversion of 2KG to 2HG would be favoured in Ndufs4 KO mice in an attempt to restore redox balance (producing NAD+ and lowering accumulating NADH levels). However, this was not the case due to the involvement of another enzyme.

The conversion of 2-hydroxyglutarate (2HG) to 2-ketoglutarate in the mitochondria is possible via 2-hydroxyglutarate dehydrogenase (2-HGDH), which utilizes FAD as coenzyme, yielding 2-ketoglutarate and $FADH_2$ in the process (Martínez-Reyes & Chandel, 2020). Accordingly, the decreased 2-OH-glutarate / 2-ketoglutarate ratio indicates that this reaction could be upregulated in the Ndufs4 KO mice, allowing an alternative route for electrons into the ETC via coenzyme Q. Not only does it help sustain the proton gradient but also help with redox imbalance seeing that it is possible that the formation of 2HG from 2KG by MDH1 occurs solely to convert the formed 2HG back to 2KG via 2-HGDH for the formation of $FADH_2$ to drive ATP production. It should also be noted that the reduction of 2KG to 2HG does not occur under normal catalytic activity of malate dehydrogenase but rather due to enzyme promiscuity (Tyrakis *et al*, 2016). As such 2-HGDH acts as a sort of rescue enzyme by converting the unwanted 2HG back to 2KG and simultaneously reducing FAD to FADH. As discussed later the production of 2-ketoglutarate from isocitrate might be hampered due to the precursors for isocitrate being in minute concentrations. Glutamate dehydrogenase (GDH) might also play a role in the insignificant decreased 2-OH-glutarate levels within the KO group. GDH catalyzes the formation of 2-ketoglutarate from glutamate with the subsequent reduction of NAD+ to NADH (Dando *et al*., 2019). Also, this enzyme is capable of catalyzing the reversible reaction, forming glutamate from 2-ketoglutarate with the oxidation of NADH to NAD+ in the presence of an ammonium ion (Moreno-Sánchez *et al*., 2020).

Since the synthesis of 2HG from 2KG is a result of uncontrolled enzymatic conversion, and that 2KG can also be converted to glutamate via GDH, the reaction that would occur more likely would be to that of glutamate production and henceforth replenishing NAD+ levels. All things considered,

this redox ratio elucidates that the imbalance in NAD+ and NADH might not be pronounced in this particular redox ratio and that this redox ratio might not be a target to assess redox status of a particular tissue type.

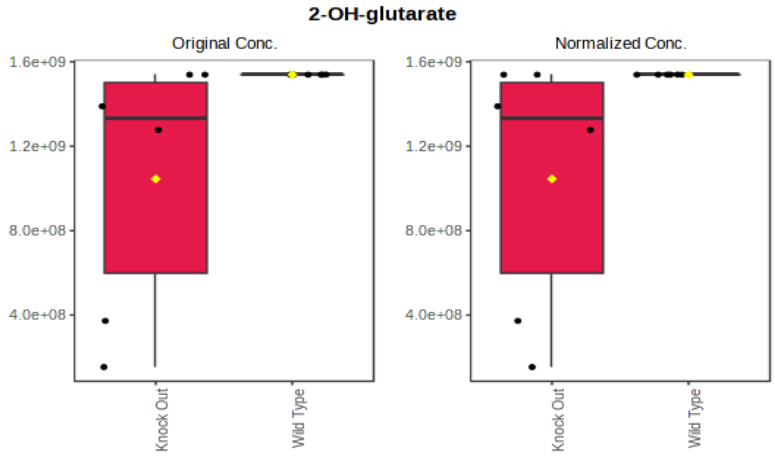

Figure 5.16: Box plots of 2-OH-glutarate measurements in KO and WT mice liver

The effect size of 2-OH-glutarate and Figure 5.16 indicates decreased levels within the KO group compared to the WT group, without being statistically significant. As previously described, 2HG can be produced via the mitochondrial enzyme malate dehydrogenase and can also be converted back to 2KG via 2-OH-glutarate dehydrogenase utilizing FAD+ as coenzyme. As previously described at the 2-OH-glutarate / 2-ketoglutarate ratio, this redox ratio might not be as profoundly affected as others. Also, as theorized, minute 2KG might be available for the synthesis of 2HG to regenerate NAD+ and therefore could be the reason as why 2HG was less pronounced in the KO group.

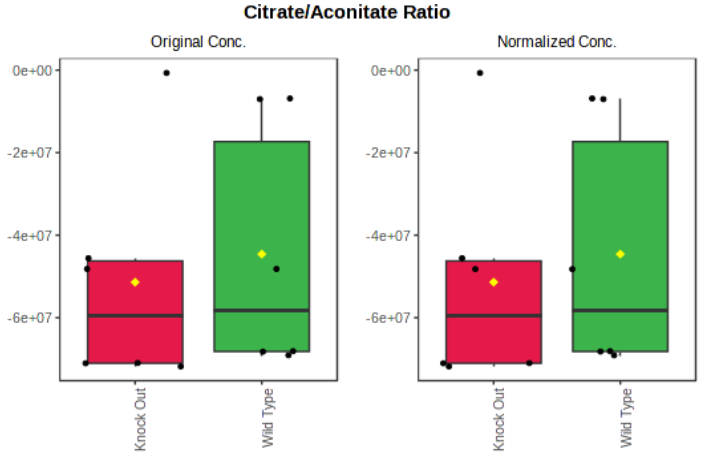

Figure 5.17: Box plots of Citrate / Aconitate ratio measurements in KO and WT mice liver

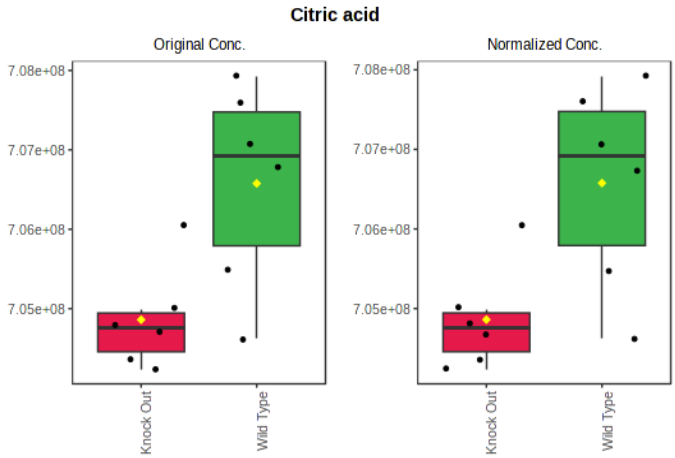

Figure 5.18: Box plots of Citric acid measurements in KO and WT mice liver

The ratio between citrate:aconitate was identified to be slightly decreased in the KO group compared to the WT group as seen in Figure 5.17, which potentially indicate a lower flux of citrate (Figure 5.18) through the TCA. As mentioned earlier, lower concentrations of citrate and isocitrate in the KO mice could play a role in the observed 2HG:2KG ratio. Indeed, citrate concentrations were significantly lower in the KO mice (Figure 5.18) supporting this hypothesis. Several factors could play a role in the lower citrate levels. Firstly, citrate is actively used in the liver for lipogenesis when the animal is in the fed (non-fasting) state. Rerouting citrate to lipogenesis would also lower NADH levels by converting it to NADPH which is required in the process. Furthermore, in the fasting state oxaloacetate is redirected to gluconeogenesis and acetyl-CoA to ketogenesis in the liver, with subsequent lower production of citrate (Gnoni *et al*., 2009). Given the energy crisis experienced in the Ndufs4 KO mice, it stands to reason that the latter two processes could be upregulated. Since the oxidative pathway of the TCA cycle requires NAD+ as coenzyme, the cycle reverses to some extent with pyruvate being converted to oxaloacetate and ultimately malate (discussed in more detail later in this section). Malate is considered an electron carrier which carries cytosolic electrons into the mitochondrion via the malate-aspartate shuttle. When gluconeogenesis is active, malate is rather exported and with it also electrons from the matrix which seems to be a way the liver mitochondria can rid themselves of reducing equivalents. As explained above, the favoured flow of the TCA cycle from pyruvate to malate rather than the more classical one to citrate, could cause a possible decrease in citrate synthesis.

Another possible explanation for the lower flux of citrate to 2KG could be due to increased ROS production within the NDUFS4 KO mice. The aconitase enzyme catalyzes the formation of aconitate from citrate and isocitrate from aconitate and does not require NAD+ as coenzyme for oxidizing equivalents. Conversely, this enzyme contains clusters of iron-sulfur bonds at its catalytic site, and this catalytic site is susceptible to reactive oxygen (ROS) and nitrogen species (RNS). More specifically, mitochondrial ROS and RNS can bind to the active site of aconitase and disrupt the iron-sulphur bonds by a conformational change in the active site causing inactivity of aconitase (Han *et al*., 2005). Moreover, it has been shown that the production of ROS within NDUFS4 KO mice is increased due to a loss of membrane potential across the intermembrane of the mitochondria (Breuer *et al*., 2013).

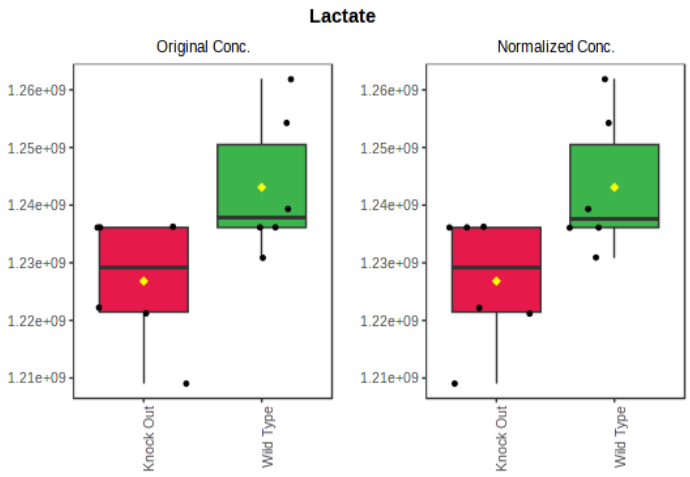

Figure 5.19: Box plots of Lactate measurements in KO and WT mice liver

According to Table 5.17A and Figure 5.19, lactate concentration was surprisingly lower in the KO group compared to the WT group according to the determined effect size (but without being statistically significant). Under aerobic conditions, glucose is metabolized through various enzymatic reactions which ultimately leads to the formation of pyruvate, which enters the TCA cycle via pyruvate dehydrogenase or pyruvate carboxylase. Pyruvate dehydrogenase requires NAD+ as oxidizing constituent for the formation of acetyl-CoA, whereas pyruvate carboxylase requires ATP for the formation of oxaloacetate. Under normal metabolic conditions pyruvate enters the TCA cycle as acetyl-CoA to drive the reductive metabolic pathways of the TCA cycle, whereas in the case of sufficient acetyl-CoA levels, pyruvate is converted to oxaloacetate by pyruvate carboxylase (Sugden & Holness, 2015). The NDUFS4 KO mice suffer from a decreased NAD+/NADH ratio due to impaired function of CI oxidizing NADH back to NAD+. Consequently, this deficiency causes the accumulation of NADH and therefore the depletion of NAD+. Lactate dehydrogenase requires NADH as coenzyme to produce lactate and NAD+ (Vina *et al*., 2016) thus, theoretically lactate should be increased in the KO group but was not. This finding could support the hypothesis that the liver is able to lower reductive stress by exporting electrons via glucose and ketones (specifically 3HBA). It may also be that the KO livers have upregulated the export of lactate to the heart (Dong *et al*., 2021). Another possibility could be the rapid utilization of lactate as gluconeogenic precursor to produce glucose and in conjunction regenerating cytosolic NAD^+.

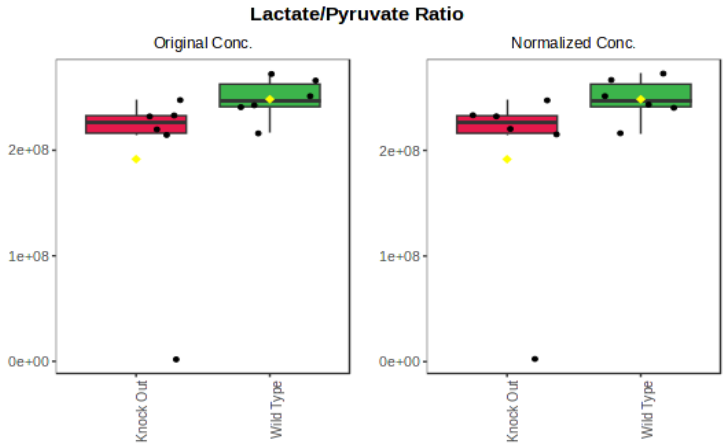

Figure 5.20: Box plots of Lactate / Pyruvate ratio measurements in KO and WT mice liver

Since lactate levels can be influenced by pyruvate levels and not only redox balance (NADH:NAD), it is useful to also investigate the lactate: pyruvate ratio. As shown in Table 5.17B and Figure 5.20, this ratio was also moderately decreased in the KO mice, without being statistically significant. This supports the notion that there is no marked accumulation of cytosolic NADH in the liver. In fact, the slight decrease indicates the opposite. The cytosol contains moderate amounts of NADH produced from glycolysis, while gluconeogenesis produces NAD+ (Blacker & Duchen, 2016). However, it should be noted that a distinguishment between cytosolic and mitochondrial NAD+/NADH ratio could not be made and would require cellular or mitochondrial extracts (Hung *et al*., 2011) for a more accurate redox ratio estimation. Moreso, lactate is one of the most abundant circulating metabolites within mammals due to the constant transport of this metabolite across different organs (Rabinowitz & Enerbäck, 2020) and therefore could cause the misinterpretation on whether the KO have upregulated lactate export or use of lactate in gluconeogenesis.

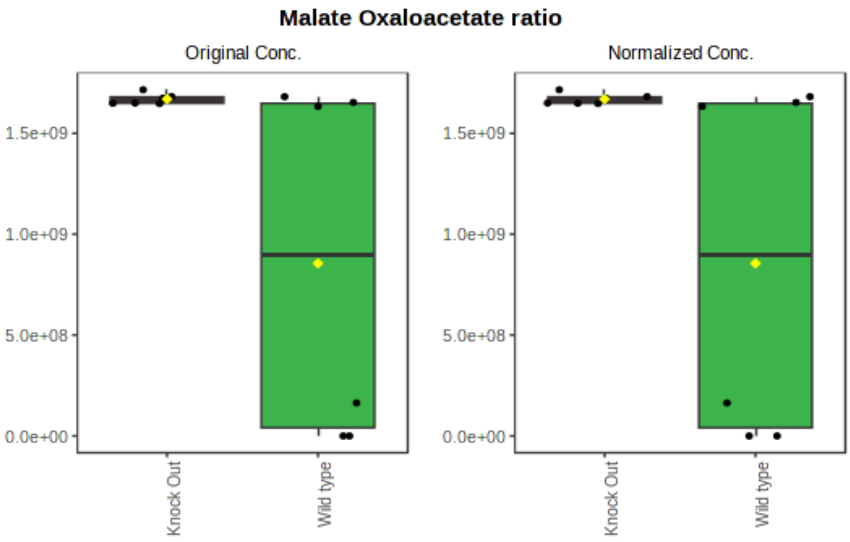

Figure 5.21: Oxaloacetate / Malate ratio measurements in KO and WT mice liver

The malate:oxaloacetate ratio was noticeably higher in the KO mice but not statistically significant. An increase in this ratio suggests the increase of malate against oxaloacetate supporting the hypothesis of upregulated gluconeogenesis in the KO mice. Indeed, malate levels were moderately higher in the KO mice, albeit not statistically significant (Figure 5.21). As explained earlier, pyruvate carboxylase activity could be increased in the KO mice due to the accumulation of acetyl-CoA (from upregulated lipolysis due to the energy crisis), favouring the formation of oxaloacetate from pyruvate. In addition, as oxaloacetate levels increase along with NADH, malate dehydrogenase 2 (MDH2) reverses and produces malate and NAD+ from oxaloacetate and NADH (Todisco *et al*., 2019). Taken together, the malate:oxaloacetate ratio suggests increased levels of NADH and decreased levels of NAD+ within the mitochondria and therefore drives the MDH2 enzyme to catalyze the conversion from oxaloacetate to malate possibly for the replenishment of NAD+ levels and therefore contributing to the increased malate pool.

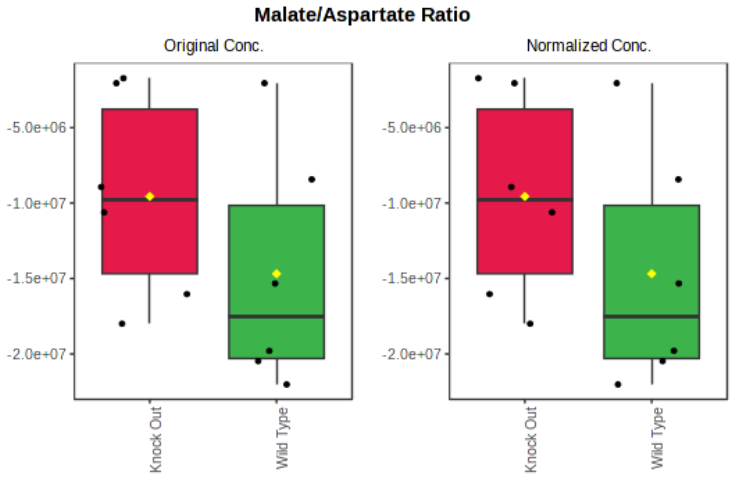

Figure 5.22: Box plots of Malate / Aspartate ratio measurements in KO and WT mice liver

The malate/ L-aspartate redox ratio (Figure 5.22) was not identified to be statistically significant between the two groups however, according to this ratio's effect size it seems to be elevated in the KO group. Oxaloacetate can be converted to L-aspartate via aspartate transaminase whilst requiring the amino group donor glutamate, with the generation of 2-ketoglutarate as a byproduct (Fendt *et al*., 2013). Although this ratio could provide insight into the malate-aspartate shuttle, it is also an indirect measurement of the malate:oxaloacetate ratio. Oxaloacetate is relatively unstable with half the concentration able to decarboxylate within 7 hours after sample collection. Although this process happens for both KO and WT samples in equal measure, we included the above-mentioned ratio as an alternative to the malate:oxaloacetate ratio. In the liver, a relatively large percentage of the oxaloacetate pool is converted to aspartate (which is more stable) due to the functioning of the urea cycle. In other words, aspartate concentration greatly depends on the available oxaloacetate pool which is affected by the redox imbalance (as mentioned above). As expected, this ratio supports the malate:oxaloacetate ratio, albeit with less significance.

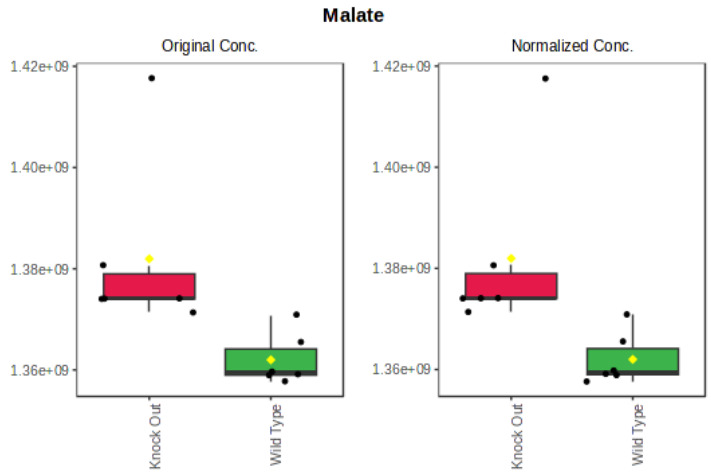

Figure 5.23: Box plots of Malate measurements in KO and WT mice liver

A possible reason for malate (Figure 5.23) not identified as statistically significant, could be due to the export of accumulated malate to the mitochondrial inner membrane. Malate can be exported out of the mitochondrial matrix via the malate-aspartate shuttle (as mentioned earlier) with the subsequent import of 2-ketoglutarate into the mitochondria (Altea-Manzano *et al*., 2022). Inside the inner membrane of the mitochondria, malate can then be converted to oxaloacetate by malate dehydrogenase 2 (MDH2) subsequently reducing NAD+ to NADH. The carbon chain and NADH can then be used to produce glucose via gluconeogenesis. With the export of the synthesized glucose from the hepatocytes, it is in theory also exporting electrons to lower the reductive stress in the liver.

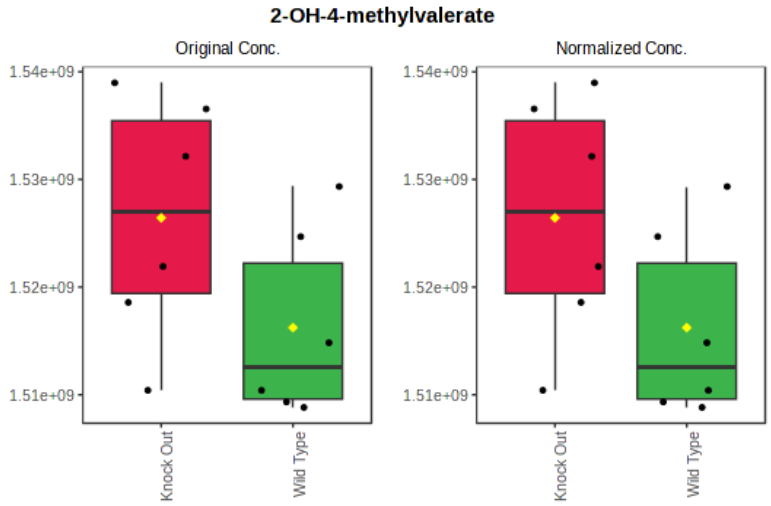

Figure 5.24: Box plots of 2-OH-4-methylvalerate measurements in KO and WT mice liver

According to Table 5.17A**,** 2-OH-4-methylvalerate (Figure 5.24) was identified to be elevated in the KO group without being statistically significant. The origin of this hydroxyacid arises from incomplete leucine catabolism. Leucine can be converted to 2-keto-4-methylvalerate via aminotransferase, whereas this ketoacid might be exported to the liver for further catabolism. Once in the liver, 2-keto-4-methylvalerate can be converted to isovaleryl-CoA through branch-chain ketoacid dehydrogenase (BCKADH) simultaneously reducing NAD+ to NADH (Knerr *et al*., 2012). As mentioned previously, BCKDH requires NAD+ as coenzyme for this conversion, and with the NDUFS4 KO mice suffering from decreased NAD+ levels, this conversion from branch chain ketoacids (BCKA's) to its respective CoA-derivative, might be hampered. With this in mind, accumulation of 2-keto-4-methylvalerate might occur and although this BCKA did not flag to be elevated or statistically significant, it can be reduced to its hydroxyacid. As mentioned earlier, BCKA's can be reduced by a dehydrogenase enzyme utilizing NADH as cofactor, yielding NAD+. It could be that 2-keto-4-methylvalerate was reduced to 2-OH-4-methylvalerate to replenish NAD+ levels to further drive the reductive TCA cycle and glycolysis.

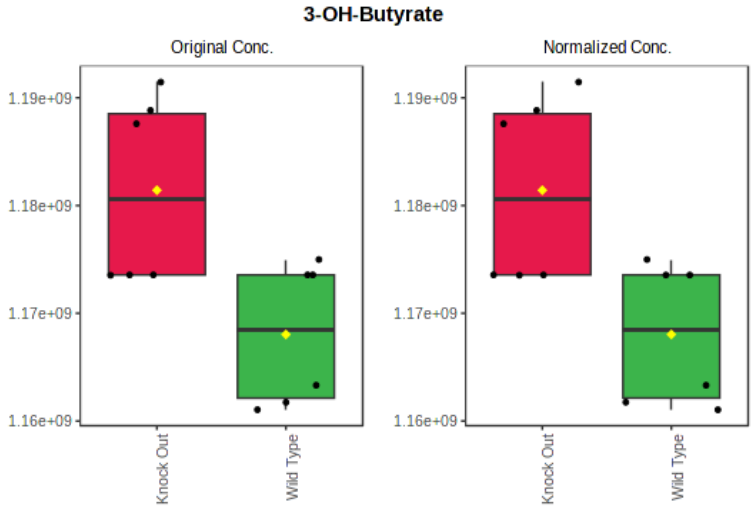

Figure 5.25: Box plots of 3-OH-butyrate measurements in KO and WT mice liver

The ketone body, 3-hydroxybutyrate (Figure 5.25), was identified to be elevated in the KO group according to its effect size without being statistically significant. Ketogenesis revolves around the formation of ketone bodies such as acetoacetate, 3-hydroxybutyrate and acetone and occurs mainly in the liver during glucose deprived conditions (McPherson & McEneny, 2012). These ketone bodies are produced by the liver and exported to other tissues for ketolysis, in which these ketone bodies are broken down by various enzymatic reactions to yield acetyl-CoA which can feed the TCA cycle. Also, seeing that the liver cannot utilize ketone bodies due to a lack of the enzyme succinyl-CoA:3-ketoacid-CoA transferase (SCOT), a key enzyme involved in ketolysis, ketone bodies are exported to other tissue types (McPherson & McEneny, 2012).

One key step involved in ketogenesis, revolves around 3-hydroxybutyrate dehydrogenase, which catalyzes the reversible conversion of acetoacetate to 3HBA and consequently oxidizing NADH to NAD+ (Vina *et al*., 2016). Since NDUFS4 KO mice suffer from decreased NAD+ levels and increased NADH levels, this conversion is favoured in the liver. With the export of 3-OH-butyrate to extrahepatic tissue, the liver is in effect ridding itself of electrons, replenishing NAD+ levels within the mitochondrial matrix, and protecting the mitochondria against reductive stress. A possibility as to why 3-OH-butyrate was not identified to be statistically significant in the KO group, could be due to the export of 3-OH-butyrate to other tissues, since the formation of 3-OH-butyrate from acetoacetate seemed like the most likely metabolic route as per the absence of SCOT to convert acetoacetate to acetoacetyl-CoA. In conjunction, other tissue such as the heart and brain does indeed express SCOT which supports the export of 3-OH-butyrate to the heart and brain (Nagao *et al*., 2016)

5.5.2 Brain Redox Metabolism

Table 5.18A: Statistical results of brain redox metabolites

Compound	p-value	FDR corrected p-value	Effect size	EF degree	HMDB Code
3-OH-butyrate	0,0003	0,0078	3,3771	↑	HMDB0000357
Pyruvate	0,0021	0,0234	2,6819	↑	HMDB0000243
2-keto-3-methylbutyrate	0,1661	0,9461	1,0017	↑	HMDB0000019
2-ketoglutarate	0,2570	0,9461	0,6778	NA	HMDB0000208
2-OH-glutarate	0,3329	0,9461	0,5331	NA	HMDB0000694
2-keto-3-methylvalerate	0,3598	0,946	0,4603	NA	HMDB0000491
Isocitrate	0,3720	0,94619	0,5206	NA	HMDB0000193
3-OH-decanoate	0,3862	0,9461	0,4866	NA	HMDB0002203
2-keto-4-methylvalerate	0,3965	0,9461	0,4579	NA	HMDB0000695
Acetoacetate	0,4300	0,9461	0,4468	NA	HMDB0000060
2-OH-3-methylbutyrate	0,4873	0,9747	0,4498	NA	HMDB0000354
Lactate	0,5881	0,9948	0,3192	NA	HMDB0000190

2-OH-adipic acid	0,6461	0,9948	0,2619	NA	HMDB0000321
2-OH-4-methylvalerate	0,6780	0,9948	0,2327	NA	HMDB0000665
3-OH-isovalerate	0,7258	0,9948	0,1964	NA	HMDB0000754
3-OH-palmitate	0,7883	0,9948	0,1516	NA	HMDB0010734
Oxaloacetate	0,8034	0,9948	0,1554	NA	HMDB0000223
Malate	0,8990	0,9948	0,0695	NA	HMDB0000744
2-ketoadipic acid	0,9174	0,9948	0,0623	NA	HMDB0000225
L-Aspartate	0,9246	0,9948	0,0504	NA	HMDB0000191
Citrate	0,9535	0,9948	0,0337	NA	HMDB0000094
Aconitate	0,9948	0,9948	0,0035	NA	HMDB0000072

Table 5.18B: Statistical results of brain redox ratios

Redox Ratio	p-value	FDR corrected p-value	Effect size	EF degree	HMDB Code
3-OH-butyrate / Acetoacetate	0,0594	0,6534	1,1595	↑	NA
2-OH-3-methylbutyrate / 2-keto-3-methylbutyrate	0,1729	0,8932	0,9562	↓	NA
Isocitrate / 2-ketoglutarate	0,3241	0,8932	0,5811	NA	NA
2-OH-glutarate / 2-ketoglutarate	0,3248	0,8932	0,5430	NA	NA
2-OH-adipic acid / 2-ketoadipic acid	0,5294	0,9491	0,3591	NA	NA
Lactate / Pyruvate ratio	0,5395	0,9491	0,3673	NA	NA
2-OH-4-methylvalerate / 2-keto-4-methylvalerate	0,8272	0,9491	0,0982	NA	NA
Citrate / Isocitrate	0,9327	0,9491	0,0489	NA	NA
Malate / L-Aspartate	0,9738	0,9491	0,0172	NA	NA
Oxaloacetate / Malate	0,9418	0,9491	0,0401	NA	NA
Citrate / Aconitate	0,9491	0,9491	0,0372	NA	NA

As seen in Table 5.18A & B, there were only a total of 3 redox metabolites and 2 redox ratios identified to be statistically significantly affected in the brain of NDUFS4 KO mice. Two redox metabolites were significantly affected, with one compound originating from the TCA cycle and the other, a ketone body. The last redox metabolite differed slightly between the two groups and form through the catabolism of the branch chained amino acid valine.

Two redox ratios were identified to be slightly affected between the KO and WT group. The ketone body ratio was identified to be increased while the ratio of the hydroxy-and BCKA intermediate of valine catabolism was found to be slightly decreased.

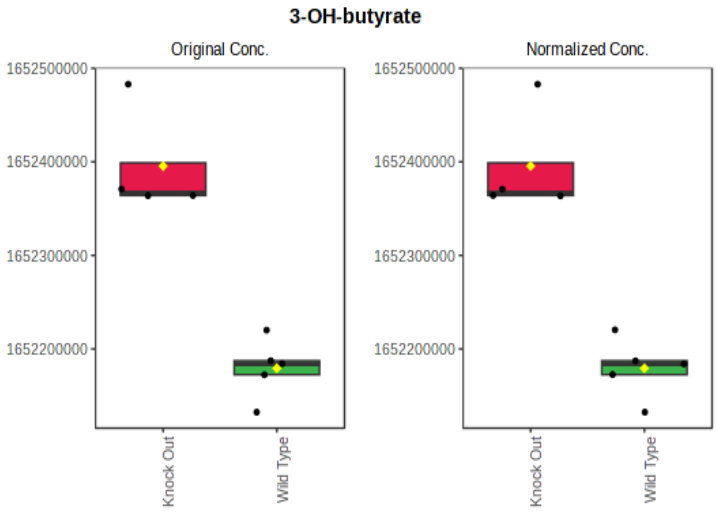

Figure 5.26: Box blots of 3-OH-butyrate measurements in KO and WT mice brain

The elevated 3HBA levels (Table 5.18A, Figure 5.26) in the brain support the view that ketogenesis is upregulated due to the energy crisis as discussed earlier. Ketogenesis occurs primarily in liver cells during glucose deprivation and since the liver lacks a key enzyme involved in ketolysis, ketone bodies are transported to extrahepatic tissue like the brain and heart for energy production. Under normal feeding conditions ketolysis is inactive in the brain, whereas in the case of glucose deprivation and impaired mitochondrial respiration, especially impaired activity of pyruvate dehydrogenase, ketogenic pathways are activated within brain tissue (Yao *et al*., 2010). Ketogenesis yields the major ketone bodies 3-OH-butyrate and acetoacetate and with the consequent export of these ketone bodies from the liver to the brain, the brain oxidizes them to form acetyl-CoA, which feeds into the TCA cycle and other metabolic pathways. For ketolysis to occur in the brain, 3-OH-butyrate should first cross the blood-brain barrier, which is made possible through monocarboxylate transporters (Pierre & Pellerin, 2005). Once inside the brain mitochondria, 3-OH-butyrate is converted to acetoacetate through 3-hydroxybutyrate dehydrogenase with the subsequent reduction of NAD+ to NADH. Acetoacetate is then converted

to acetoacetyl-CoA and succinate via SCOT. Lastly, acetoacetyl-CoA is converted to acetyl-CoA via a thiolase enzyme, whereas acetyl-CoA feeds into the TCA cycle to drive the reductive metabolic conversions (Dilliraj *et al*, 2022). With complex I impaired, the brain's ability to utilize 3HBA is likely restricted because of high NADH levels. This could have contributed to the elevated levels detected in the frontal cortex of KO mice.

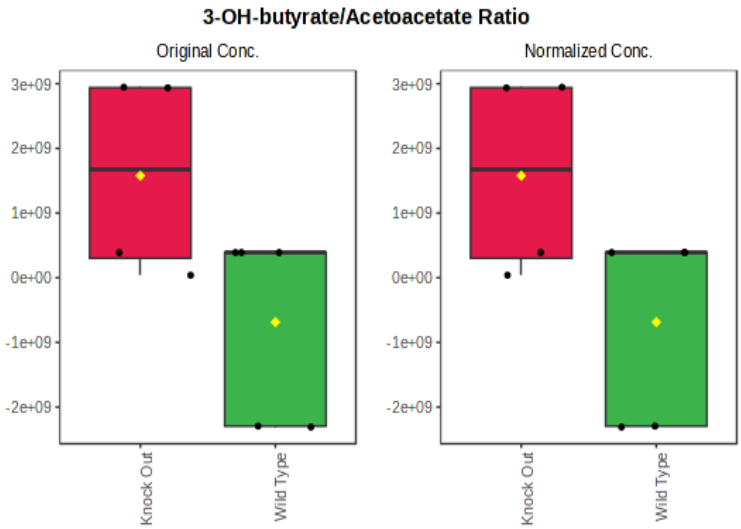

Figure 5.27: Box plots of 3-OH-butyrate / acetoacetate ratio measurements in KO and WT mice brain

The redox ratio, 3-OH-butyrate / Acetoacetate (Figure 5.27), was moderately elevated in the KO group (but not statistically significant) which points towards a redox imbalance within the brain (especially within mitochondria). Unlike lactate dehydrogenase (lactate:pyruate) and malate dehydrogenase (malate:oxaloacetate), 3-hydroxybutyrate dehydrogenase is exclusively found in mitochondria. Hence, the 3-OH-byturate: acetoacetate ratio provides a more accurate view of the redox status inside the mitochondria.

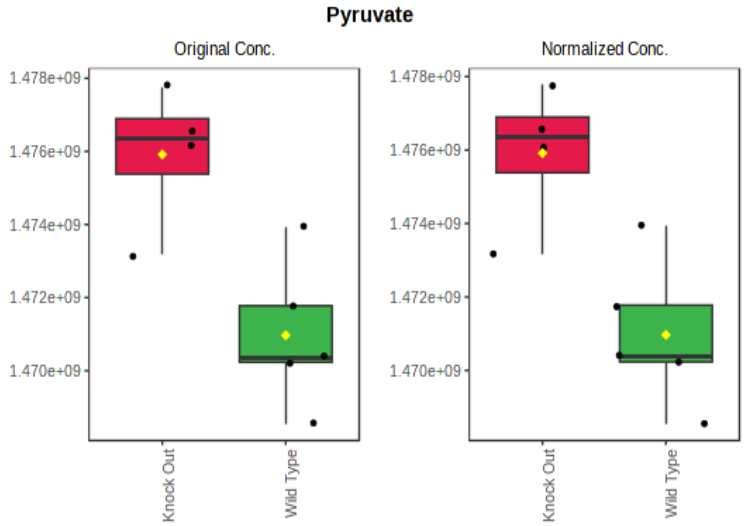

Figure 5.28: Box plots of pyruvate measurements in KO and WT mice brain

As prescribed in Table 5.18A, pyruvate was identified to be elevated in the KO group while being a statistically significant metabolite between the two groups (Figure 5.28). As the neurons of the brain depend mainly on glucose availability for energy production, glucose oxidation occurs rapidly yielding pyruvate as end product, which enters the mitochondria where it is further oxidized through the TCA cycle (Cotter *et al*., 2012). The entry of pyruvate into the TCA cycle can be done through two enzymatic reactions, either through pyruvate dehydrogenase which utilizes NAD+ to form acetyl-CoA and NADH (Yao *et al*., 2010), or through pyruvate decarboxylase, which utilizes ATP and carbon dioxide (CO_2) to produce oxaloacetate (McKenna *et al*., 2016). As mentioned, pyruvate dehydrogenase requires NAD+ as coenzyme, conversely the NDUFS4 KO mice suffer from a decreased NAD+/NADH ratio and as a consequence of this imbalance in the NAD+/NADH redox ratio, pyruvate dehydrogenase activity is impaired causing the accumulation of pyruvate. Pyruvate carboxylase is activated by elevated levels of acetyl-CoA usually produced by ketolysis. However, with increased NADH, this process is also inhibited (along with pyruvate dehydrogenase) which could have contributed to higher pyruvate levels. Moreover, since pyruvate carboxylase requires the hydrolysis of ATP, the energy crisis in KO mice is also making this conversion less likely.

Seeing that the conversion of pyruvate to either acetyl-CoA or to oxaloacetate is hampered, pyruvate is converted to lactate, by lactate dehydrogenase with the simultaneous oxidation of NADH to NAD+ (Valvona *et al*., 2015). Through this action of lactate dehydrogenase, the brain mitochondria can regenerate (cytosolic) NAD+ from the accumulated NADH to keep glycolysis active for substrate level phosphorylation. Taking this into account, theoretically lactate should have then also been identified to be elevated in the KO group however, this was not the case. An explanation to this conundrum could be the exportation of lactate from the brain to the other organs like the liver. The liver is the main metabolic hub for metabolism and can utilize carbon

sources such as lactate and pyruvate for glucose synthesis via gluconeogenesis (Evans & Heather, 2022). In the liver, lactate is converted back to pyruvate requiring the reduction of NAD+ to NADH. Pyruvate then enters various enzymatic conversions, in which one of them is a dehydrogenase enzyme oxidizing NADH to NAD+, and at the end yields glucose. Taking this into account, through the exportation of lactate to the liver, glucose is regenerated via gluconeogenesis, which is then transported back to the brain via a glucose transporter (GLUT) to continue the oxidation of glucose for the high energetic demand of the brain.

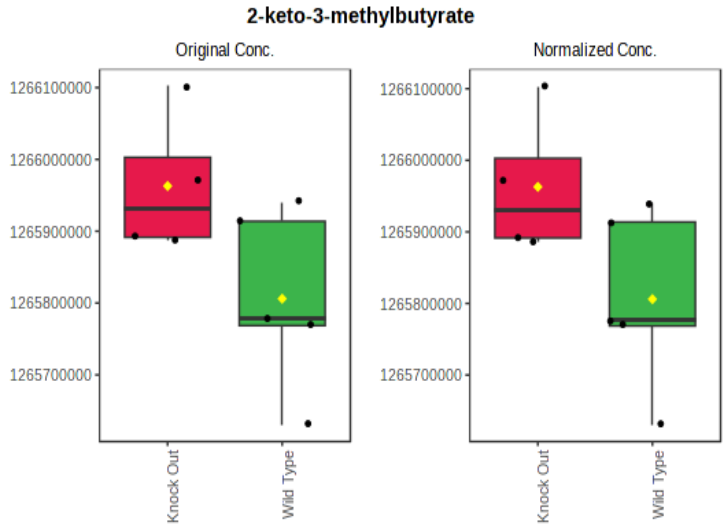

Figure 5.29: Box plots of 2-keto-3-methylbutyrate measurements in KO and WT brain samples

The BCKA produced during valine catabolism, 2-keto-3-methylbutyrate, was identified to be moderately elevated in the KO group (Figure 5.29), without being statistically significant. The catabolism of BCAA's is quite interconnected between different tissue types with the export and import of intermediates to tissues containing the necessary enzymes for the complete catabolism of BCAA's (Sperringer *et al*., 2017). Initially BCAA catabolism can't start in the liver due to the lack of the aminotransferase enzyme, thus valine passes through the liver without being metabolized. Other tissues such as the brain and heart do express the aminotransferase enzyme required for the first enzymatic conversion of valine to 2-keto-3-methylbutyrate. Next, the main site for further catabolism of BCKA's is the liver however, research dating back to the 1970's has found that other tissues such as the brain, heart and skeletal muscle can metabolize these BCKA's via the BCKADH, but at a lower rate (Shinnick & Harper, 1977). Taking this into account, BCAA's are either exported to extrahepatic tissue for the first enzymatic conversion and then exported back to the liver for oxidation or once the BCAA finds itself in extrahepatic tissue, BCAA's are fully metabolized to acetoacetate, acetyl-CoA and propionyl-CoA. Regardless of the of 2-keto-3-methylbutyrate catabolism location, BCKADH requires NAD+ as coenzyme and with the impaired NAD+/NADH redox ratio observed in NDUFS4 KO mice, a possibility exists that the conversion of 2-keto-3-methylbutyrate to isobutyryl-CoA might be impaired. Inhibition of this

conversion causes 2-keto-3-methylbutyrate to be elevated in the KO group compared to the WT group. The other two measured branch chain BCKA's and their respective hydroxyacids showed no difference between the two groups. This might be due to isoleucine and leucine catabolic products (acetyl-CoA and acetoacetate) being in already increased concentrations such as in the case with acetyl-CoA. Valine catabolism ultimately leads to the formation of succinate which feeds into CII, which could be upregulated due to the energy crises and henceforth causes the moderate increase in only the BCKA of valine.

As mentioned above, this BCKA can be exported from the brain to keep the concentration in check. Moreover, 2-keto-3-methylbutyrate can be reduced to 2-hydroxy-3-methylbutyrate, via lactate dehydrogenase or an unknown dehydrogenase enzyme (explained later in this chapter), oxidizing NADH back to NAD+. The ratio of the reduced and oxidized metabolite could thus provide useful insight into the redox status of the frontal cortex. However, the redox ratio 2-OH-3-methylbutyrate / 2-keto-3-methylbtuyrate in the KO group did not significantly differ from the WT mice (Fig 5.30).

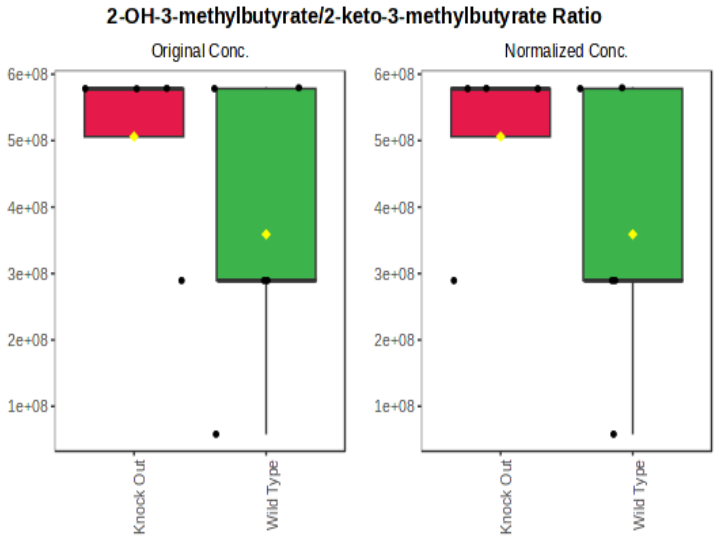

Figure 5.30: Box plots of 2-OH-3-methylbutyrate / 2-keto-3-methylbutyrate ratio measurements in KO and WT mice brain

5.5.3 Heart Redox Metabolism

Table 5.19A: Statistical results of heart redox metabolites

Compound	p-value	FDR corrected p-value	Effect size	EF degree	HMDB Code
3-OH-palmitate	0,00005	0,0012	2,9848	↑	HMDB0010734
3-OH-decanoate	0,0004	0,0052	2,4782	↑	HMDB0002203
3-OH-butyrate	0,0023	0,0173	1,9341	↑	HMDB0000357
Acetoacetate	0,0039	0,0219	1,6995	↑	HMDB0000060
2-keto-3-methylbutyrate	0,0267	0,1178	1,1374	↑	HMDB0000019
L-Aspartate	0,0451	0,1475	0,9553	↑	HMDB0000191
2-OH–4-methylvalerate	0,0469	0,1475	0,9466	↑	HMDB0000665
2-keto-3-methylvalerate	0,0856	0,1973	0,8164	↑	HMDB0000491
Pyruvate	0,0886	0,1973	0,8554	↑	HMDB0000243
Malate	0,0923	0,1973	0,8403	↑	HMDB0000744
Oxaloacetate	0,0986	0,1973	1,0467	↑	HMDB0000223
2-ketoglutarate	0,1135	0,2082	0,8316	↑	HMDB0000208

2-OH-adipic acid	0,1449	0,2452	0,6454	NA	HMDB0000321
2-ketoadipic acid	0,2018	0,3171	0,5642	NA	HMDB0000225
2-OH-gluterate	0,3265	0,4643	0,4613	NA	HMDB0000694
2-keto-4-methylvalerate	0,3376	0,4643	0,4339	NA	HMDB0000695
Citrate	0,3994	0,5168	0,4832	NA	HMDB0000094
Lactate	0,7432	0,9083	0,1716	NA	HMDB0000190
Aconitate	0,8010	0,9275	0,1303	NA	HMDB0000072
Isocitrate	0,8943	0,9647	0,0720	NA	HMDB0000193
3-OH-isovalerate	0,9208	0,9647	0,0461	NA	HMDB0000754
2-OH-3-methylbutyrate	0,9798	0,9798	0,0114	NA	HMDB0000354

Table 5.19B: Statistical results of heart redox ratios

Redox Ratio	p-value	FDR corrected p-value	Effect size	EF degree	HMDB Code
3-OH-butyrate / Acetoacetate	0,00327	0,03599	1,80609	↑	NA
2-OH-3-methylbutyrate / 2-keto-3-methylbutyrate	0,02224	0,12236	1,10844	↓	NA
Malate / L-Aspartate	0,07006	0,25691	0,84709	↓	NA
2-OH-adipic acid / 2-ketoadipic acid	0,24714	0,53923	0,50330	NA	NA
Malate / Oxaloacetate	0,28893	0,53923	0,61784	NA	NA
Citrate / Isocitrate	0,29413	0,53923	0,62669	NA	NA
Citrate / Aconitate	0,41274	0,64859	0,44885	NA	NA
2-OH-4-methylvalerate / 2-keto-4-methylvalerate	0,48072	0,66099	0,31922	NA	NA
Lactate / Pyruvate	0,71441	0,81324	0,19131	NA	NA
Isocitrate / 2-ketoglutarate	0,79566	0,81324	0,12362	NA	NA
2-OH-gluterate / 2-ketoglutarate	0,81324	0,81324	0,11987	NA	NA

Some differences in redox metabolites were identified between the KO and WT group according to t-test and effect size as stipulated in Table 5.19A and B. The most significantly affected metabolites were long and medium chain fatty acids, which were identified to be increased in the KO mice heart tissue. The ketone bodies, acetoacetate and 3-OH-butyrate were also identified to be increased in the KO group, whereas the ratio of the mentioned ketone bodies signified 3-OH-butyrate to be in higher concentration than its oxidized counterpart. All other significantly affected metabolites and ratios belonged to metabolites from the TCA cycle and BCAA catabolic intermediates in which all of these metabolites were found to be increased with the exception of decreased Malate / L-Aspartate ratio and 2-OH-3-methylbutyrate / 2-keto-3-methylbutyrate ratio.

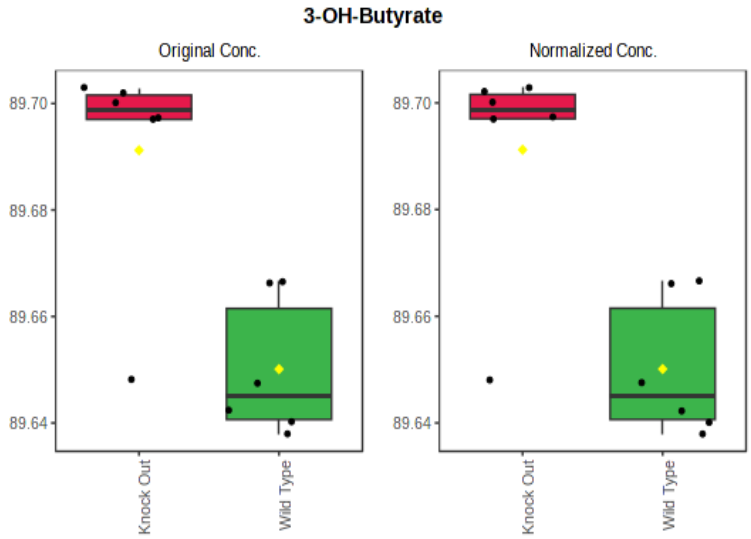

Figure 5.31: Box plots of 3-OH-butyrate measurements in KO and WT mice heart

3-OH-butyrate was quantified to be significantly elevated in the KO group compared to the WT group as seen in Table 5.19A and Figure 5.31. This ketone body can be converted to acetoacetate via 3-hydroxybutyrate dehydrogenase, with subsequent reduction of NAD+ to NADH (Vina *et al.*, 2016). The reverse reaction may also occur during certain metabolic states via the same enzyme, oxidizing NADH back to NAD+. With a CI deficiency such as the case with NDUFS4 KO, NAD+ levels are decreased while NADH accumulates due to ineffective electron transfer at CI. With this in mind, the conversion of 3-OH-butyrate to acetoacetate should be decreased in a NDUFS4 KO model due to the requirement of NAD+ as a cofactor for 3-hydroxybutyrate dehydrogenase. As such, 3-OH-butyrate will accumulate inside the mitochondrial matrix as seen in the KO group. Considering the elevated production and export of 3-OH-butyrate levels produced by the liver, it seems that the heart is unable to utilize this ketone fully. The additional electrons added to acetoacetate to produce 3-OH-butyrate lowers reductive stress in the liver but is shifting the stress to extrahepatic tissue like the brain and heart (also hinted by the ratio discussed later). Comparing

the WT group against the KO group, the 3-OH-butyrate concentration was significantly less in the WT group, indicating that sufficient levels of NAD+ was available for the conversion of 3-OH-butyrate to acetoacetate. Since these two ketone bodies are strictly produced inside the mitochondria, it is evident that the KO group suffered from a decreased mitochondrial NAD+/NADH ratio.

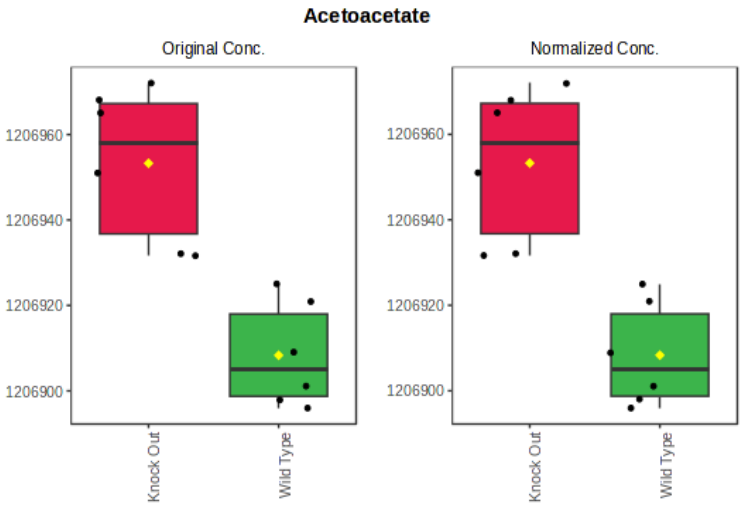

Figure 5.32: Box plots of acetoacetate measurements in KO and WT mice heart

As seen in Table 5.19A, according to the FDR corrected p-value and effect size of acetoacetate, acetoacetate was identified to be increased in the KO group compared to the WT group (Figure 5.32). As previously explained, the liver is solely responsible for ketogenesis with ketolysis occurring in extrahepatic tissue. The accumulated NADH in the KO mice causes less oxidation of 3-OH-butyrate to acetoacetate however, this reaction is still able to take place as per the finding of increased acetoacetate in KO mice hearts. Compared to the brain's findings, the heart received less 3-OH-butyrate from the liver. As per the degree of 3-OH-butyrate import between the brain and heart, the brain seemed to contain more of this ketone body than the heart, which is most likely due to 3-OH-butyrate being a preferred substrate for energy production in the brain (Cunnane *et al*., 2016) while the heart prefers fatty acids as opposed to ketones. Taking this into account with the accumulation of NADH in KO mice, the brain might have not been able to oxidize the ever-increasing amounts of 3-OH-butyrate as per its preferred energy source. As such, the heart was still able to utilize limited amounts of NAD+ to oxidize the accumulating 3-OH-butyrate.

Additionally, it is thought that as a result of respiratory chain deficiencies hampering the TCA cycle, a direct or indirect accumulation of acetyl-CoA can occur within the mitochondria (Jones *et al*., 2021). This accumulation of acetyl-CoA is also described by possible product inhibition of TCA cycle enzymes when NADH levels within the mitochondrial matrix of muscle and cardiac tissue increases, which in turn causes hampering of the TCA cycle and ultimately accumulation of acetyl-

CoA (Ikon & O. Ryan, 2016). Since acetyl-CoA accumulates in the mitochondria, ketolysis might be hampered to an extent due to the already increased 3-OH-butyrate concentrations. The conversion of acetoacetate back to 3-OH-butyrate to regenerate NAD+ might also be hampered due to the increased 3-OH-butyrate concentrations. Also, it is known that fatty acids are the preferred substrate for energy production in the heart (discussed later in this chapter) which catabolic end product is acetyl-CoA. Seeing that acetoacetate catabolism by ketolysis and reduction by 3-OH-butyrate dehydrogenase is hampered, accumulation of acetoacetate could therefore be expected.

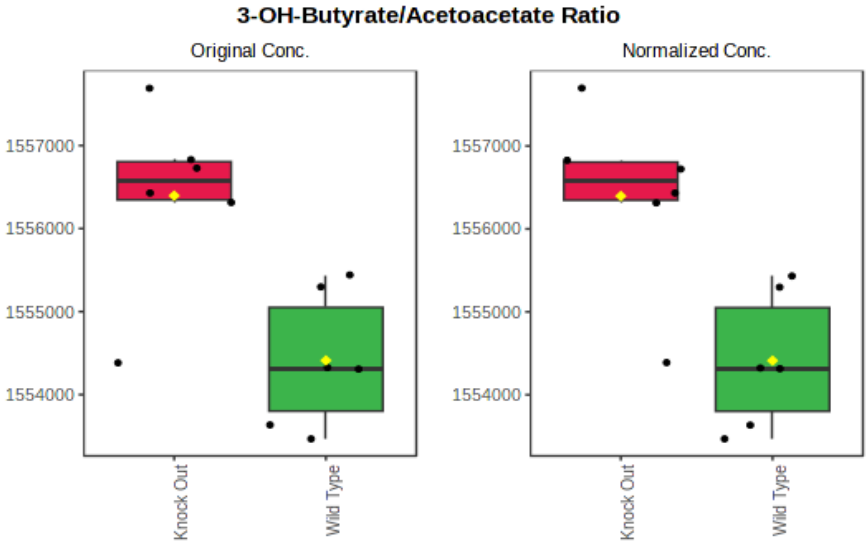

Figure 5.33: Box plots of 3-OH-butyrate / acetoacetate ratio measurements in KO and WT mice heart

Since both 3-OH-butyrate and acetoacetate concentrations were elevated in the heart of the KO mice, one could argue that the energy crisis in these mice is causing overactivation of ketogenesis in the liver and subsequent higher ketone levels in most extrahepatic tissue without redox imbalance playing a role. Fortunately, however, the ratio between 3-OH-butyrate and acetoacetate represented in Figure 5.33, was also significantly higher in the KO mice hearts. This indicates a decreased ratio of NAD+ against NADH, and therefore indicative of NADH accumulation due to the NDUFS4 deficiency in these mice, and the subsequent increased reductive stress within the KO mice heart.

Affected fatty acids

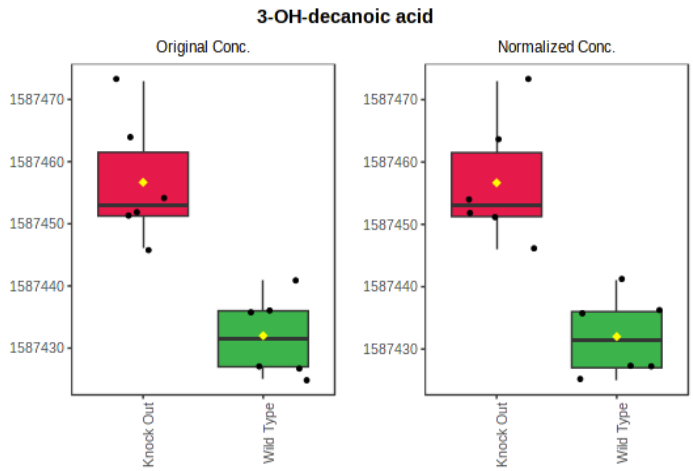

Figure 5.34: Box plots of 3-OH-decanoic acid measurements in KO and WT mice heart

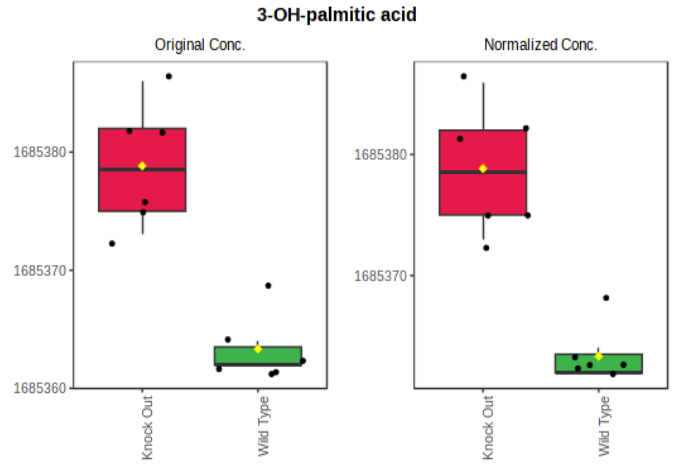

Figure 5.35: Box plots of 3-OH-palmitic acid measurements in KO and WT mice heart

3-OH-decanoate and 3-OH-palmitate (Figure 5.34 & 5.35) were also quantified at significantly higher concentrations in the KO group compared to the WT group, with the effect size of 3-OH-palmitate indicating an increased concentration to a higher degree than 3-OH-decanoate. The catabolism of fatty acids occurs through the β-oxidation of short, medium, and long chain fatty acids inside the mitochondria, providing the cell with an alternative source of energy especially during fasting conditions (Bartlett & Eaton, 2004). The cycle of β-oxidation occurs with 4 enzymatic conversions, which ultimately causes the shortening of the fatty acid with each β-oxidation cycle. Each β-oxidation cycle yields acetyl-CoA, the fatty acid (2 carbons shorter of the original fatty acid) and the reducing constituents NADH and FADH2. The generated fatty acid enters another cycle of β-oxidation whereas acetyl-CoA feeds into the TCA cycle and the reducing constituents to the electron transport chain (Houten & Wanders, 2010). One enzyme in the β-oxidation cycle, 3-hydroxyacyl-CoA dehydrogenase, catalyzes the oxidation of 3-hydroxy fatty acids to 3-keto fatty acids and NAD+ to NADH. Decreased NAD+/NADH ratio observed in a NDUFS4 deficient mice could cause the impaired function of 3-hydroxyacyl-CoA dehydrogenase due to the utilization of NAD+ as cofactor and therefore could cause the accumulation of the hydroxyl versions of the fatty acids. In tissue such as the cardiac muscle, long chain fatty acids are imported into the mitochondria as a leading substrate for β-oxidation to provide the cell with up to 70 % of the generated ATP (Gerber et al., 2006). Additionally, long chain fatty acids are catabolized before medium chain fatty acids by membrane-bound enzymes inside the mitochondria (Houten & Wanders, 2010), yielding medium chain fatty acids after subsequent β-oxidation cycles which enters more rounds of β-oxidation again for the ultimate production of acetyl-CoA.

This is evident as 3-OH-palmitate and 3-OH-decanoate showed accumulation in the KO group compared to the WT group, while according to the statistical power presented Table 5.19A, the

long chain fatty acid 3-OH-palmitate's accumulation surpassed that of 3-OH-decanoate accumulation.

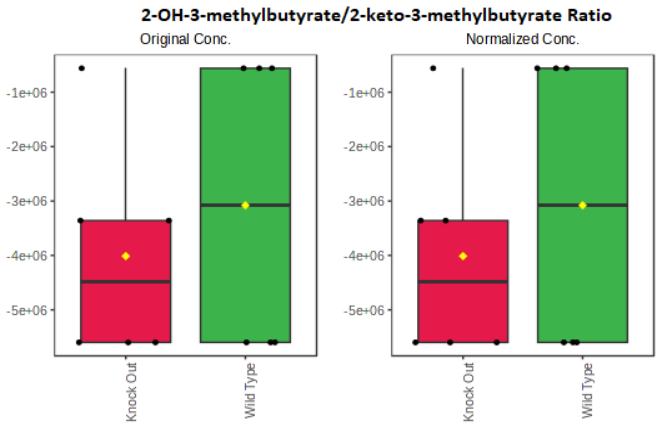

Figure 5.36: Box plots of 2-OH-3-methylbutyrate / 2-keto-3-methylbutyrate ratio measurements in KO and WT mice heart

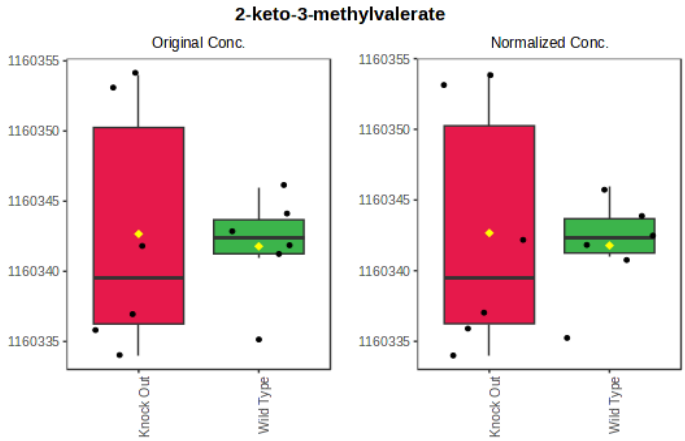

Figure 5.37: Box plots of 2-keto-3-methylvalerate measurements in KO and WT mice heart

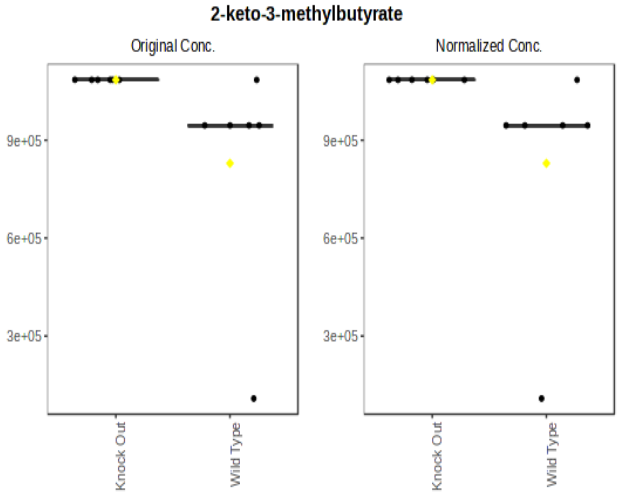

Figure 5.38: Box plots of 2-keto-3-methylbutyrate measurements in KO and WT mice heart

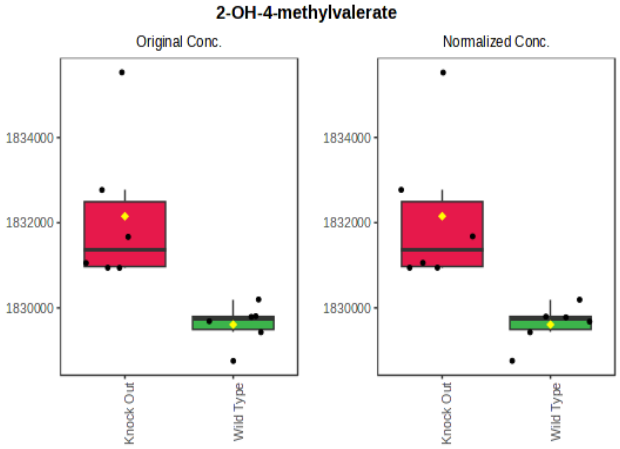

Figure 5.39: Box plots of 2-OH-4-methylvalerate measurements in KO and WT mice heart

As seen through Figures 5.36 - 5.39, two BCKA's were slightly increased in the KO group compared to the WT group. The branched-chain amino acids (BCAA) valine, leucine and isoleucine, are all essential amino acids, meaning that their source comes from the diet of the organism. Moreso, studies have eluded that another source of these BCAA's could come from the gut microbiome (Pedersen *et al.*, 2016., Ridaura *et al.*, 2013) and protein degradation (Sun & Wang, 2016). The first step in BCAA catabolism involves the conversion of valine, leucine and isoleucine to their respective BCKA's, whilst utilizing 2-ketoglutarate as amino acceptor. The BCKA's are then oxidized to their respective acyl-CoA esters through BCKADH with the subsequent reduction of NAD^+ to NADH (Adeva-Andany *et al.*, 2017). Conversely, as prescribed

before the liver has been identified to be a key-player in the oxidation however, it has been elucidated that the heart can also oxidize BCKA's at a high rate. Considering that BCKADH utilizes NAD+ as a cofactor and that NAD+ levels are relatively low in the NDUFS4 KO mice, impaired function of BCKADH could ensue. This is therefore evident as shown by the increased levels of the BCKA's prescribed above.

Seeing that the heart is an organ requiring large amounts of energy for normal cardiac function, the main pathways for energy production in heart tissue are glycolysis, the TCA cycle and β-oxidation (Kolwicz *et al*., 2013). As previously described, a CI deficiency such as in the case of NDUFS4 KO mice, ultimately results in the accumulation of acetyl-CoA and NADH which both cause the allosteric inhibition of pyruvate dehydrogenase. This enzyme is responsible for the conversion of pyruvate to acetyl-CoA and the reduction of NAD+ to NADH, linking the glycolysis pathway with the TCA cycle. In a sense, seeing that a possible metabolic impairment exists at glucose oxidation and β-oxidation of fatty acids, the cardiac muscle of KO mice could undergo a metabolic switch to BCAA's as substrates for energy production to yield propionyl-CoA, acetyl-CoA and acetoacetate (Adeva-Andany *et al*., 2017). This could also explain increased BCKA's observed in the KO mice heart. Apart from just the BCKA's, the hydroxyacid 2-OH-4-methylvalerate displayed increased concentrations in the KO group compared to the WT group. As previously described, the cardiac muscle of the KO mice might have switched to BCAA catabolism for energy production due to the high energy demand of heart tissue. The BCKA 2-keto-4-methylvalerate arises from leucine catabolism and this amino acid with its BCKA are especially toxic to the mitochondria in high concentrations, resulting in a serious altered metabolic state and energy homeostasis (Amaral *et al*., 2010).

The BCKA's and hydroxyacid intermediates have been found to be elevated in patients with Maple Urine Syrup Disease (MSUD), due to the defective BCKDC enzyme catalyzing the second enzymatic conversion of BCAA catabolism (Knerr *et al*., 2012). However, the reduction of BCKA's to their respective hydroxyacids remains a mystery. Various studies have tried to investigate the reduction of the BCKA's to hydroxyacids and most studies have hypothesized that this is either the enzymatic conversion via lactate dehydrogenase or spontaneous reduction (Liebich & Först, 1984., Treacy *et al*., 1992., Knerr *et al*., 2012., Heemskerk *et al*., 2016). Taking this into account, the conversion of 2-keto-4-methylvalerate to 2-OH-4-methylvalerate, due to decreased NAD+ levels within NDUFS4 KO mice, seems likely. This reduction could either be due to lactate dehydrogenase, oxidizing NADH back to NAD+, another unknown dehydrogenase enzyme or spontaneous reduction. Regardless, such a conversion could lower reductive stress and measurement of this ratio could be informative regarding the redox status of the organ and organelle (mitochondria).

Considering the hypothesis that accumulated BCKA's of BCAA catabolism can undergo spontaneous reduction to their respective hydroxyacids, theoretically accumulated 2-keto-3-methylbutyrate should have undergone spontaneous reduction to its hydroxyacid, 2-OH-3-methylbutyrate. Taking this into account, 2-OH-3-methylbutyrate should have accumulated. Consequently, looking at Table 20A 2-OH-3-methylbutyrate did not flag as a perturbed metabolite according to its FDR corrected p-value and effect size, while it's BCKA, 2-keto-3-methylbutyrate did. To that end, we hypothesize that the conversion of BCKA's to their respective hydroxyacids was done by either lactate dehydrogenase or an unknown dehydrogenase enzyme, and not through spontaneous reduction.

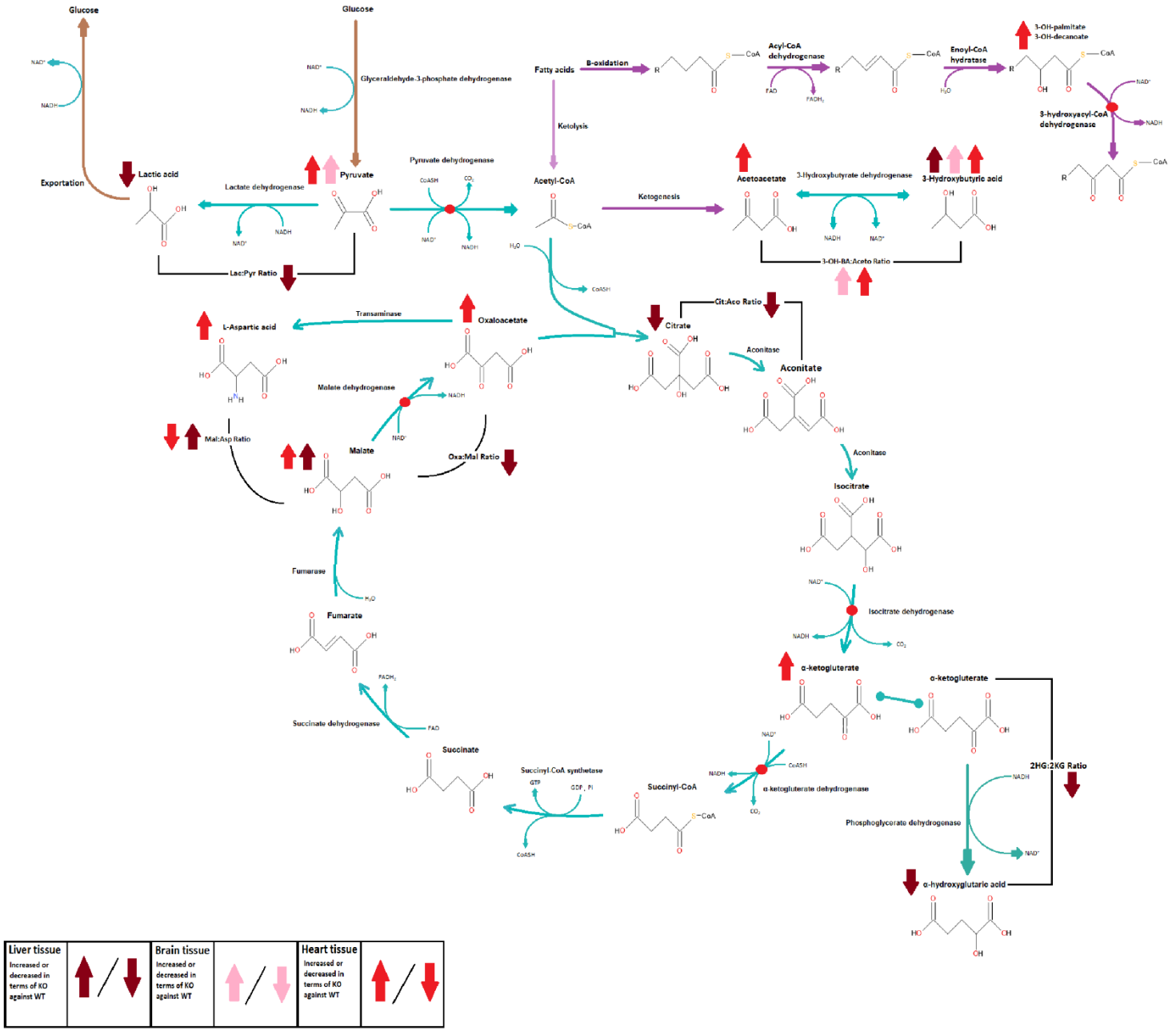

Figure 5.40: Perturbed TCA Cycle redox metabolite differences between NDUFS4 KO and WT mice

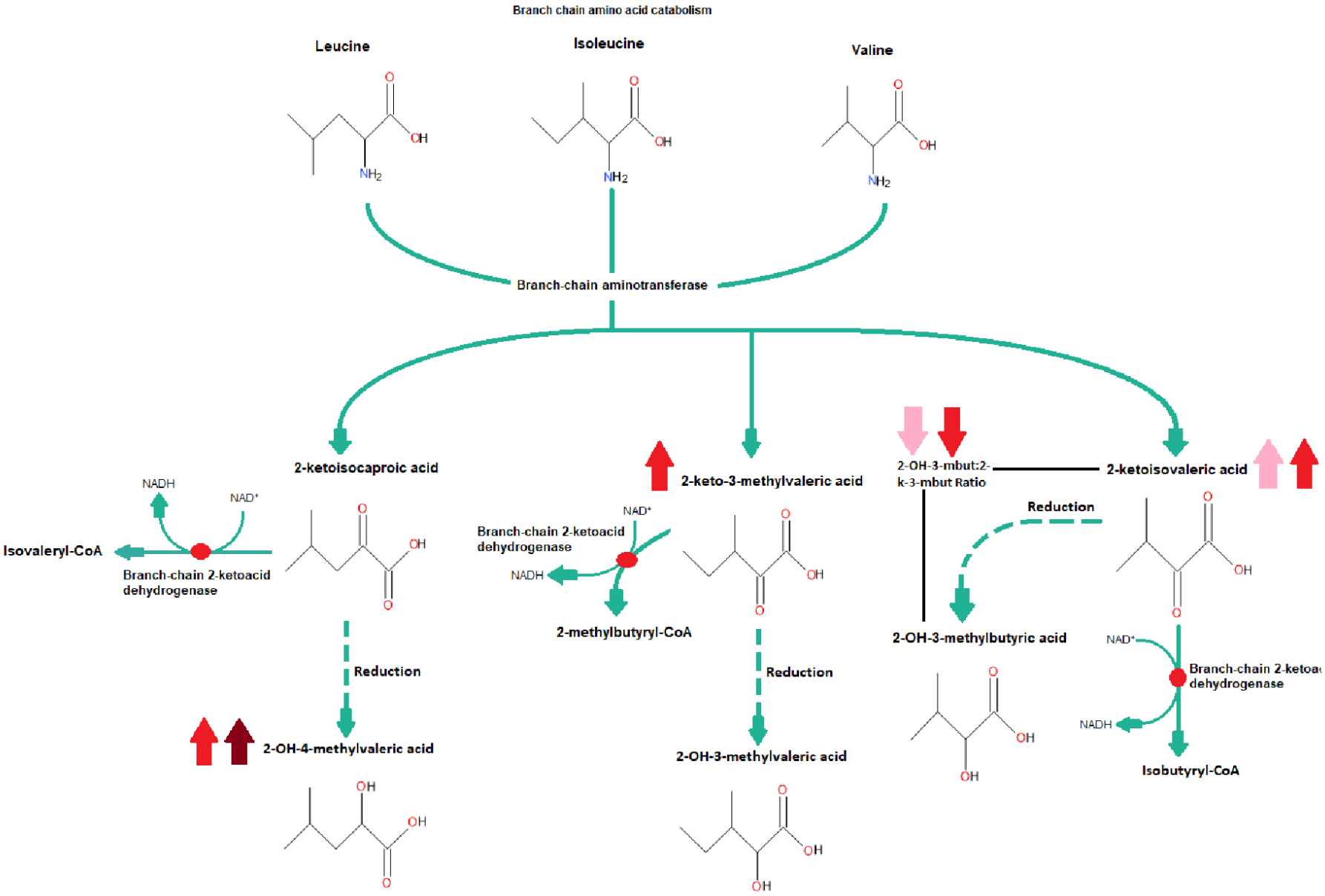

Figure 5.41: Perturbed Branch-chain amino acid redox metabolite differences between NDUFS4 KO and WT mice

5.5.4 Perturbed metabolites as a whole: The bigger picture

Throughout the targeted analysis on liver, brain and heart tissue, various metabolic perturbations were identified as presented in the summarized metabolic diagram Figure 5.40 and Figure 5.41, with little of the same metabolic perturbations seen across all 3 tissue types whilst most redox markers differed between tissue types. The liver is known to be the metabolic hub and more importantly plays an enormous role in the exportation of metabolites to extrahepatic tissue (Rui, 2014). Consequently, intermediates of the TCA cycle such as citrate, aconitate and oxaloacetate were markedly decreased in the KO liver samples while malate exhibited an increase. As for the KO mice's heart, oxaloacetate and malate were found to be slightly increased.

Ketogenesis occurs strictly in the liver to produce the ketone bodies 3HBA and acetoacetate, with 3HBA being the more exportable ketone body throughout various tissues. Ketogenesis is mainly active during the oxidation of fatty acids and produces this alternative energy source to extrahepatic tissue to compensate for "metabolic" starvation in the brain and heart. Through our analysis of KO and WT mice tissue, the accumulation of this ketone body was observed in all the tissues albeit, somewhat less in the liver. Since the brain and heart are unable to undergo ketogenesis, but can become ketogenic, exportation of this alternative energy source to the brain and heart is necessary to keep up with the energetic demand of the brain and heart. As such, to utilize the imported 3-OH-butyrate as energy source, NAD+ is required, which is already diminished in these tissues which in turn resulted in a larger accumulation of 3-OH-butyrate in these two tissues than in the liver. Bringing markers for mitochondrial redox status into account, previous studies usually quantify the lactate / pyruvate ratio to elucidate redox imbalance; however, the quantification of the mitochondrial lactate / pyruvate ratio is no easy feat. Quantification of this ratio is possible but becomes cumbersome to differentiate between the cytosolic and mitochondrial ratio, as lactate is a major circulating metabolite that undergoes constant import and export in and out of various tissues. Our results indicated in most instances that the lactate / pyruvate ratio was decreased in the KO group, whilst insignificant in some tissues, reflecting the constant export, import, utilization of lactate as energy source or precursor to generate metabolites used for energy production. Moreso, the metabolic fate of pyruvate once inside a cell with a CI deficiency could be more directed towards gluconeogenesis to support the cell's energetic demand through the synthesis of glucose and regeneration of NAD+ in the process. Investigating plasma and urinary lactate levels might provide more insight on redox status as per lactate export in the case of accumulating NADH. Pyruvate dehydrogenase (PDH) is regulated by pyruvate dehydrogenase kinase, which phosphorylates PDH when NADH levels are high. Phosphorylation of PDH causes inhibition of PDH and as a consequence promotes the export of lactate into the circulation (Rabinowitz & Enerbäck, 2020), making the plasma and urine excellent targets for the assessment of lactate concentration in the case of respiratory chain

deficiency. In consequence to this, quantification of the lactate / pyruvate ratio with the sole usage of organ tissue might not be able to provide researchers with the full picture and definitive information about the effect of respiratory chain deficiency on mitochondrial redox status.

Of note, studies utilizing measurements of just 3HBA cannot make definitive conclusions of the mitochondrial redox status since 3HBA can solely provide an estimate of cytoplasmic ketones. With that said, using the 3HBA / acetoacetate ratio provides clear information on the oxidative fate of 3HBA as it enters the mitochondria of cells for further catabolism. Including the quantitation of acetoacetate provides one with additional information regarding the mitochondrial NAD+/NADH ratio and therefore could be a much better target for assessing mitochondrial redox status in organs.

An interesting finding was observed at the branched-chain keto and hydroxyacids. In the liver, which is thought to be the main site of BCKA oxidation, only 2-OH-4-methylvalerate was found to be elevated. Entailing that it's BCKA, 2-keto-4-methylvalerate underwent reduction as a result of diminished branched-chain ketoacid dehydrogenase activity, which also occurred in the heart tissue. While in the brain and heart, 2-keto-3-methylbutyrate is depicted to be increased. Moreso, across these two tissue types the 2-OH-3-methylbutyrate / 2-keto-3-methylbutyrate ratio was decreased. The heart also showed increased levels of 2-keto-3-methylvalerate, indicating that across all three tissue types, BCKA's and their respective hydroxyacids accumulated the most in the heart tissue, and in certain cases, the accumulation was more profound. Michael*., et al* (2019) conducted a study to quantify the flux of branched-chain amino acids and their catabolic intermediates through injecting C^{13} labeled BCAA intravenously in mice and assessing the flux and oxidation rate of various tissues. They found that the heart was one of the organs with the highest BCAA oxidation flux, and not the liver. As such, this was also seen when we analysed the flux of the BCKA and their respective hydroxyacids in KO hearts, owing up to that the heart's BCAA oxidation flux is increased and their accumulation occurs as a result of diminished NAD+.

The medium and long chain hydroxy-fatty acids we targeted only accumulated in the heart tissue. The accumulation of these fatty acids in the heart supports the fact that the heart prefers fatty acids as substrates for energy production. Comparing the altered redox metabolites between the liver, brain and heart, the heart seemed to be the most profoundly affected, followed by the liver and lastly the brain. As mentioned previously, the liver acts as a sort of metabolic hub in which hepatic metabolism plays an important role in the regulation of carbon metabolism through various catabolic and anabolic reactions (Morio *et al*., 2021). Since most of these catabolic and anabolic pathways are carried out within mitochondria, the mitochondrial hepatocyte content remains high with estimates at more than a thousand mitochondria per hepatocyte (An *et al*., 2020). The brain is an organ that requires large numbers of ATP for normal cellular function as per the high energetic demands of the central nervous system and neural synaptic terminals (Benaroya H.,

2020). The brain mitochondrial content is roughly around hundreds to thousands of mitochondria per neuron (Rango & Bresolin, 2018), reflecting the energetic requirements for maintaining energy homeostasis in the brain. The heart on the other hand, is one of the organ types in this study that consists of the most mitochondria, with the myocyte mitochondrial content roughly estimating at more than 5000 mitochondria per cardiac cell (Wang *et al*., 2016). This high number of mitochondria reflects the relatively large activity exerted by cardiac cells to maintain heart contraction in instances of exertion or rest. Considering the range of perturbed metabolites and redox ratios in the heart, the energy requirements for the heart seemed to exceed that of the liver and brain. Moreso, the heart might be utilizing some form of communication mechanism in order to release intermediates from the liver, for keeping up with the myocardial energy demand. We hypothesize that as metabolic alterations in redox metabolism occur within the liver, a great amount of these accumulated byproducts of metabolism are released into the circulation (as a response from extrahepatic communication), which consequently provide some form of protection to the liver, ensuring that some form of metabolic normality is attained. As a result of such metabolic intermediate release, the heart and brain import most of these metabolites to try and restore their energy imbalance, discovering in turn the redox imbalance hindering redox metabolism and henceforth redox metabolite accumulation.

The redox pairs of the TCA cycle seemed to be minimally affected by the redox imbalance with the exception of citrate / aconitate, oxaloacetate / malate and malate / L-aspartate in the liver. A decreased citrate / aconitate and oxaloacetate / malate ratios were observed whilst the malate / L-aspartate was increased, indicating a slowing of metabolic conversions further upstream of citrate and aconitate, possibly due to oxaloacetate's participation in the malate / aspartate shuttle. The ratios containing malate indicates an increased shift to malate production (also seen as per the individual increase in malate) via the reverse of malate dehydrogenase activity, possibly due to the fact that malate can be exported out of the mitochondria into the mitochondrial inner membrane via the malate / aspartate transport system, and in turn getting rid of accumulating reducing constituents. As for heart tissue, the decreased malate / l-aspartate ratio indicates less production of malate from l-aspartate (oxaloacetate). Since malate and oxaloacetate were both increased in the heart, a possible reverse of the malate / aspartate transporter system might occur which rather exports l-aspartate which is then converted into oxaloacetate and further reduced to malate for the subsequent oxidation of NADH back to NAD+, and therefore possible replenishing NAD+ levels.

Conclusively, the investigated redox metabolites and their respective pairs gave insights on the flux of reduction / oxidation reactions occurring to regenerate NAD+ from accumulated NADH. Moreso, investigation of certain redox ratios gave an estimate of NAD+ and NADH levels coupled to metabolic pathways and their respective metabolites which ultimately links into mitochondrial

redox status and to which degree the mitochondrial redox balance was affected in three different tissue types.

Comparison to previous untargeted metabolomics studies

Untargeted metabolomics studies usually employ methods and instruments to identify a wide range of metabolites in biofluid or tissue samples. Untargeted studies make use of relative quantification to elucidate metabolic differences between different groups, as such the findings related to redox metabolism needs confirmation through utilizing targeted methods. Previous studies at our institution investigating metabolic differences between NDUFS4 deficient and WT mice, all employed GC-TOFMS analysis (untargeted) and in some cases LC-MS/MS targeted analysis on amino acids and carnitine and its derivatives. The targeted LC-MS/MS method employs internal standard division without running calibration curves adjacent to samples, which also generates relative concentration. Also, untargeted GC-based metabolomics studies at our institution employ BSTFA + trimethylchlorosilane (TMCS) as silylation agent.

By establishing relatively fast and sensitive GC-MS/MS methods adjacent to calibrators, redox markers can be targeted more accurately to confirm the findings of previous studies at our institution. A study conducted by Esterhuizen K, (2018) investigated urine of mitochondrial encephalomyopathy, lactic acidosis and stroke-like episodes (MELAS) patients while another study utilizing selective brain regions (Coetzer J., 2020) found increased pyruvate levels, with these two studies and another (Horak W., 2020) identifying increased urinary lactate. Our results confirmed increased pyruvate levels in brain and heart however, found lactate levels to be decreased in the liver. All the above-mentioned studies also found 2-OH-glutarate to be decreased, which was confirmed by our results and indirectly by the decreased 2-OH-glutarate / 2-ketoglutarate ratio of the analysed mice liver. The increased levels of urinary malate levels found by Horak W., (2020), was also confirmed in our analyses of the heart and liver. A study investigated the skeletal muscle and blood of NDUFS4 KO mice and found increased levels of the hydroxyl forms of fatty acids C16 & C18 (Terburgh *et al*., 2019), which could also tie into our findings of increased 3-OH-palmitate and 3-OH-decanoate in the heart tissue.

In most cases, previous findings could be confirmed however, in some studies investigating urinary metabolic changes, lactate, pyruvate, and malate was found to be increased with decreased levels of 2-OH-adipic acid and the BCAA valine, leucine and isoleucine. Most of the above-mentioned studies did not find the BCAA intermediate keto acids and hydroxy acids to be significantly affected. In our investigation, a ratio of the keto and hydroxyl acid was affected in all three tissue types. Consequently, these ratios could be included in screening procedures for redox imbalance since targeting the keto and hydroxyl acid gives clear information about the direction of flux for BCAA catabolism. Moreso, the ketone body ratio we investigated, 3-OH-

butyrate and acetoacetate, was significantly affected in each tissue type whereas these two ketone bodies were not found to be altered in the above-mentioned studies. This was most probably due to these studies incubating samples at high temperatures during nitrogen drying, which could cause evaporation of these ketone bodies and therefore a major loss of these two important metabolites. In our investigation, these two ketone bodies and their ratio seemed to be a better target for studying mitochondrial redox imbalance than the lactate / pyruvate ratio and therefore we recommend including the ketone body ratio in following studies wanting to elucidate mitochondrial redox status within different tissue types.

CHAPTER 6 - CONCLUSION

6 Study objective summary and future prospects

6.1 Summary of objectives

6.1.1 Phase I: method development

The study initially started with detection of the chosen metabolites linked to redox metabolism, which was all done through analysing analytical standards with a pre-set GC oven temperature gradient. The detection of these metabolites was optimised in the sense of: identifying unique precursor ions which were either the [M-57] ion, characteristic to MTBSTFA derivatization, or another ion unique to the compound. Product ion scans were conducted to identify product ions yielding the best sensitivity, whereas the selected precursor and product ions were used to set up MRM transitions (two transitions per compound). Complete separation of all compounds was achieved through adjusting the initial oven temperature gradient at various time segments. NDUFS4 KO and WT mice tissue (brain, liver and heart) from a previous study was used and underwent a modified two-phase Bligh and Dyer extraction protocol, to identify possible interfering compounds for the setup of dynamic MRM's for each compound. The dynamic MRM's were set up in such a situation that the dwell time for each transition was at least above 50 milliseconds. As such, all compounds were successfully separated and detected with increased sensitivity with little biological interference per transition observed for all the tissue types mentioned. Conclusively, this entailed that the first objective of the study was successfully met.

6.1.2 Phase II: method characterisation

To characterize the developed method, calibration curves had to be set up for each transition in each tissue type, to depict a possible linear curve representing a linear relationship between instrument response and chosen concentration range. To analyze each compound in an increasing concentration range of 0, 100, 250, 500, 750 and a 1000 ng metabolite / mg tissue, each tissue type was stripped of most metabolites via a dialysis tube, suspended in saline water. Following metabolite stripping, each concentration range was spiked with all the compounds, dried through speedvac and resuspended with the respective stripped tissue matrix and finally analysed on the final temperature gradient. Consequently, calibration curves were successfully constructed and the precision and accuracy for quantifying each compound in the mentioned concentration range was determined. Across all tissue types, most compounds exhibited a linear range ranging from 0 - 750 calibration points whilst some had a 0 - 500 linear range. The R^2-value across all tissue types ranged from 0.8931 - 0.9755, for LOD's it was 0.171 - 213.55 (ng/mg),

LOQ's from 5.561 - 560.103 (ng/mg). Moreso, the accuracy of each transition across all tissue types ranged from 71.97 % - 122.51 %, with only one compound per tissue type above or below the 15 % accuracy cut off. The precision determined through % CV indicated the most variation at the 100 calibration point for liver and brain tissue, while the heart tissue had the most variation at 0. With that said, construction of calibration curves in all three tissue types to determine method characterisation parameters were successful.

6.1.3 Phase III: method application

Six brain, heart and liver samples were collected from 6 WT (*Ndufs4*$^{+/+}$) and 6 KO (*Ndufs4*$^{-/-}$) mice at postnatal day 40-45. The harvested tissue was immediately snap-frozen in liquid nitrogen to halt any metabolic activity. Animal (sample) genotype was confirmed with PCR and electrophoresis before metabolic analyses. The established method was successfully applied to quantify redox metabolites in the collected tissue samples with the help of tissue-specific external calibrators. Multiple perturbations in the targeted redox markers were identified in the liver, brain and heart tissue, with perturbations in the brain being much lower than those found in the liver and heart. The heart tissue between mice exhibited the most perturbed redox metabolites as well as the most redox ratio changes between KO and WT mice. As a whole, it seemed that the heart and brain absorbed the available nutrients from the circulation which in this case possibly originated from accumulated redox metabolites in the liver. As per the high energetic needs of the brain and heart tissue, as well as the energetic crises occurring in each tissue type, redox metabolites from the circulation are imported to restore energy homeostasis and support normal cardiac and brain function.

6.2 The main aim of the study

Mitochondrial disorders are rare and usually manifests early in life with a wide spectrum of clinical biomarkers and phenotypical presentations. CI deficiencies of the respiratory chain make up a large percentage of mitochondrial disorders which affects the ratio of NAD+/NADH. As a result of this perturbed redox ratio, enzymatic reactions utilizing either NAD+ or NADH as a co-substrate can cause accumulation of certain metabolic intermediates. Since the direct measurement of NAD+ and NADH within patients is no easy feat, targeting metabolic intermediates of enzyme coupled NAD+/NADH reactions seems to be a much better fit to assess redox status in organs and as such possibly identify new perturbed redox metabolites that can be screened for metabolic disorders relating to respiratory chain deficiencies in patient biofluids.

Untargeted metabolomics studies employ relative quantification of metabolites and studies from our institution, more often than not, identify a wide range of perturbed metabolites with some of

the perturbations linking into redox metabolism (NAD+ / NADH coupled reactions). Some perturbations of redox metabolites from previous studies could be confirmed with our targeted methods, while in some instances different results were obtained from our investigation which is attributed to the difference in biofluid or organ used for investigation. The keto and hydroxyl acids from BCAA catabolism were altered in our investigation which was not previously found to be of significance in studies at our institution. The catabolic reactions of BCAA's reside inside the mitochondria and with the measurement of BCAA intermediates and their ratios, the flux of BCAA catabolism can be elucidated. Through targeting these intermediates coupled to NAD+ / NADH reactions, the mitochondrial redox status can be assessed. Moreso, throughout investigation of these BCAA intermediates, their ratios indicated that reduction of the respective keto-forms to their hydroxyl acids had to occur via enzymatic conversion and not through previously hypothesized spontaneous reduction.

More often than not, untargeted metabolomics studies regarding CI deficiencies find the lactate / pyruvate ratio to be of significance, which only provide researchers with information regarding the cytosolic redox state. Additionally, a definitive conclusion about impaired mitochondrial redox status cannot solely be based on relative quantitation of the lactate / pyruvate ratio, since lactate is a major contributing metabolite to the systemic environment of the cell. The synthesis and catabolism of 3-OH-butyrate and acetoacetate occur strictly inside the mitochondria, and with the accurate measurement of this ketone body ratio, mitochondrial redox status could be elucidated. Through the established method, the ketone bodies 3-OH-butyrate and acetoacetate could be targeted in each tissue type, revealing a decreased mitochondrial NAD+/NADH ratio, which demonstrates mitochondrial redox imbalance in the NDUFS4 deficient mice as a result of a CI deficiency. Lastly, as per the analysis of the three tissue types, the brain seemed to be affected the least except for 3-OH-butyrate, which accumulation was more profound in the brain. The liver seemed to be affected more than the brain, with metabolites native to the TCA cycle or entry points to the TCA cycle being mostly affected. The tissue type which displayed the most redox metabolite differences was the heart. These affected redox metabolites were scattered across the TCA cycle, fatty acid oxidation pathway and the BCAA catabolic pathway, signifying perturbations in the redox status at multiple metabolic pathways.

6.3 Limitations and strengths

Considering the target organs of choice that had to be harvested, possible metabolic variations might occur between previously stored organs and organs harvested long after the first sacrifice. Also, during the thawing process of these organs, enzymatic activity might still occur before sample preparation and extraction, subsequently causing an increase or decrease in one of the targeted redox metabolites. Since the target matrices destined for analysis are quite complex, a

possible microenvironment might exist in homogenised tissue and the tissue pellet during the extraction procedure. As such, a possible trapping of metabolites might occur, making these target compounds unable to dissolve in the extraction solvent. Also, due to the complexity of these organs as target matrix, setting up external calibrators within such a matrix could result in poorer correlation coefficients and high LOD's. Through the metabolome extractions carried out on all three tissue types, a wide range of compound classes are extracted, complicating the creation of blank matrices from biological samples. Commercially available calibrators for specific mouse matrices are rare and although methods exist for stripping biological matrices, they are usually time consuming and require expensive materials. Some of the redox markers measured exhibited variation across the 12 samples, and therefore including more samples per group could have helped keep the observed biological difference between NDUFS4 KO and WT mice to a minimum. With a larger sample size, the calculated standard deviation between the two groups would be smaller and as such the margins of error in such a study would be kept to a minimum. Lastly, for the development of the MRM methods targeting redox markers on the GC-MS/MS, all future troubleshooting of the methods must be carried out on this system due to the lack of available application notes and articles employing the same instrumentation and sample preparation. Also, all MRM transitions developed could not be incorporated into one method without sacrificing significant portion of dwell time for each of the targeted redox markers. Hence the splitting of MRM's into 3 different methods increased analysis time.

GC based metabolomics studies at our institution make use of BSTFA + 1 % TMCS as silylation agent, which requires long periods of incubation at high temperature. This setup exclusively is not well suited for routine analysis due to longer waiting periods, and a risk of losing volatile compounds as a result of high temperature incubation. In contrast, the established GC-MS/MS method makes use of a different silylation agent with minimal incubation time at room temperature, making this method ideal for routine analysis requiring fast turnover times, especially such as in the clinical setting. Moreso, using MTBSTFA + 1 % TBDMCS as derivatization agent, unique precursor and product ions can be selected for the set organic acid MRM transitions, as opposed to the precursor ions generated by BSTFA which in most cases generate non unique fragment ions. Through the establishment of this method, quantification of metabolites linked to redox (NAD+/NADH) metabolism can be made, including the elucidation of mitochondrial redox imbalance as a result of a CI deficiency. With the use of external calibration samples catered to mouse liver, brain and heart matrices, more reproducible data can be acquired to compare to existing findings from similar studies. As mentioned earlier regarding the utilization of biological extraction methods, untargeted metabolomics studies usually employ the same extraction methods for biological samples. These studies make use of detection methods in either an untargeted way or without external calibrators, resulting in relative quantification. Through the development of the methods in this study, redox markers can be quantified with better precision

and therefore reproducibility. With more reproducible data regarding the redox balance in different tissue types, data from studies employing untargeted methods can be aligned with the findings from more targeted methods. Also, this method is able to target and quantify certain redox metabolites that are generally not identified by untargeted means due to too low biological concentrations. As such, this method elucidates more redox metabolites affected by a CI deficiency in different tissue types. Enclosing the list of screenable markers for redox imbalance, some of the compounds measured were affected differently in the liver, brain and heart, while some were not affected at all, and therefore brings to light the best suitable targets for investigating perturbed redox metabolism in different mouse tissues.

6.4 Future prospects

Investigation of the catabolic BCAA intermediates showed promising results regarding the flux of the BCAA keto-acid reduction to the respective BCAA hydroxy-acids. As such, adding each BCAA to the target list of redox markers would allow for assessing whether the reduction reactions are favoured or if the catabolic intermediates are converted back to each BCAA respectively. With these measurements a comprehensive interpretation can be made regarding the breakdown of BCAA's for energy production, the flux of hydroxy and BCKA catabolic intermediates back to their respective BCAA as well as what BCAA has been affected the most as a result of the disturbed NAD^+/NADH ratio. Tying in with BCAA catabolism, the addition of succinate to the target redox list could be useful to assess whether BCAA's are fully metabolized to their respective end products. One BCAA end product, propionyl-CoA, is a precursor to succinate which then ultimately ties in with the formation of $FADH_2$ and electron transfer via the mitochondrial Q-pool for energy production.

As per the prominent findings of the hydroxy-fatty acids targeted in this method, the addition of a short-chain hydroxy-fatty acid to the target list of redox markers would give a thorough estimation of what fatty acid chain length is preferred for energy production through β-oxidation, especially in the heart tissue. Also, the addition of each fatty acid and its keto form to the targeted method, measurements of a keto / hydroxy-fatty acid ratio can be made. As such, short, medium and long-chained fatty acid oxidation and reduction reactions could provide insight on what fatty acid chain length is the most prominently affected due to the decreased NAD^+/NADH ratio.

Apart from adding additional redox metabolites to the target compound list, specific biomarkers of inborn errors of metabolism can also be a great addition. As per the relatively short sample preparation techniques involved, and production of more selective precursor ions after MTBSTFA derivatization, IEM biomarkers can be targeted selectively throughout complex biological matrices and might also be possible in patient biofluids, and therefore could provide clinicians with more reproducible data, possibly owning up to faster diagnosis and treatment.

Considering that the target matrix for this method was three different organs, the addition of biofluids such as urine and blood / plasma would give an overview of redox marker excretion and circulation. Through the measurement of the set redox markers in urine an estimate can be made whether redox markers are being used by organs for energy production or if they have been excreted into the urine. Analysing blood / plasma, could approximate the number of redox markers currently in circulation and henceforth, the ratio of redox markers excreted, in circulation or in organs can be measured to elucidate the overall fate of these markers as a result of a CI deficiency.

Since most redox markers in this targeted method are found in a wide range of organisms, this method can be applied to other model organisms like *C. elegans* and Zebrafish as well as various cell cultures. Moreso, assessment of redox status in humans can also be achieved by utilizing patient biofluids. The only exception to this application would be to re-validate the method on the aforementioned matrices in order to accurately quantify the set redox markers.

BIBLIOGRAPHY

Acree, W.E. & Chickos, J.J.S. Mass Spectra. In NIST Chemistry WebBook, NIST Standard Reference Database Number 69, Eds. P.J. Linstrom and W.G. Mallard, National Institute of Standards and Technology, Gaithersburg MD, 20899. https://doi.org/10.18434/T4D303

Adeva-Andany, M. et al. 2017. Enzymes involved in branched-chain amino acid metabolism in humans. *Amino Acids*, 49(1):1005-1015. https://doi.org/10.1007/s00726-017-2412-7

Adiels, M. et al. 2010. Optimization of N-methylN-[tert-butyldimethylsilyl]-trifluoroacetamide as derivatization agent for determining isotopic enrichment of glycerol in very-low density lipoproteins. *Rapid Communications in Mass Spectrometry*, 24(1):586-592. https://doi.org/10.1002/rcm.4422

Adina-Zada, A., Zeczycki, T.N. & Attwood, P.V. 2012. Regulation of the structure and activity of pyruvate carboxylase by acetyl CoA. *Archives of Biochemistry and Biophysics*, 519(2):118-124. https://doi.org/10.1016/j.abb.2011.11.015

Agin, A., Heintz, D., Ruhland, E., Chao de la Barca, J.M., Zumsteg, J., Moal, V., Namer, I.J. 2016. Metabolomics – an overview. From basic principles to potential biomarkers (part 1). *Médecine Nucléaire*, 40(1):4-10. https://doi.org/10.1016/j.mednuc.2015.12.006

Agledal, L., Niere, M. & Ziegler, M. 2010. The phosphate makes a difference: Cellular functions of NADPH. *Redox Repor*t, 15(1):2-10. https://doi.org/10.1179/174329210X12650506623122

Ahn, C.S. & Metallo, C.M. 2015. Mitochondria as biosynthetic factories for cancer proliferation. *Cancer & metabolism*, 3(1):1-10. https://doi.org/10.1186/s40170-015-0128-2

Akram, M. 2014. Citric Acid Cycle and Role of its Intermediates in Metabolism. *Cell Biochemistry and Biophysics*, 68(1):475-477. https://doi.org/10.1007/s12013-013-9750-1

Allard, P. et al. 2004. Newborn screening for hepatorenal tyrosinemia by tandem mass spectrometry: analysis of succinylacetone extracted from dried blood spots. *Clinical Biochemistry*, 37(11):1010-1013. https://doi.org/10.1016/j.clinbiochem.2004.07.006

Altea-Manzano, P. et al. 2020. Reversal of mitochondrial malate dehydrogenase 2 enables anaplerosis via redox rescue in respiration-deficient cells. *Molecular Cell*, 82(23):4537-4544. https://doi.org/10.1016/j.molcel.2022.10.005

Amaral, A.U. et al. 2010. α-Ketoisocaproic acid and leucine provoke mitochondrial bioenergetic dysfunction in rat brain. *Brain Research*, 1324(1):75-82. https://doi.org/10.1016/j.brainres.2010.02.018

An, P. et al. 2020. Hepatocyte mitochondria-derived danger signals directly activate hepatic stellate cells and drive progression of liver fibrosis. *Nature Communications*, 11(2362):1-2. https://doi.org/10.1038/s41467-020-16092-0

Baertling, F., Rodenburg, R.J., Schaper, J., Smeitink, J.A., Koopman, W.J., Mayatepek, E., Distelmaier, F. 2014. A guide to diagnosis and treatment of leigh syndrome. *Journal of Neurology, Neurosurgery & Psychiatry*, 85(3):257-265. https://doi.org/10.1136/jnnp-2012-304426

Bakare, A.B., Rao, R.R. & Lyer, S. 2021. Cell-Permeable Succinate Increases Mitochondrial Membrane Potential and Glycolysis in Leigh Syndrome Patient Fibroblasts. *Cell*, 9(10):2-8. https://doi.org/10.3390/cells10092255

Barlett, K. & Eaton, S. 2004. Mitochondrial beta-oxidation. *European Journal of Biochemistry*, 271(3):462-468. https://doi.org/10.1046/j.1432-1033.2003.03947.x

Baumgartner, M.R. et al. 2014. Proposed guidelines for the diagnosis and management of methylmalonic and propionic acid acidemia. *Orphanet Journal of Rare Disease*, 9(1):35-38. https://doi.org/10.1186/s13023-014-0130-8

Beale, D.J., Pinu, F.R., Kouremenos, K.A., Poojary, M.M., Narayana, V.K., Boughton, B.A., Dias, D.A. 2018. Review of recent developments in GC-MS approaches to metabolomics-based research. *Metabolomics*, 14(1):152-158. https://doi.org/10.1007/s11306-018-1449-2

Becker, J. et al. 2015. Top value platform chemicals: bio-based production of organic acids. *Biotechnology*, 36(1):168-172. https://doi.org/10.1016/j.copbio.2015.08.022

Benard, G. et al. 2007. Mitochondrial bioenergetics and structural network organization. *Journal of Cell Science*, 120(1):838-843. https://doi.org/10.1242/jcs.03381

Benaroya, H. 2020. Brain energetics, mitochondria, and traumatic brain injury. *Reviews in Neurosciences*, 31(4):1-23. https://doi.org/10.1515/revneuro-2019-0086

Beskan, U., Yildirim, S.T. & Yapar, E.A. 2020. An overview of analytical method validation. *Universal Journal of Pharmaceutical Research*, 5(1):47-51. DOI:10.22270/ujpr.v5i1.362

Bilan, D.S. & Belousov, V.V. 2016. Genetically encoded probes for NAD+/NADH monitoring. *Free Radical Biology and Medicine*, 100(1):32-42. https://doi.org/10.1016/j.freeradbiomed.2016.06.018

Blacker, T.S. & Duchen, M.R. 2016. Investigating mitochondrial redox state using NADH and NADPH autofluorescence. *Free Radical Biology and Medicine*, 100(1):53-58. https://doi.org/10.1016/j.freeradbiomed.2016.08.010

Bligh, E.G. & Dyer, W.J. 1959. A rapid method of total lipid extraction and purification. *Canadian Journal of Biochemistry and Physiology*, 37(8):911-917. https://doi.org/10.1139/o59-099

Breuer, M.E. et al. 2013. Cellular and animal models for mitochondrial complex I deficiency: a focus on the NDUFS4 subunit. *IUBMB Life*, 25(1):202-206. https://doi.org/10.1002/iub.1127

Brooks G.A. 2018. The science and translation of lactate shuttle theory. *Cell Metabolism*, 27(1):757-764. https://doi.org/10.1016/j.cmet.2018.03.008

Cantó, C., Menzies, K.J. & Auwerx, J. 2015. Nad+ metabolism and the control of energy homeostasis: A balancing act between mitochondria and the nucleus. *Cell metabolism*, 22(1):31-53. https://doi.org/10.1016/j.cmet.2015.05.023

Caprioli, G., Nzekoue, F.K., Giusti, F., Vittori, S. & Sagratini, G. 2018. Optimization of an extraction method for the simultaneous quantification of sixteen polyphenols in thirty-one pulse samples by using HPLC-MS/MS dynamic-MRM triple quadrupole. *Food chemistry*, 266(2):490-497. https://doi.org/10.1016/j.foodchem.2018.06.049

Castelli, F.A., Rosati, G., Moguet, C., Fuentes, C., Marrugo-Ramírez, J., Lefebvre, T., Fenaille, F. 2021. Metabolomics for personalized medicine: The input of analytical chemistry from biomarker discovery to point-of-care tests. *Analytical and Bioanalytical Chemistry*, 12(1):1-31. https://doi.org/10.1007/s00216-021-03586-z

Chakrapani, A., Gissen, P. & McKiernan, P. 2022. Disorders of Tyrosine Metabolism. *Inborn Metabolic Diseases*, Springer, Berlin, Heidelberg. https://doi.org/10.1007/978-3-662-63123-2_17

Chernushevich, I.V., Loboda, A.V. and Thomson, B.A. 2001. An introduction to quadrupole-time-of-flight mass spectrometry. *Journal of Mass Spectrometry*, 36(1):849-852. 10.1002/jms.207

Chinnery, P.F. & Hudson, G. 2013. Mitochondrial genetics. *British medical bulletin*, 106(1)135-159. https://doi.org/10.1093/bmb/ldt017

Chinopoulos, C. 2020. Acute sources of mitochondrial NAD+ during respiratory chain dysfunction. *Experimental neurology*, 327(1):113-218. https://doi.org/10.1016/j.expneurol.2020.113218

Christou, C., Gika, H.G., Raikos, N. & Theodoridis, G. 2014. GC-MS analysis of organic acids in human urine in clinical settings: A study of derivatization and other analytical parameters. *Journal of Chromatography B*, 964(1):195-201. https://doi.org/10.1016/j.jchromb.2013.12.038

Coetzer, J. 2020. *A metabolomics and biochemical investigation of selected brain regions from Ndufs4 knockout mice*. Potchefstroom: North-West University. (Dissertation – MSc).

Colvin, H. et al. 2016. Oncometabolite D-2-hydroxyglutarate directly induces epithelial-mesenchymal transition and is associated with distant metastasis in colorectal cancer. *Scientific Reports*, 6(1):1-4. https://doi.org/10.1038/srep36289

Corkey, B.E. & Deeney, J.T. 2020. The Redox CommunincationNetwork as a Regulator of Metabolism. *Frontiers in Physiology*, 11(1):1-6. https://doi.org/10.3389/fphys.2020.567796

Cotter, D.G. et al. 2012. Successful adaptation to ketosis by mice with tissue-specific deficiency of ketone body oxidation. *American Physiological Society Journal*, 17(1):336-338. https://doi.org/10.1152/ajpendo.00547.2012

Cunnane, S.C. et al. 2016. Can Ketones Help Rescue Brain Fuel supply in Later Life? Implications for Cognitive Health during Aging and the Treatment of Alzheimer's Disease. *Frotiers in Molecular Neuroscience*, 53(9):1-2. https://doi.org/10.3389/fnmol.2016.00053

Dando, I. et al. 2019. Oncometabolites in cancer aggressiveness and tumour repopulation. *Biological Reviews*, 94(1):1531-1536. https://doi.org/10.1111/brv.12513

De Haas, R. et al. 2017. Therapeutic effects of the mitochondrial ROS-redox modulator KH176 in a mammalian model of Leigh Disease. *Scientific Reports*, 7(1):1-8. https://doi.org/10.1038/s41598-017-09417-5

De Jesús, V.R., Adam, B.W., Mandel, D., Cuthbert, C.D. & Matern, D. 2014. Succinylacetone as primary marker to detect tyrosinemia type i in newborns and its measurement by newborn screening programs. *Molecular genetics and metabolism*, 113(1-2):67-75. https://doi.org/10.1016/j.ymgme.2014.07.010

DeBalsi, K.L., Hoff, K.E. & Copeland, W.C. 2017. Role of the mitochondrial DNA replication machinery in mitochondrial DNA mutagenesis, aging and age-related diseases. *Ageing research reviews*, 33(1):89-104. https://doi.org/10.1016/j.arr.2016.04.006

Detmer, S.A. & Chan, D.C. 2007. Functions and dysfunctions of mitochondrial dynamics. *Nature Reviews*, 8(12):871-875. https://doi.org/10.1038/nrm2275

Dettmer-Wilde, K. & Engewald, W. 2014. Practical gas chromatography. A Comprehensive Reference. *Springe*r, 902(1):1-4.

Dilliraj, L.N. et al. 2022. The Evolution of Ketosis: Potential Impact Clinical Conditions. *Nutrients*, 14(1):3613-3618. https://doi.org/10.3390/nu14173613

DiMauro, S. & Davidzon, G. 2005. Mitochondrial DNA and disease. *Annals of medicine*, 37(3):222-232. https://doi.org/10.1080/07853890510007368

Dong, S. et al. 2021. Lactate and Myocardiac Energy Metabolism. *Frontiers in Physiology*. 12(1):1-6. https://doi.org/10.3389/fphys.2021.715081

Elamin, M., Ruskin, D.N., Masino, S.A. & Sacchetti, P. 2017. Ketone-based metabolic therapy: Is increased NAD+ a primary mechanism? *Frontiers in molecular neuroscience*, 10(1):37. https://doi.org/10.3389/fnmol.2017.00377

Erdem, E., Cayonu, N., Uysalol, E. & Yildirmak, Z.Y. 2010. Chronic intermittent form of isovaleric acidemia mimicking diabetic ketoacidosis. *Journal of Pediatric Endocrinology & Metabolism*, 23(1):503-504. https://doi.org/10.1515/jpem.2010.082

Esterhuizen, K. 2018. *A metabolomics investigation of selected m.3243A>G mutation phenotypes*. Potchefstroom: North-West University. (Thesis – PhD).

Evans, R.D. & Heather, L.C. 2020. Human metabolism: pathways and clinical aspects. *Surgery*, 40(4):219-222. https://doi.org/10.1016/j.mpsur.2022.01.004

Fancy, S. & Rumpel, K. 2008. GC-MS-Based Metabolomics. *Biomarker Methods in Drug Discovery and Development*, 1(1):317-325.

Fendt, S.M. et al. 2013. Reductive glutamine metabolism is a function of the α-ketoglutarate to citrate ratio in cells. *Nature Communications*, 4(3):2236-2239. https://doi.org/10.1038/ncomms3236

Filee, R., Schoos, R. & Boemer, F. 2013. Evaluation of physiological amino acids profiling by tandem mass spectrometry. *Springer*, 13(1):119-128. https://doi.org/10.1007/8904_2013_265

Gerards, M., Sallevelt, S.C.E.H & Smeets, H.J.M. 2015. Leigh syndrome: Resolving the clinical and genetic heterogeneity paves the way for treatment options. *Molecular Genetics and Metabolism*, 117(3):2-10. https://doi.org/10.1016/j.ymgme.2015.12.004

Gerber, L.K., Aronow, B.J. & Matlib, M.A. 2006. Activation of a novel long-chain free fatty acid generation and export system in mitochondria of diabetic rat hearts. American Journal of *Physiology Cell Physiology*, 291(1):1198-1205. https://doi.org/10.1152/ajpcell.00246.2006

Glancy, B. & Balaban, R.S. 2012. Role of mitochondrial Ca^{2+} in the regulation of cellular energetics. *Biochemistry*, 51(14):2959-2973. https://doi.org/10.1021/bi2018909

Glancy, B. et al. 2021. Mitochondrial lactate metabolism: history and implications for exercise and disease. *Journal of Physiology*, 599(1):863-888. https://doi.org/10.1113/JP278930

Gnoni, G.V. et al. 2009. The Mitochondrial Citrate Carrier: Metabolic role and Regulation of its Activity and expression. *IUBMB Life*, 61(10):987-990. https://doi.org/10.1002/iub.249

Goldberg, I. Rokem, J.S. & Pines, O. 2006. Organic acids: old metabolites, new themes. *Journal of Chemical Technology and Biotechnology*, 81(10):1601-1603. https://doi.org/10.1002/jctb.1590

Goulet-Pelletier J. & Cousineau, D. 2018. A review of effect sizes and their confidence intervals, Part I: The Cohen's *d* family. *The Quantitative Methods for Psychology*, 14(4):242-259. 10.20982/tqmp.14.4.p242

Gowda, G. & Djukovic, D. 2014. Overview of mass spectrometry-based metabolomics: Opportunities and challenges. *Mass Spectrometry in Metabolomics*, 12(1):3-12.

Grange, R.M.H. et al. 2021. Hypoxia ameliorates brain hyperoxia and NAD+ deficiency in a murine model of Leigh syndrome. *Molecular Genetics and Metabolism*, 133(1):84-88. https://doi.org/10.1016/j.ymgme.2021.03.005

Griffiths, W.J. & Wang, Y. 2009. Mass spectrometry: from proteomics to metabolomics and lipidomics. *Royal Society of Chemistry*, 38(1):1882-1887.

Gullberg, J. et al. 2004. Design of experiments: and efficient strategy to identify factors influencing extraction and derivatizaiton of *Arabidopis thaliana* samples in metabolomics studies with gas chromatography/mass spectrometry. *Analytical Biochemistry*, 331(1):283-293. https://doi.org/10.1016/j.ab.2004.04.037

Gunnar, T. Ariniemi, K. & Lillsunde, P. 2005 Determination of 14 benzodiazepines and hydroxy metabolites, zaleplon and zolpidem as *tert*-butyldimethylsilyl derivatives compared with other common silylating reagents in whole blood by gas chromatography-mass spectrometry. *Journal of Chromatography B*, 818(2):223-225. https://doi.org/10.1016/j.jchromb.2004.12.032

Han, D. et al. 2005. Sites and Mechanisms of Aconitase Inactivation by Peroxynitrite: Modulation by Citrate and Glutathione. *Biochemistry*, 44(36):11987-11990. https://doi.org/10.1021/bi0509393

Handy, D.E. & Loscalzo, J. 2017. Responses to reductive stress in the cardiovascular system. *Free Radical Biology and Medicine*, 109:114-124. https://doi.org/10.1016/j.freeradbiomed.2016.12.006

Heemskerk, M.M. et al. 2016. Reanalysis of mGWAS results and in vitro validation show that lactate dehydrogenase interacts with branched-chain amino acid metabolism. *European Journal of Human Genetics*, 24(1):142-145. https://doi.org/10.1038/ejhg.2015.106

Ho, H. et al. 2017. Nicotinamide nucleotide transhydrogenase (nnt) deficiency dysregulates mitochondrial retrograde signaling and impedes proliferation. *Redox biology*, 12:916-928. https://doi.org/10.1016/j.redox.2017.04.035

Hoffmann, F.G. & Feyh, P. 2003. Organic Acid Analysis. Physician's Guide to the Laboratory Diagnosis of Metabolic Disease. *Springer*, 2(1):56-76. 10.1007/978-3-642-55878-8

Horak, W. 2020. *Urinary metabolomics investigation of Ndufs4 knockout mice*. Potchefstroom: North-West University. (Dissertation – MSc).

Houten, S.M. & Wanders, J.A. 2010. A general introduction to the biochemistry of mitochondrial fatty acid β-oxidation. *Journal of Inherited Mitochondrial Disease*, 1(2):469-476. https://doi.org/10.1007/s10545-010-9061-2

Houtkooper, R.H., Cantó, C., Wanders, R.J. & Auwerx, J. 2010. The secret life of NAD+: An old metabolite controlling new metabolic signaling pathways. *Endocrine reviews*, 31(2):194-223. https://doi.org/10.1210/er.2009-0026

Hsieh, J. et al. 2019. Functional Roles of Metabolic Intermediates in Regulating the Human Mitochondrial NAD(P)+-Dependent Malic Enzyme. *Scientific Reports*, 9(1):1-11. https://doi.org/10.1038/s41598-019-45282-0

Hung, Y.P. et al. 2011. Imaging Cytosolic NADH-NAD+ Redox State with a Genetically Encoded Fluorescent Biosensor. *Cell Metabolism*, 14(3):545-547. https://doi.org/10.1016/j.cmet.2011.08.012

Ikon, N. & Ryan. R.O. 2016. On the origin of 3-methylglutaconic acid in disorders of mitochondrial energy metabolism. *Journal of Inherited Metabolic Diseases*, 39(1):749-751. https://doi.org/10.1007/s10545-016-9933-1

Intlekofer, A.M. et al. 2015. Hypoxia induces production of L-2-hydroxyglutarate. *Cell Metabolism*, 22(1):304-308. https://doi.org/10.1016/j.cmet.2015.06.023

Irwin, M.H., Parameshwaran, K. & Pinkert, C.A. 2013. Mouse models of mitochondrial Complex I deficiency. *The International Journal of Biochemistry & Cell Biology*, 45(1):34-37. https://doi.org/10.1016/j.biocel.2012.08.009

Jarukas, L. et al. 2020. Investigation of Organic Acids in Saffrons Stigmas (Crocus sativus L.) Extract by Derivatization Method and Determination by GC/MS. Molecules, 25(1):3426-3428. https://doi.org/10.3390/molecules25153427

Jones, D.E., Klacking, E. & Ryan, R.O. 2021. Inborn errors of metabolism associated with 3-methylglutaconic aciduria. *Clinica Chimica Acta*, 522(1):96-101. https://doi.org/10.1016/j.cca.2021.08.016

Jones, P.M. & Bennett, M.J. 2010. Urine Organic Acid Analysis for Inherited Metabolic Disease Using Gas Chromatography-Mass Spectrometry. *Clinical Applications of Mass Spectrometry*, 603(1):423-426.

Katsyuba, E. et al. 2020. NAD^+ homeostasis in health and disease. *Nature Metabolism*, 2(1):1-3. https://doi.org/10.1038/s42255-019-0161-5

Knerr, I. et al. 2012. Advances and challenges in the treatment of branched-chain amino/keto acid metabolic defects. *Journal of Inherited Metabolic Disease*, 35(1):29-36. https://doi.org/10.1007/s10545-010-9269-1

Koek, M.M., Jellema, R.H., van der Greef, J., Tas, A.C. & Hankemeier, T. 2011. Quantitative metabolomics based on gas chromatography mass spectrometry: *Status and perspectives. Metabolomics*, 7(3):307-328. https://doi.org/10.1007/s11306-010-0254-3

Kohler, I., Verhoeven, A., Derks, R.J. & Giera, M. 2016. Analytical pitfalls and challenges in clinical metabolomics. *Bioanalysis*, 8(14):1509-1532. https://doi.org/10.4155/bio-2016-0090

Kolwicz Jr, S.C., Purohit, S. & Tian, R. 2013. Cardiac Metabolism and its Interactions with Contraction, Growth, and Survival of Cardiomyoctes. *Circulation Research*, 113(5):1-5. https://doi.org/10.1161/CIRCRESAHA.113.302095

Konieczka, P. 2007. The Role of and the Place of Method Validation in the Quality Assurance and Quality Control (QA/QC) system. *Critical Reviews in Analytical Chemistry*, 37(3):173-187. https://doi.org/10.1080/10408340701244649

Koopman, W.J., Distelmaier, F., Smeitink, J.A. & Willems, P.H. 2013. Oxphos mutations and neurodegeneration. *The EMBO journal*, 32(1):9-29. https://doi.org/10.1038/emboj.2012.300

Koopman, W.J., Willems, P.H. & Smeitink, J.A. 2012. Monogenic mitochondrial disorders. *New England Journal of Medicine*, 366(12):1132-1141. 10.1056/NEJMra1012478

Kruse, S.E. et al. 2008. Mice with mitochondrial complex I deficiency develop a fatal encephalomyopathy. *Cellular Metabolism*, 7(1):312-318. 10.1016/j.cmet.2008.02.004

Kvitvang, H.F., Andreassen, T., Adam, T., Villas-Bôas, S.G. & Bruheim, P. 2011. Highly sensitive GC/MS/MS method for quantitation of amino and nonamino organic acids. Analytical chemistry, 83(7):2705-2711.Lim, A.Z. & R. McFarland. 2019. Leigh Syndrome. *Diagnosis and Management of Mitochondrial Disorders*, 1181(1):151-160. https://doi.org/10.1021/ac103245b

Lake, N.J., Bird, M.J., Isohanni, P. & Paetau, A. 2015. Leigh syndrome: Neuropathology and pathogenesis. *Journal of Neuropathology & Experimental Neurology*, 74(6):482-492. https://doi.org/10.1097/NEN.0000000000000195

Leshinsky-Silver, E. et al. 2009. NDUFS4 mutations cause Leigh syndrome with predominant brainstem involvement. Molecular *Genetics Metabolism*, 97(1):185-187. https://doi.org/10.1016/j.ymgme.2009.03.002

Leong D.W. et al. (2012). Proteomic and metabolomics analyses of mitochondrial complex-I deficient mouse model generated by spontaneous B2 short interspersed nuclear element (SINE) insertion into NADH dehydrogenase (ubiquinone) Fe-S protein 4 (Ndufs4) gene. *Journal of Biological Chemistry*, 287(24):20652-20661. https://doi.org/10.1074/jbc.M111.327601

Li, Y., Ruan, Q., Li, Y., Ye, G., Lu, X., Lin, X., & Xu, G. 2012. A novel approach to transforming a non-targeted metabolic profiling method to a pseudo-targeted method using the retention time locking gas chromatography/mass spectrometry-selected ions monitoring. *Journal of Chromatography A*, 1255(1):228-236. https://doi.org/10.1016/j.chroma.2012.01.076

Liebich, H. & Först. 1984. Hydroxycarboxylic and oxocarboxylic acids in urine: Products from branched-chain amino acid degradation and from ketogenesis. *Journal of Chromatography A*, 309(1):225-230. https://doi.org/10.1016/0378-4347(84)80031-6

Lim, A.Z. & McFarland, R. 2019. Leigh syndrome. In. Diagnosis and management of mitochondrial disorders: *Springe*r, 1(4):151-167.

Marshall, D.D. & Powers, R. 2017. Beyond the paradigm: Combining mass spectrometry and nuclear magnetic resonance for metabolomics. *Progress in nuclear magnetic resonance spectroscopy*, 100(1):1-16. https://doi.org/10.1016/j.pnmrs.2017.01.001

Martínez-Reyes, I. & Chandel, N.S. 2020. Mitochondrial TCA metabolites control physiology and disease. *Nature communications*, 11(102):1-8. https://doi.org/10.1038/s41467-019-13668-3

Matuszczyk, J.C., Teleki, A., Pfizenmaier, J. & Takors, R. 2015. Compartment-specific metabolomics for CHO reveals that ATP pools in mitochondria are much lower than in cytosol. *Biotechnology Journal*, 10(10):1639-1650. https://doi.org/10.1002/biot.201500060

McCommis, K.S. & Finck, B.N. 2015. Mitochondrial pyruvate transport: a historical perspective and future research directions. *Biochemical Journal*, 466(3):443-450. https://doi.org/10.1042/BJ20141171

McKenna, M.C. et al. 2016. Glutamate oxidation in astrocytes: Roles of glutamate dehydrogenase and aminotransferases. *Journal of Neuroscience Research*, 94(12):1561-1566. https://doi.org/10.1002/jnr.23908

McKenna, M.C., Waagepetersen, H.S., Schousboe, A. & Sonnewald, U. 2006. Neuronal and astrocytic shuttle mechanisms for cytosolic-mitochondrial transfer of reducing equivalents: Current evidence and pharmacological tools. *Biochemical pharmacology*, 71(4):399-407. https://doi.org/10.1016/j.bcp.2005.10.011

McPherson, P.A.C. & McEneny, J. 2012. The biochemistry of ketogenesis and its role in weight management, neurological disease and oxidative stress. *Journal of physiology and biochemistry*, 68(1):141-151. https://doi.org/10.1007/s13105-011-0112-4

Michael, D. et al. 2019. Quantitative Analysis of the Whole-Body Metabolic Fate of Branched-Chan Amino Acids. *Cell Metabolism*, 29(1):417-427. https://doi.org/10.1016/j.cmet.2018.10.013

Mirnaghi, F.S. & Caudy, A.A. 2014. Chalenges of analyzing different classes of metabolites by a single analytical method. *Bioanalysis*, 6(24):3393-3399. https://doi.org/10.4155/bio.14.236

Morava, E. et al. 2006. Mitochondrial disease criteria. *Neurology*, 67(1):1823. https://doi.org/10.1212/01.wnl.0000244435.27645.54

Moreno-Sánchez, R. et al. 2020. Physiological Role of Glutamate Dehydrogenase in Cancer Cells. *Frontiers in Oncology*, 10(1):1-14. https://doi.org/10.3389/fonc.2020.00429

Morio, B., Panthu, B., Bassot, A., Rieusset, J. 2020. Role of mitochondria in liver metabolic health and diseases. *Cell Calcium*, 94(1):1-7. https://doi.org/10.1016/j.ceca.2020.102336

Mullen, A.R. et al. 2014. Oxidation of alpha-ketoglutarate is required for reductive carboxylation in cancer cells with mitochondrial defects. *Cell Respiration*, 7(2):1679-1690. https://doi.org/10.1016/j.celrep.2014.04.037

Nagao, M. et al. 2016. β-hydroxybutyrate elevation as a compensatory response against oxidative stress in cardiomyocytes. *Biochemical and Biophysical Research Communications*, 475(1):322-326. https://doi.org/10.1016/j.bbrc.2016.05.097

Neinast, M., Murashige, D. & Arany, Z. 2019. Branched Chain Amino Acids. *Annual Reviews*, 81(1):139-154. https://doi.org/10.1146/annurev-physiol-020518-114455

Nel, D. 2022. *Investigating the adaptive mitochondrial shuttles and metabolic reprogramming of transporters in complex I (Ndufs4) knock out mice.* Potchefstroom: North-West University. (Dissertation – MSc).

Newgard, C.B. 2017. Metabolomics and Metabolic Disease: Where Do We Stand? *Cell Metabolism*, 25(1):43-46. https://doi.org/10.1016/j.cmet.2016.09.018

Ohie, T. et al. 2000. Gas chromatography-mass spectrometry with *tert*.-butyldimethylsilyl derivatization: use of the simplified sample preparations and the automated data system to screen for organic acidemias. *Journal of Chromatography B*, 746(1):63-72. https://doi.org/10.1016/S0378-4347(00)00105-5

Ortigoza-Escobar, J.D. et al. 2016. Ndufs4 related Leigh syndrome: a case report and review of the literature. *Mitochondrion*, 28(1):73-75. https://doi.org/10.1016/j.mito.2016.04.001

Pang, Z. et al. 2021. MetaboAnalyst 5.0: narrowing the gap between raw spectra and functional insights. *Nucleic Acids Research*, 49(1):388-394. https://doi.org/10.1093/nar/gkab382

Patel, D.P. et al. 2017. Metabolic profiling by gas chromatography-mass spectrometry of energy metabolism in high-fat diet-fed obese mice. *Plos One*, 12(5):1-13. https://doi.org/10.1371/journal.pone.0177953

P. Benit, J. Steffann, S. Lebon, D. Chretien, N. Kadhom, P. de Lonlay, A. Goldenberg, Y. Dumez, M. Dommergues, P. Rustin, A. Munnich, A. Rotig. 2003. Genotyping microsatellite DNA markers at putative disease loci in inbred/multiplex families with respiratory chain complex I deficiency allows rapid identification of a novel nonsense mutation (IVS1nt-1) in the NDUFS4 gene in Leigh syndrome, *Human Genetics*, 112(1):563-566. https://doi.org/10.1007/s00439-002-0884-2

Pedersen, H.K. et al. 2016. Human gut microbes impact host serum metabolome and insulin sensitivity. *Nature*, 535(4):376-380. https://doi.org/10.1038/nature18646

Pierre, K. & Pellerin, L. 2005. Monocarboxylate transporters in the central nervous system: distribution, regulation and function. *Journal of Neurochemistry*, 94(1):1-9. https://doi.org/10.1111/j.1471-4159.2005.03168.x

Rabinowitz, J.D. & Enerbäck, S. 2020. Lactate: the ugly duckling of energy metabolism. *Nature Metabolism*, 2(1):566-570. https://doi.org/10.1038/s42255-020-0243-4

Rango, M & Bresolin, N. 2018. Brain Mitochondria, Aging, and Parkinson's Disease. *Genes*, 9(5):1-8. https://doi.org/10.3390/genes9050250

Reinecke, C.J. et al. 2012. Metabolomics of urinary organic acids in respiratory chain deficiencies in children. *Metabolomics*, 8(1):264-275. https://doi.org/10.1007/s11306-011-0309-0

Ridaura, V.K. et al. 2013. Gut microbiota from twins discordant for obesity modulate metabolism in mice. *Science*, 341(1):124-129. DOI: 10.1126/science.1241214

Ronchi, J.A., Francisco, A., Passos, L.A.C., Figueira, T.R. & Castilho, R.F. 2016. The contribution of nicotinamide nucleotide transhydrogenase to peroxide detoxification is dependent on the respiratory state and counterbalanced by other sources of NADPH in liver mitochondria. *Journal of Biological Chemistry*, 291(38):20173-20187. https://doi.org/10.1074/jbc.M116.730473

Rudaz, S. Feinberg, M. 2018. From method validation to result assessment: Established facts and pending questions. *Trends in Analytical Chemistry*, 105(1):68-73. https://doi.org/10.1016/j.trac.2018.04.013

Rui, L. 2014. Energy Metabolism in the Liver. *Comprehensive Physiology*, 4(1):1-20. 10.1002/cphy.c130024

Ruta, J., Rudaz, S., McCalley, D.V., Veuthey, J.-L. & Guillarme, D. 2010. A systematic investigation of the effect of sample diluent on peak shape in hydrophilic interaction liquid chromatography. *Journal of chromatography A*, 1217(52):8230-8240. https://doi.org/10.1016/j.chroma.2010.10.106

Rydström, J. 2006. Mitochondrial NADPH, transhydrogenase and disease. *Biochimica et Biophysica Acta (BBA)-Bioenergetics*, 1757(5-6):721-726. https://doi.org/10.1016/j.bbabio.2006.03.010

Sandlers, Y. 2017. The future perspective: Metabolomics in laboratory medicine for inborn errors of metabolism. *Translational Research*, 189:65-75. https://doi.org/10.1016/j.trsl.2017.06.005

Saneto, R.P. & Sedensky, M.M. 2013. Mitochondrial disease in childhood: Mtdna encoded. *Neurotherapeutics*, 10(2):199-211. https://doi.org/10.1007/s13311-012-0167-0

Scheffler, I.E. 2015. Mitochondrial disease associated with complex I (NADH-oxidoreductase) deficiency. *Journal of Inherited Metabolic Diseases*, 1(38):406-411. https://doi.org/10.1007/s10545-014-9768-6

Schieber, M. & Chandel, N.S. 2014. Ros function in redox signalling and oxidative stress. *Current biology*, 24(10):453-462. https://doi.org/10.1016/j.cub.2014.03.034

Schubert Baldo, M. & Vilarinho, L. 2020. Molecular basis of leigh syndrome: A current look. *Orphanet journal of rare diseases*, 15(1):1-14. https://doi.org/10.1186/s13023-020-1297-9

Shinnick, F. & Harper, A.E. 1977. Effects of Branched-chain Amino acid Antagonism in the Rat on Tissue Amino Acid and Keto Acid Concentrations. *The Journal of Nutrition*, 107(5):887-890. https://doi.org/10.1093/jn/107.5.887

Shrivastava, A. & Gupta, V.B. 2011. Methods for the determination of limit of detection and limit of quantitation of the analytical methods. *Chronicles of young scientists*, 2(1):21-25. 10.4103/2229-5186.79345

Smith, H.Q. et al. 2019. Glutamate Dehydrogenase, a Complex Enzyme at a Crucial Metabolic Branch Point. *Neurochemical Research*, 44(1):117-123. https://doi.org/10.1007/s11064-017-2428-0

Sperringer, J.E., Addington, A. & Hutson, S.M. 2017. Branched-chain amino acids and brain metabolism. *Neurochemical Research*, 42(6):1697-16705. https://doi.org/10.1007/s11064-017-2261-5

Spinelli, J.B. & Haigis, M.C. 2018. The multifaceted contributions of mitochondria to cellular metabolism. *Nature Cell Biology*, 20(745):1-5. https://doi.org/10.1038/s41556-018-0124-1

Stewart, J.B. & Chinnery, P.F. 2015. The dynamics of mitochondrial DNA heteroplasmy: Implications for human health and disease. *Nature Reviews Genetics*, 16(9):530-542. https://doi.org/10.1038/nrg3966

Sugden, M.C. & Holness, M.J. 2015. The pyruvate carboxylase-pyruvate dehydrogenase axis in islet pyruvate metabolism: Going round in circles? *Islets*, 3(6):302-315. https://doi.org/10.4161/isl.3.6.17806

Sullivan, L.B. et al. 2015. Supporting Aspartate Biosynthesis Is an Essential Function of Respiration in Proliferating Cells. *Cell*, 162(1):552-563. http://dx.doi.org/10.1016/j.cell.2015.07.017

Sun, H. & Wang, Y. 2016. Branched chain amino acid metabolic reprogramming in heart failure. *BBA*, 1862(1):2270-2275. https://doi.org/10.1016/j.bbadis.2016.09.009

Swalwell, H. et al. 2011. Respiratory chain complex I deficiency caused by mitochondrial DNA mutations. *European Journal of Human Genetics*, 19(1):769-774. https://doi.org/10.1038/ejhg.2011.18

Szabadkai, G. & Duchen, M.R. 2008. Mitochondria: The hub of cellular Ca^{2+} signalling. *Physiology*, 23(2):84-94. https://doi.org/10.1152/physiol.00046.2007

Terburgh, K *et al*. 2019. Metabolomics of *Ndufs4-/-* skeletal muscle: Adaptive mechanisms converge at the ubiquinone-cycle. *BBA*, 1865(1):98-105. https://doi.org/10.1016/j.bbadis.2018.10.034

Terburgh, K. et al. 2021. Cross-comparison of systemic and tissue-specific metabolomes in a mouse model of Leigh syndrome. *Metabolomics*, 17(1):2-10. https://doi.org/10.1007/s11306-021-01854-8

Tiwari, G. & Tiwari, R. 2010. Bioanalytical method validation: An updated review. *Pharmaceutical methods*, 1(1):25-38. https://doi.org/10.1016/S2229-4708(10)11004-8

Todisco, S. et al. 2019. TCA Cycle Rewiring as Emerging Metabolic Signature of Hepatocellular Carcinoma. *Cancers*, 12(68):1 – 15. https://doi.org/10.3390/cancers12010068

Trammell, S.A. & Brenner, C. 2013. Targeted, lcms-based metabolomics for quantitative measurement of NAD+ metabolites. *Computational and structural biotechnology journal*, 4(5):7-10. https://doi.org/10.5936/csbj.201301012

Treacy, E. et al. 1992. Maple syrup urine disease: interrelations between branched-chain amino-,oxo- and hydroxyacids; implications for treatment; associations with CNS dysmyelination. *Journal for Inherited Metabolic Disease*, 15(1):121-129. https://doi.org/10.1007/BF01800354

Tsoukalas, D. et al. 2017. Application of metabolomics: Focus on the quantification of organic acids in healthy adults. *Internaltional Journal of Molecular Medicine*, 40(1):112-115. https://doi.org/10.3892/ijmm.2017.2983

Tsugawa, H. et al. 2014. Highly sensitive and selective analysis of widely targeted metabolomics using gas chromatography/triple-quadrupole mass spectrometry. *Journal of Bioscience and Bioengineering*, 117(1):122-28. https://doi.org/10.1016/j.jbiosc.2013.06.009

Tyrakis, P.A. et al. 2016. S-2-hydroxyglutarate regulates $CD8^+$ T-lymphocyte fate. *Nature*, 540(1):236-240. https://doi.org/10.1038/nature20165

Valvona, C. et al. 2015. Inhibition of lactate dehydrogenase A (LDHA) using sodium oxamate leads to metabolic changes, decreased growth and migration in medulloblastoma cell lines. *Neuro-Oncology*, 17(8):1-3. 10.1093/neuonc/nov284.49

Van de Wal, M.A.E. et al. 2022. Ndufs knockout mouse models of Leigh syndrome: pathophysiology and intervention. *Brain*, 145(1):46-52. https://doi.org/10.1093/brain/awab426

Van der Walt, G., Lindeque, J.Z., Mason, S. & Louw, R. 2021. Sub-Cellular Metabolomics Contributes Mitochondria-Specific Metabolic Insights to a Mouse Model of Leigh-Syndrome. *Metabolites*, 11(1):1-18. https://doi.org/10.3390/metabo11100658

Venter, L. et al. 2017. Uncovering the metabolic response of abalone (*Haliotis midae*) to environmental hypoxia through metabolomics. *Metabolomics*, 14(49):49. https://doi.org/10.1007/s11306-018-1346-8

Vielhauer, O., Zakhartsev, M., Horn, T., Takors, R. and Reuss, M. 2011. Simplified absolute metabolite quantification by gas-chromatography-isotope dilution mass spectrometry on the basis of commercially available source material. *Journal of Chromatography*, 2(879):3867. https://doi.org/10.1016/j.jchromb.2011.10.036

Vina, J., Saez, G.T., Gambini, J., Gomez-Cabrera, M.C. & Borrás, C. 2016. Role of NAD(+)/NADH redox ratio in cell metabolism: A tribute to helmut sies and theodor bucher and hans a. Krebs. *Archive Biochemistry and Biophysics*, 595:176-180. https://doi.org/10.1016/j.abb.2015.11.027

Vogel, B., Bradley, S., Adams, D., D'Aco, K., Erbe, R., Fong, C., Morrissey, M. 2015. Newborn screening for x-linked adrenoleukodystrophy in New York State: Diagnostic protocol, surveillance protocol and treatment guidelines. *Molecular genetics and metabolism*, 114(4):599-603. https://doi.org/10.1016/j.ymgme.2015.02.002

Vujic, A. et al. Mitochondrial redox and TCA cycle metabolite signalling in the heart. *Free Radical Biology and Medicine*, 166(1):287-290. https://doi.org/10.1016/j.freeradbiomed.2021.02.041

Walsh, C.T., Tu, B.P. & Tang, Y. 2018. Eight kinetically stable but thermodynamically activated molecules that power cell metabolism. *Chemical reviews*, 118(4):1460-1494. https://doi.org/10.1021/acs.chemrev.7b00510

Wang, X. et al. 2016. Mitochondrial flashes regulate ATP homeostasis in the heart. *eLife*, 6(1):1-8. https://doi.org/10.7554/eLife.23908

Wang, Y., Liu, S., Hu, Y., Li, P. & Wan, J.-B. 2015. Current state of the art of mass spectrometry-based metabolomics studies–a review focusing on wide coverage, high throughput and easy identification. *Rsc Advances*, 5(96):78728-78737. https://doi.org/10.1039/C5RA14058G

Watt, I.N., Montgomery, M.G., Runswick, M.J., Leslie, A.G. & Walker, J.E. 2010. Bioenergetic cost of making an adenosine triphosphate molecule in animal mitochondria. *Proceedings of the National Academy of Sciences*, 107(39):16823-16827. https://doi.org/10.1073/pnas.1011099107

Wu, H., Xu, C., Gu, Y., Yang, S., Wang, Y. & Wang, C. 2020. An improved pseudotargeted gc–ms/ms-based metabolomics method and its application in radiation-induced hepatic injury in a rat model. *Journal of Chromatography B*, 1152:122250. https://doi.org/10.1016/j.jchromb.2020.122250

Xiao, W., Wang, R.-S., Handy, D.E. & Loscalzo, J. 2018. NAD (H) and NADP (H) redox couples and cellular energy metabolism. *Antioxidants & redox signaling*, 28(3):251-272. https://doi.org/10.1089/ars.2017.7216

Xu, J., Li, J., Zhang, R., He, J., Chen, Y., Bi, N., Abliz, Z. 2019. Development of a metabolic pathway-based pseudo-targeted metabolomics method using liquid chromatography coupled with mass spectrometry. *Talanta*, 192:160-168. https://doi.org/10.1016/j.talanta.2018.09.021

Yang, H. et al. 2019. Inborn errors of mitochondrial acyl-coenzyme a metabolism: acyl-CoA biology meets the clinic. *Molecular Genetics and Metabolism*, 128(1-2):30-44. https://doi.org/10.1016/j.ymgme.2019.05.002

Yang, Y. & Sauve, A.A. 2016. NAD+ metabolism: Bioenergetics, signalling and manipulation for therapy. *Biochimica et Biophysica Acta (BBA)-Proteins and Proteomics*, 1864(12):1787-1800. https://doi.org/10.1016/j.bbapap.2016.06.014

Yao, J. et al. 2010. Decline in mitochondrial bioenergetics and shift to ketogenic profile in brain during reproductive senescence. *BBA*, 1800(10):1121-1125. https://doi.org/10.1016/j.bbagen.2010.06.002

Ying, W. 2008. NAD+/NADH and NADP+/NADPH in cellular functions and cell death: Regulation and biological consequences. *Antioxidants & redox signalling*, 10(2):179-206. https://doi.org/10.1089/ars.2007.1672

Yoon, JY. et al. 2022. Metabolic rescue ameliorates mitochondrial encephalocardiomyopathy in murine and human iPSC models of Leigh syndrome. *Clinical Translation* Medicine, 12(7):2-13. https://doi.org/10.1002/ctm2.954

Zaitsu, K. & Hayashi, Y. 2019. GC/MS/MS-based targeted metabolomics for pathophysiological analysis of animal models. *Medical Mass Spectrometry*, 3(1):11-18.

Zarate, E. et al. 2017. Fully Automated Trimethylsilyl (TMS) Derivatisation Protocol for Metabolite Profiling by GC-MS. *Metabolites*, 7(1):1-5. https://doi.org/10.3390/metabo7010001

Zhao, Y. & Yang, Y. 2016. Real-time and high-throughput analysis of mitochondrial metabolic states in living cells using genetically encoded NAD+/NADH sensors. *Free Radical Biology and Medicine*, 100:43-52. https://doi.org/10.1016/j.freeradbiomed.2016.05.027

Zhou, J. & Yin, Y. 2016. Strategies for large-scale targeted metabolomics quantification by liquid chromatography-mass spectrometry. *Analyst*, 141(23):6362-6373. https://doi.org/10.1039/C6AN01753C

Appendix A

Table A1: Brain organic acid LOD, LOQ, Linearity and other validation parameters.

Compound	LOD (ng/mg)	LOQ (ng/mg)	Accuracy (%)	Linearity	Linear range (ng/mg)
Lactate Quali	25.977	34.472	92.60	0.9378	0 – 1000
Lactate Quant	19.143	27.979	100.53	0.9485	0 – 1000
2-OH-gluterate Quali	23.586	25.042	97.14	0.9282	0 – 1000
2-OH-gluterate Quant	26.165	27.709	102.15	0.9282	0 - 1000
2-keto-3-mval 1tBDMS Quant	92.499	93.245	101.15	0.9363	0 – 1000
2-k-3mval 1tBDMS Quali	95.808	96.496	98.80	0.9342	0 – 1000
2-k-3-mbut 1tBDMS Quali	63.113	64.343	90.79	0.9297	0 – 1000
2-k-3mbut 1tBDMS Quant	58.922	64.449	91.49	0.9427	0 – 1000
2KG 3tBDMS Quali	29.908	29.933	94.42	0.9652	0 – 1000
2KG 3tBDMS Quant	24.709	24.800	93.93	0.9673	0 – 1000
3-OH-BA Quant	36.078	36.155	104.45	0.9279	0 – 1000
3-OH-BA Quali	63.849	63.960	111.16	0.9104	0 – 1000
Acetoacetate (1) Quali	11.849	13.581	104.22	0.912	0 – 750
Acetoacetate (1) Quant	24.722	29.543	101.37	0.9257	0 – 750
Acetoacete (2) Quant	20.891	22.716	95.78	0.9004	0 – 750
Acetoacetate (2) Quali	26.922	28.572	101.52	0.8894	0 – 750
2-OH-adipic acid Quant	7.205	8.068	107.65	0.9513	0 – 750
2-OH-adipic acid Quali	15.044	15.325	100.72	0.9521	0 – 750
2-ketoadipic acid Quant	57.393	58.220	98.09	0.9431	0 – 750
2-ketoadipic acid Quali	64.586	65.132	95.83	0.9231	0 – 750
Aconitate Quant	46.572	47.168	100.56	0.9598	0 – 1000
Aconitate Quali	55.552	55.997	97.80	0.9476	0 – 1000
Citric acid Quali	6.376	10.286	89.82	0.9407	0 – 1000

Isocitrate Quali	27.788	28.198	111.08	0.9552	0 – 1000
Isocitrate Quant	14.238	14.310	92.55	0.9466	0 – 1000
2-k-3mbut 2tBDMS Quali	31.559	33.104	111.29	0.9045	0 – 750
2-k-3mbut 2tBDMS Quant	27.360	28.166	112.75	0.9077	0 – 750
2-OH-3mbut Quant	29.557	29.653	109.01	0.9513	0 – 1000
2-k-3mval 2tBDMS Quant	61.617	63.163	92.51	0.8825	0 – 1000
3-OH-propionate Quant	7.472	7.721	97.92	0.9411	0 – 1000
3-OH-propionate Quali	18.573	18.847	88.18	0.9326	0 – 1000
2-Methylcitric acid Quant	42.724	66.388	88.53	0.9572	0 – 750
Succinylacetone (3) Quant	54.565	54.873	96.27	0.9346	0 – 1000
Succinylacetone Quali (3)	57.448	57.551	112.06	0.9406	0 – 1000
Succinylacetone (2) Quant	87.599	87.833	97.17	0.8962	0 – 1000
Succinylacetone (2) Quali	93.628	93.705	94.77	0.8914	0 – 1000
Succinylacetone (1) Quali	83.803	83.953	94.65	0.9107	0 – 1000
Succinylacetone (1) Quant	81.829	81.985	95.63	0.9059	0 – 1000
Methylmalonate Quali	34.290	34.673	114.96	0.9367	0 - 1000
Malate Quant	81.380	83.431	90.37	0.9141	0 – 1000
L-Asp Quali	55.488	66.062	98.41	0.9581	0 – 1000
L-Asp Quant	45.842	58.631	108.88	0.9521	0 – 1000
Pyr Dimer Quant	91.200	92.281	71.97	0.9053	0 – 1000
Pyr Dimer Quali	94.457	96.825	75.57	0.9037	0 – 1000
3-OH-isoval Quali	60.816	94.994	97.43	0.929	0 - 500
2-k-4mval Quali	88.722	94.050	85.32	0.9236	0 – 1000
2-OH-4mval Quant	67.571	86.605	91.00	0.9041	0 - 1000

Table A2: Liver organic acid LOD, LOQ, linearity and other validation parameters.

Compound	LOD (ng/mg)	LOQ (ng/mg)	Accuracy (%)	Linearity	Linear range (ng/mg)
Lactate Quali	29.021	64.022	97.40	0.915	0 - 1000
Lactate Quant	22.834	58.848	98.42	0.9216	0 - 1000
2-OH-gluterate Quant	7.173	14.986	106.58	0.9066	0 – 1000
2-OH-gluterate Quali	2.826	11.304	101.31	0.9077	0 – 1000
Pyruvate Quali	30.576	33.381	88.75	0.9632	0 – 1000
Pyruvate Quant	35.659	38.223	95.99	0.9627	0 – 1000
2-k-3-mbut 1tBDMS Quant	42.632	44.361	90.01	0.9025	0 – 1000
2-k-3-mbut 1tBDMS Quali	44.803	46.831	96.29	0.8938	0 – 1000
2-k-3-mval 1tBDMS Quali	41.538	43.069	103.70	0.9322	0 – 1000
2-k-3-mval 1tBDMS Quant	33.424	34.916	109.30	0.9261	0 – 1000
2-OH-3mbut Quant	33.979	41.629	99.80	0.9745	0 – 1000
2-OH-3mbut Quali	35.688	43.915	105.19	0.9722	0 – 1000
Acetoacetate (2) Quali	34.057	34.354	94.655	0.9468	0 – 1000
Acetoacetate (2) Quant	31.587	31.798	93.325	0.9444	0 – 1000
Acetoacetate (1) Quali	48.690	50.577	94.12	0.9634	0 – 1000
Acetoacetate (1) Quant	19.130	28.552	90.525	0.9467	0 - 1000
2KG 3tBDMS Quant	17.403	23.425	93.69	0.9575	0 – 750
2KG 3tBDMS Quali	27.115	33.127	89.74	0.954	0 - 750
2-OH-adipic acid Quali	14.000	15.293	100.54	0.9202	0 – 1000
2-OH-adipic acid Quant	4.829	5.561	104.12	0.8915	0 – 1000
2-ketoadipic acid Quant	40.221	41.214	99.72	0.9546	0 – 1000
2-ketoadipic acid Quali	37.206	38.561	91.49	0.9442	0 – 1000
3-OH-BA Quant	74.269	75.065	89.78	0.9022	0 – 1000
3-OH-BA Quali	75.703	80.792	88.89	0.8869	0 – 1000

2-k-3-mbut 2tBDMS Quali	77.718	81.552	92.96	0.9354	0 – 1000
2-k-3-mbut 2tBDMS Quant	73.090	77.285	92.16	0.9384	0 – 1000
2-k-3-mval 2tBDMS Quali	52.394	57.827	85.63	0.9459	0 – 1000
2-k-3-mval 2tBDMS Quant	8.393	14.586	89.45	0.9442	0 – 1000
Malate Quant	35.098	41.027	105.74	0.9445	0 – 750
Malate Quali	49.760	53.067	101.23	0.9358	0 – 750
L-Asp Quali	28.371	54.233	122.51	0.936	0 – 750
L-Asp Quant	27.485	58.812	122.53	0.9384	0 – 750
Oxaloacetate Quali	97.604	159.515	92.69	0.9103	0 – 750
Oxaloacetate Quant	213.559	560.103	109.64	0.9381	0 – 750
Aconitic acid Quanti	59.284	59.705	97.84	0.9101	0 – 750
2-k-4-mval 2tBDMS Quali	49.557	50.551	90.85	0.9326	0 – 750
2-OH-4mval	69.252	110.275	90.56	0.9454	0 - 1000
3-OH-decanoic acid Quali	33.938	42.297	97.89	0.969	0 – 500
3-OH-propionate Quant	23.138	24.616	106.70	0.9366	0 – 1000
3-OH-propionate Quali	30.186	31.863	99.79	0.9301	0 - 1000
2-Methylcitric acid Quali	19.401	22.740	95.95	0.9751	0 – 1000
Methylmalonate Quali	25.250	25.992	111.41	0.909	0 – 500
Methylmalonate Quant	23.295	23.757	113.72	0.9102	0 - 500
Succinylacetone (1) Quali	30.504	31.476	101.29	0.9621	0 – 1000
Succinylacetone (1) Quant	34.989	39.228	113.00	0.9619	0 - 1000
Succinylacetone (2) Quali	53.380	54.706	101.80	0.9549	0 – 1000
Succinylacetone (2) Quant	46.060	48.941	90.46	0.9573	0 – 1000
Succinylacetone (3) Quant	37.478	39.010	103.25	0.9718	0 – 1000
Succinylacetone (3) Quali	38.103	39.057	104.39	0.9755	0 – 1000

Table A3: Heart organic acid LOD, LOQ, linearity and other validation parameters.

Compound	LOD (ng/mg)	LOQ (ng/mg)	Accuracy (%)	Linearity	Linear range (ng/mg)
Lactate Quant	36.681	39.459	112.31	0.9714	0 – 1000
Lactate Quali	69.121	71.184	96.453	0.9121	0 – 1000
Pyruvate Quali	49.214	51.628	109.54	0.9601	0 – 500
Pyruvate Quant	47.819	50.242	104.55	0.9616	0 – 500
2-k-3-mbut 1tBDMS Quant	47.414	47.415	87.15	0.9475	0 – 750
2-k-3-mbut 1tBDMS Quali	49.6624	49.6628	92.83	0.9452	0 – 750
2-k-3-mval 1tBDMS Quali	7.779	8.045	111.67	0.9724	0 – 1000
2-k-3-mvalerate 2tBDMS Quali	69.615	69.851	87.39	0.9203	0 – 750
2-k-3-mvalerate 2tBDMS Quant	62.487	63.019	89.69	0.935	0 – 750
Oxaloacetate Quali	2.449	13.626	96.67	0.9505	0 – 750
Oxaloacetate Quant	2.726	58.617	103.21	0.9145	0 – 750
Malate Quant	25.083	47.979	100.70	0.9667	0 – 750
Malate Quali	32.044	47.767	102.99	0.9681	0 – 750
L-Asp Quali	5.748	19.733	101.15	0.9434	0 – 750
L-Asp Quant	0.171	15.481	86.18	0.9321	0 – 750
2-OH-gluterate Quali	50.244	59.215	108.06	0.9075	0 – 750
2-OH-gluterate Quant	49.582	58.614	102.54	0.9106	0 – 750
Aconitic acid Quali	4.065	8.894	99.36	0.9454	0 – 750
Citric acid Quali	8.659	15.892	97.49	0.9554	0 – 750
Citric acid Quant	1.011	11.704	99.17	0.9567	0 – 750
Isocitric acid Quant	50.954	52.669	88.05	0.9214	0 – 750
2-k-3mbut 2tBDMS Quali	34.344	69.131	90.14	0.975	0 – 500

2-k-3-mbut 2tBDMS Quant	33.181	68.627	89.14	0.9738	0 – 500
3-OH-isovalerate Quali	35.608	83.028	103.15	0.9782	0 – 500
3-OH-decanoic acid Quali	1.505	19.027	95.93	0.9773	0 – 500
2-OH-4-mvalerate	87.922	270.115	113.23	0.978	0 – 500
2-k-4-mval 2tBDMS	152.966	484.765	92.38	0.9614	0 – 500
Methylmalonate Quali	55.488	62.784	87.79	0.9398	0 – 750
Mehtylmalonate Quant	37.983	45.981	89.10	0.9433	0 – 750
2-Methylcitric acid Quali	94.229	234.024	95.67	0.9594	0 – 500
Pyruvate Dimer (1) Quali	74.234	76.432	89.60	0.9379	0 – 750
Pyruvate Dimer (1) Quant	104.479	172.090	94.76	0.9357	0 – 750
3-OH-BA quali	78.727	143.919	98.81	0.9476	0 – 750
Acetoacetate Quant (2)	61.459	71.965	100.29	0.9152	0 – 750
2KG 3tBDMS Quali	79.376	81.450	94.75	0.8931	0 – 750
2KG 3tBDMS Quant	75.107	76.978	93.48	0.9095	0 – 750
2-OH-adipic acid Quant	67.297	79.561	92.69	0.9436	0 – 750
2-OH-adipic acid Qual	63.512	79.267	92.75	0.9622	0 – 750
2-ketoadipic acid Quant	72.859	79.574	111.56	0.91	0 – 750
3-OH-propionate Quali	60.052	67.296	84.32	0.9597	0 – 1000
3-OH-propionate Quant	55.070	63.347	86.33	0.9591	0 – 1000

Table A4: Amount (mg) of mouse liver tissue used for Bligh and Dyer extraction

Knock Out liver tissue (mg)	Sample	Wild Type liver tissue (mg)	Sample
55.4	40	49.9	59
50.7	5	51.6	26
49.7	4	50.7	55
53.5	4_1	52.2	51
49.6	81	53.9	18
50.5	80	54	44

Table A5: Amount (mg) of mouse brain tissue used for Bligh and Dyer extraction

Knock Out Brain tissue (mg)	Sample	Wild Type Brain tissue (mg)	Sample
55.0	40	50.7	59
52.3	5	65.2	26
56.4	4	54.6	55
54.4	4_1	52.6	51
53.6	81	55.1	18
50.3	80	48.7	44

Table A6: Amount (mg) of mouse heart tissue used for Bligh and Dyer extraction

Knock Out Brain tissue (mg)	Sample	Wild Type Brain tissue (mg)	Sample
56.5	40	80.4	59
55.2	5	52.4	26
56.1	4	58.1	55
33.5	4_1	69.8	51
67.4	81	53.7	18
51.3	80	46.4	44

Table A7: Amount of tissue homogenate (µL) and analytical standards (µL) used for calibration throughout KO & WT tissue analysis

Calibration point (ng metabolite / mg tissue)	Homogenate (µL)	Volume per analytical standard (µL)
Blank	506.6	0
100	506.6	2.5
500	506.6	12.5
1000	506.6	25
250 / QC	506.6	6.25

Table A8: Compound MRM transitions and other identification parameters

Compound	Precursor ion	Product ion	CE	Quantifier/Qualifier	Rt
3-methyl-2-ketobutyrate (1tBDMS)	174,2	159	6	Qualifier	4,718
3-methyl-2-ketobutyrate (1tBDMS)	129,1	75	5	Quantifier	4,718
2-keto-3-methylvalerate (1tBDMS)	188,2	159	5	Quantifier	5,654
2-keto-3-methylvalerate (1tBDMS)	143,2	75,1	6	Qualifier	5,655
Lactate	261,2	147,2	6	Quantifier	7,79
Lactate	233,3	147,2	5	Qualifier	7,79
Pyruvate (2tbdms)	259,2	147,1	7	Qualifier	8,426
Pyruvate (2tbdms	259,2	189,2	6	Quantifier	8,426
3-OH-propionate	261,2	147	9	Quantifier	9,085
3-OH-propionate	261,2	189,2	6	Qualifier	9,086
3-OH-butyrate (2tBDMS)	275,2	147,1	6	Qualifier	9,357
3-OH-butyrate (2tBDMS)	233,2	147,1	7	Quantifier	9,357
3-methyl-2-OH-butyrate	289,3	147,1	7	Qualifier	9,526
3-methyl-2-OH-butyrate	261,3	147,1	6	Quantifier	9,526
Methylmalonate	289,3	147,2	6	Quantifier	10,313
Methylmalonate	289,3	73,3	8	Qualifier	10,313
3-phenylbutyric acid	221,3	105,1	5	Quantifier	10,393
3-phenylbutyric acid	105,3	77	20	Qualifier	10,393
3-OH-isovaleric acid	289,3	147,1	7	Quantifier	11,203
3-OH-isovaleric acid	289,3	189,2	6	Qualifier	11,203
2-keto-3-methylvalerate (2tBDMS)	301,3	147,1	5	Qualifier	11,655
2-keto-3-methylvalerate (2tBDMS)	301,3	189	6	Quantifier	11,656
2-keto-4-methylvalerate (2tBDMS) / 2-keto-3-methylvalerate	301,3	147,2	10	Qualifier	11,7
2-keto-4-methylvalerate (2tBDMS) / 2-keto-3-methylvalerate	301,3	189,2	10	Quantifier	11,7
2-ketogluterate (2tBDMS)	215,3	73,1	10	Quantifier	12,599
2-ketogluterate (2tBDMS)	317,2	157	7	Qualifier	12,6
3-OH-decanoic acid	359,3	147	9	Qualifier	13,847
3-OH-decanoic acid	313,4	147	7	Quantifier	13,848
Acetaminophen	308,3	267,2	8	Quantifier	13,917
Acetaminophen	322,3	248,2	12	Qualifier	13,917
Malate	287	73,1	10	Quantifier	13,978

Malate	419,4	73,1	5	Qualifier	13,98
Oxaloacetate	417,4	147	16	Quantifier	14,093
Oxaloacetate	417,4	73,1	16	Qualifier	14,093
L-Aspartate	418,3	390,2	7	Qualifier	14,169
L-Aspartate	390,3	73	13	Quantifier	14,17
2-OH-gluterate	433,4	73	16	Quantifier	14,431
2-OH-gluterate	433,4	147,1	16	Qualifier	14,431
2-ketogluterate (3tBDMS)	431,3	147,2	17	Qualifier	14,551
2-ketogluterate (3tBDMS)	375,3	147,1	15	Quantifier	14,551
2-OH-adipic acid	447,4	245,2	7	Quantifier	14,889
2-OH-adipic acid	245,2	147,1	7	Qualifier	14,889
2-ketoadipic acid	445,4	375,4	13	Quantifier	14,967
2-ketoadipic acid	375,3	147,1	6	Qualifier	14,967
Trans-Aconitic acid	327,2	147,1	12	Quantifier	15,07
Trans-Aconitic acid	461,4	73,1	17	Qualifier	15,072
C19	355,5	75,1	12	Qualifier	15,809
C19	355,5	131,2	12	Quantifier	15,809
Citric acid	591,5	431,4	12	Quantifier	15,967
Citric acid	459,4	73,1	13	Qualifier	15,967
Isocitrate	591,6	459,3	14	Qualifier	15,98
Isocitrate	431	403,3	12	Quantifier	15,98
3-OH-palmitate	327,4	73	15	Qualifier	16,08
3-OH-palmitate	443,5	147,1	11	Quantifier	16,08
Acetoacetate	273,2	147,2	15	Qualifier	10,345; 10,770
Acetoacetate	199,2	73,1	11	Quantifier	10,345; 10,770
3-methyl-2-ketobutyrate (2tBDMS)	287,2	147	11	Quantifier	11,100; 11,420
3-methyl-2-ketobutyrate (2tBDMS)	287,2	189,1	11	Qualifier	11,100; 11,420
2-OH-4-methylvalerate / 2-OH-3-methylvalerate	303,3	147,1	10	Quantifier	11,651; 11,46
2-OH-4-methylvalerate / 2-OH-3-methylvalerate	275,3	147,2	7	Qualifier	11,651; 11,46
Pyruvate dimer (2tBDMS)	197,1	169,1	7	Quantifier	12,454; 12,970
Pyruvate dimer (2tBDMS)	329,2	147,1	8	Qualifier	12,454; 12,972
Succinylacetone	329	169,1	13	Qualifier	13,579; 13,859; 13,979
Succinylacetone	169,1	75,1	20	Quantifier	13,579; 13,861; 13,980
2-methylcitrate	447,4	73	20	Qualifier	16,123; 16,213
2-methylcitrate	605,6	447,4	10	Quantifier	16,125;16,213

Calibration curves of calibration samples ran throughout mouse heart tissue analysis.

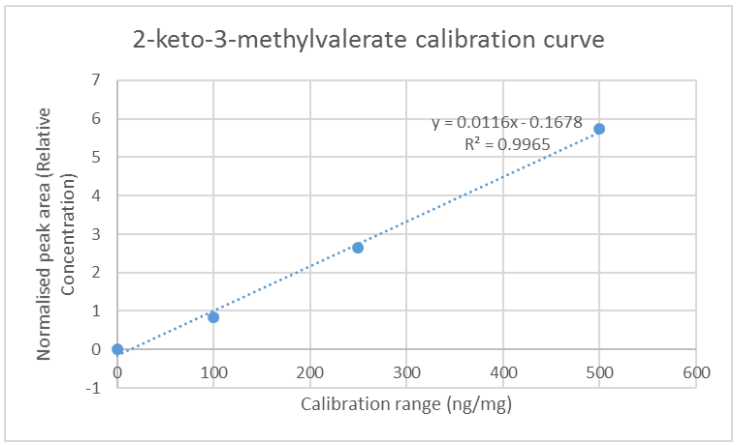

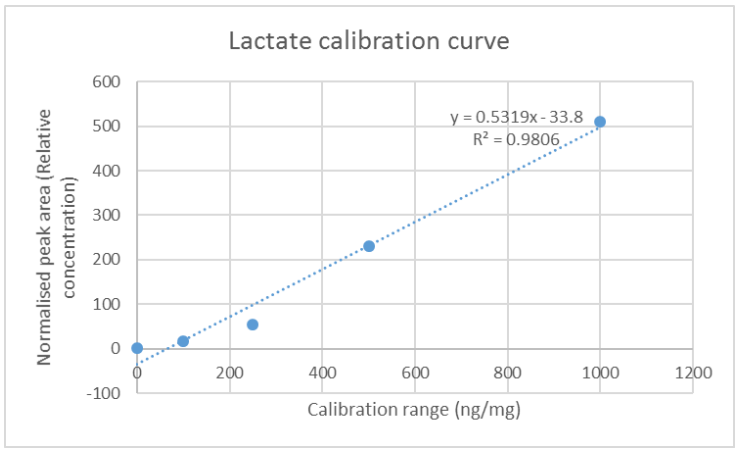

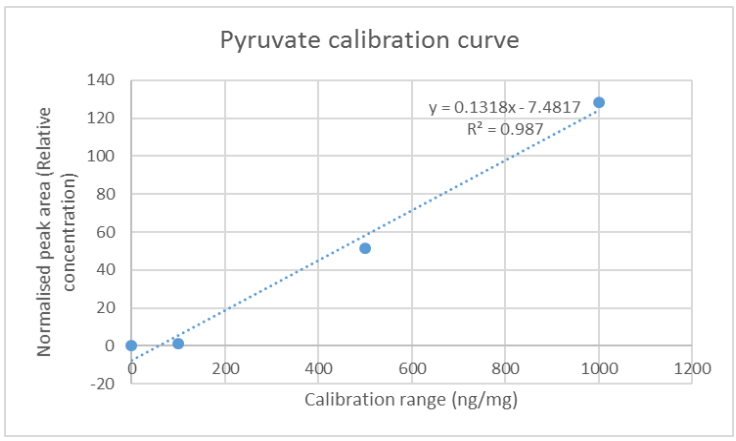

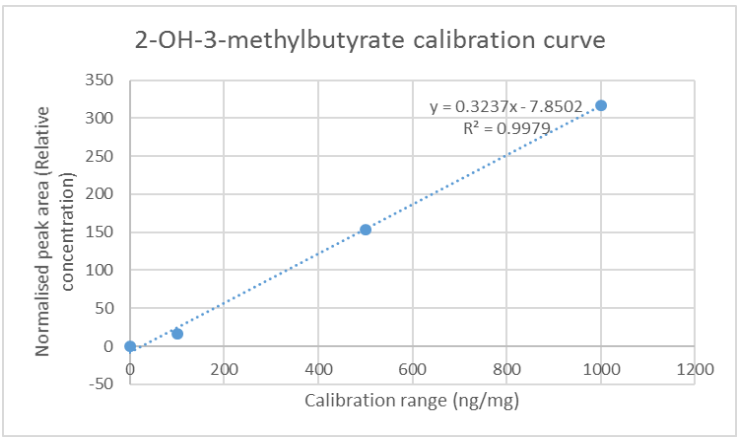

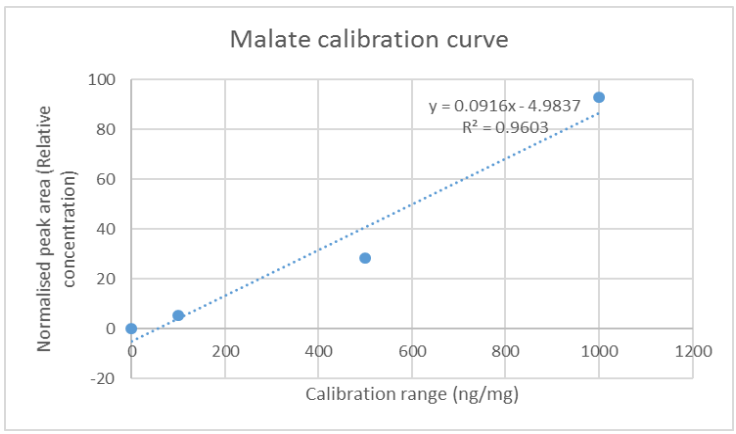

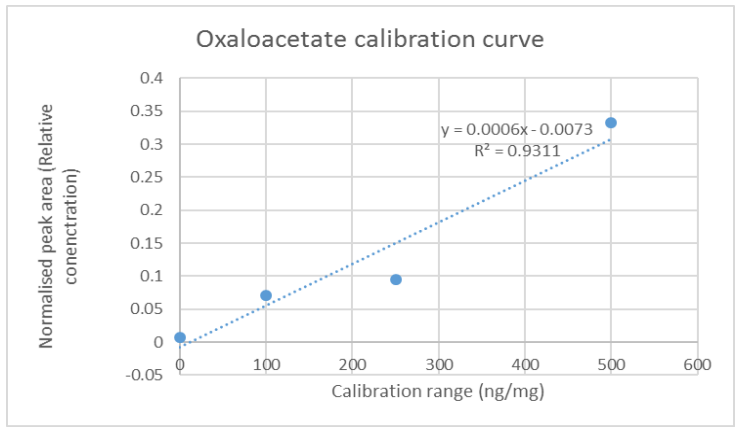

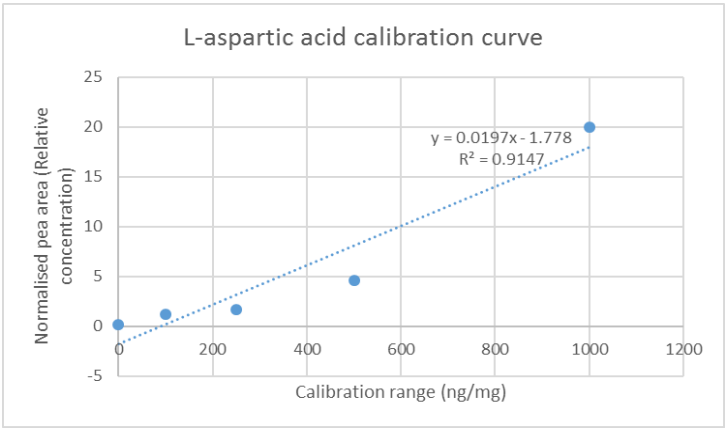
L-aspartic acid calibration curve
y = 0.0197x - 1.778
R² = 0.9147
Normalised pea area (Relative concentration)
Calibration range (ng/mg)

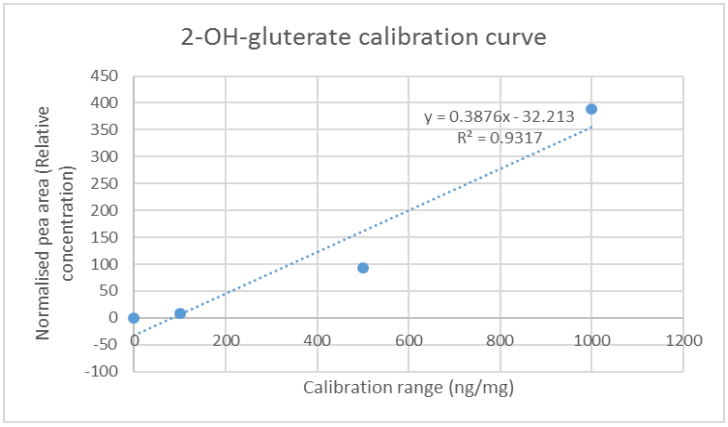
2-OH-gluterate calibration curve
y = 0.3876x - 32.213
R² = 0.9317
Normalised pea area (Relative concentration)
Calibration range (ng/mg)

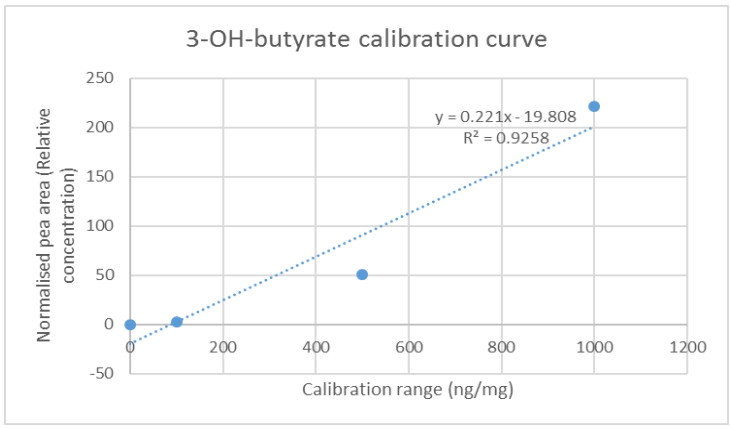
3-OH-butyrate calibration curve
y = 0.221x - 19.808
R² = 0.9258
Normalised pea area (Relative concentration)
Calibration range (ng/mg)

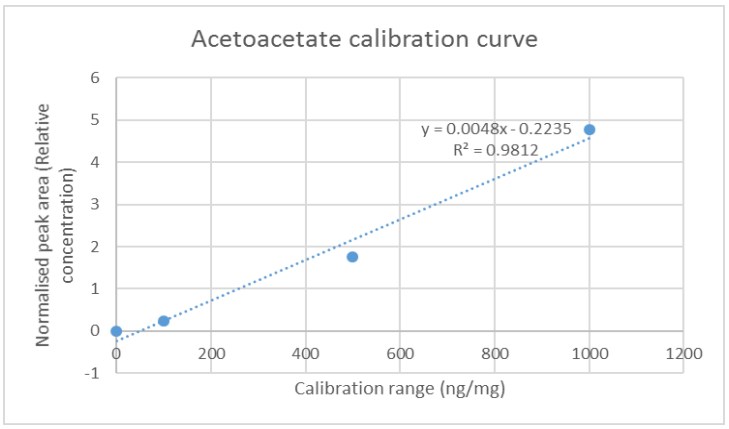
Acetoacetate calibration curve
y = 0.0048x - 0.2235
R² = 0.9812
Normalised peak area (Relative concentration)
Calibration range (ng/mg)

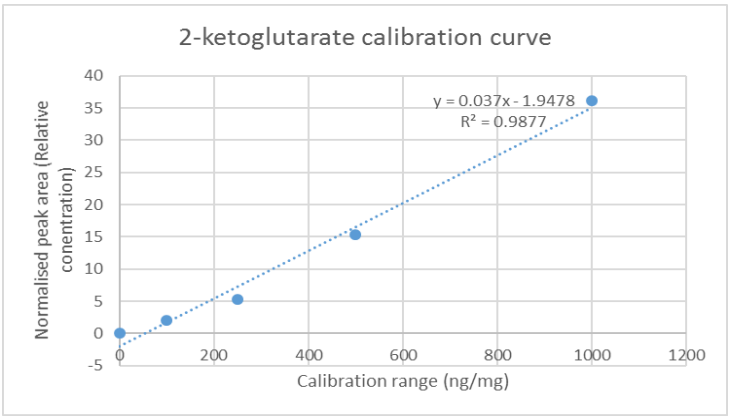
2-ketoglutarate calibration curve
y = 0.037x - 1.9478
R² = 0.9877
Normalised peak area (Relative conentration)
Calibration range (ng/mg)

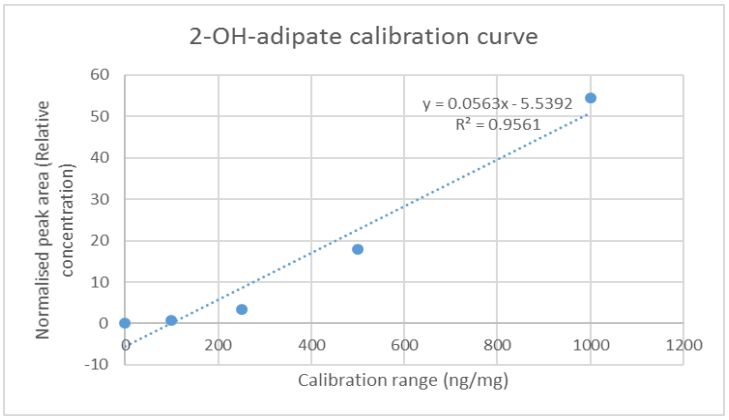
2-OH-adipate calibration curve
y = 0.0563x - 5.5392
R² = 0.9561
Normalised peak area (Relative concentration)
Calibration range (ng/mg)

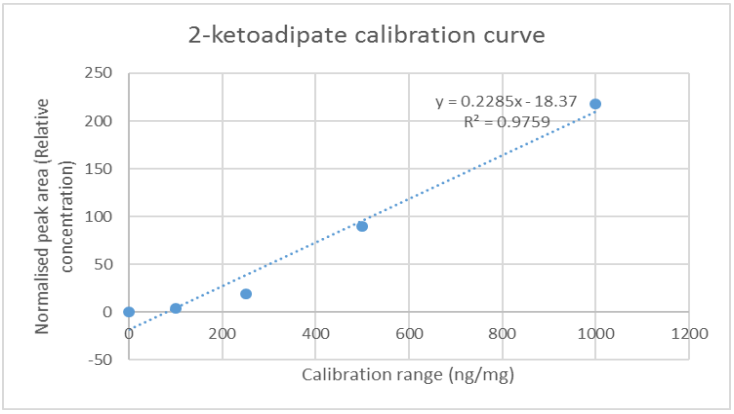
2-ketoadipate calibration curve
y = 0.2285x - 18.37
R² = 0.9759
Normalised peak area (Relative concentration)
Calibration range (ng/mg)

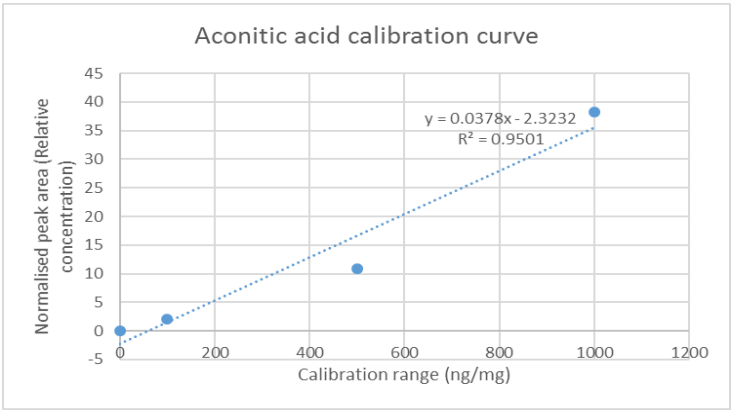
Aconitic acid calibration curve
y = 0.0378x - 2.3232
R² = 0.9501
Normalised peak area (Relative concentration)
Calibration range (ng/mg)

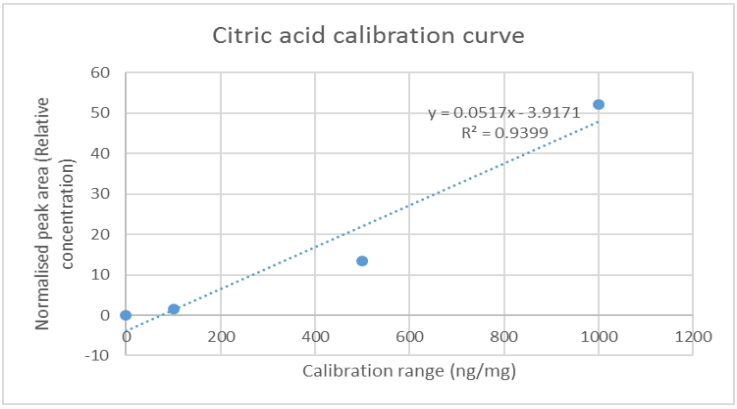
Citric acid calibration curve
y = 0.0517x - 3.9171
R² = 0.9399
Normalised peak area (Relative concentration)
Calibration range (ng/mg)

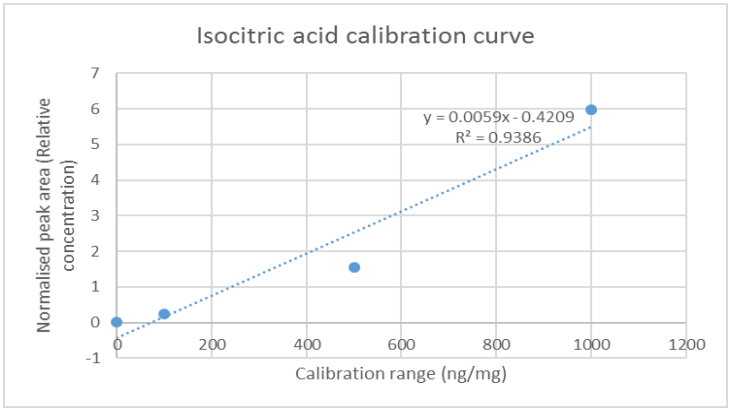
Isocitric acid calibration curve
y = 0.0059x - 0.4209
R² = 0.9386
Normalised peak area (Relative concentration)
Calibration range (ng/mg)

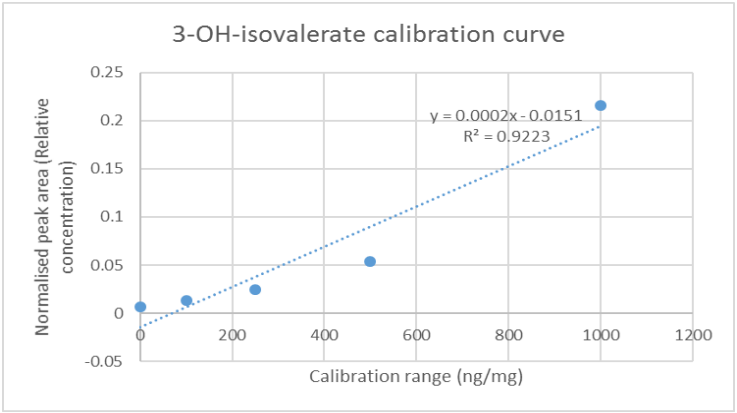
3-OH-isovalerate calibration curve
y = 0.0002x - 0.0151
R² = 0.9223
Normalised peak area (Relative concentration)
Calibration range (ng/mg)

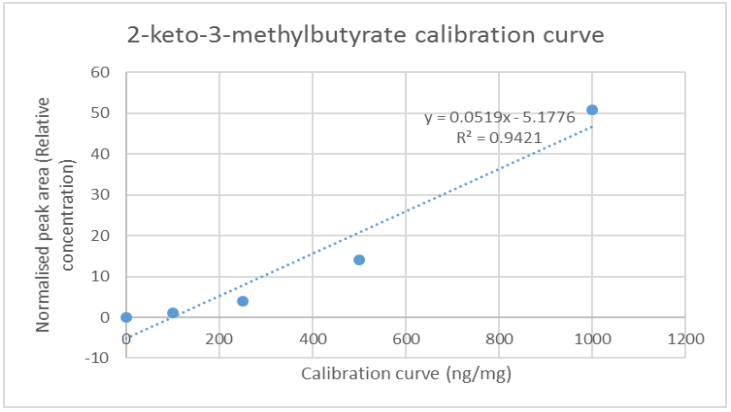
2-keto-3-methylbutyrate calibration curve
y = 0.0519x - 5.1776
R² = 0.9421
Normalised peak area (Relative concentration)
Calibration curve (ng/mg)

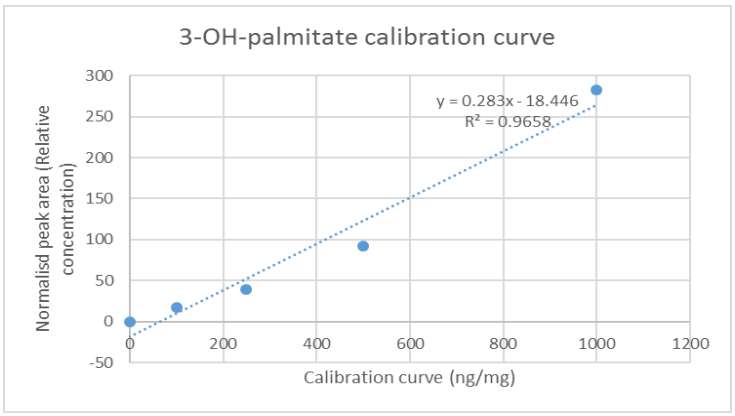

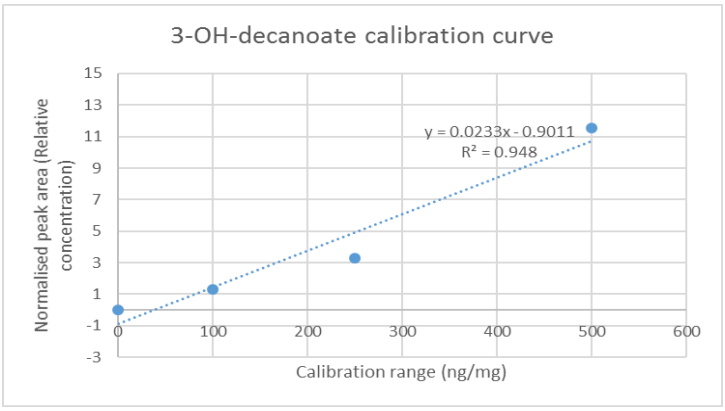

Figures 6.1: Calibration curves of calibrator samples ran adjacent to KO and WT mice heart samples.

Calibration curves of calibration samples ran throughout mouse brain sample analysis.

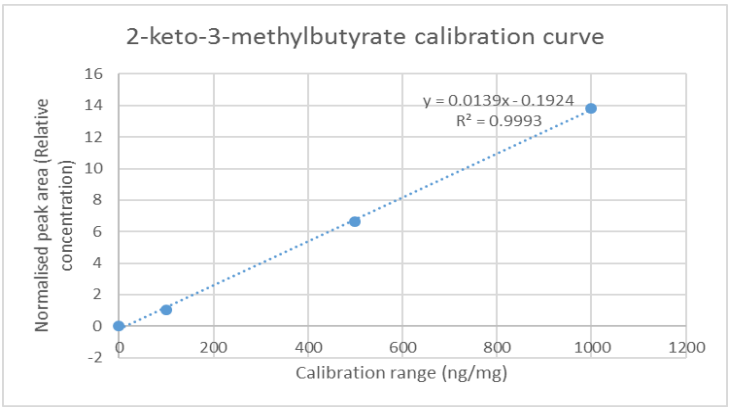

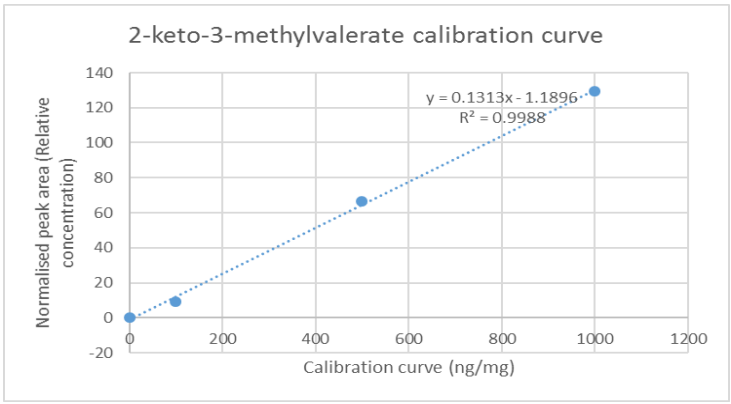

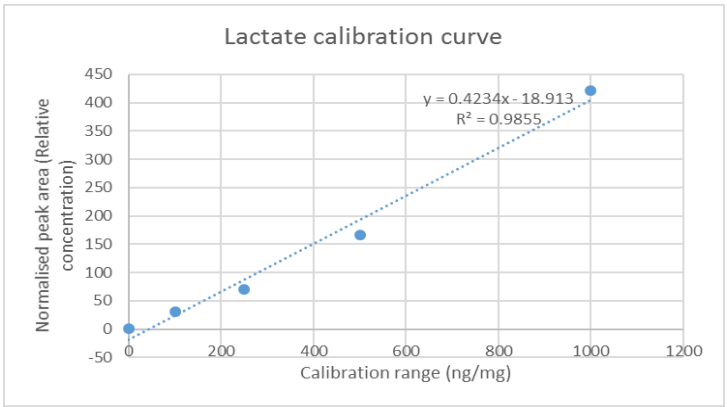

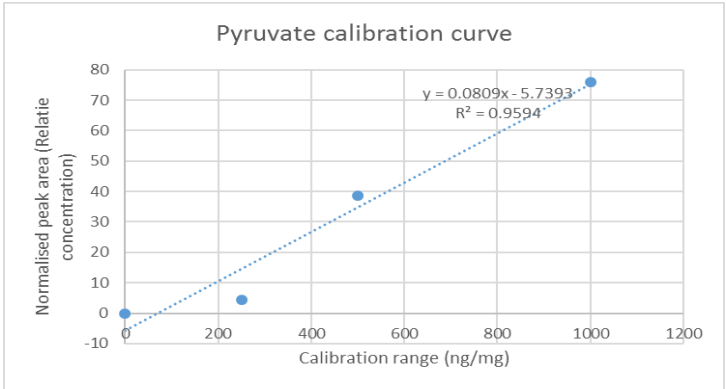

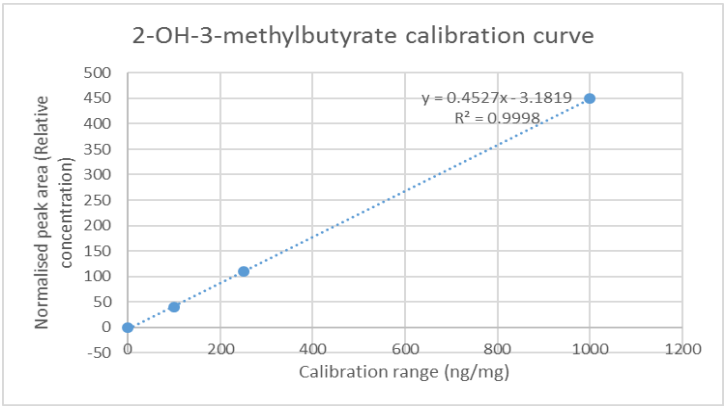
2-OH-3-methylbutyrate calibration curve
y = 0.4527x - 3.1819
R² = 0.9998
Normalised peak area (Relative concentration)
Calibration range (ng/mg)

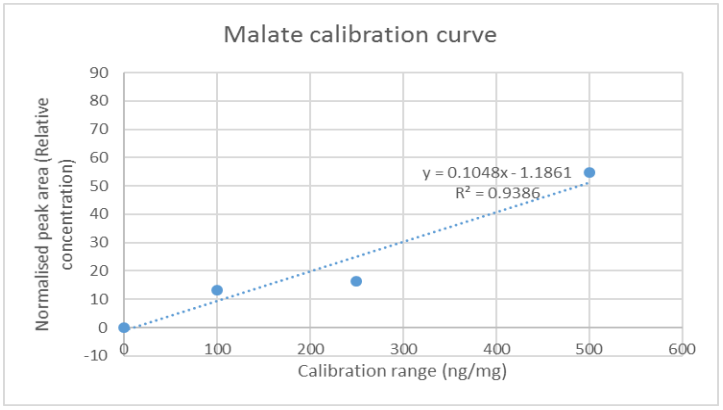
Malate calibration curve
y = 0.1048x - 1.1861
R² = 0.9386
Normalised peak area (Relative concentration)
Calibration range (ng/mg)

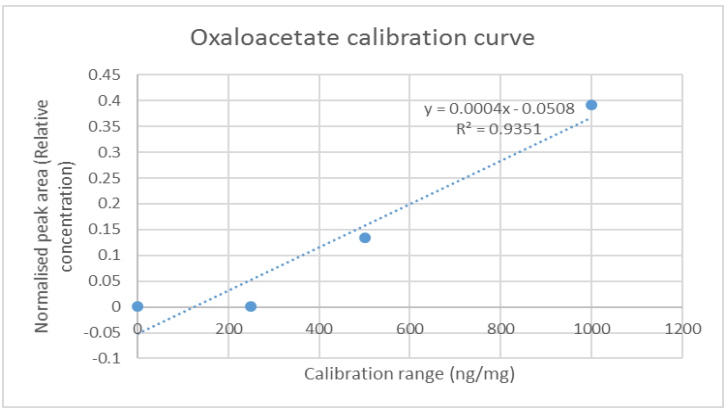
Oxaloacetate calibration curve
y = 0.0004x - 0.0508
R² = 0.9351
Normalised peak area (Relative concentration)
Calibration range (ng/mg)

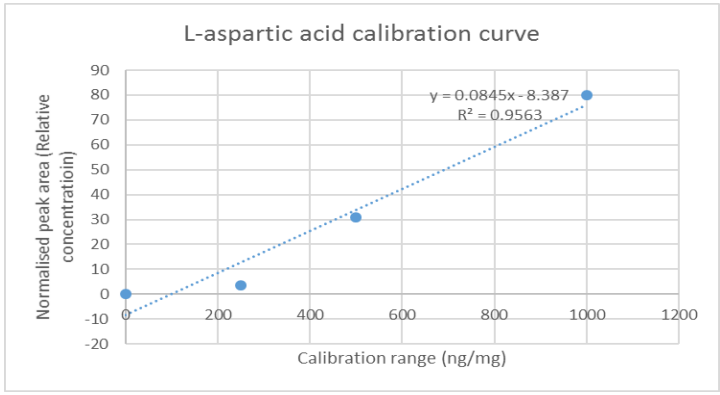
L-aspartic acid calibration curve
y = 0.0845x - 8.387
R² = 0.9563
Normalised peak area (Relative concentratioin)
Calibration range (ng/mg)

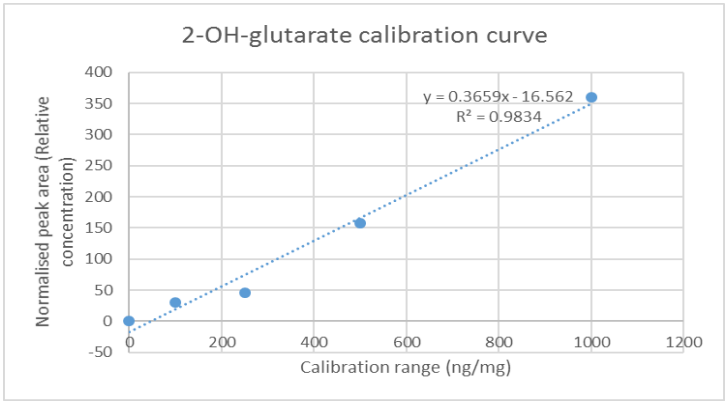
2-OH-glutarate calibration curve
y = 0.3659x - 16.562
R² = 0.9834
Normalised peak area (Relative concentration)
Calibration range (ng/mg)

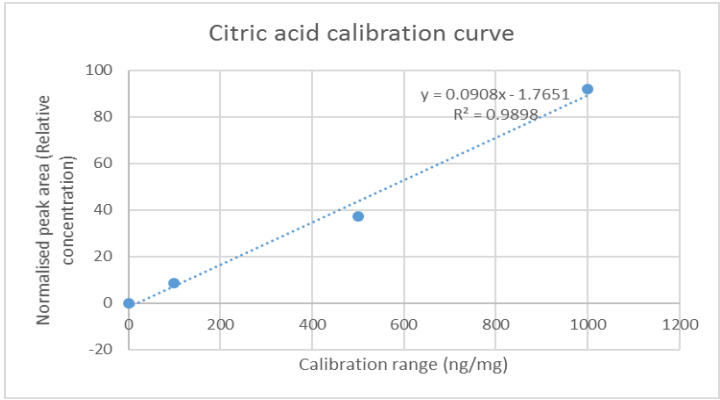
Citric acid calibration curve
y = 0.0908x - 1.7651
R² = 0.9898
Normalised peak area (Relative concentration)
Calibration range (ng/mg)

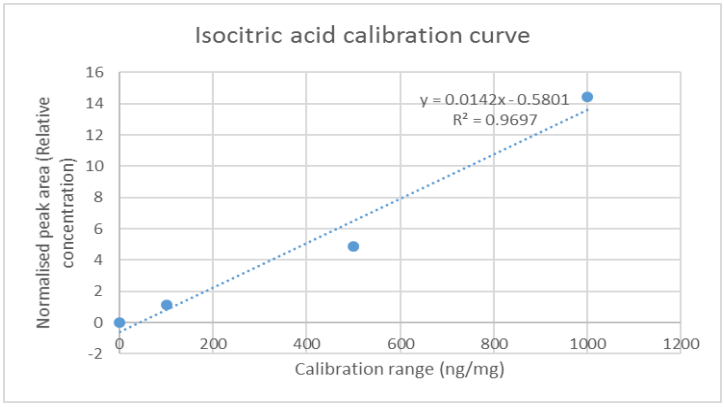
Isocitric acid calibration curve
y = 0.0142x - 0.5801
R² = 0.9697
Normalised peak area (Relative concentration)
Calibration range (ng/mg)

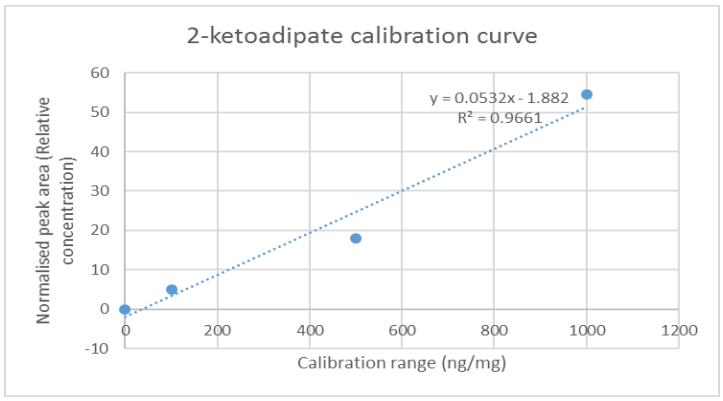
2-ketoadipate calibration curve
y = 0.0532x - 1.882
R² = 0.9661
Normalised peak area (Relative concentration)
Calibration range (ng/mg)

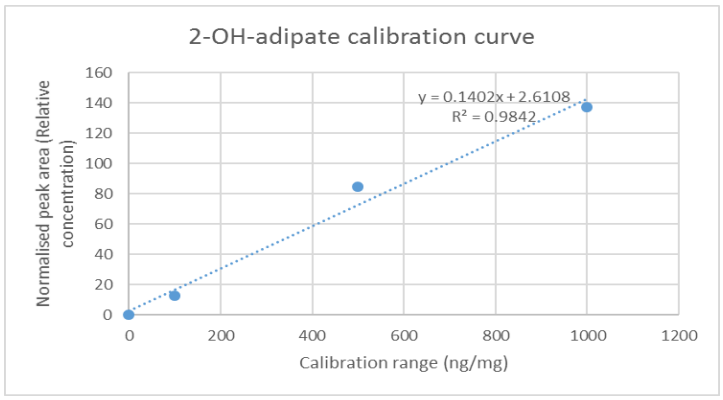
2-OH-adipate calibration curve
y = 0.1402x + 2.6108
R² = 0.9842
Normalised peak area (Relative concentration)
Calibration range (ng/mg)

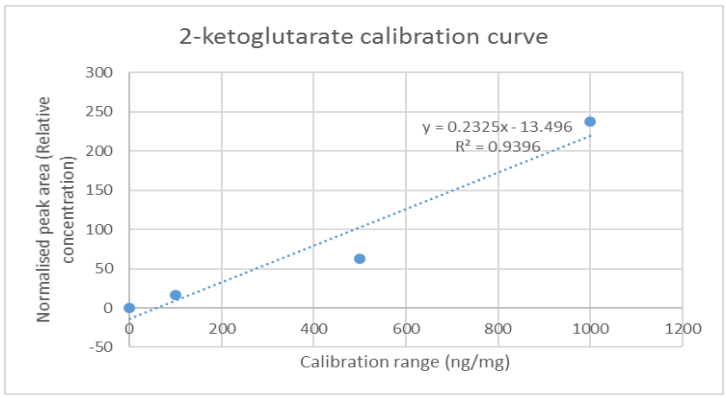
2-ketoglutarate calibration curve
y = 0.2325x - 13.496
R² = 0.9396
Normalised peak area (Relative concentration)
Calibration range (ng/mg)

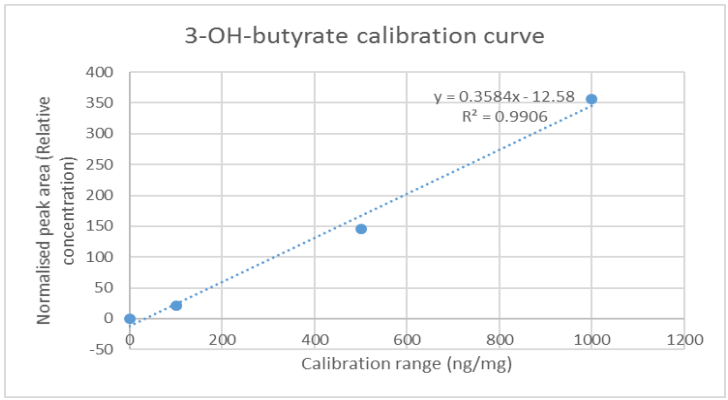
3-OH-butyrate calibration curve
y = 0.3584x - 12.58
R² = 0.9906
Normalised peak area (Relative concentration)
Calibration range (ng/mg)

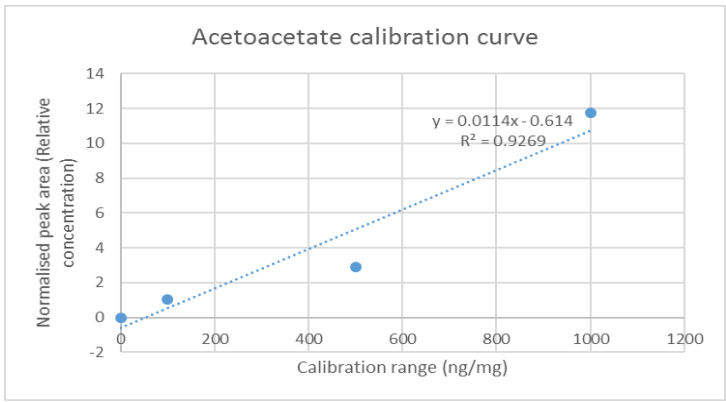
Acetoacetate calibration curve
y = 0.0114x - 0.614
R² = 0.9269
Normalised peak area (Relative concentration)
Calibration range (ng/mg)

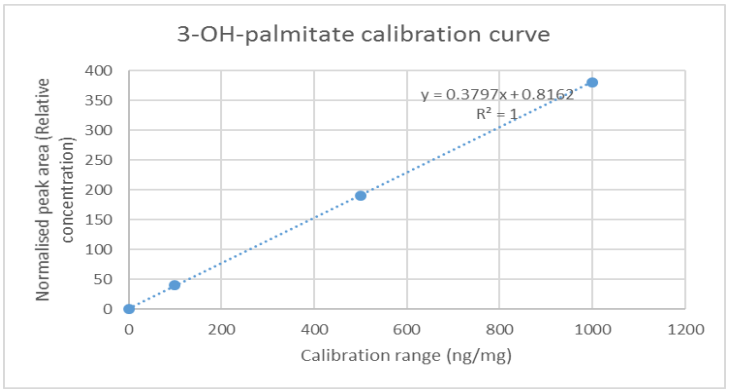

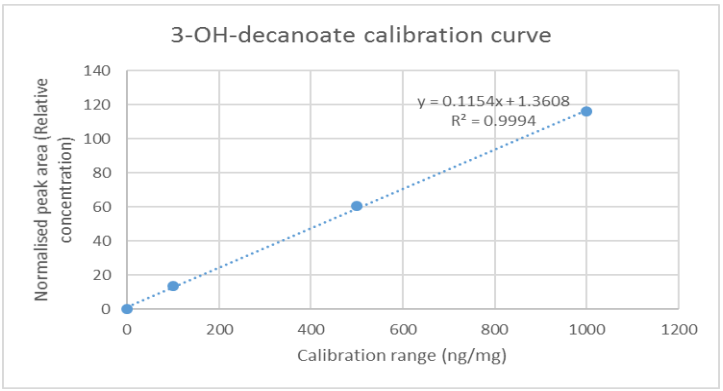

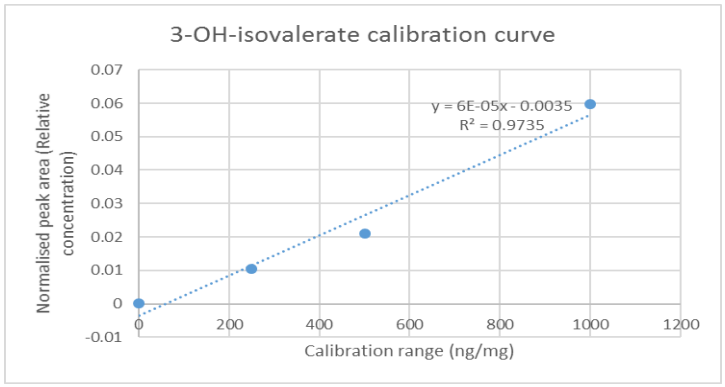

Figures 6.2: Calibration curves of calibrator samples ran adjacent to KO and WT brain samples.

Calibration curves of calibration samples ran throughout the analysis of mouse liver samples.

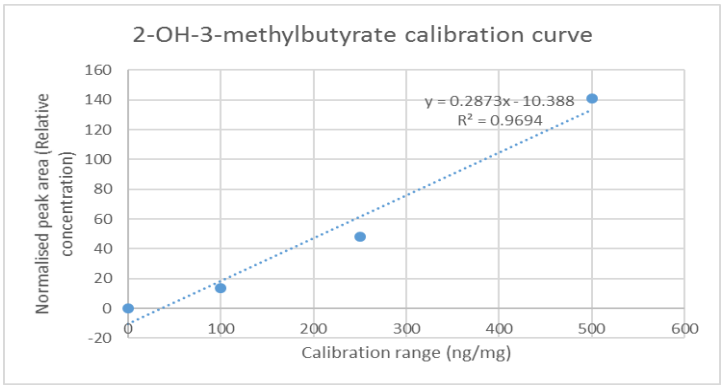

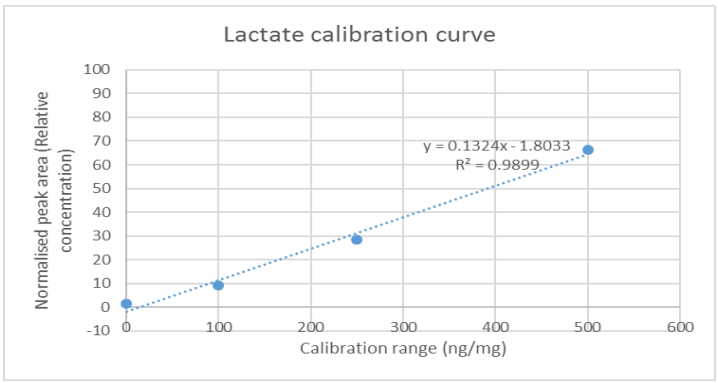

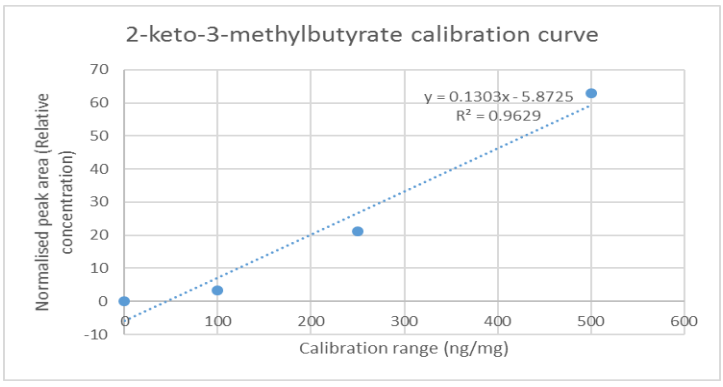

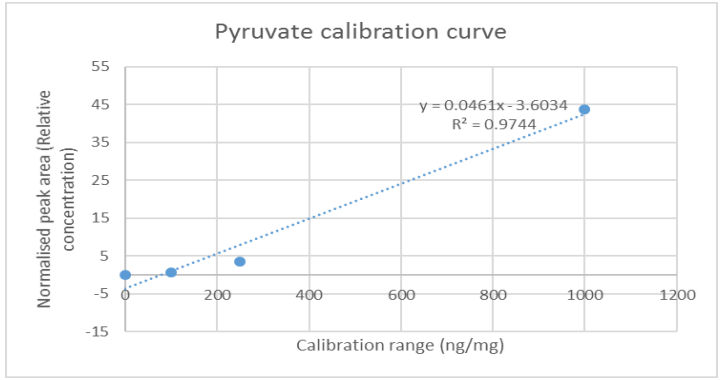

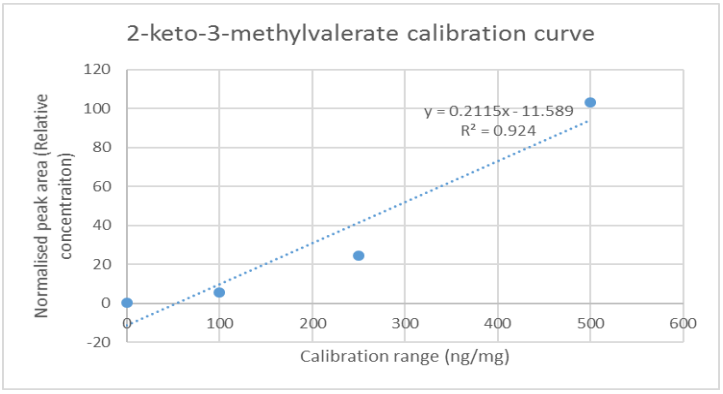
2-keto-3-methylvalerate calibration curve
y = 0.2115x - 11.589
R² = 0.924
Normalised peak area (Relative concentraiton)
Calibration range (ng/mg)

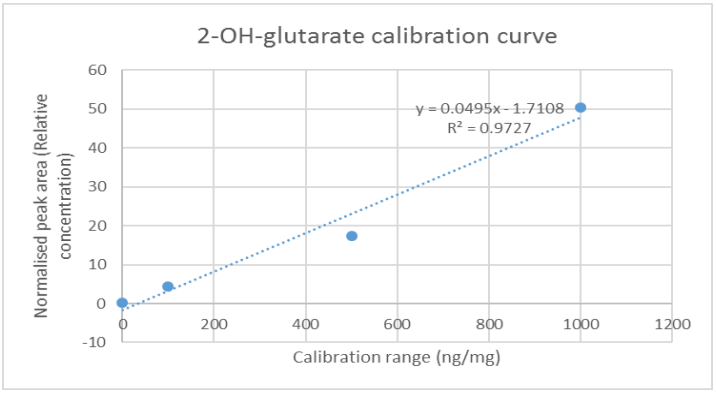
2-OH-glutarate calibration curve
y = 0.0495x - 1.7108
R² = 0.9727
Normalised peak area (Relative concentration)
Calibration range (ng/mg)

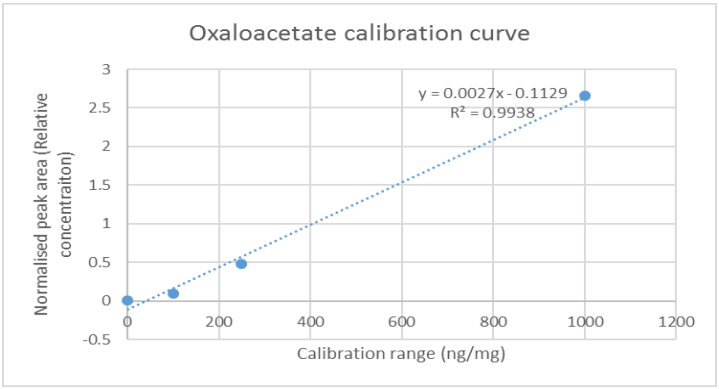
Oxaloacetate calibration curve
y = 0.0027x - 0.1129
R² = 0.9938
Normalised peak area (Relative concentraiton)
Calibration range (ng/mg)

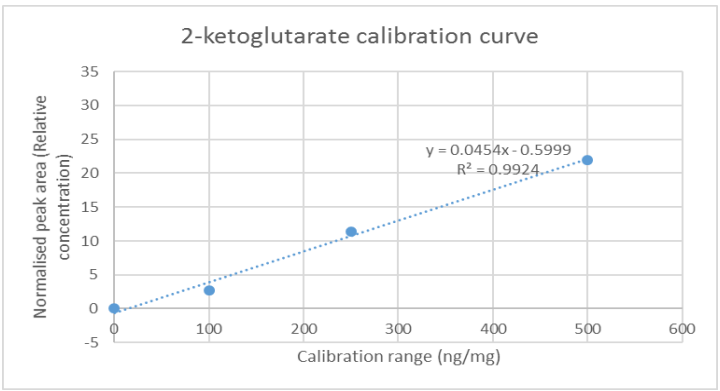
2-ketoglutarate calibration curve
y = 0.0454x - 0.5999
R² = 0.9924
Normalised peak area (Relative concentration)
Calibration range (ng/mg)

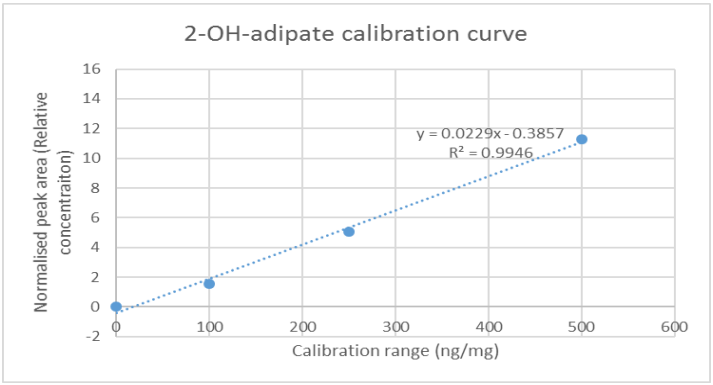
2-OH-adipate calibration curve
y = 0.0229x - 0.3857
R² = 0.9946
Normalised peak area (Relative concentraiton)
Calibration range (ng/mg)

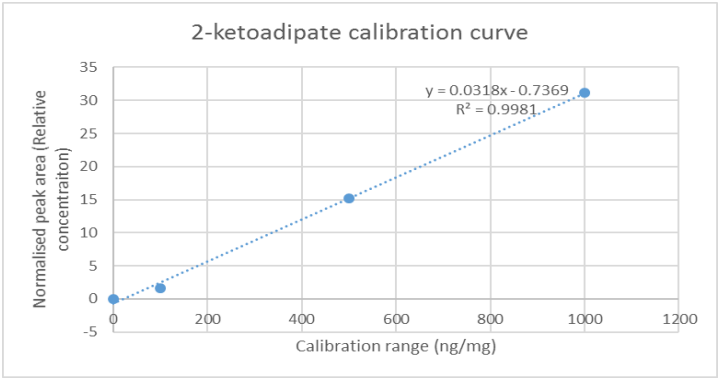
2-ketoadipate calibration curve
y = 0.0318x - 0.7369
R² = 0.9981
Normalised peak area (Relative concentraiton)
Calibration range (ng/mg)

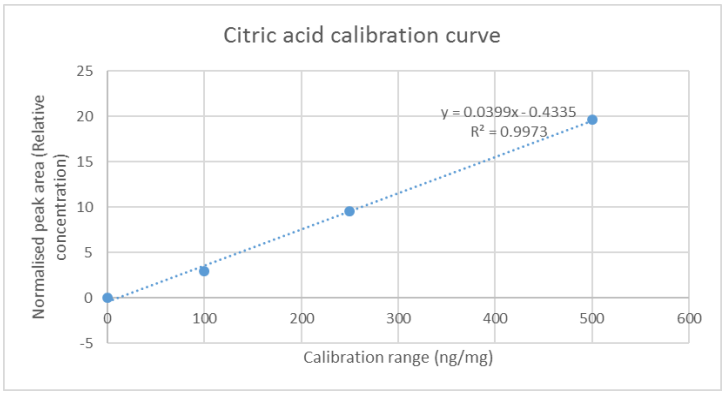

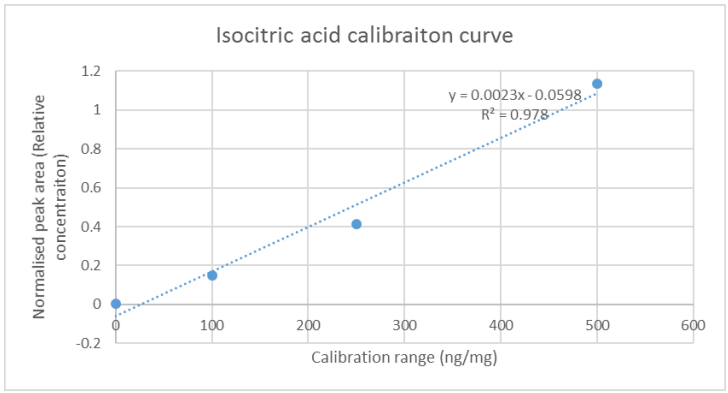

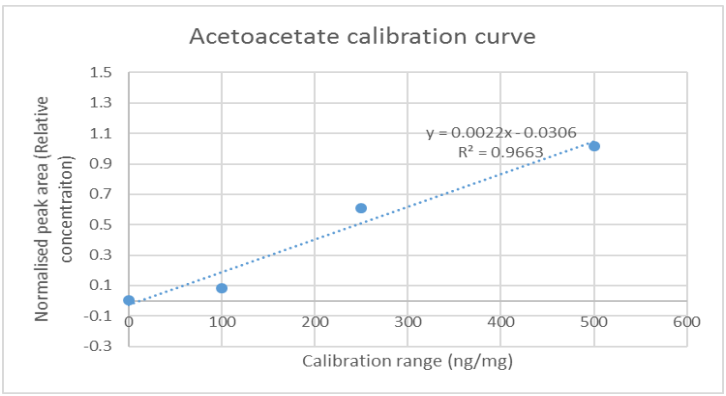

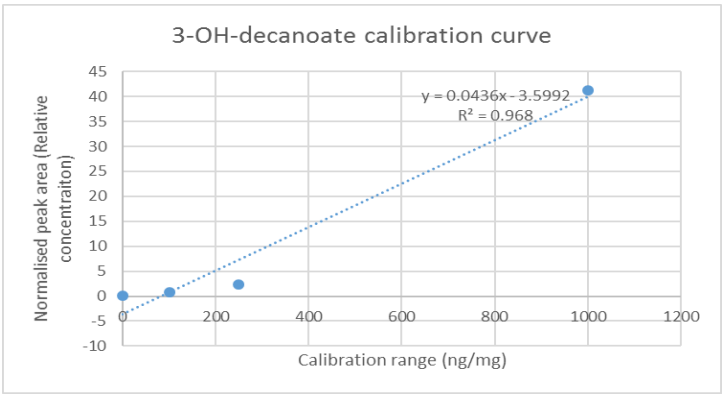

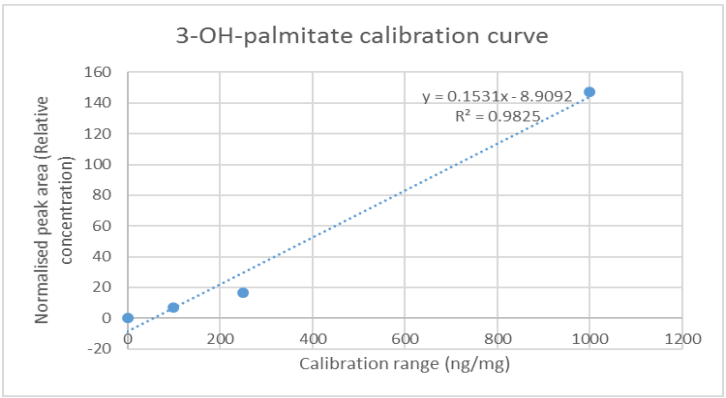

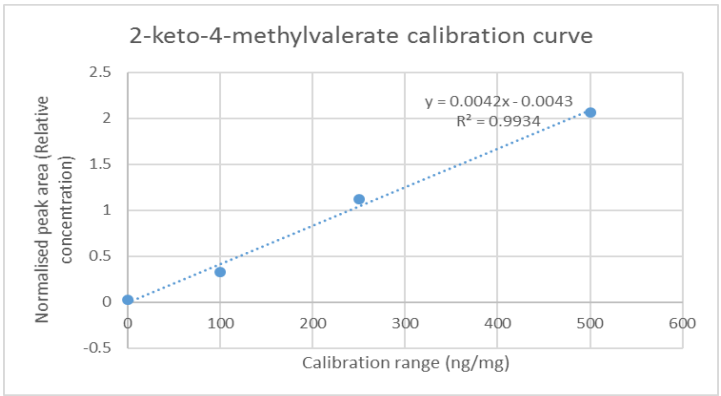

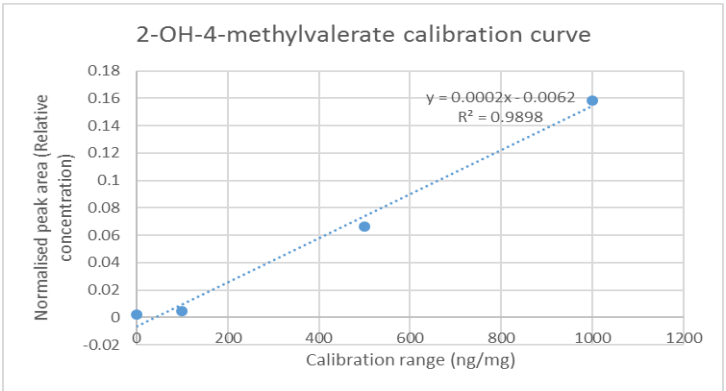

Figures 6.3: Calibration curves of calibrator samples ran adjacent to KO and WT mice liver samples.

Appendix B

The following compounds: Methylmalonate, Succinylacetone and 3-OH-propionate, all underwent the same MRM optimisation after MTBSTFA derivatization. These compounds are metabolic markers for specific inborn errors of metabolism and were compiled into a separate method (Method 4), which was also used to elucidate differences of these compounds in NDUFS4 mice liver, brain and heart samples. As per the derivatization with MTBSTFA, yielding more specific precursor and ions and therefore more selective MRM transitions, expanding this method to markers of inborn errors of metabolism could be useful in the early detection of such mitochondrial disorders.

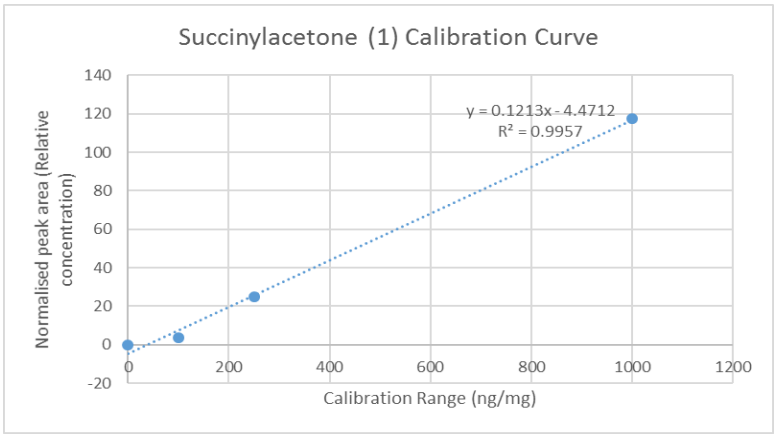

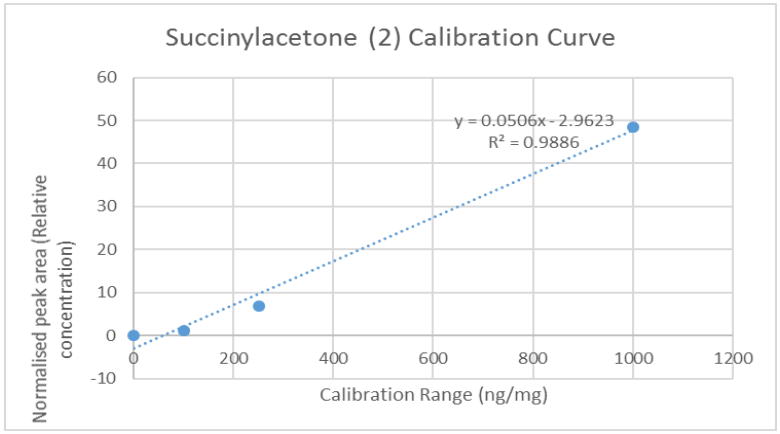

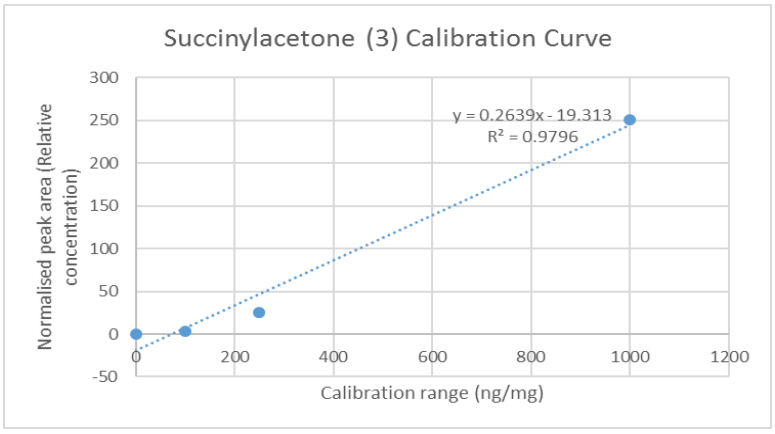

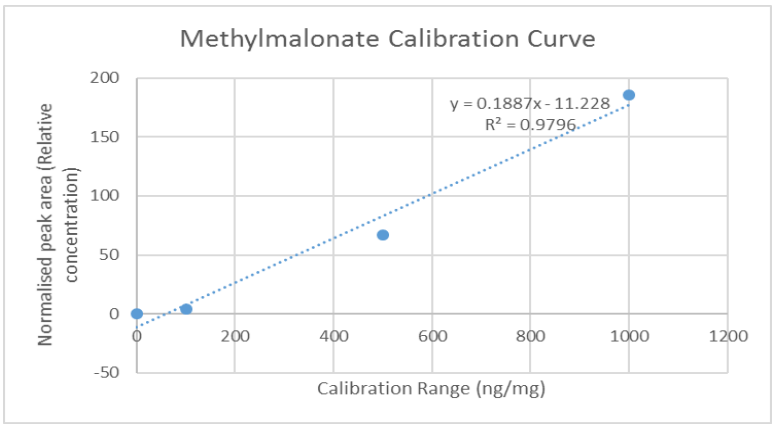

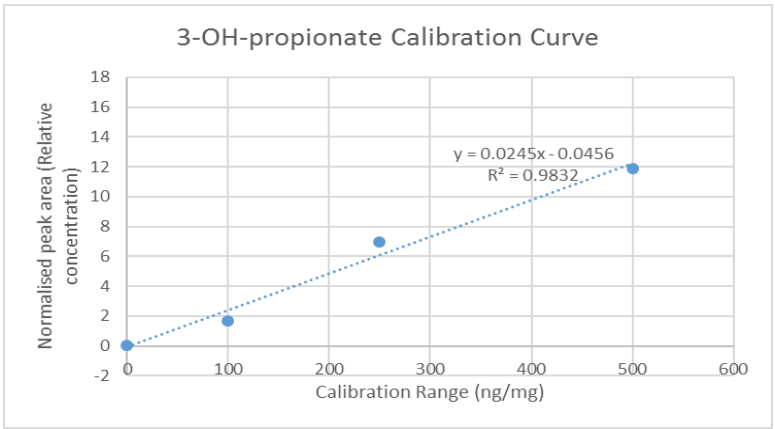

Figures 6.4: Calibration curves of calibrator samples ran adjacent to KO and WT heart samples.

Table B1: KO and WT heart analysis statistical parameters of the measured compounds in method 4.

Compound	p-value Raw	FDR corrected	Effect size	ES degree	HMDB code
Succinylacetone	0.00333729	0.01001187	1.733304667	↑	HMDB0000635
3-OH-propionate	0.213579981	0.271553769	0.732959622	NA	HMDB0000700
Methylmalonate	0.271553769	0.271553769	0.49164614	NA	HMDB0000202

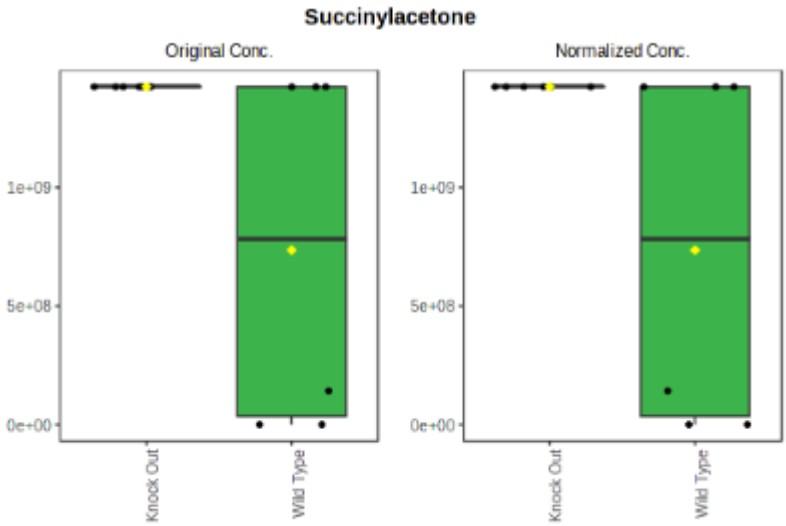

Figure 6.5: Box plots of succinylacetone measurements in KO and WT mice heart samples.

Tyrosinemia type I is a hereditary autosomal recessive trait resulting from mutations in the fumarylacetoacetate hydrolase (FAH) gene (Charkrapani *et al*, 2012), which encodes for a key enzyme in the breakdown of tyrosine. This disorder causes the inability of the production of fumarate and acetoacetate from fumarylacetoacetate, which ultimately causes the subsequent conversion of fumarylacetoacetate to succinylacetoacetate which decarboxylates into succinylacetone. Succinylacetone is a metabolite known to cause the inhibition of the enzyme 5-aminolevulinic acid dehydratase, causing inhibition of heme synthesis and resulting in acute liver failure, coagulopathy, hypotonia and more clinical symptoms that all manifest within the first 6 months of the newly born neonate. Tyrosine screening methods have been used in the past for the assessment of tyrosinemia type I however, these screening methods usually lack specificity since the accumulation of tyrosine does not always occur in patients with tyrosinemia type I (Allard *et al*, 2004). Henceforth, targeting the specific biomarker succinylacetone might be a better option for screening patients with suspected mutations in the FAH gene.

Although NDUFS4 KO mice do not pertain mutations in the FAH gene, succinylacetone was only found to be elevated in the KO mice heart samples (Figure B2). As the energy crises in these

mice persists, alternative routes for energy production might cause the upregulation of non-essential amino acid catabolism. The catabolic products of tyrosine are fumarate and acetoacetate, which fuels the TCA cycle with fumarate and directs acetoacetate for ketolysis. Seeing that the TCA cycle intermediate malate was already found to be slightly elevated in the KO group, incorporating the formed fumarate into the TCA cycle for malate production might be slowed. Also, the two ketone bodies 3-OH-butyrate and acetoacetate were found to be significantly increased in the KO mice. With acetoacetate levels already being elevated in the KO mice heart, the catabolic breakdown of tyrosine might only occur partially, causing left over fumarylacetoacetate to be converted to succinylacetoacetate and ultimately succinylacetone.

This provides some insight to the possible link between biomarkers of specific inborn errors of metabolism and model organisms with a CI deficiency, provoking the thought that redox balance might also play a role in the production of biomarkers specific to other diseases not relating to NDUFS4 gene mutations.

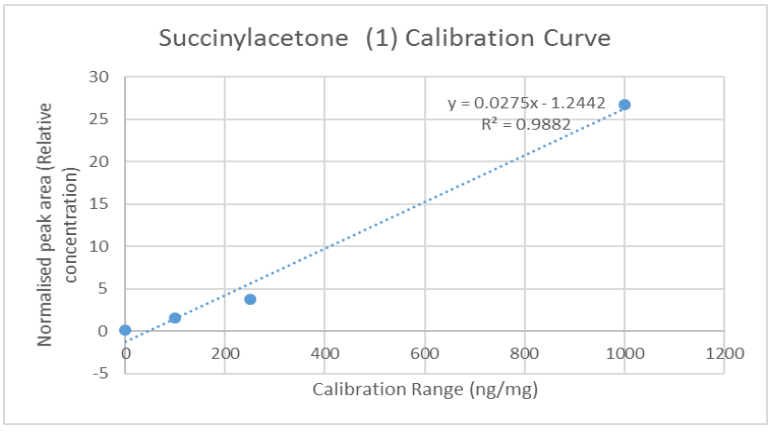

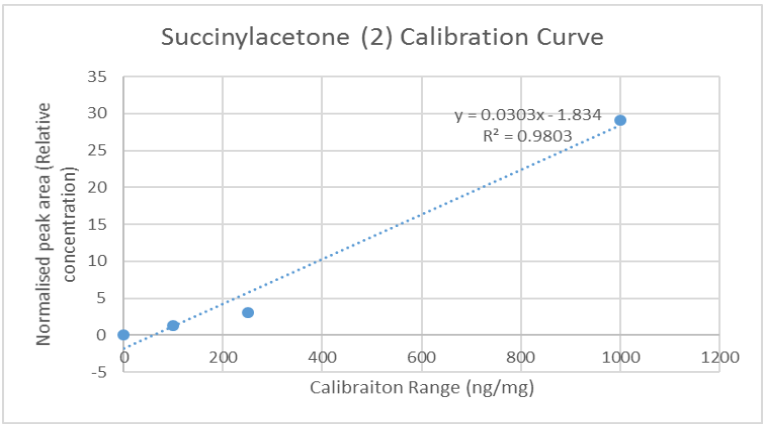

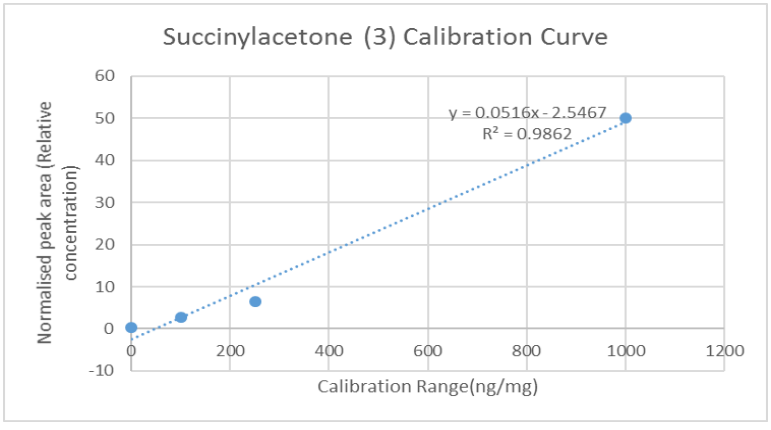

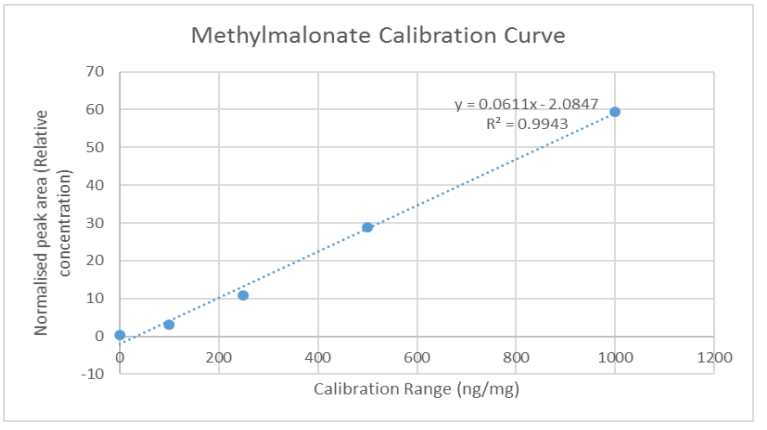

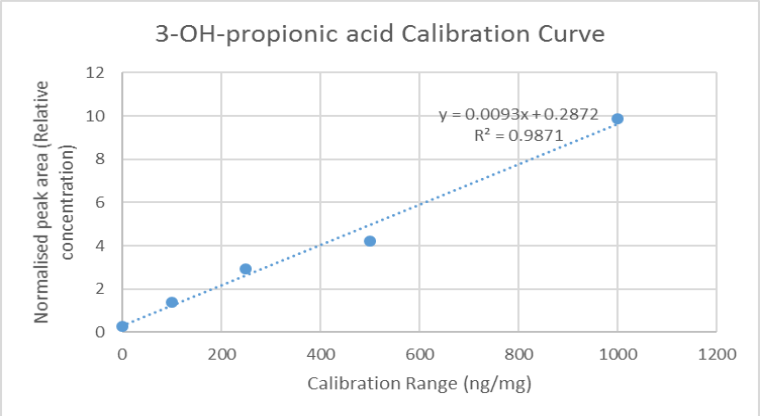

Figures 6.6: Calibration curves of calibrator samples ran adjacent to KO and WT mice brain samples.

Table B2: KO and WT brain analysis statistical parameters of the measured compounds in method 4.

Compound	p-value Raw	FDR corrected	Effect size	ES degree	HMDB code
Methylmalonate	0.352493916	0.352493916	0.509335611	NA	HMDB0000202
Succinylacetone	0.238899642	0.352493916	0.696352384	NA	HMDB0000635

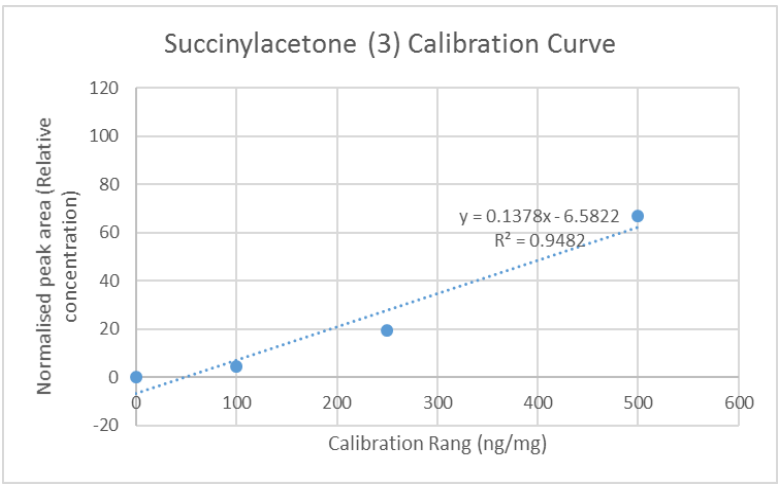

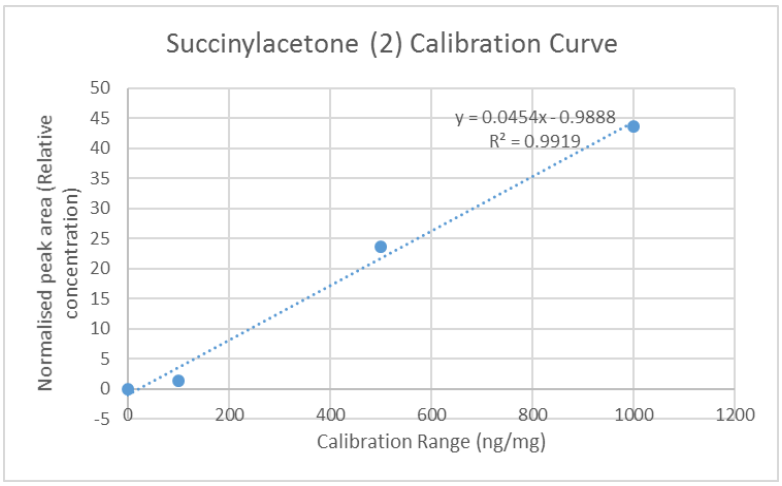

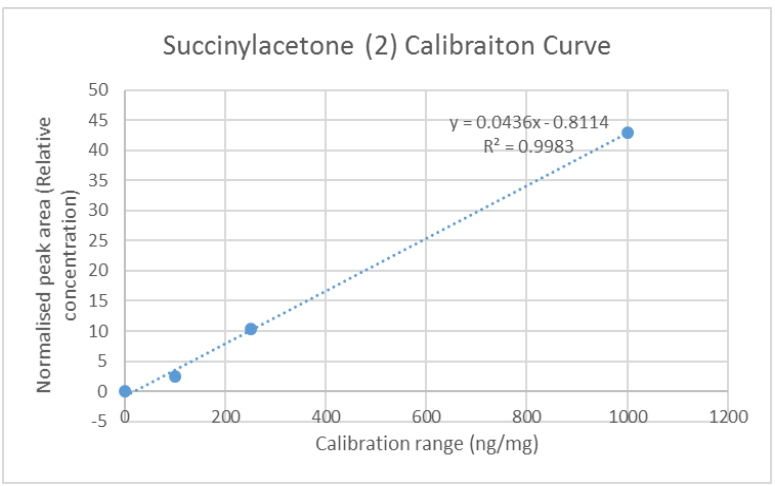

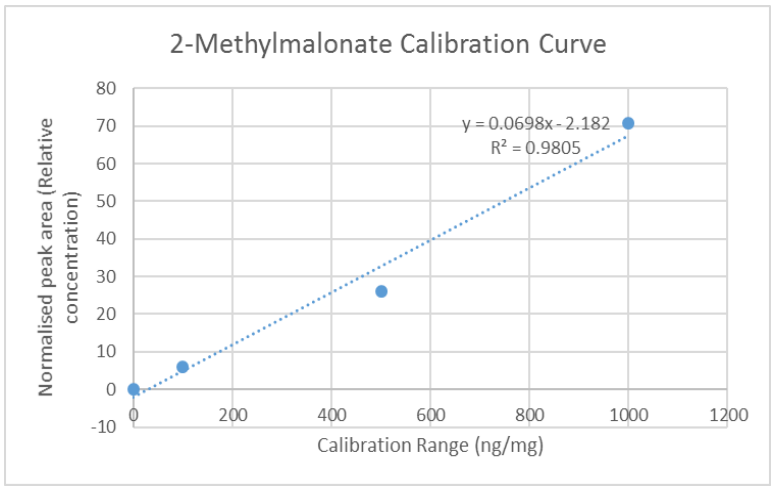

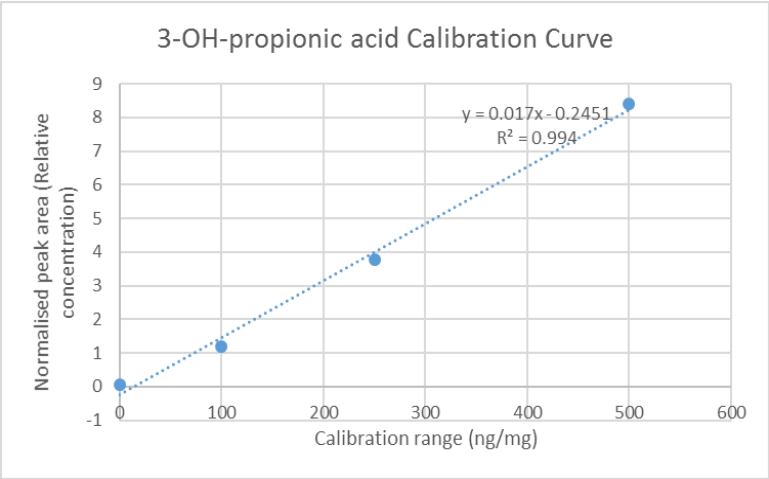

Figures 6.7: Calibration curves of calibrator samples ran adjacent to KO and WT mice liver samples.

Table B3: KO and WT liver analysis statistical parameters of the measured compounds in method 4.

Compound	p-value Raw	FDR corrected	Effect size	ES degree	HMDB code
Succinylacetone	0.204502756	0.321956826	0.72468446	NA	HMDB0000635
3-OH-propionate	0.214637884	0.321956826	0.5725977	NA	HMDB0000700
Methylmalonate	0.575819707	0.575819707	0.26917036	NA	HMDB0000202